Application of Modal Decomposition Techniques to Study Flow Behavior in Aneurysms

A Dissertation

Presented in Partial Fulfillment of the Requirements for the

Degree of Doctor of Philosophy

with a

Major in Mechanical Engineering

in the

College of Graduate Studies

University of Idaho

by

Paulo V. Yu

Approved by:

Major Professor: Vibhav Durgesh, Ph.D.

Committee Members: Ralph Budwig, Ph.D.P.E.; John Crepeau, Ph.D.,P.E.;

Tao Xing, Ph.D.,P.E.

Department Administrator: Gabriel Potirniche, Ph.D., P.E.

December 2021

Abstract

Aneurysms are localized expansions of weakened blood vessels that can be debilitating or fatal in some cases upon rupture. Previous studies have shown that aneurysm formation, growth, and rupture are complex processes influenced by factors from different disciplines like biology, material science, and fluid dynamics. Fluid mechanics is one of these factors that is important in better understanding aneurysm behavior and may lead to design of better treatment methods. However, analyzing flows in aneurysms can be challenging as the flows exhibit complex spatial and temporal behavior. For this investigation, there are two overarching goals: 1) to quantify the spatial and temporal behavior of the large-scale flow structures in aneurysms for a range of inflow conditions and two different aneurysm models, and 2) to quantify the observed flow features using modal decomposition techniques. For this study, two different, idealized, rigid, sidewall aneurysm models were used, one with a low risk of rupture and another with a high risk of rupture. An in-house experimental setup was developed using a ViVitro Labs pump system where non-dimensional inflow conditions such as Womersley number (α) and peak Reynolds number (Re_p) were varied to match conditions typically found in the human circulatory system. An aqueous glycerin solution was used to match the index of refraction of the models. Particle Image Velocimetry (PIV) was used to measure the flow field in the aneurysm models. The hardware synchronization-based alias imaging approach was used to capture the behavior of large-scale flow structures at different phases in the flow cycle. Advanced analysis methods such as Proper Orthogonal Decomposition (POD) and Dynamic Mode Decomposition (DMD) were utilized to identify the spatial and temporal behavior of the large-scale flow structures in the aneurysm.

This investigation showed that large-scale flow structures in the aneurysm are influenced by changes in Re_p, α, and morphology. The complex behavior of large-scale flow structures, in turn, influences the path and strength of these vortical structures, their

growth and decay, and the impinging location and wall shear stress distribution. These variations in high-shear stress zones and impinging locations can be correlated to high and low risk of rupture in the studied aneurysm models. POD provided an optimal modal description of the observed large-scale flow structures. POD analysis showed the interplay of modes and highlighted how the large-scale structures evolved during the different phases of the flow and impacted fluid dynamics parameters. Furthermore, the mathematical description of the flow fields defined by POD modes also provided a method to qualitatively compare the observed flow features in aneurysm studies. In contrast, the DMD modes are not optimal, but they provided critical information about the dynamics of flows and the spatiotemporal behavior of the flow structures. DMD provided frequencies and growth rates of the spatial structures. DMD analysis clearly demonstrated that the large-scale flow features and dynamics are influenced by the Re_p, α, and aneurysm shapes. We also developed a framework for using DMD with traditional velocity field measurements with a low-frame rate setting for this investigation. This framework allowed us to observe high-frequency flow features despite using low-frame rate PIV systems. Finally, this study also showed that both POD and DMD provide flow information at any desired phase in the flow cycle, saving considerable experimental time compared to phase-locked measurements.

Acknowledgements

I would like to express my sincerest gratitude to my major professor, Dr. Vibhav Durgesh, who guided me and supported me throughout the course of this research. I would have never attempted to achieve something this great in my life and realized my potential and I owe that to him.

I would also like to thank Dr. John Crepeau, Dr. Ralph Budwig, and Dr. Tao Xing for their continued support and being part of the committee. I appreciate them for reviewing my dissertation and providing insightful feedback on my work.

I would like to thank the University of Idaho's Mechanical Engineering for their financial support. The assistantships have helped throughout the program and have allowed to find my career path.

I also gratefully acknowledge the American Society of Mechanical Engineers Graduate Teaching Fellowship Program. This fellowship has helped me pursue a career path in academia.

The accomplishments throughout my graduate studies would not have been possible without the constant support and motivation from my friends and family: Girlie, Irish, Erin, Edgar, Johnny, Kevin, Macrey, Pam, and Rodrigo.

Dedication

To my mother and father,

for your never ending love and support. I will be forever grateful.

Table of Contents

List of Tables

List of Figures

Nomenclature

$\mathbf{A}$	Linear coefficient operator matrix
$\tilde{\mathbf{A}}$	Approximated linear coefficient operator matrix to $\mathbf{A}$
$a_i(t)$	Time-varying coefficient for ith POD mode at time t
a_m	Complex fitting parameter for multi-modal Womersley solution
BF	Bottleneck factor
CCD	Charged-coupled device
CFD	Computational Fluid Dynamics
D	Diameter (m)
$\mathbf{D}$	Data set containing snapshot s_1 to s_{m-1}
$\mathbf{D}'$	Data set containing snapshot s_2 to s_m
DMD	Dynamic Mode Decomposition
d_p	Particle diameter (m)
ϵ_{min}	Minimum RMS error (%)
ϵ_{max}	Maximum RMS error (%)
ϵ_{avg}	Average RMS error (%)
f	Frequency (Hz)
f_i	DMD frequencies from imaginary component of Λ
g_i	DMD decay rates from real component of Λ
J_0	Bessel function of order zero
j	Imaginary unit $(\sqrt{-1})$
L_e	Pipe entry length
M	Number of frequencies used for multi-modal Womersley solution
m	Number of snapshots
PIV	Particle Image Velocimetry
P_s	SuperPump setting $(mL/stroke)$

$\mathbf{R}$	Spatial velocity correlation matrix
r	Pipe radial distance (m)
R	Pipe radius (m)
Re_p	Peak Reynolds number
s_i	ith velocity field snapshot
St	Stokes number
t	Time (s)
T	Time period (s)
$\overrightarrow{U}(x,y)$	Velocity vector
u	Streamwise velocity component (m/s)
$\mathbf{U}$	Right singular vector from SVD
v	Transverse velocity component (m/s)
$\mathbf{V}$	Left singular vector from SVD
V_{max}	Maximum centerline velocity in the pipe (m/s)
x, y	Cartesian coordinates, x and y axis
α	Womersley number
β	DMD amplitudes
Δt	Time step (s)
Λ	Eigenvalues of $\tilde{\mathbf{A}}$
ρ_b	Blood density (kg/m^3)
ρ_f	Working fluid density (kg/m^3)
ρ_p	Particle density (kg/m^3)
ν_b	Blood kinematic viscosity (m^2/s)
ν_f	Working fluid kinematic viscosity (m^2/s)
μ_f	Dynamic viscosity of fluid (kg/ms)
Φ	DMD modes
$\overrightarrow{\Psi^i}(x,y)$	ith Proper Orthogonal Decomposition mode

$\psi^i_{uu}(x,y)$	Streamwise component of ith Proper Orthogonal Decomposition mode
$\psi^i_{vv}(x,y)$	Transverse component of ith Proper Orthogonal Decomposition mode
Ω_{xy}	Domain of interest
Σ	Rectangular diagonal matrix from SVD
ω_m	Frequency used for multi-modal Womersley solution
λ^i	Energy captured by ith Proper Orthogonal Decomposition mode
$\mathbf{V_{and}}$	Vandermonde matrix
$\otimes$	Tensor product
$\langle ... \rangle$	Ensemble averaging

CHAPTER 1

Introduction

There are many different types of flows that can be observed in nature or in engineering systems. Simple flows such as flow over a flat plate or a pipe flow can be justified using by using basic physics and engineering principles [3]. Others are complex, such as cavity flows [4] and artery flows [5], which multi-factorial components encompasses geometry, biology, material and fluid compositions, and chemistry to name a few. Understanding different flows, simple or complex, is important as it translates to efficient engineering designs, increased engineering productivity, reduced operational costs, increased lifetime of components, and reduced catastrophic events leading to loss of lives. However, understanding complex flows can be challenging as they require extensive knowledge, resources, and ingenuity.

Aneurysms are examples of arterial flows which exhibit complex flow phenomena. Aneurysms are an abnormal localized expansion of a weakened blood vessel, and researchers have classified them based on their shape or location. Typical shapes of aneurysms are fusiform or saccular [6], and they are found in the aorta (called abdominal aortic aneurysms (AAA)) [2], in the portion of the aorta through the chest area (called thoracic aortic aneurysms) [7], and in the brain (called cerebral or intracranial aneurysms) [8]. A few examples of aneurysms are shown in Fig. 1.1. An intracranial aneurysm imaged using digital subtraction angiography is shown in Fig. 1.1(a), and an abdominal aortic aneurysm imaged using magnetic resonance imaging (MRI) is shown in Fig. 1.1(b). These imaging techniques are used for detection and detailed diagnosis of aneurysms. Meanwhile, aneurysms, when left untreated or undetected, can impact blood circulation as well as lead to thrombosis and blood clots [9, 10, 11]. A ruptured aneurysm can cause stroke or internal bleeding which are life-threatening scenarios. Current aneurysm treatment options are limited to observation, clipping, placement of coils or stents [8]. However, each treatment method has their associated risks such as pa-

tient discomfort after surgery, recurrence, and infections. Access to the aneurysm during operation also poses a challenging task of managing and assessing aneurysms [8].

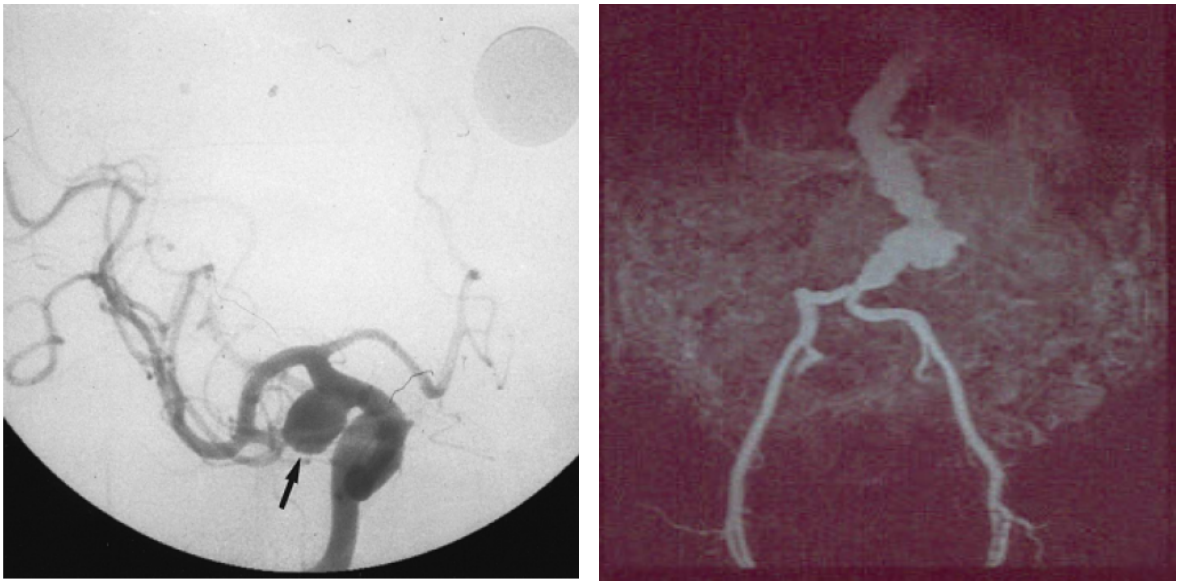

(a) (b)

Figure 1.1: Aneurysm examples in the human circulatory system. (a) cerebral aneurysm [1], and (b) abdominal aortic aneurysm [2].

There is an exhaustive list of studies that have made efforts to provide explanations on different aspects of aneurysm behavior, from initiation, growth, and rupture, and to develop assessment and treatment methods for patients accordingly. For instance, earlier studies used aneurysm size to quantify likelihood of rupture [12, 13]. With advancements in technology and computational capabilities, other studies used non-dimensional geometrical characterization of different sizes and shapes to identify aneurysms with low and high risk of rupture [14, 15, 16]. A few studies have focused on hemodynamics using computational [17, 18, 19] and experimental [20, 21, 22, 23] approaches. These studies have identified hemodynamics to play an important role in aneurysm behavior particularly in the aneurysm progression and rupture. Although these studies have shown the presence and complex nature of large-scale flow structures in aneurysm flows, focus on these flow structures' impact on hemodynamic parameters has surprisingly not been investigated

in detail. This includes investigations focusing on different geometries, inflow conditions, and the ability to create mathematical models to accurately predict the large-scale flow behavior.

Despite significant progress in the overall understanding of aneurysms, predictability of their flow behavior and its contribution to the aneurysm pathophysiology in the presence of unsteady inflow conditions still requires further investigation. For example, large-scale flow structures in aneurysms are shown to be complex and their behavior remains to be understood. Flow structures in aneurysms can consist of a single recirculating structure that can remain stationary or move throughout the cardiac cycle. Other flow structures may contain one or more recirculating regions that remain stationary or become unstable during the cardiac cycle. These different large-scale flow patterns are shown in previous studies [24, 25, 26, 27, 19]. Budwig et al. [24] reported that for steady flow in AAAs, the flow field is characterized by a jet of fluid surrounded by a recirculating vortex. Fukushima et al. [25] reported that in pulsatile flow in AAA, vortices appeared and disappeared at different phases in the cardiac cycle. During this time, the center of the vortex moved from upstream to the downstream side of the aneurysm. Yu and Zhao [26] reported that for steady flow of their sidewall aneurysm studies, a large recirculating vortex occupies the entire aneurysm sac. Le et al. [27] described in their numerical studies that for sidewall aneurysm models, the vortex structure can remain stable or move within the aneurysm sac. These observed flow complexities and presence of large-scale structures have motivated us to further investigate the behavior through the use of advance data analyses methods.

Modal decomposition methods have been growing in popularity as data analyses tools to aid researchers in gaining an understanding of complex flows. They are used to extract physically important features or modes in the flow field. These modes or spatial features are associated with characteristic values which represent either the energy levels or frequencies and growth rates [28]. Examples of these decomposition methods

are Proper Orthogonal Decomposition (POD) which provides modes that are optimally determined to capture the most possible energy in the fewest amount of modes [29, 30, 31], and Dynamic Mode Decomposition (DMD) which provides modes that are defined by a single frequency of oscillation and growth behavior [32, 33]. Review articles from Taira et al. [28, 34] and Rowley and Dawson [35] provide an excellent broad overview of different modal decomposition techniques as well as applications of these methods to flows over a cylinder, an airfoil, and a rectangular cavity.

The application of POD and DMD to aneurysm flows have been applied to velocity data obtained either from experimental [36] or computational fluid dynamics (CFD) investigations [37, 38, 39, 40]. A few of these studies have used these modal decomposition techniques as a means to improve computational simulations, or to quantify different flow regimes. For example, Byrne et al. [37] used POD on CFD simulations to classify the hemodynamics of patient-specific intracranial aneurysm geometries according to spatial complexity and temporal stability using parameters derived from vortex core lines. The results from their study found ruptured aneurysms have complex and unstable dynamics while unruptured aneurysms have simple and stable dynamics. Daroczy et al. [38] used POD to determine the spectral entropy of different flow regimes, and quantified the flow state between laminar, transitional, or turbulent regimes for use with their hybrid simulations. Janiga [40] used POD for comparison of different time-varying three-dimensional hemodynamic data and showed the ability of POD to reduce the complexity of the time-dependent data for quantitative assessment. With DMD studies, Abulkhair [36] used POD and DMD on AAAs to reveal hidden dynamical structures. Lastly, Lozowy [39] used DMD to remove high-frequency turbulent oscillations from the reconstructed velocity field. These initial studies have provided valuable insight and motivation to researchers on how modal decomposition methods can be used in analyzing complex aneurysm flows.

The existing body of knowledge about aneurysms have shown that they are a widely

studied fluid dynamics problem, and researchers have attempted to answer fundamental questions on aneurysm behavior with different levels of success. The advancements in experimental and computational methods have allowed researchers to look at the aneurysm problem in greater detail than before, and enabled them to gain deeper insights into the flow dynamics of aneurysms using advanced analyses methods. However, additional work is still needed to expand the current knowledge on aneurysm flows, particularly in characterizing flow structures at different inflow conditions and their influence on the aneurysm hemodynamics. There is still a lack of comprehensive experimental studies that capture these large-scale flow structures and quantify their importance to the overall flow dynamics. Although different studies show certain flow behavior to be similar or different in their investigations, they have not provided an answer on why certain flow behavior (i.e., large-scale structure movement) will move in similar/different fashion when the inflow condition changes. Understanding and capturing this behavior will allow us to create a mathematical description of the flow which can be used to predict or control the flow in aneurysms. With the help of advanced decomposition methods such as POD and DMD, these important flow features can be captured, differentiated, and analyzed to help identify the similarities or differences across different inflow conditions.

Objectives

The goal of the present study is to provide an overarching work of investigating spatial and temporal behavior of large-scale flow structure on impinging location, vortex strength, movement, and wall shear stress in aneurysms for a range of inflow conditions. Decomposition methods such as POD and DMD will be used as diagnostic tools to analyze flow behavior in aneurysms. They will also be used to highlight important spatial features responsible for the changes in fluid behavior. The results from this study will highlight the impact of large-scale flow structures on the flow behavior in aneurysms and make way for further research on mitigating or controlling these structures. Furthermore, the

results from the advanced analyses methods can be used to predict flow behavior for similar aneurysm geometry across different inflow scenarios outside of this study. This is beneficial as creating mathematical models can aid researchers in further parametric studies without running experiments which can be time-consuming, expensive, and take a lot of resources. With this in mind, the following objectives will be outlined and addressed in this dissertation as follows:

- To capture the large-scale structures for a complete pressure cycle at different inflow scenarios using hardware synchronization. For this study, two different, idealized, saccular aneurysm models are considered. These models are characterized with bottleneck ratio (BF) of 1 and BF of 1.6. BF is defined to be the ratio of maximum aneurysm diameter (D_{max}) to the aneurysm neck diameter (D_{neck}) (i.e., $BF = D_{max}/D_{neck}$). BF of 1 is defined to low risk of rupture while BF of 1.6 is considered to be of high risk of rupture [15, 16]. In order to capture the large-scale flow structures and their behavior in this investigation, several experimental methods are implemented and discussed in the Approach section.

- To demonstrate application of POD to extract the energetic modes pertaining to the large-scale flow structures captured from the phase-averaged data. The use of POD will provide key information about the flow dynamics in aneurysm flows such as isolating different flow features and identifying uniqueness and similarities of the large-scale flow structure across different inflow scenarios. Furthermore, the use of POD will allow us to gain an insight into the interplay of the modes used to describe the flow field.

- To demonstrate application of DMD to extract spatiotemporal information of the large-scale flow structures which the POD method is not able to provide. DMD will provide temporal information on flow structures and their associated frequency and growth behavior.

- First task is to validate the use of traditional flow field measurements such as Particle Image Velocimetry (PIV) with a low-frame rate setting for use with DMD.
- Second task is to implement the DMD with low-frame rate PIV data and analyze the spatiotemporal behavior of the large-scale structures for $BF = 1.0$ at different inflow conditions.

The dissertation is organized as follows: Chapter 2 provides a brief overview of aneurysm studies. Chapter 3 lays out the experimental methodology while Chapter 4 provides the analyses tools utilized in this study. Next, Chapter 5 provides the results from the flow behavior in the two different aneurysm models. Here in this chapter, POD results will be presented. It will be shown that POD provides unique modal descriptions for each inflow scenario and can effectively reconstruct the flow data using few energetic modes. DMD results will be presented for one of the aneurysm models. Here it will be shown that DMD can also effectively represent the flow evolution using appropriately selected DMD modes and frequencies. Lastly, Chapter 6 summarizes the important findings of this study.

CHAPTER 2

Background

This chapter provides a background on studying aneurysms as well as background on advanced data techniques. The chapter is organized such that aneurysm studies are first discussed. Background studies on Proper Orthogonal Decomposition and Dynamic Mode Decomposition are then provided to give insight on their potential uses and applications to studying complex flows. Initial attempts of using these methods on aneurysm flows will also be discussed further in the chapter.

2.1 The aneurysm problem

The cardiovascular system is an internal flow loop in which blood circulates. It functions to transport oxygen, nutrients, and waste throughout the body [5]. The system consists of the heart, blood, and blood vessels. The heart pumps blood into a complex network of muscular elastic arteries and distributes blood to different organs and supplies them with nutrition [5, 6]. The blood returns to the heart through a network of veins with a system of valves regulated by secondary muscular activity and the action of the heart itself [41]. The pumping process is repeated approximately 70 times per minute, 100,000 times per day, or almost 3 billion times throughout the expected lifetime in a healthy individual [42]. During this time, the arteries adapt to the changes in the flow and pressure conditions by enlarging and shrinking themselves to meet hemodynamic demands [5]. Furthermore, this enlarging and shrinking of the arteries requires the arterial walls to regenerate and remodel to maintain the function and integrity of the system [6]. However, a portion of the arterial wall can weaken due to a disease or other complex process that causes the wall to expand and to form an aneurysm. These abnormal dilatations can appear anywhere where there is a weakened blood vessel, but they primarily appear in the abdominal and thoracic portions of the aorta as well as in the intracranial

arteries [6].

The formation, growth, and rupture mechanisms of an aneurysm are still unknown as it is a multi-factorial process which includes complex interaction among physiological conditions, biological processes, and hemodynamics to name a few. Unruptured aneurysms are a public health concern [43] as they can be asymptomatic remain undetected until time of rupture [44]. A ruptured aneurysm can be debilitating and can be fatal if left untreated. In the United States, an estimated six million people have an unruptured brain aneurysm, and 1 in 50 people suffer from brain aneurysm rupture annually according to the Brain Aneurysm Foundation. Several studies performed on the stages of aneurysm have shown the complexity and multi-disciplinary nature of aneurysm behavior. Numerous aneurysm studies [45, 46, 47] provide an excellent overview of the current understanding of aneurysm behavior. The investigations on aneurysm behavior can be classified into three broad categories: 1) clinical studies, 2) experimental and computational fluid dynamic studies, and 3) experimental and computational biomechanical studies. Previous studies on these categories are briefly discussed in the following sections.

2.1.1 Clinical studies

Clinical studies on aneurysms have attempted to quantify aneurysm behavior based on morphological parameters, and suggest treatment options based on the risk associated with the treatment method. McCormick and Acosta-Rua [12] observed a correlation between aneurysm rupture and average diameter. In their study, the diameter of ruptured aneurysm was greater than 7.4 mm for female patients and 9.2 mm for male patients. A similar study by Mizoi [48] found that surgeries are recommended for patients with aneurysms larger in 5 mm in diameter. Beck [49] used height to neck ratio to determine the difference between ruptured and unruptured aneurysms regarding lobulation. The study found that irregular multilobular appearance was more common in aneurysms of

5-9 mm size that ruptured. Ma et al. [15], Raghavan et al. [16], Shum et al. [50], and You et al. [51], Valencia et al. [52] categorized different aneurysm morphologies, such as aspect ratio (AR) and BF, into different shape indices and their associated risk of rupture. Hoh et al. [53] has shown that bottleneck factor and height-width ratio are associated with aneurysm rupture using patient data. Ujiie et al. [54] used AR and found that AR greater than 1.6 can be associated with an increased risk of rupture. A similar study by Prestigiacomo et al. [55] found that AR was significantly larger in ruptured aneurysms than unruptured aneurysms. Ryu et al. [56] used volume-to-neck ratio (VNR) to indicate that larger aneurysm volume in proportion to the neck can determine higher rupture risk. Tremmel et al. [57] found that aneurysm-to-parent vessel size ratio (SR) is directly correlated to aneurysm rupture, with 83% of unruptured aneurysms with a value of SR of 2 or less, and 77% of ruptured aneurysms with an SR value of more than 2.

Other clinical studies focused on the hemodynamics in aneurysms. Work by Chien et al. [58] found that hemodynamic values, such as wall shear stress (WSS) and flow rate, change at different locations. Hans et al. [59] reported that changes in hemodynamics lead to changes in vessel architecture and that aneurysms can be flow-related. Meckel et al. [60] performed an in vivo study using 4-D MRI to study intra-aneurysmal hemodynamics. In this study, flow patterns, distribution of flow velocities, and WSS seem to be determined by vascular geometry of the aneurysm. Patti et al. [61] found that the blood flow pulsatility was different between ruptured and unruptured aneurysms. These difference were particularly pronounced at the aneurysm neck, which may be an important factor for aneurysm rupture.

Further clinical studies focused on the interaction between aneurysms and peri-aneurysmal environment [62, 63]. Others have reported a rare case of multiple mirror-like aneurysms [64] and rare cases of basilar artery aneurysms [65]. Studies on the circle of Willis have also been performed [66, 67]. Other clinical studies have also suggested that age plays a crucial role in aneurysm growth and rupture [68]. Medical protocols have been placed

for patients with aneurysms that reach 6 cm in diameter or a growth rate of 1 mm/ year [69, 70], although there are cases of smaller aneurysms culminating in rupture [71].

2.1.2 Experimental and computational fluid dynamic studies

Experimental and computational studies of aneurysm blood flow have also been investigated to address different stages of aneurysm pathophysiology. These studies have shown a wide variety of intra-aneurysm flow patterns, ranging from simple to highly complex flow behavior. Budwig et al. [72], Drexler [73], Bluestein et al. [74] investigated the steady inflow through fusiform aneurysms, and found that the flow field through the concentric bulge is characterized by a recirculating vortex. Fukushima [25] and Egelhoff [75] studied the pulsatile inflow conditions in fusiform and saccular aneurysms, and observed different flow behaviors when compared to the steady inflow conditions. It was also observed that the vortices appeared and disappeared at different phases of the cardiac cycle. In similar studies, Steiger [76, 77, 78] and Gobin et al. [79] investigated the flow structure for saccular aneurysms under pulsatile flow conditions and observed that the center of the vortex grew as the flow velocity increased, while the center of the vortex moved from the proximal end to the distal end. This was followed by the transient reversal of flow at the minimum flow phase. Taylor and Yamaguchi [80] performed a computational study of abdominal aneurysms and showed that in the pulsatile flow case, regions of maximum pressure moved based on the flow cycle time. The study also showed that local maximum pressures formed at the distal neck and then declined, which led to the additional strain on the distal neck of the aneurysm bulge. Ferguson [20] worked on identifying the mechanism that could contribute to the initiation, growth, and rupture of aneurysms. The results of the study found that turbulence causes degenerative changes that weaken the wall of an aneurysm which allows it to enlarge. Moreover, the study showed the probability of rupture increases with an increase in intra-aneurysmal pressure, an increase in aneurysmal size, a decrease in the minimum wall thickness of

an aneurysm, or a decrease in the strength of its structural components. Liou and Liao [81] performed Laser Doppler Velocimetry (LDV) measurements on aneurysms with various sizes and found that with decreasing aneurysm size, the inflow angle into the aneurysm, the maximum shear stress acting on the distal lip of the aneurysm, and the intra-aneurysmal vortical motion increased. Studies by Stehbens [82] found that for Re considerably below critical levels for turbulence, flow disturbances in the aneurysm (fusiform, cylindrical, spherical and lateral forms) may be a jet edge phenomenon.

Other investigations focused on the flow structures in aneurysms with curved parent vessels. Niimi [83] found that the vortices induced in aneurysms influenced flow structure and the presence of secondary flow due to vessel curvature. Meanwhile, work by Liou and Liao [84] found that the intra-aneurysmal flow velocity, vorticity, and wall shear stresses increase with increasing curvature of the parent vessel. Furthermore, Liou et al. [85] investigated aneurysms arising from curved parent vessels at various angles and found that aneurysms oriented at $\gamma = 45^{\circ}$ is the riskiest angle where the dome is at risk.

There were also studies that focused on the effect of inflow waveform on the hemodynamics of sidewall aneurysms. Le et al. [27, 86] and Bouillot et al. [23] found that the inflow waveform had a strong influence on intracranial aneurysm hemodynamics, particularly in the vortex formation phenomena. Yu and Zhao [26] investigated the steady flow on stented and non-stented sidewall aneurysm models and found that flow movement inside the aneurysm sac can be suppressed to less than 5% of the bulk mean velocity for both stents and springs. The study also found that the highest level of wall shear stresses always appear at the distal neck of the aneurysmal pouch. Yu and Zhao [26, 22] worked on the pulsatile flow conditions on saccular aneurysms with and without stents or springs. Their investigation showed that the flow velocities inside the aneurysm bulge could not be suppressed completely, but could be reduced by more than 80%.

Baharoglu et al. [87] investigated the impact of aneurysm inflow-angle (IA) and found that increasing IA resulted in higher inflow velocity and greater wall shear stress magni-

tude and spatial gradients in both the inflow zone and dome. Cebral et al. [88] categorized aneurysm hemodynamics depending on the complexity and stability of flow pattern, location and size of flow impingement region, and size of inflow jet. The study found that unruptured aneurysms were more likely to have simple stable patterns, large impingement regions, and jet sizes. On the other hand, ruptured aneurysms were more likely to have disturbed flow patterns, small impingement regions, and narrow jets. Hope et al. [89] used 3D phase-contrast MRI to evaluate aneurysms and found that an unstable flow pattern with a more focal jet may have a high likelihood of rupture compared to one that had a stable helical flow pattern with a large jet. Lu et al. [90] investigated the hemodynamics in mirror aneurysms and found that ruptured aneurysms have lower WSS compared with their parent arteries, a higher portion of the low WSS area to the whole area of aneurysm, and higher oscillatory shear index (OSI) compared with the unruptured aneurysms. Salsac et al. [91] investigated the evolution of WSS during the growth of abdominal aneurysms and found that the mean WSS becomes negative along most of the aneurysmal wall, and the magnitude of the WSS can be as low as 26% of the value in a healthy abdominal aorta.

2.1.3 Experimental and computational biomechanical studies

Work has also been done on experimental and numerical biomechanical studies regarding mechanics of the artery. These can include vessel reconstruction methods to rupture-criterion based on artery properties are presented here. Several comprehensive studies [92, 93, 94, 95] provide an overview of current understanding of mechanics and modeling of arteries. Chen et al. [96] performed CFD on reconstructed hypothetical geometry of a healthy vasculature prior to intracranial formation using Frenet frames. Results of the study observed that locally elevated WSS and gradient oscillatory number (GON) are highly correlated with regions susceptible to sidewall aneurysm formation while hemodynamic indices associated with oscillation of WSS have much lower cor-

relations. Tateshima et al. [97] used rapid prototyping technique from a patient 3D computerized tomography angiogram to reconstruct a basilar aneurysm model. Geoghan [98] used rigid and flexible transparent flow phantoms suitable for PIV and other optical methods.

Several studies worked on quantifying aneurysm behavior and rupture risk based on mechanical properties such as wall stress. Galarreta et al. [99] focused on assessing characteristics of AAA on wall stress. The study found that the local mean curvature as a potential surrogate for wall stress which in turn is related to AAA rupture risk. Results from Kyriacou and Humphrey's [100] studies found that lesion shape, material properties, and loading conditions, not just size, in governing the distributions of stress and strain within a sub-class of axisymmetric saccular aneurysms. Lu et al. [101] used an inverse shell based approach to predict pressure induced wall stress in intracranial aneurysms. Results of the study found that this inverse method may be a viable tool for patient-specific analysis, as patient-specific tissue properties are difficult to obtain. Polzer et al. [102] determined that using residual strains (RS) in computational models lead to homogenized wall stress and reduces peak wall stress (PWS) values. Gasser et al. [103] observed that Peak Wall Stress (PWS) and Peak Wall Rupture Risk (PWRR) were 1.17 and 1.43 times higher in ruptured AAAs than diameter-matched unruptured aneurysms.

CHAPTER 3

Experimental methodology

The organization of this chapter is focused on outlining the design parameters of the experimental setup and test conditions used to help achieve the goal of this study. The aneurysm design models are first discussed which will be followed by the working fluid selection. Next, the theoretical setup of the PIV will also be provided in this section. The flow-loop design will be presented with the focus on controlling the inflow conditions. Lastly, the test inflow conditions that are considered in this study will be presented.

3.1 Aneurysm models

The aneurysm models used in this study are designed to model and simulate the fluid conditions in the human circulatory system. As aneurysm flows are complex in nature, several assumptions and idealizations are made in order to simplify the flow problem and have full control of the experimental study. The design process begins with selecting different criteria to satisfy the aneurysm geometries, flow regimes, and experimental method capability. The first assumption is that the flow will go through a straight, rigid, and circular tube with sufficiently long entry length before reaching the aneurysm cavity. This design allows to control and to determine the fully developed profile upstream of the aneurysm where the behavior is known for steady [3] and unsteady [104] flows. The rigid assumption allows for further simplification as elasticity on the walls has minimal impact on the flow [105, 5, 106]. For steady laminar flows, this entry length can be designed using

$$\frac{L_e}{D} = 0.06Re, \tag{3.1}$$

where L_e is the entry length, D is the tube inside diameter, and Re is the Reynolds number. Thus, the entry length L_e depends on tube diameter D to be used in the experiment,

and Re which depends on the flow regime typically found in human circulatory system. The Reynolds number, which is the ratio of fluid inertia to viscous forces, is determined using

$$Re = \frac{\rho_f V_{avg} D}{\mu_f}, \tag{3.2}$$

where ρ_f is the fluid density, V is the average fluid velocity, and μ_f is the dynamic viscosity of the fluid. In human circulatory system, typical Re varies from 1 in small arterioles to 4000 in the aorta [5].

For unsteady flows, the entrance region now depends on the Womersley parameter (α) and Re. The Womersley number [104] is given as

$$\alpha = R\sqrt{\frac{2\pi f}{\nu_f}}, \tag{3.3}$$

where R is the tube radius, f is the flow frequency, and ν_f is the fluid kinematic viscosity. The Womersley number is a measure of the ratio of unsteady forces to viscous forces. For low α numbers, the viscous forces are more dominant than unsteady forces, the velocity profiles are parabolic in shape, and the centerline velocity oscillates in phase with the driving pressure gradient. On the other hand, α above 10 has unsteady forces more dominant than viscous forces, which results in the flow with a flat velocity profile [104, 5]. In the human circulatory flow, α varies from 1 to 10 depending on the size of the artery [107, 108]. With these in mind, the maximum entrance length for low α unsteady flow scenarios is approximately the same as the steady peak flow and dependent on Re [109, 5]. Thus, the design is based on Re using peak velocity that are to be used in this investigation.

The next design criteria to capture the large scale flow structures is that the aneurysm model material should allow optical access to the flow as well as it can easily match the refractive index of the working fluid used in the study. Optical access to the flow is necessary as the experimental method (i.e., PIV) is an optical-based technique which

records velocity field measurements using a laser and a camera. Furthermore, the PIV system to be used has a laser with a wavelength of $532nm$ which requires the model material to have a high transmissivity for the light to pass through. For this design constraint, several studies have provided a list of solid materials which can easily match a compatible fluid [110, 111, 112, 113], and have been used to help in the design of the aneurysm models.

The design constraints from previous paragraphs are then used to create the aneurysm models using a computer-aided design (CAD) software, and the schematics are shown in Figs. 3.1 and 3.2. The rigid tubes selected are made from borosilicate glass with total length of 443 mm (17 in.), outside pipe diameter of 12.7 mm (0.5 in.), and inside diameter of 9.37 mm (0.369 in). The material and dimensions are selected for their commercial availability and costs. The aneurysm geometries are then fabricated using a local and professional glass shop (TG Scientific Glass, 23041 La Cadena Dr., Laguna Hills, CA 92653). After fabrication, the actual aneurysm geometries are measured using images of model slices at different locations. The aneurysm dimensions acquired are then used to characterize the aneurysm geometry using studies from Ma et al. [15] and Raghavan et al. [16]. Note that although the physical dimensional values obtained here are not what is typically found in the human circulatory system, the models' length and velocity scales are appropriately adjusted such that Re and α match the values typically found in the human arteries. Thus, using these design parameters, the maximum Re that will have a fully developed profile in a steady laminar case is $Re = 586$. As for the downstream conditions, the exit length of the tubes are shorter than the entry length as flow instabilities will get smoothen out in the flow reservoir, and thus will not be of interest in the study.

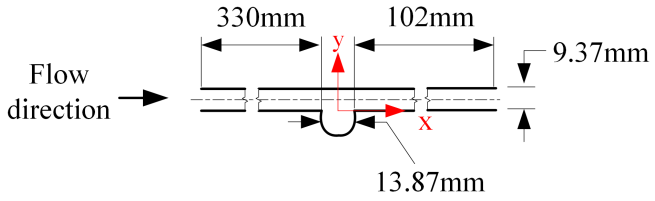

Figure 3.1: Aneurysm dimensions for $BF = 1.0$.

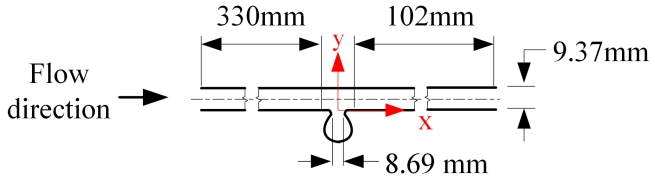

Figure 3.2: Aneurysm dimensions for $BF = 1.6$.

3.1.1 Aneurysm housing

Each of aneurysm models is placed in a Plexiglass housing as shown in Fig. 3.3. To gain optical access to the region of interest in a flow investigation, common experimental setups require a clean outside fluid and a matching working fluid mixed with seeding particles. The current design allows to isolate the region of interest, which is the aneurysm region, to have an outside fluid for flow visualization. It also allows for ease of access especially during maintenance. The surface of the Plexiglass are required to be scratch-free to allow optical access to the aneurysm region. The aneurysm housing is put together using an acrylic glue, while the surfaces that contact with the aneurysm model are sealed with a silicon sealant to prevent the outside glycerin mixture to leak during the experiment. Due to the silicone sealant applied between the aneurysm model and Plexiglass, the models become fixed with the housing. This requires the aneurysm model to be oriented with its sac facing the bottom of the housing. This orientation of the aneurysm sac prevents any air bubbles to be stuck inside the sac if the bulge is orientated upwards.

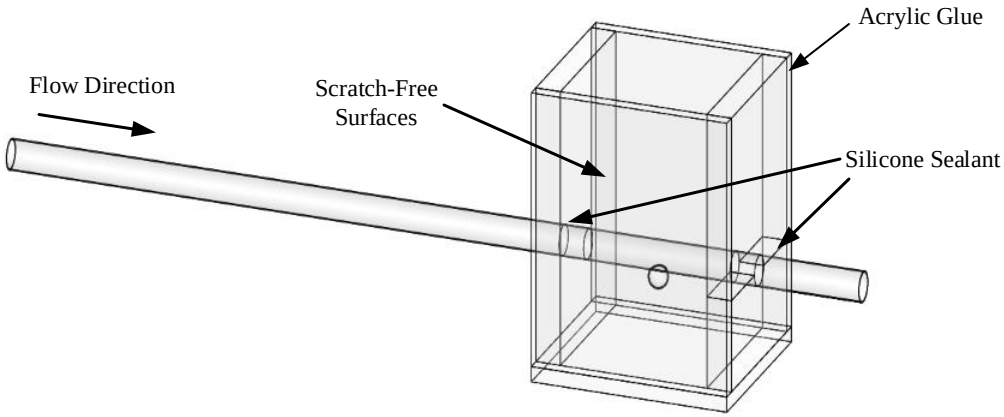

Figure 3.3: 3-D view of housing to contain aneurysm models.

3.2 Fluid selection

In this study, velocity field measurements will be acquired by performing PIV measurements in the aneurysm region. To perform these measurements, it is critical for the refractive index of the working fluid and the aneurysm models to accurately match and minimize image distortion. As PIV is an optical-based measurement tool that will be used for this study, it is then important to closely match the refractive index of fluid and the solid material to precisely illuminate region of interest. If the refractive index is not matched, refraction through a cylindrical tube wall for instance, can generate hidden regions and multiple images [114]. An example of refractive index matching can be seen in Fig. 3.4 where grid lines are placed behind the borosilicate glass model used in this study ($n = 1.47$ [110, 111, 113]). If the refractive index of the fluid is not matched with the glass model, as shown in Fig. 3.4(a) where light goes through the interfaces of air, borosilicate, and air, it results into a distorted image of the grid lines. The distortion in the grid lines disappears when the refractive index of the fluid matches with the model as shown in Fig. 3.4(b) using pure glycerin.

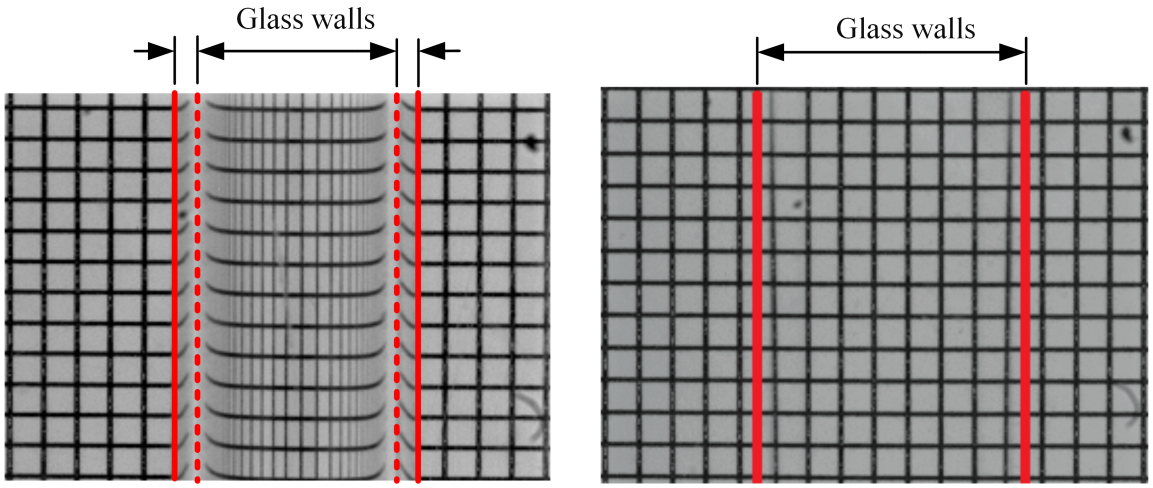

(a) (b)

Figure 3.4: View of grid lines through liquid-solid interfaces. (a) Index of refraction mismatch with air and borosilicate interfaces, and (b) Matching index of refraction with glycerin and borosilicate interfaces.

Several studies have provided excellent lists of materials and fluids with their refractive index values [110, 111, 112, 113]. Previous investigations have found success in using glycerin to match refractive index of their solid models [76, 115, 25, 79, 26, 116, 23, 117] . Furthermore, glycerin has been widely used for investigations as it is low-cost, commercially available, and easy to handle in terms of use and disposal. Thus, for this currently study, an aqueous glycerin solution of 60% by volume is used. This aqueous solution is prepared such that the fluid properties can be used to match the inflow conditions in the human circulatory system while still matching the index of refraction of the solid material.

3.2.1 Validation of index of refraction

Experiments are performed to quantify the impact of index of refraction mismatch between the borosilicate glass model and aqueous glycerin solution. For this quantification, a set of grid lines of known spacing are placed inside the tube with the aqueous solution. The objective in mind is to identify the change from the known grid line spacing and the

new grid line spacing after submerging the lines in the aqueous glycerin solution. Details of this experiment are provided in the next following paragraphs.

Grid lines of $0.5mm$ in spacing are first generated from a commercial software to ensure full control of thickness and quality of the lines. The grid lines are printed on a transparency paper which are then cut to fit the inside diameter of borosilicate glass tube. Next, tube and grid lines setup are placed in a rectangular Plexiglas container. Aqueous glycerin of 60% glycerin by volume is then prepared and poured into the container, and an image of the glycerin-water mixture is taken using a high-resolution camera (8MP Imager LX8M, LaVision Inc.) with a macro lens attached (Tokina ATX, $f = 100mm$). Once the image is acquired, it is then analyzed using MATLAB to identify the grid line spacing.

An image analysis built in-house is used to determine and to compare the grid line distortions occurring for the aqueous glycerin. The goal of this image analysis is to determine the grid spacing by extracting the image intensities across a given image. The analysis begins by opening the image, and the user selects the inner diameter of the tube as well as the end location to extract the image intensities. The program then extracts the intensities row-wise and performs an ensemble averaging of these intensities. The valleys found in the figure correspond to the center of each grid line. A second-degree polynomial curve fitting is performed to the ensemble average to have a sub-pixel accuracy of the valley detection. The newly found valleys are then used to determine the change in grid line spacing.

The result of this analysis is shown in Fig. 3.5. In this plot, the pixel difference is normalized to the pure glycerin while the distance is normalized to the pipe radius (R). It is observed from this figure that a good agreement with the 100% glycerin with minimal distortion of the grid lines (i.e., within 95-100%). From these results, the 60% glycerin by volume is able to be justified for use in this study.

Here we note that index of refraction experiment was performed on a cylindrical tube,

the results would be different for a spherical geometry such as an aneurysm shape. This is because different angles of incidence occur at different locations in the sphere when compared to a round tube. However, we expect the difference in the optical distortion between the round tube and sphere to be acceptable for the purpose of this investigation. Further quantification of this difference can be quantified using a ray tracing approach which can be part of future studies.

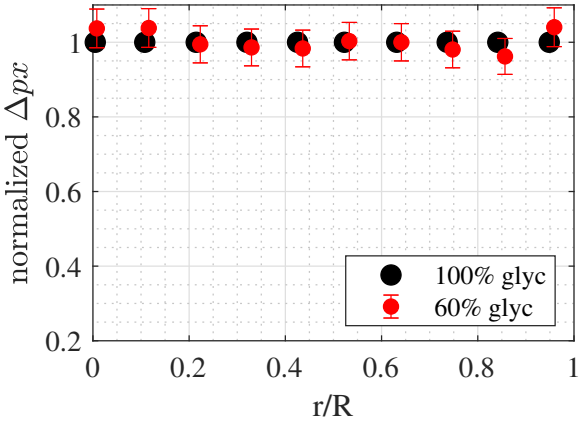

Figure 3.5: Normalized pixel difference for different glycerin-water mixtures.

3.2.2 Validation of fluid parameters

The fluid properties of the aqueous glycerin solution such as density ρ_f and ν_f are determined in order to calculate the Re and α values for this study. As glycerin is a widely used fluid for different applications and studies [76, 115, 25, 79, 26, 118, 116, 23, 117], the properties of the fluid and its aqueous solutions at different temperatures can easily be determined. These values are readily available using published data [119, 120, 121, 122]. The viscosity values are verified using a Cannon-Fenske viscometer, and experiments are repeated several times for accuracy and repeatability. Thus, using this mixture yields a density value of ρ_f=1168.3 kg/m^3 and a kinematic viscosity of ν_f=1.453·10^{-5} $m^2/s \pm 3.5794x10^{-7}m^2/s$ for 95% confidence level.

3.3 Particle Image Velocimetry (PIV)

In this section, Particle image velocimetry (PIV) will be discussed. PIV is an optical-based velocity field measurement technique which utilizes a laser, charged-coupled device (CCD) cameras, seeding particles, and optically-accessible model. A basic PIV arrangement is shown in Fig. 3.6. The basic principle of PIV is that the laser sheet illuminates the flow field seeded with light-reflecting particles. The CCD camera takes two successive images (i.e., image pairs) of this illuminated flow field. By knowing the displacement of each particle and the time difference between the image pairs, the velocity of the particles and thus the entire velocity field can be determined.

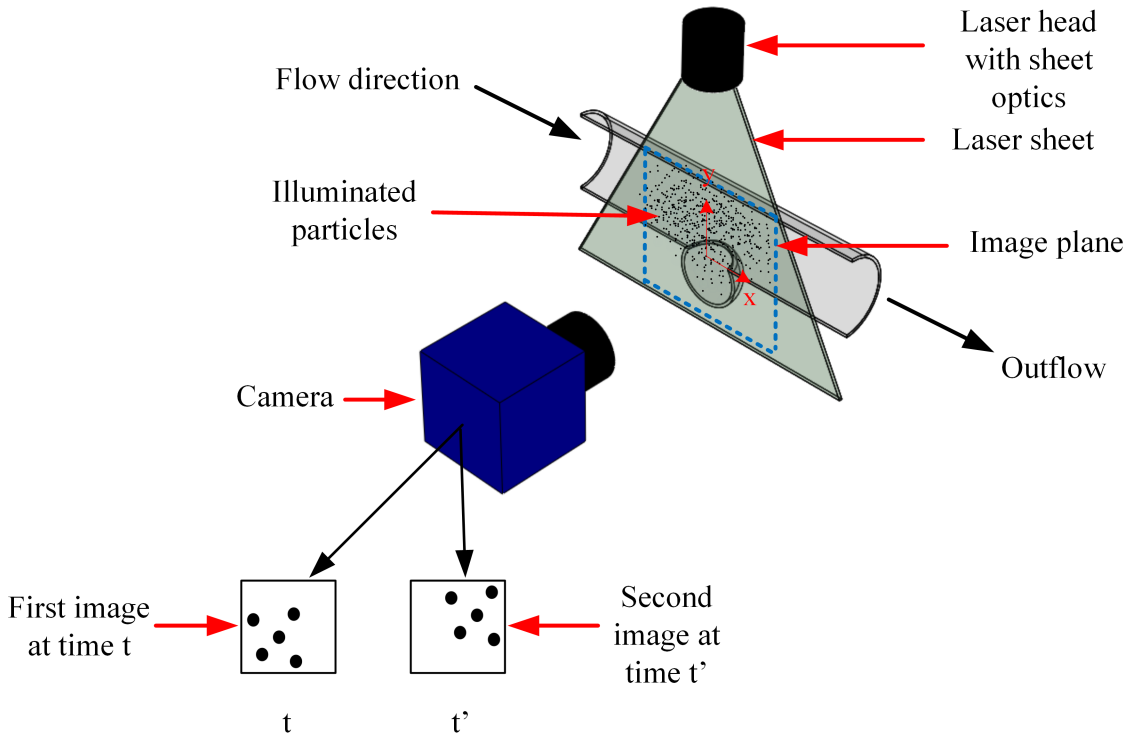

Figure 3.6: Particle image velocimetry arrangement.

The velocity determination of the entire flow field involves several steps. This is because the images which contains numerous particles are not moving in the same speed, each image are then divided into small sections called interrogation areas. These areas

can take any shape (square, circular, etc.) as well as take size (4-128 pixels). Auto or cross-correlation algorithm is then performed for the image pairs' interrogation area to determine the direction and speed of the particles. A correlation map is then generated for each interrogation. area. By finding the peak location, and thus the location of maximum correlation, the displacement of the particle can be found. To speed up the analysis, Fast Fourier Transform (FFT) is implemented. The entire process of velocity vector determination for a single interrogation area can be seen in Fig. 3.7 for cross-correlation as an example.

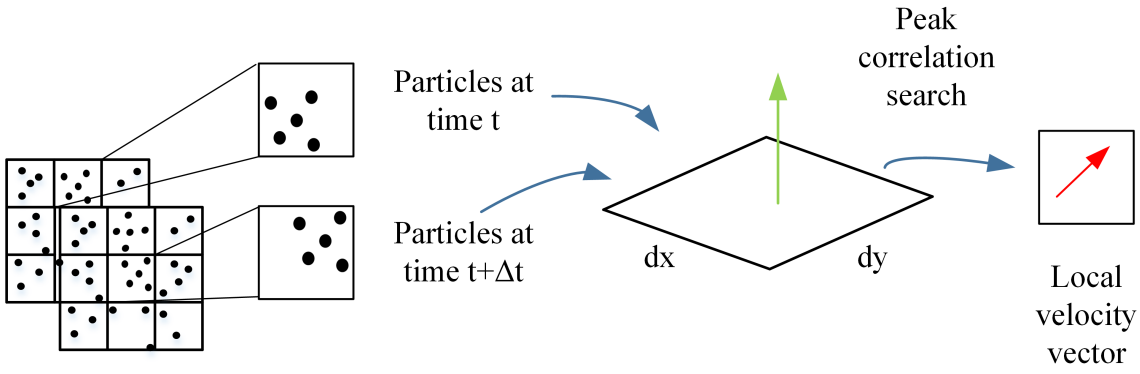

Figure 3.7: Evaluation of velocity vector using cross-correlation.

The next few subsection discusses the components in a typical PIV system and further details on PIV technique. Each subsection provides information on the role of each component as well as the process involved in performing a basic PIV measurement.

3.3.1 PIV system components

Camera

The first component of the PIV system to be discussed here is the camera. The camera is a device to detect and store optical information. In this case, the image recording is performed electronically which provides immediate availability and feedback during the operation or experiment. The camera used in the experiment is based on a charged-

coupled device (CCD) which is an electronic image sensor to convert light into electric charge. A CCD is made from a semi-conducting substrate which comprises of metal conductors on the surface, an insulating oxide layer, an n-layer and a p- layer.

The basic working principle of a CCD is as follows. Voltage is applied between the metal conductors which allows the p-layer to generate an electric field. Now, when light of some wavelength enters the p-n junction of the semiconductor, an electron-hole pair (i.e., photoelectric effect) is generated. This hole is then absorbed in the p layer which generates an electron and migrates along the gradient of the electric field towards the potential well. Electrons then accumulate during the duration of the CCD's exposure to light or until it reaches its capacity measured in electrons per pixel. With this in mind, each CCD are arranged into an array of individual CCD's (line or rectangular) which makes up the entire image sensor. Each CCD in the sensor refers to a picture element or pixel which generally is on the order of $10 \times 10\mu m^2$.

For the sensor to be read out, the pixels are then addressed sequentially by shifting the electrons vertically one row at a time. These sensor readout is shown in Fig. 3.8 Each row in the analog shift register is then clocked pixel by pixel using a charge to voltage converter. The converter then generates the voltage for each pixel that correlates to the amount of detected light for this pixel.

With this background, the camera used for the experiment is an 8MP (3312 x 2488 pixel), dual frame CCD camera (Imager LX 8M GigE). The dual frame is a camera feature which allows to take two separate exposures at a very short time period between the frames. The image acquisition using the two frames are then synchronized with a light source which is pulsed to allow exposures for each frame to be different. This can be a continuous-wave light (cw-light) which generates two different intensities for both frames.

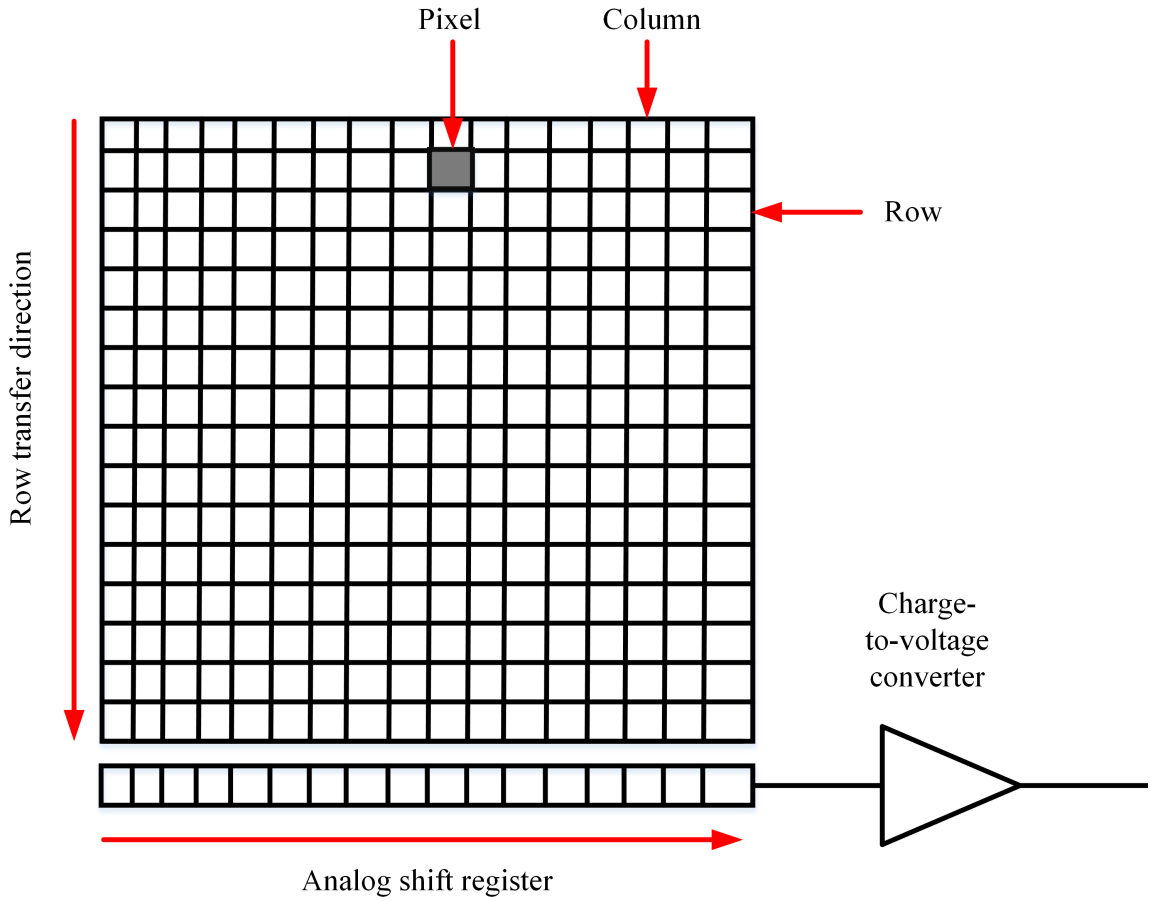

Figure 3.8: Schematic of a CCD sensor geometry.

Laser

The next component used in the PIV system is the laser. Lasers are typically used in PIV measurements as they give out high energy density, monochromatic light. This is beneficial as they can be clustered into thin light sheets for use in illuminating the particles (see 3.3.1) in the region or flow field of interest. A typical laser consists of a three main components which are the laser material, a pump source, and a mirror arrangement. The laser material can be a semiconductor or solid material, or atomic or molecular gas. The pump source introduces electrical or chemical energy to excite the laser material. The mirror arrangement allows oscillation within the laser material.

The working principle of a laser used in PIV can be briefly explained as follows.

In quantum mechanics, it is known that an atom can possible occupy different energy levels with electromagnetic radiation. These possible states are absorption, spontaneous emission, and stimulated emission. In absorption, an atom in state E_1 receives energy $h\nu$ to raise to E_2 and the photon is absorbed. In spontaneous emission, the excited atom at state E_2 drops back to E_1 at short period of time, and emits energy $h\nu$ in the form of a randomly directed photon. For stimulated emission, an incident photon can stimulate an atom at state E_2 to a specific and non-spontaneous state E_1, and an additional second photon in phase with the first photon occurs.

Absorption or stimulated emission predominate the processes when there are large number of atoms involved. Absorption occurs if there are more atoms in state E_1 than in the state E_2 (i.e., population density $N_2 < N_1$) while stimulated emission occurs if there are more atoms in E_2 than E_1 (i.e., $N_2 > N_1$). Now the laser can operate if population inversion takes place where an external energy is transferred to the laser material since atoms usually exist in their ground state. This is attained by a pump mechanism which depends on the laser material. Solid laser materials are pumped by electromagnetic radiation, semiconductor lasers are pumped by electronic current, and gas lasers are pumped by collision of atoms or molecules with electrons and ions. The population inversion can be achieved by at least three energy levels of the laser medium. However, a three level energy system is not very efficient as in order to amplify the impinging photon, a fraction of more than 50% of the atoms have to be excited. With a four level laser, a substantially less pumping power is required and thus more efficient than a level three laser.

The current study uses a Neodym-YAG laser (Nd: YAG laser $\lambda = 532nm$), and a typical PIV system laser setup is shown in Fig. 3.9. This laser system means that the laser material and thus the laser beam is generated by Nd^{3+} ions. Furthermore, the Nd^{3+} ions can be incorporated with different host materials such as YAG crystals (i.e., yttrium-aluminum-garnet). Thus, the Nd:YAG laser is four-level, solid-state, laser system

typically used in PIV as it has high amplification and good mechanical and thermal properties. It also emits the strongest wavelength (i.e., $\lambda = 1064nm$) and depending on the laser cavity design, the population inversion can take place as soon as the threshold is reached. The cylindrical shape of the laser material allows to increase the radiation in a preferred orientation as the amplification correlates to the length of the material. In this case, an optical resonator is used to extend the laser material and form an oscillator using two aligned mirrors. The mirrors allow the randomly produced photon to reflect and amplify again as it penetrates the laser material once more.

A quality switch (i.e.,*Q-switch*) shown in Fig. 3.9 allows the energy in the resonator to be controlled as well as it allows the laser to be operated in triggered mode. The Q-switch consist of polarize Pockel cell crystal driven by high voltage. This means that the Q-switch can alter the resonance of the optical cavity, allowing the cavity to resonate and reach the most energetic point during a flashlamp cycle (i.e., pumping cycle). For this process to occur, at beginning of the pumping process, the Q-switch is closed, and amplification is possible since there is no laser oscillation. When the stored energy reaches the maximum, the Q-switch is then opened, laser oscillation occurs, and the energy stored is then extracted in a pulse at a very short time duration. Typically, PIV systems are designed with a double oscillator which functions to control the time between the laser pulses independently. Furthermore, the laser beams are combined using a beam combining polarizer. As the PIV wavelength is $\lambda = 1064nm$, it is frequency-doubled using KDP crystal, with the separation of the frequency-doubled using a second harmonic generator (SHG) to convert approximately one-third of the original light energy at $\lambda = 532nm$.

Timing

With the camera and light source defined, the timing between these devices can be explained in Fig. 3.10. Here the exposure times for the first and second frames are

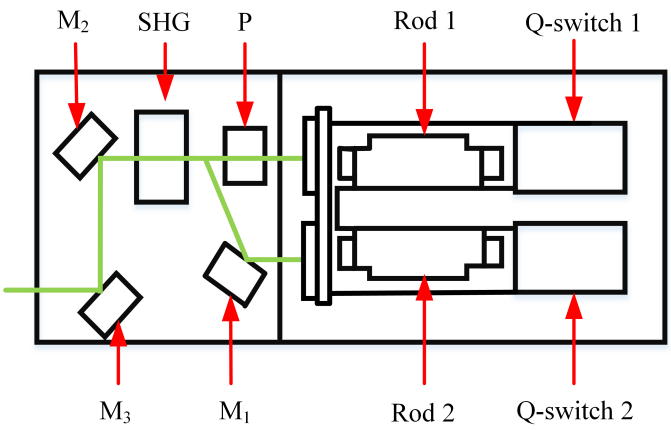

Figure 3.9: Schematic of a double oscillator laser system.

different. The first frame exposure is in the range of microseconds, which is then followed by first frame readout, and the exposure for the second frame occurs. This entire process happens within the order of hundred milliseconds and repeats based on the camera frame rate setting.

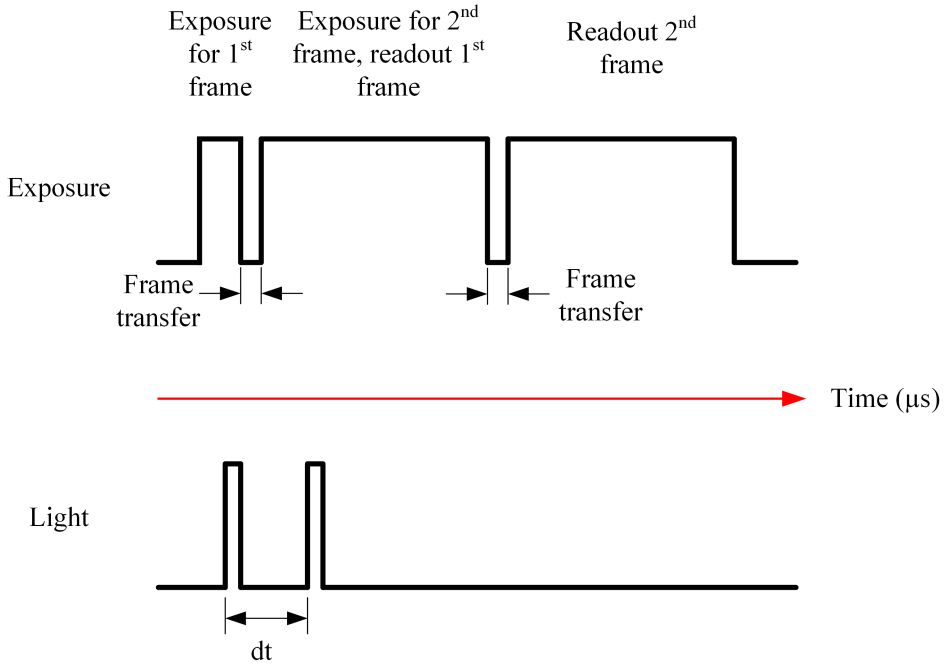

Figure 3.10: Timing diagram for double frame image recording.

Flow seeding

For the current study, the PIV seeding particles are silver hollow coated glass spheres with diameters from 9-13 μm. The density of the particles is $1.1 g/cm^3$ according to LaVision manufacturing data. These seeding particles are chosen for compatibility and stability with the fluid used in the experiment and are neutrally buoyant with the fluid. To determine the residence time of the particle, the Stokes number is number is determined. For this investigation, the time response of the particle and the characteristic time of the flow are considered. In this case, the ratio between the two numbers gives an indication of the Stokes number. Stokes number is the ratio of the particle response time (τ_p) to a representative time scale in the fluid flow (τ_f) and given as [123]

$$St = \frac{\tau_p}{\tau_f}. \tag{3.4}$$

If $St \gg 1$, then the particles will travel on their own path, and if $St \ll 1$, the particles will follow the fluid. The time response for the particle is determined using [123]

$$\tau = \frac{(2\rho_p + \rho_f) d_\rho^2}{36 \mu_f} \tag{3.5}$$

where ρ_p is the density of the particles, ρ_f is the density of the fluid, d_p is the diameter of the particles and μ_f is the viscosity of the fluid. Using the equation, the time response of the particle 9-13 μm in diameter results in $1.38 \times 10^{-6} s$. The characteristic time of the flow is around 0.2s (convection time for the vortex to move across the aneurysm). Using this information, the St $\approx 3.43 \times 10^{-6} \ll 1$. Thus, it is reasonable to assume the particles are following the fluid flow.

3.3.2 Triggering and image synchronization

Now that the camera and laser system have been described, synchronization and triggering of these devices is crucial in order to appropriately illuminate the flow field and capture the illumination of the particles in a timely and appropriate sequence. This is done through a Programmable Timing Unit (PTU) which takes control over the synchronization of the devices. For this investigation, PTU X is used which is a software-controlled synchronization unit by *LaVision*.

With the PTU, the concept of reference time is important as it describes the time between the PTU trigger, the moment the image is taken by the camera, and the illumination time by the laser. A common reference point in time is needed such that the light pulse from the laser illuminates the flow field of interest which then leads to the camera exposure. The reference time is set so that the camera can activate its sensor, the laser gets charged with the flash lamp, and all other electronics can be monitored and triggered. The *DaVis* software takes care of the individual timings of each devices and triggers them before the reference time.

A timing diagram shown in Fig. 3.11 illustrates the reference time for the PIV double frame double exposure setting. The red vertical line refers to the reference time for the system. Here the laser 1 requires two trigger pulses. The first trigger (i.e., Flash Lamp Trigger 1) is to activate the flash lamp for pumping the laser while the second trigger (i.e., Q-Switch 1) emits the laser at the reference time. The camera trigger is activated right before the reference time to expose the camera sensor. The process is similar for the second laser at slightly different timing to allow the laser pulses to be separated at some time dt.

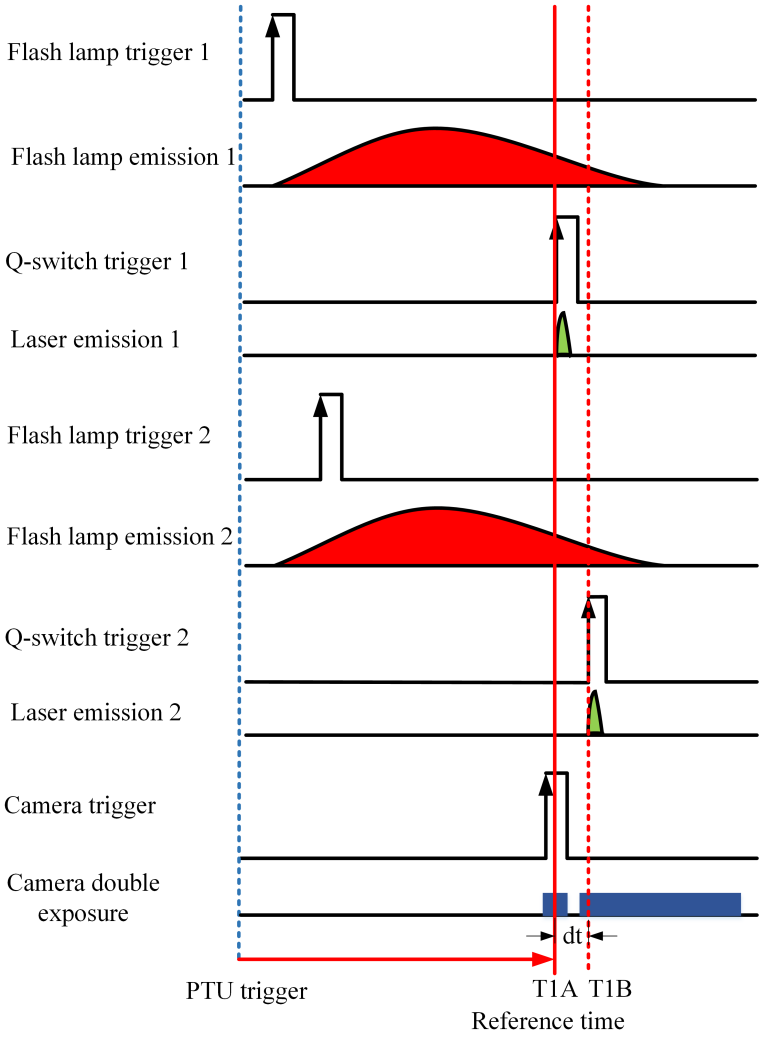

Figure 3.11: PTU timing diagram for camera and laser.

PIV analysis

The images acquired with PIV are evaluated in the post-processing step to acquire the velocity field. The objective is to determine the displacement between two patterns of particle images. This is done by subdividing the images into interrogation windows and evaluating the windows using correlation techniques such as auto or cross-correlation. Details of these methods for use in PIV evaluation can be found in [124].

For this study, the velocity fields are estimated using cross-correlation, multi-pass approach with 50% overlap with final interrogation window of 32 $\times$ 32 pixels. These

settings in the post-processing step yielded approximately 9000 vectors in the pipe region, 6000 vectors in the neck region, and 6800 vectors in the sac region for each of the studied scenarios.

3.4 Pump system

In this section, a pump system is described which will be used to generate controlled inflow conditions for this study. A piston pump system (SuperPump System AR Series, ViVitro Labs Inc., Victoria, BC, Canada) will be used which has several components. In this study, the pump system consist of the hydraulic piston pump, Viscoelastic Impedance Adapter (VIA), pump head, and pump encoder. Each component will be described including their role in generating the inflow condition.

The first component is the ViVitro SuperPump which is a pulsatile pump that utilizes a hydraulic piston. This piston can be controlled digitally using preconfigured waveforms or through a customizable ViViTest software input for the piston to follow. This allows the pump to replicate physiological flows for *in vitro* investigations. A sample figure of the pump system is shown in Fig. 3.12 while the critical features of the pump are summarized in Table 3.1.

Table 3.1: SuperPump specifications.

Specifications	
Cycle Rate	3-200 BPM
Waveform Accuracy	<4% of stroke volume at 70 BPM
	<5% of stroke volume at 200 BPM Pressure limit 360mmHg
Displacement Volume	0-180 mL
Standard Waveforms	Physio at 70 BPM
	Sine 30% at 45 BPM
	Sine 35% at 70 BPM
	Sine 50% at 70 BPM
	Sine 50% at 120 BPM

The second component of the SuperPump system is the Pump Controller which is

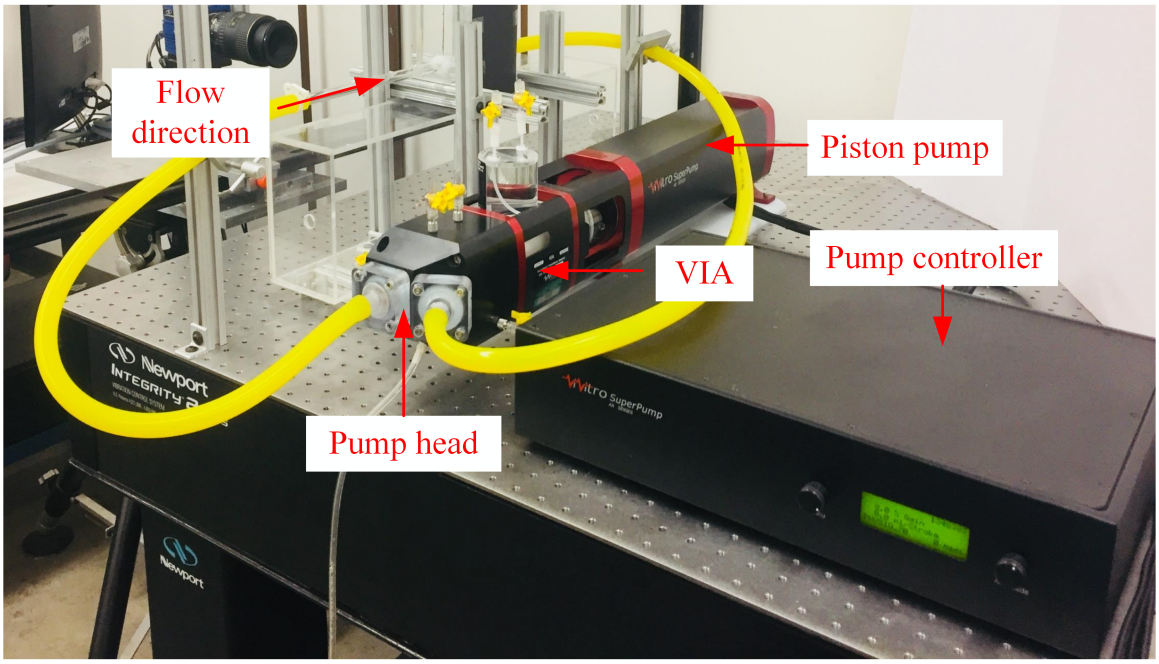

Figure 3.12: ViVitro SuperPump used in the experiment.

shown in Fig. 3.12. The controller has a front panel which the controls are rotary encoders to select the amplitude and output waveforms. The rear panel contains different connectors to monitor different signals such as position, instantaneous flow rate, and triggering. The controller also has a waveform input to allow an external signal to control the SuperPump.

The third component of the SuperPump system is a Viscoelastic Impedance Adapter (VIA) and is shown in Fig. 3.12. For this study, smooth and realistic changes in pressure cycle is important to simulate in order capture the flow evolution in the aneurysm study and thus a VIA is used. The VIA consists of a fixed resistive element and two compliance chambers that are adjustable for simulating the ventricular viscoelastic behavior. The purpose of this adapter is to produce realistic physiological pressures in the flow and correct flow rate waveforms by dampening the sharp changes in the momentum of the fluid surrounding the ventricle generated by the piston [125]. The damping can be controlled by changing the volume of the air inside the VIA output compliance and the VIA source compliance chambers [125]. The critical features of the VIA are summarized in Table 3.2.

Table 3.2: Viscoelastic Impedance Adapter specifications.

Specifications	
Fixed Resistance	200 c.g.s. units
Compliance Air Volume	Source: 0-120 mL
	Output: 0-60 mL
Total Liquid Volume	500 mL with Source/Output compliance air volumes zero

The last item in the SuperPump system is the Pump Head which is shown in Fig. 3.12. The Pump Head's function in the experiment is to create circulatory pulsatile loop. When this is combined with VIA, the flow loop will have attenuated pressure traces and pressure spikes from the piston reversal. The Pump Head consists of a silicone ventricle membrane which isolates the SuperPump piston fluid (typically distilled water) from the test fluid. It also has spring-loaded disc valves to allow for uni-directional flow in the flow-loop system.

3.5 Flow-loop and hardware synchronization

The PIV system, pump system, and the aneurysm model are now put together as part of the experimental setup to acquire velocity field measurements, and the schematic of this entire setup is shown in Fig. 3.13. To capture the flow evolution and large-scale structures in the aneurysm at different inflow scenarios, the two systems (i.e., PIV system and pump system) are synchronized. Doing this synchronization step allows to accurately determine when a PIV image is taken in a given phase in the pump pressure cycle. This is done by simultaneously tracking the PIV trigger signal and the pump piston signal shown as dashed lines in the figure. These signals are recorded using a data acquisition system, and acquired using an in-house LabView code. The information acquired also allowed to correlate the sub-regions of the aneurysm (discussed in the Test conditions section) and used for analysis with POD and DMD.

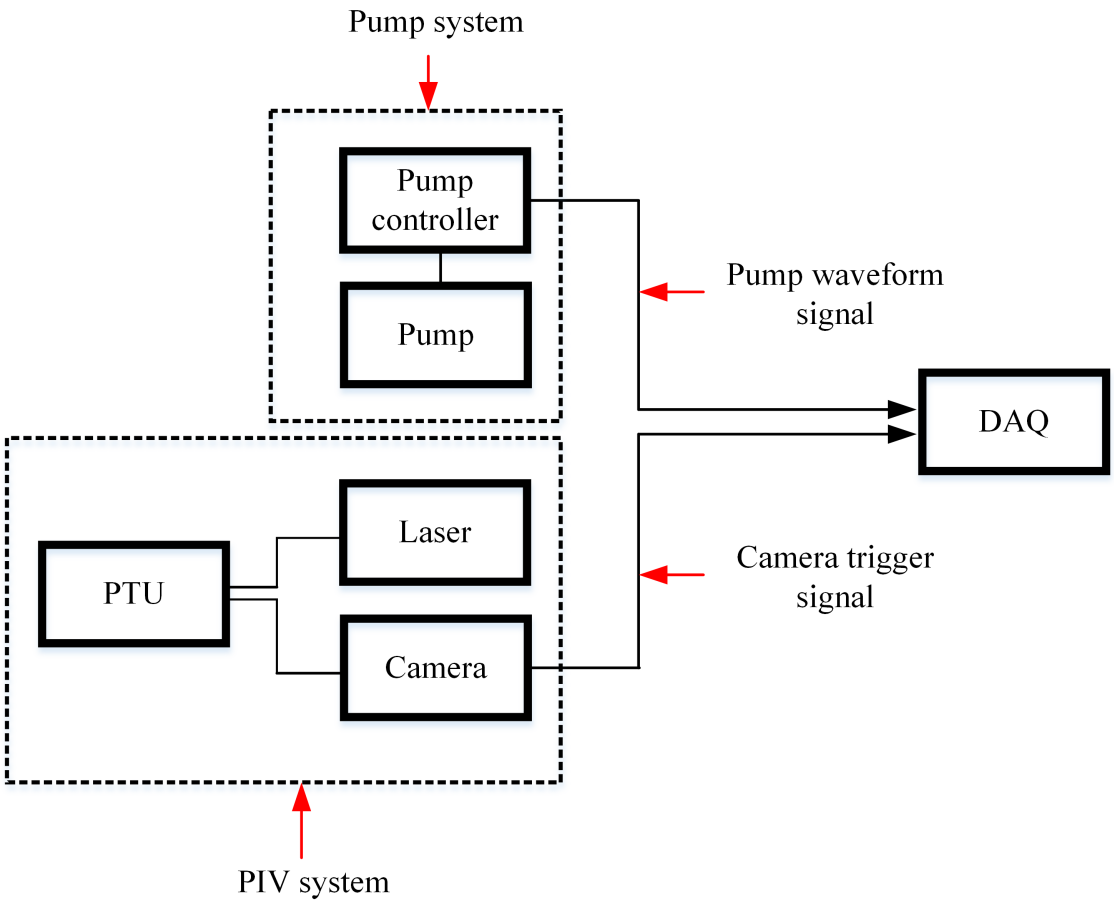

Figure 3.13: Schematic of experimental setup for fluid flow investigation. Broken lines represent the system, bold solid lines represent subsystem components, and black solid lines represent the signals.

3.6 Velocity profile validation

The piston pump described in the previous section was set to generate a controlled and well-behaved flow for experiments. In this study, a sinusoidal waveform was used for the piston to follow. The periodic cycle of the flow results in a total pump cycles of 170 and 1040 for $\alpha = 2$ and $\alpha = 5$, respectively. To assess the quality of the inflow condition, a multi-modal Womersley solution [126] was fitted to the upstream pipe velocity profile. The multi-modal solution for a velocity profile $u(r, t)$ at time instance t is given as

$$u(r,t) = a_0(1 - \frac{r^2}{R^2}) + \sum_{m=1}^{M-1} Re\left\{a_m\left(1 - \frac{J_0(\lambda_m r)}{J_0(\lambda_m R)}\right)\exp(j\omega_m t)\right\}, \tag{3.6}$$

where a_m is the complex fitting parameter, R is the pipe radius, r is the radial distance, j is the $\sqrt{-1}$, $\omega_m = m\pi/T$, T is the time period of the pump flow, and $\lambda_m = j\,(\omega_m/\nu)^{3/2}$, M is the number of frequencies and J_0 is the Bessel function of order zero.

An example of a typical velocity waveform along with its piston phase for a flow condition of $Re_p = 50$ and $\alpha = 2$ is shown in Fig. 3.14(a) while the upstream velocity profile for non-dimensional period of $t/T = 0.60$ is shown in Fig. 3.14(b). The results showed that the velocity profile was periodic using three frequency modes to fit the multi-modal solution with the velocity profile. Other time instances and inflow conditions were also verified and found good agreement with the multi-modal solution which are not shown here.

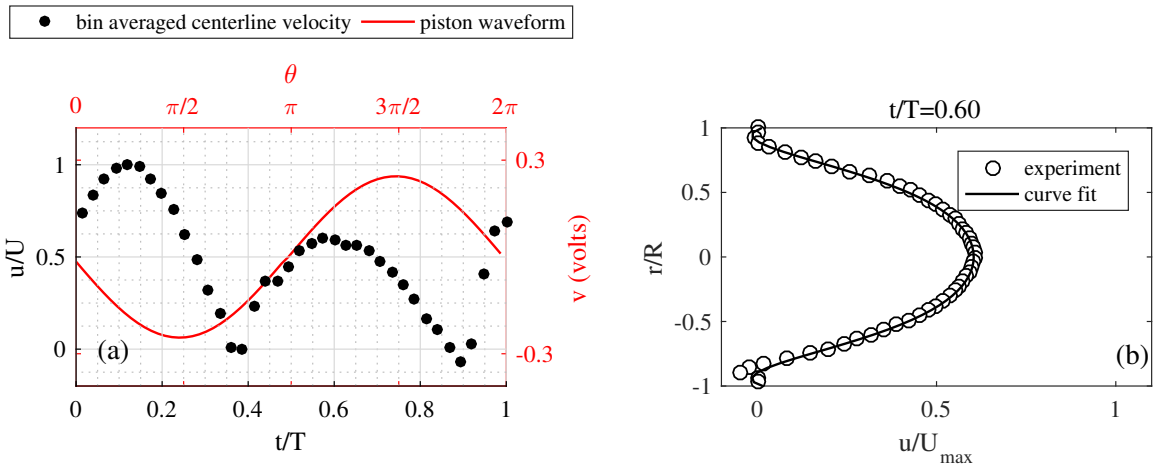

Figure 3.14: Pipe velocity information for $Re_p = 50$ and $\alpha = 2$. (a) Velocity waveform. (b) Velocity profile with fitted multi-modal Womersley solution.

3.7 Test conditions

For this study, Re and α are the two dimensionless parameters that will be used to characterize the inflow conditions in the aneurysm. These parameters are selected since they play key roles in the flow behavior in aneurysm. Furthermore,these have been

used in previous saccular aneurysm studies. For instance, studies by Ku [5] have shown that the mean Reynolds number is around 300 and Womersley number is about 4 in the carotid artery bifurcations located along the sides of the neck. Liou and Liou [127] used mean Reynolds number of 500 to study human basilar tip aneurysms. Steiger et al. [128] investigated basic flow structures in saccular aneurysms using mean Reynolds number of 300 and an α of 1.3 for pulsatile flow investigations. Le et al. [27] used peak Reynolds number range of 375 to 800 and α of 3.3-4.8. Lastly, Asgharzadeh and Borazjani [19] in their computational study investigated the effect of mean Reynolds number and α in intracranial aneurysms for mean Reynolds number of 173-914, and α of 5 to 30. Using these parameters, the inflow conditions were varied for this study. Re_p was varied from $\sim$50-270 using the stroke length of the pump, while α was varied from $\sim$2 to 5 using the frequency setting of the pump. The diameter of the tube was used for the characteristic length scale, and the maximum centerline velocity was used for the velocity scale. The selected α for this study represents quasi-steady flow and unsteady flow regimes as identified by White [129].

Initial PIV measurements and previous studies indicate a velocity magnitude difference between the pipe section and the aneurysm sac [23]. This difference becomes a challenge in selecting an appropriate Δt to capture the movement of the particle between the PIV image pairs. To overcome this challenge, the velocity field measurements are divided into distinct sections, namely the pipe, neck and sac regions. This allows for optimization of the time delay between the PIV image pairs for minimal uncertainties in the velocity field vectors. The calculated velocity field used for the experiment is cross-correlation, multi-pass with decreasing window size analysis technique with final interrogation window of 32x32 pixels. Furthermore, PIV measurements are also taken at different planes which are shown in Fig. 3.16. These measurements are taken to get a 3D reconstruction of the flow inside the aneurysm sac.

The flow conditions are summarized in Table 3.3. The field of view for each region

of interest and the corresponding time delay (dt) for the PIV image pair for each Re are summarized in Table D1 for α of 2 and Table D2 for α of 5 for mid-plane measurements. Furthermore, Table D3 show the region of interest and time delay for different flow conditions for α of 2 while Table D4 show the parameters for α of 5. Note that the plane measurements are only acquired for BF of 1.0 since it had the aneurysm volume to allow these plane measurements.

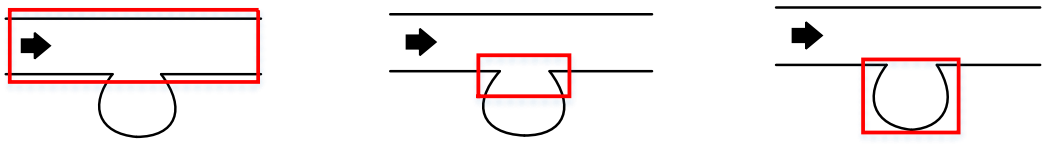

(a) (b) (c)

Figure 3.15: PIV Image Sections used in flow investigation for (a)Pipe, (b) Neck, (c) Sac. The arrows indicate the flow direction.

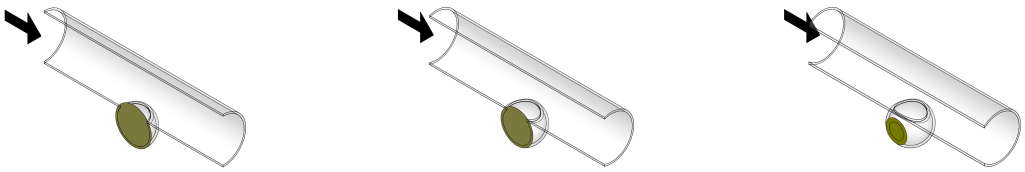

(a) (b) (c)

Figure 3.16: PIV Image Sections used in flow investigation for (a)Mid-plane, (b) 2mm from mid-plane, (c) Near edge. The arrows indicate the flow direction.

Table 3.3: Flow conditions and measurements performed for this study.

BF	Re	α	PIV Images	PIV Frame Rate (Hz)	Pump Frequency (Hz)
1.0	50	2	500	1.17	0.4
1.0	150	2	500	1.17	0.4
1.0	270	2	500	1.17	0.4
1.0	50	5	500	1.17	2.4
1.0	150	5	500	1.17	2.4
1.0	270	5	500	1.17	2.4
1.6	50	2	500	1.17	0.4
1.6	150	2	500	1.17	0.4
1.6	270	2	500	1.17	0.4
1.6	50	5	500	1.17	2.4
1.6	150	5	500	1.17	2.4
1.6	270	5	500	1.17	2.4

CHAPTER 4

Analysis approach

This chapter discusses the methods used to analyze the velocity field data and extract the large-scale flow features in the pressure cycle. The hardware synchronization approach which captures the flow evolution is first presented. This is followed by the vortex center detection approach to identify vortex core location. The impinging location and wall shear stress analysis methods are then presented. The chapter continues with the presentation and implementation of the advanced analysis methods such as POD and DMD methods to extract pertinent flow features in the velocity field data.

4.1 PIV measurement with hardware synchronization

The first method discussed in this chapter is the hardware synchronization approach. The method requires to set the sampling rate (i.e., PIV camera frame rate) at a slightly different setting than the sub-multiple of the driving pump frequency. This allows the PIV images to capture the flow fields at different phases in the pressure cycle. Holman et al. [130] used this technique in their PIV experiment of synthetic jets to determine the onset of jet formation. In their work, the method allowed them to acquire different vortex structure in each image at different phases of their flow cycle. The resulting images are sequenced over one cycle that forms an "aliased movie" of the flow field.

A sample illustration of this method is shown in Fig. 4.1. Here, the pump setting is set to 1 Hz and the camera frame rate is set to 1.6 Hz. The figure shows where the camera has taken images in relation to the pump frequency, and the images are assigned numbers from 1-8. Since the pump frequency is a well-behaved signal and cyclic in nature, the images that are outside of the single cycle of the pump are transposed to the single period cycle. These are indicated by the dashed arrows where the images should be in the single period cycle. The resulting single pressure cycle with transposed images is shown in

Fig. 4.2. The new arrangement of images allows for flow field information for a complete pressure cycle. In the current study, each experiment is run for several pump cycles in order to cover the entire flow field information for a single period cycle. Table 3.3 shows the PIV camera frame rate and super pump frequency (i.e. the driving frequency) used in the experiments. The test conditions in Table 3.3 gave 1025 pump cycles for α of 5, while 170 pump cycles for α of 2. Furthermore, the hardware synchronization approach was applied to different sections of the aneurysm which allowed and capture the complete flow evolution for each sections.

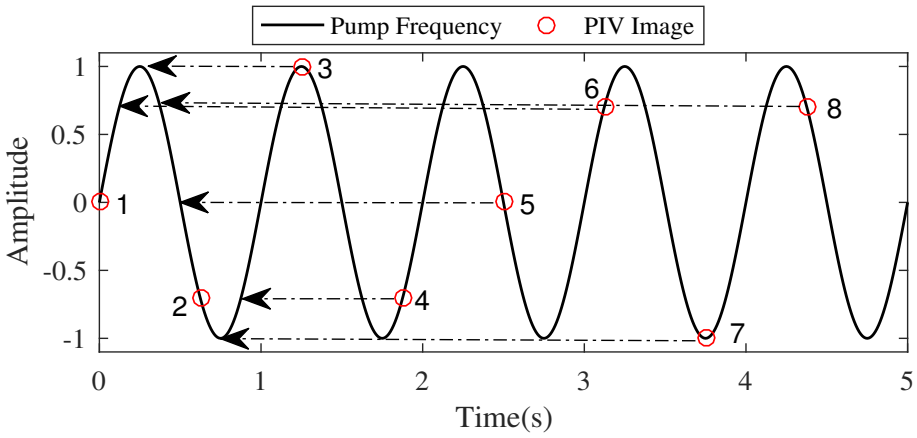

Figure 4.1: Image sequencing illustration for pump frequency and camera frame rate. Each number represents the image number taken at a particular point in the pump cycle.

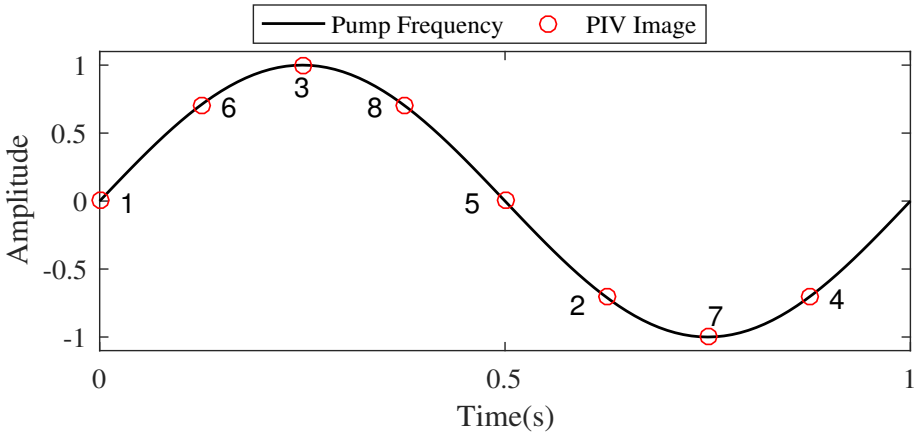

Figure 4.2: Image sequencing illustration result for one pump cycle.

4.2 Vortex path

The sequenced PIV images are analyzed for further flow structure behavior and pattern. The initial analysis showed presence of vortex structures in the aneurysm at different time phases and inflow conditions, and thus a vortex core identification is used to identify the vortices and their location in the aneurysm. This approach is important for the study as it allows us to quantify the vortical structure behavior at different inflow conditions in conjunction with other analysis methods. For this analysis, a vortex identification algorithm by Graftieaux et al. [131] is implemented to locate the center of the vortex of each image. According to the method, let Γ_1 be a dimensionless scalar function at a fixed point P in the measurement domain. This is defined as [131]

$$\Gamma_1(P) = \frac{1}{S}\int_{M\in S} \frac{(PM \wedge U_M)\cdot z}{\parallel PM \parallel \cdot \parallel U_M \parallel} dS = \frac{1}{S}\int_S sin(\theta_M) dS \tag{4.1}$$

where S is two dimensional area surrounding P, M lies in S, z is the unit vector normal the measurement plane, θ_M is the angle between the velocity vector U_M and the radius vector PM. Γ_1 results to a dimensionless scalar with magnitude $|\Gamma_1|$ bounded by 1. For PIV measurements, where the velocity vectors are at discrete spatial locations, Γ_1 is approximated using

$$\Gamma_1(P) = \frac{1}{N}\sum_S \frac{(PM \wedge U_M)\cdot z}{\parallel PM \parallel \cdot \parallel U_M \parallel} = \frac{1}{N}\sum_S sin(\theta_M) \tag{4.2}$$

S is a rectangular domain of fixed sized and geometry centered at P, and N is the number of points M inside S. Note that the parameter N plays a role of a spatial filter. The vortex center, Γ_1, has typical values from 0.9 to 1 depending on the number of points used in S using the Eq. 4.2.

4.2.1 Vortex center implementation

The vortex center algorithm is implemented using Matlab and used to determine the vortex center for each binned PIV images. The process of this implementation is as follows: First, a single binned PIV image P_1 is divided into K windows. A sample window K_1 is shown in Fig. 4.3, and the velocity vectors inside this window are extracted and shown in Fig. 4.4. Next, the center is determined for this window where it is indicated by the red "+" in Fig. 4.4. A radius vector from the center location of the window is connected to each velocity vector present in the window, and a sample of this step that shows an angle θ between the two vectors is illustrated in Fig. 4.4. A cross-product operation is performed for between the radius vector and the velocity vector, and the step is repeated for all the vectors present in the window. The resulting cross-products are summed together to determine Γ_{1,K_1} for this window. In equation form this is written as

$$\Gamma_{1,K_1} = \sum_{i=1}^{M} sin(\theta_M) \tag{4.3}$$

where M is the number of velocity vectors and θ_M is the angle created between the radius vector and each velocity vector. The process is repeated for the subsequent windows in the PIV image. Thus, the PIV binned image will contain Γ_{1,K_j} where $j = 1, 2, 3, ..., K$ values. The next step is determining the maximum $\Gamma_1(P)$ for the entire flow field. The location of this maximum Γ_1 relates to the location of the vortex center (i.e., x and y values) of the observed flow structure for each image.

A sample result of vortex center detection is shown in Fig. 4.5 where center is marked with red 'x' symbol. It can be seen from the figure that the method is able to determine the vortex core location. The entire process is then applied to all PIV images to determine the vortex path for each test condition. Note that for the binned PIV images that do not contain any vortex, this algorithm will not work and thus resulting locations for these

images will be excluded from the analysis.

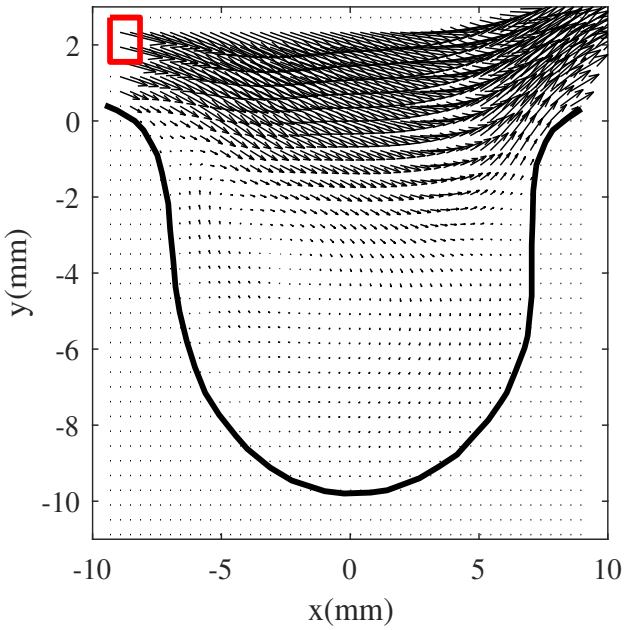

Figure 4.3: Sample binned image with sample window size.

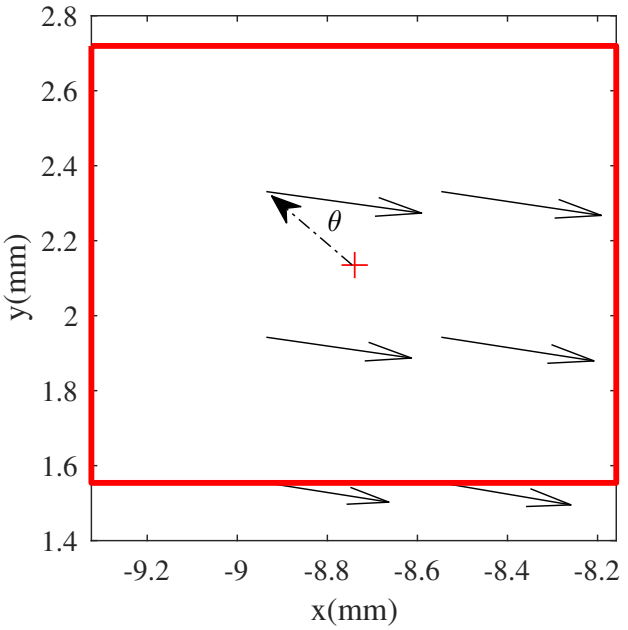

Figure 4.4: Extracted velocity vectors inside the sample window size.

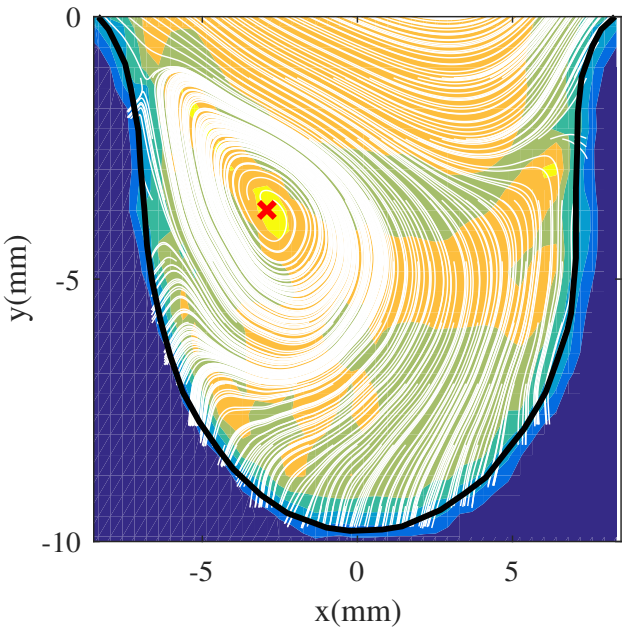

Figure 4.5: Estimated vortex location for the sample image. The center of the vortex is marked with the red 'x' symbol.

4.3 Impinging location

Part of the analysis approach of this dissertation is to quantify the flow structure impact to fluid dynamics parameters. One of the ways to quantify this is to look at the impinging location along the aneurysm geometry. The impinging locations are important to study as they indicate the high pressure points in the aneurysm sac which may be correlated to the increased risk of rupture [88, 132]. In this study, the impinging location is defined to be the stagnation point in the velocity flow field. The PIV images are individually analyzed for flow stagnation, and the implementation of this concept is presented in the next section.

4.3.1 Impinging location implementation

The determination of flow impingement is implemented in Matlab and used to identify the locations along the aneurysm geometry. The analysis begins by looking at the flow evolution results and identifying the possible region of the impinging location.

For each individual PIV image, velocity vectors in the region of the flow field where flow stagnation might occur are extracted. An example of this step is shown in Fig. 4.6 for a single PIV image. A strip dl is drawn along the aneurysm wall close to the stagnation location, and the velocity vectors in the extracted region are projected onto dl as shown in Fig. 4.7. Thus, for k number of vectors in the extracted region, each projection P_i is the dot product between the strip dl and the velocity vector V_i and shown as

$$P_i = \|M_L\|\|V_i\|cos(\theta)_i \tag{4.4}$$

where M_L is the length of the imaginary line, V_i is the velocity magnitude of each vector in the extracted window, and θ_i is the angle created by each vector to the imaginary line. Next, a contour plot is created for the PIV image, and the contour value that goes close to zero is the impinging location as shown in Fig. 4.8.

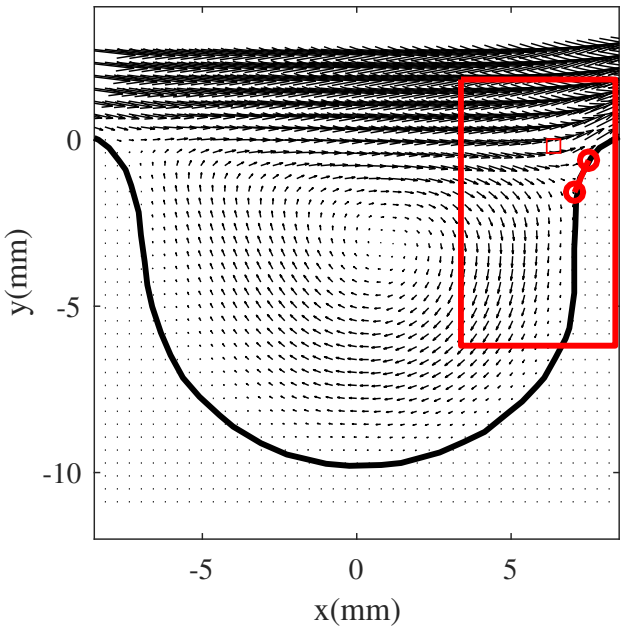

Figure 4.6: Original image with window size and strip dl.

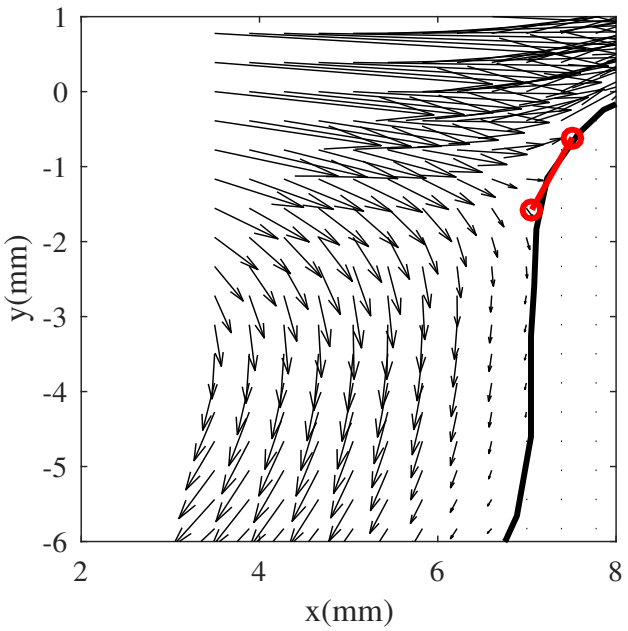

Figure 4.7: Extracted velocity vectors and strip *dl*.

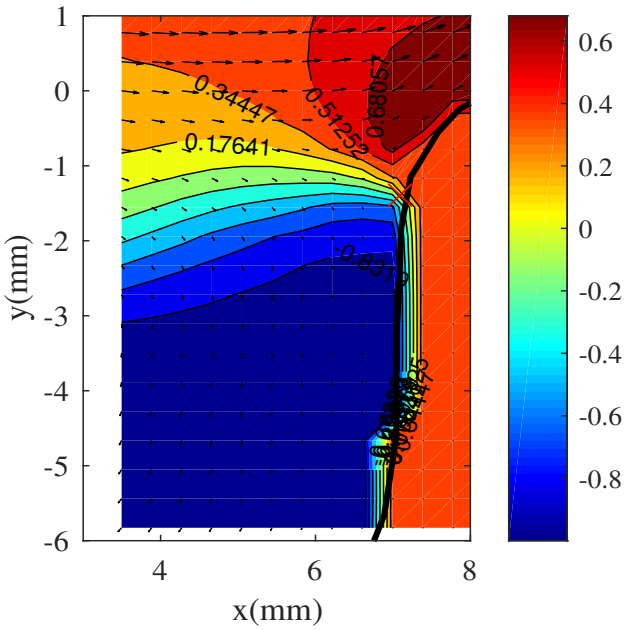

Figure 4.8: Estimated impinging location for a sample image.

The impinging locations for each phase in the pressure cycle are determined on the distal side of the aneurysm cavity. The distal side was chosen as for this analysis current study shows flow enters at the distal wall of the aneurysm. Furthermore, Cebral et al. [88] reported frequent flow impingement are located on the distal portion of the neck. Only

few cases in their study showed inflow impingement on the proximal neck which were influenced by the parent artery curvature. With this in mind, the impinging locations are then determined and presented as frequency distribution. For this part of the impinging location analysis, an arc length s shown in Fig. 4.9 is divided into several equal intervals from $0 - s$. The impinging locations are then counted in each interval. The number of impinging location occurrences that falls for each interval are then divided by the total number phases in the pressure cycle which then gives the frequency distribution.

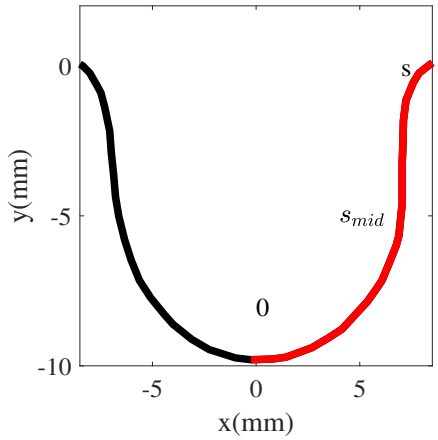

Figure 4.9: Aneurysm wall geometry where the impinging locations are tracked.

4.4 Proper Orthogonal Decomposition

Proper Orthogonal Decomposition (POD) is utilized in this dissertation to extract the energetic features or modes in the flow field. Using POD will enable us to understand the flow behavior in the aneurysm by isolating different flow features and describe these through their energy content levels. Furthermore, the interplay of these modes along with their time-varying coefficients will allow us to describe the flow field in a mathematical approach.

POD is a method first introduced in the fluid dynamics community by Lumley [29] as a mathematical approach to extract coherent structures from turbulent flow fields. It is a method commonly used for extracting coherent structures from experimental

or computational data. To do this, POD optimally determines a basis of orthogonal functions which span the data in the L^2 sense [133]. The most important property of POD is its optimality as it provides an efficient way of capturing the dominant components of a high-dimensional process using only a finite amount of modes [30].

Since its introduction, POD has been used in variety of studies which are briefly introduced here [29, 131, 134, 37, 38, 40]. Lumley [29] used POD to separate 'large eddies' in shear flows. Graftieux et al. [131] suggested using POD to separate pseudo-fluctuations attributed to unsteady nature of the large-scale vortices from the fluctuations due to small-scale turbulence. Chen et al. [134] used POD to quantitatively distinguish internal combustion engine flows with extreme flow properties. In biofluids, Byrne et al. [37] used POD on computational fluid dynamics simulations to classify aneurysm hemodynamics according to spatial complexity and temporal stability for the parameters estimated from vortex core lines. They found that ruptured aneurysms complex and unstable dynamics while simple and stable dynamics are found with unruptured aneurysms. Daroczy et al. [38] used POD to determine the spectral entropy in the flow which helped them to appropriately select computational models based on the flow regimes. Janiga [40] introduced POD for analysis of different time-varying three-dimensional hemodynamic data. His work showed the ability of POD of reducing the complexity of the time-dependent data for quantitative assessment.

The mathematical background and description of POD are provided by several authors [29, 135, 30, 31]. For this dissertation, a traditional (i.e.,vector POD) approach is used to ensure coupling of u and v components of velocity. The methodology and implementation are described in the next few sections.

4.4.1 Mathematical background

Proper Orthogonal Decomposition is a method that aims to find a basis in the Hilbert space (i.e., L^2) that is optimal for the dataset that can be represented in the form

$$\overrightarrow{U}(x,y,t) = \sum_{i=1}^{N} a_i(t)\overrightarrow{\Psi^i}(x,y), \tag{4.5}$$

where $\overrightarrow{U}(x,y,t)$ is a velocity field, $a_i(t)$ is the time-varying coefficient of the ith basis function ($\overrightarrow{\Psi^i}(x,y)$) at time t. To find the basis functions $\overrightarrow{\Psi^i}(x,y)$, they are chosen such that the averaged projection of the velocity field $\overrightarrow{U}(x,y,t)$ onto $\overrightarrow{\Psi^i}(x,y)$ is maximized. This is shown as

$$\underset{\Psi \in L^2([0,1])}{max} \frac{\langle | \left(\overrightarrow{U}(x,y), \overrightarrow{\Psi} \right)^2 | \rangle}{\| \overrightarrow{\Psi} \|^2}, \tag{4.6}$$

where $|.|$ denotes the modulus, $\langle . \rangle$ is the ensemble average, $(.)$ represents the inner product and $\|.\|$ denotes the L^2 norm. The solution to Eq. 4.6 yields to the approximation to the velocity field by a single function, but other critical points of this function are also physically significant. Thus, the set of functions, when taken together, provide the desired basis. This yields variational calculus problem shown as

$$J[\Psi] = \langle | \left(\overrightarrow{U}(x,y), \overrightarrow{\Psi} \right)^2 | \rangle - \lambda(\|\Psi\|^2 - 1). \tag{4.7}$$

A necessary condition is that the derivative vanish for all variations $\Psi + \delta\Psi \in L^2$, $\delta \in \mathbb{R}$ i.e.,

$$\frac{d}{d\delta} J[\Psi + \delta\Psi]|_{\delta=0} = 0. \tag{4.8}$$

Using calculus principles, the equation reduces to an Euler-Lagrangian equation shown as

$$\int_{\Omega_{xy}} \langle \overrightarrow{U}(x,y) \otimes \overrightarrow{U}(x',y') \rangle \overrightarrow{\Psi}(x',y') dx'dy' = \lambda \overrightarrow{\Psi}(x,y), \tag{4.9}$$

where Ω_{xy} is the domain of interest, $\langle \overrightarrow{U}(x,y) \otimes \overrightarrow{U}(x',y') \rangle$ is the spatial correlation of the velocity field, $\otimes$ is the tensor product, and λ is the energy associated with each POD

mode. With further simplification and substitution, the formulation in Eq. 4.9 can be seen as

$$\mathbf{R}\overrightarrow{\Psi}(x,y) = \int_{\Omega_{xy}} \langle \overrightarrow{U}(x,y) \otimes \overrightarrow{U}(x',y') \rangle \overrightarrow{\Psi}(x',y') dx'dy' \tag{4.10}$$

where $\mathbf{R}$ is the kernel of the POD formulation, i.e., the spatial velocity correlation matrix that results from the definition of velocity vector tensor product. The resulting simplification can be seen as eigenvalue problem shown as

$$\mathbf{R}\overrightarrow{\Psi}(x,y) = \lambda\overrightarrow{\Psi}(x,y), \tag{4.11}$$

where the eigendecomposition will have eigenvectors (i.e., POD modes) $\psi_{uu}(x,y)$ and $\psi_{vv}(x,y)$, and λ represents the eigenvalues or energies captured by the POD modes. The velocity field reconstruction in Eq. 4.5 requires to find the coefficients $a_i(t)$ which can be found by projecting the original velocity fields $\overrightarrow{U}(x,y,t)$ to each of the POD modes and given as

$$a_i(t) = \left(\overrightarrow{U}(x,y,t), \overrightarrow{\Psi^i}(x,y)\right). \tag{4.12}$$

POD was implemented in-house using MATLAB. For each experimental scenario, 500 PIV images were acquired spanning several minutes. For instance, for $\alpha = 2$ case, images were acquired over 170 pump cycles, while for $\alpha = 5$ case, images were acquired over 1040 complete pump cycles (see Table 3.3). The average velocity flow field was subtracted for each inflow scenario before using POD which allows to capture the POD modes based on the flow fluctuations in the data set. Next, auto and cross correlations for the velocity flow field were calculated to obtain POD kernel (i.e., $\mathbf{R}$). For this study, the POD kernel was a square matrix of $\sim$13000 $\times$ 13000 elements. The mathematical formulation provided in Eq. 4.11 was solved to calculate the eigenvalues (i.e., λ^i), eigenvectors (i.e., $\Psi^i_{uu}(x,y)$ and $\Psi^i_{vv}(x,y)$) and the subscript i represents the POD mode numbers. The typical calculation processing time for POD analysis was approximately one hour. The obtained

eigenvectors (i.e., POD modes) were then used to calculate the time-varying coefficients (i.e., Eq. 4.12) at a given time instance and the low-order velocity field was performed using Eq. 4.5. The complete implementation of POD is attached in the Appendix.

4.5 Dynamic Mode Decomposition

Part of the objective of this dissertation is to utilize Dynamic Mode Decomposition (DMD) to gain additional insight to the flow structures present in the aneurysm flow. As POD discussed in the previous section will be used to extract modes characterized by their energy content levels, we will use DMD to extract dynamically important features in the flow and describe these modes by their growth rates and frequencies. This will allow us to understand and capture the dynamically important modes that are impacting certain fluid motion in the flow field. Furthermore, the modes of oscillation obtained from DMD and their combination can be used to represent the flow dynamics in the data set.

The DMD method is introduced by Schmid [33] as an alternative algorithm to approximate the eigenvalues and eigenvectors of the infinite-dimensional Koopman operator using only the snapshots of the flow field. Since its introduction to the fluids community, DMD has found its use in different studies in fluids as well as beyond fluid applications which are briefly discussed here [136, 36, 39, 137]. For instance, Grosek and Kutz [136] used DMD to separate video frames into background and foreground components in real time. Abulkhair [36] used DMD on AAA to reveal the hidden dynamics of the flow behavior inside the AAA. He found that low flow conditions are characterized by occurrences of backflow and less temporal vortical structures. Lozowy [39] used DMD to remove frequencies other than the pulse frequency from the velocity field. Using DMD allowed him to represent the flow dynamics that consist of a single large-scale vortex. Wu et al. [137] used DMD to investigate the flow structures of the jet in channel crossflow using direct numerical simulation results. They found that the modes reveal the frequency information and corresponding spatial structures in the entire field and the interactions

between different parts of the flow domain.

The mathematical background and review of DMD are provided by several references [33, 138, 139, 28, 34]. As DMD is rooted from linear algebra, the method is very extensible and allows for further developments and optimization. There have been numerous different formulations and interpretations of the results from the method [33, 140, 141, 142, 139, 143]. In this dissertation, we implement the methods according to Kutz et. al. [139] and Jovanovic et al. [142]. The DMD methodology and implementation used in this dissertation are summarized in the next few sections.

4.5.1 Mathematical background

We now consider the mathematical background of DMD to be used in this dissertation. We will first look at a linear dynamical system which can be described as

$$\dot{\mathbf{x}}(\mathbf{t}) = \mathbf{A}\mathbf{x}(\mathbf{t}), \tag{4.13}$$

which is a first-order ordinary differential equation and has a solution of

$$\mathbf{x}(\mathbf{t}) = \exp(\mathbf{A}\mathbf{t})\mathbf{x}(\mathbf{0}), \tag{4.14}$$

where $\mathbf{x}(\mathbf{0})$ is the initial condition. The eigenvalues contained in $\mathbf{A}$ are the behavior of the linear dynamical system for $\mathbf{x}(\mathbf{t})$. The real components of the eigenvalues of represent the growth or decay rate while the imaginary components of the eigenvalues represent the frequency at which the system behaves. Next, we now consider a series of consecutive snapshots $\{s_1\, s_2 ... s_m\}$ separated by a time step Δt. The snapshots s_i represent a single flow field constructed with u, v components of velocity. The entire flow evolution is then stored in matrix form $\mathbf{D}$ such that

$$\mathbf{D} = \{s_1\, s_2 \dots s_{m-1}\} \in \mathbb{R}^{nxm}, \tag{4.15}$$

where m represents the total number of snapshots and n represents the number of vectors containing u and v. A second data matrix $\mathbf{D}'$ is defined such that the dataset $\mathbf{D}$ is shifted forward in time by Δt where

$$\mathbf{D}' = \{s_2\, s_3 \ldots s_m\} \in \mathbb{R}^{nxm}. \tag{4.16}$$

Here we assume a linear mapping between the snapshots using a coefficient matrix $\mathbf{A}$ that connects the flow field s_i to the subsequent flow field s_{i+1} shown as

$$s_{i+1} = \mathbf{A}s_i. \tag{4.17}$$

In general, the datasets $\mathbf{D}$ and $\mathbf{D}'$ can be expressed in following form with the operator $\mathbf{A}$ defined as

$$\mathbf{D}' = \mathbf{A}\mathbf{D} \tag{4.18}$$

By this definition, the flow is assumed to be linearly dependent although the flow field is non-linear in nature. Thus, the current approach is to determine a best-fit linear operator that relates the two matrices $\mathbf{D}$ and $\mathbf{D}'$. The matrix $\mathbf{A}$ is then a linear mapping matrix that connects the velocity field data at time instant t with $t + \Delta t$. We can find the operator $\mathbf{A}$ by taking inverting the equation such that

$$\mathbf{D}'\mathbf{D}^{\dagger} = \mathbf{A} \in \mathbb{R}^{nxn} \tag{4.19}$$

where † denotes the Moore-Penrose pseudoinverse operation. The eigenvalues and eigenvectors of $\mathbf{A}$ thus describe the dynamical behavior of the fluid system. However, due to the large size of n, the matrix $\mathbf{A}$ is not directly computed and may produced an ill-conditioned matrix, but instead projected onto a lower-dimensional subspace which still contains similar dynamics of $\mathbf{A}$. The objective of DMD then is to find a lower approxi-

mation of $\mathbf{A}$ (i.e., $\tilde{\mathbf{A}}$). To find the low-order mapping of $\mathbf{A}$ (i.e., $\tilde{\mathbf{A}}$), Schmid [33] suggests a preprocessing step using singular value decomposition (SVD) to the first data matrix $\mathbf{D}$ (i.e., $\mathbf{D}$=$U\ \Sigma\ V^*$). Substituting the results to Eq. 4.18 and rearranging yields

$$\mathbf{U}^*\mathbf{A}\mathbf{U} = \mathbf{U}^*\mathbf{D}'\mathbf{V}\Sigma^{-1} \equiv \tilde{\mathbf{A}} \tag{4.20}$$

where $\mathbf{U}$ is the left singular vector,$\mathbf{V}$ is the right singular vector, Σ is a diagonal singular matrix, $*$ denotes conjugate transpose, and -1 denotes a matrix inverse operation. The matrix $\tilde{\mathbf{A}}$ can be viewed as a minimization problem of the Frobenius norm between the difference of data matrices $\mathbf{D}'$ and $\mathbf{AD}$ using $\mathbf{A} = \mathbf{U}\tilde{\mathbf{A}}\mathbf{U}^*$

$$\underset{\tilde{A}}{minimize} \parallel \mathbf{D}' - \mathbf{U}\tilde{\mathbf{A}}\Sigma\mathbf{V}^* \parallel_F^2 \tag{4.21}$$

Equation 4.20 shows the idea of DMD. The method aims to determine matrix $\tilde{\mathbf{A}}$ which is a low-order approximation of matrix $\mathbf{A}$. With SVD, the eigenvalues and eigenvectors of $\mathbf{A}$ are approximated with eigenvalues and eigenvectors of $\tilde{\mathbf{A}}$ via similarity transformation (i.e., $\mathbf{A} = \mathbf{U}\tilde{\mathbf{A}}\mathbf{U}^*$). The key property of this transformation is it preserves the eigenvalues of $\mathbf{A}$. We also note here that the DMD operator $\mathbf{A}$ in Eq. 4.18 is related to operator $\exp(\mathbf{A}\Delta t)$ in Eq. 4.14.

The resulting low order mapping of $\mathbf{A}$ (i.e., $\tilde{\mathbf{A}}$) has the eigenvalues (i.e., $\Lambda = diag(\lambda_1\ \lambda_2 ... \lambda_m)$) which provide information on the growth/decay rate as well as frequency oscillations of each dynamic mode [33]. To extract this information, a logarithmic mapping of the eigenvalue [33, 28] is used such that

$$\lambda_i = \frac{log(\Lambda_i)}{\Delta t} = g_i + if_i, \tag{4.22}$$

where the real part of each eigenvalue ($g_i = \mathfrak{Re}(\lambda_i)/2\pi$) represents the growth/decay rate while the imaginary part ($f_i = \mathfrak{Im}(\lambda_i)/2\pi$) contains the frequency for each dynamic mode.

The DMD modes (Φ) are determined using the eigenvector ($\mathbf{W}$) of $\tilde{\mathbf{A}}$ along with left singular vector $\mathbf{U}$ given as

$$\Phi = \mathbf{U}\mathbf{W}. \tag{4.23}$$

The interpretation of the DMD modes is it is a projection of the eigenvectors $\mathbf{W}$ on the vector space $\mathbf{U}$. This vector space $\mathbf{U}$ contains the POD modes [33] which have flow behavior at multiple frequencies.

Since the determined DMD mode represents oscillations of spatial structures at a given frequency, each flow field snapshot s_i at time t can be reconstructed by superposition of DMD modes Φ, DMD eigenvalues Λ, and corresponding DMD amplitudes β given as [139]

$$s_i = \sum_{k=1}^{r} \phi_k \exp[\lambda_k t]\beta_k = \Phi \exp(\lambda t)\beta. \tag{4.24}$$

Thus, the low-order flow reconstruction can be used to provide insight to the flow field which contain flow structures oscillating at different frequencies. By selecting low frequencies to approximate the flow field, the flow behavior representation can contain only the large-scale structures [39]. Equation 4.24 also provides information on growth rate behavior of these DMD modes as each mode progresses over time, while DMD amplitude β gives insight to the contribution of each DMD mode. The amplitude β can be seen as the selection of the modes with the strongest influence on the system's response from the use of the initial condition and the time interval on which the snapshots are collected [142]. To determine β, the optimal amplitude approach by Jovanovic et al. [142] is used. Equation 4.24 can be written in matrix form shown as

$$\underbrace{[s_1, s_2, ..., s_{m-1}]}_{\mathbf{D}} \approx \underbrace{[\phi_1, \phi_2, ..., \phi_r]}_{\mathbf{\Phi}} \underbrace{\begin{bmatrix} \beta_1 & & \\ & \ddots & \\ & & \beta_r \end{bmatrix}}_{\beta} \underbrace{\begin{bmatrix} 1 & \Lambda_1 & \cdots & \Lambda_1^{m-1} \\ 1 & \Lambda_2 & \cdots & \Lambda_2^{m-1} \\ \vdots & \vdots & \ddots & \vdots \\ 1 & \Lambda_r & \cdots & \Lambda_r^{m-1} \end{bmatrix}}_{\mathbf{V_{and}}}, \tag{4.25}$$

with the $\mathbf{V_{and}}$ is the Vandermonde matrix representing the temporal evolution of the dynamic modes. Since the DMD modes $\mathbf{\Phi}$ and temporal behavior $\mathbf{V_{and}}$ are known, the unknown amplitudes β are solved through an optimization problem shown as

$$\underset{\beta}{minimize} \parallel \mathbf{D} - \mathbf{\Phi}\beta\mathbf{V_{and}} \parallel_F^2 . \tag{4.26}$$

Using the economy-size SVD of $\mathbf{D}$=$U\ \Sigma\ V^*$ and the definition of the the matrix Φ (i.e., Eq. 4.23), the problem is of the following form

$$\underset{\beta}{minimize}\, J(\beta) = \parallel \mathbf{\Sigma V}^* - \mathbf{W}\beta\mathbf{V_{and}} \parallel_F^2, \tag{4.27}$$

which is a convex optimization problem and can be solved with standard methods [144]. Following Jovanovic et al. [142] solution to the optimization problem in Eq. 4.27, the DMD amplitudes β can be found as

$$\beta = \left((\mathbf{W}^*\mathbf{W}) \circ \left(\overline{V_{and}V_{and}^*}\right)\right)^{-1} \overline{diag(V_{and}\Sigma^*\mathbf{W})}. \tag{4.28}$$

This allows us to determine the optimal amplitudes from all the snapshots apart from using the initial snapshot to determine the coefficients (i.e., $\beta = \Phi\ s_1$). Equation 4.28 is a result of the optimization problem finding the minimum β that best approximate s_1 using Eq. 4.24. Here the overline in Eq. 4.28 means the complex-conjugate of a vector, $\circ$ is an elementwise multiplication of matrices, *diag* of a vector is a diagonal matrix with

the main diagonal containing the elements of the given vector, and *diag* of a matrix is a vector containing the main diagonal of the given matrix.

The DMD implementation is developed in-house using MATLAB. Unlike POD, the mean flow is not removed for each inflow scenario, and the data matrices are constructed such that the columns contain the u and v components of the velocity field. Thus, the data matrices $\mathbf{D}$ and $\mathbf{D'}$ contain tall and skinny matrices containing the velocity fields. The algorithm and implementation of DMD can be found in the Appendix.

CHAPTER 5

Results

This chapter discusses the results obtained from the experimental methods and analysis techniques implemented for this study. The chapter is organized such that the objectives of the study are addressed. In the first section, the PIV results are shown which contain details about the mean flow, flow evolution, impinging location and wall shear stress behavior for different models and inflow conditions. The second section shows the results using POD to extract the important spatial features related to the large-scale structures. The third section provides the DMD results applied on different inflow scenarios to extract the spatiotemporal information of the large-scale structures.

5.1 Mean flow analysis

In analyzing the data set, the mean flow is first analyzed to give an overview of the bulk features of the flow field. This is important as it can quickly allow simple and basic insight on the behavior of the large-scale structure in the aneurysm. This is similar to previous studies that used steady flows to study basic aneurysm behavior [20, 76, 24, 18]. For example, Ferguson [20] studied steady and pulsatile flows in a bifurcation by dye injection and found that the impingement of the central stream to the apex of bifurcation could be an important factor in initiation of aneurysms. Steiger et al. [76] used steady flow in saccular aneurysms and found that the flow field matched well with pulsatile flows particularly with the systolic flow field. Budwig et al. [24] used steady flow in abdominal aortic aneurysms and found that the flow field is characterized by jet of fluid passing directly through the aneurysm and surrounded by a recirculating vortex. Bluestein et al. [18] used steady flow in their numerical simulations of abdominal aortic aneurysms and found that the recirculation zone can create conditions that promote thrombus formation (i.e., blood clots) and viability of rupture. Thus, the mean flow

analysis can provide a general sense of the phenomena inside the aneurysm and a direction on how to quantify the large-scale structure behavior.

5.1.1 Mean flow behavior results for BF=1.0

The mean flow results are first shown here to provide an overview of the bulk flow features at different inflow conditions. The time-averaged velocity field over the total number of images at different Re_p are shown in Fig. 5.1 and 5.2 for $\alpha = 2$ and $\alpha = 5$, respectively. For each inflow condition, 500 PIV images are used to calculate the time-averaged flow field. As seen from the figures, the mean flow results qualitatively show that the aneurysm is dominated by a clockwise vortex structure at different inflow conditions. At $Re_p = 50$ (i.e., Figs. 5.1(a) and 5.2(a)), the vortex structure is pushed deep near the proximal side of the aneurysm sac with the average impinging location near the maximum aneurysm diameter (i.e., $x = 7mm$, $y = -5mm$). The closely compact streamlines near the distal neck (i.e., $x = 7mm$, $y = 0mm$) show high velocity gradients which suggest increase in shear stresses in this area. For $Re_p = 150$, there is a shift in flow behavior where the vortical structure(i.e., Fig. 5.1(b) and 5.2(b)) has engulfed the aneurysm sac. The average impinging location for $Re_p = 150$ cases has moved closer near the distal neck (i.e., $x = 7.4mm$, $y = -0.4mm$) when compared to $Re_p = 50$, while high shear stress are still observed in this area. The vortical structure shape and characteristics (i.e., location of average impinging location and shear stresses) remain the same for $Re_p = 270$ for both α (i.e., Figs. 5.1(c) and 5.2(c)).

The average flow field results show that Re_p highly impacts the vortex structure shape than α. This is in agreement with studies performed by O'Brien [145] where she showed that the mean flow shape in the cavity is dependent on the cavity dimensions and incoming velocity profile. For this study, the cavity dimension is kept the same while the flow profile is varied by changing Re_p.

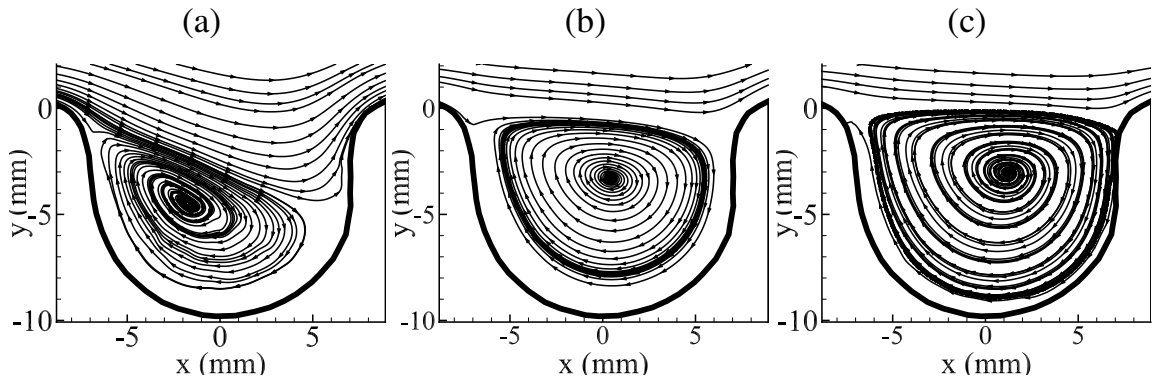

Figure 5.1: Average flow field in aneurysm sac at $\alpha = 2$ for (a) $Re_p = 50$, (b) $Re_p = 150$, and (c) $Re_p = 270$.

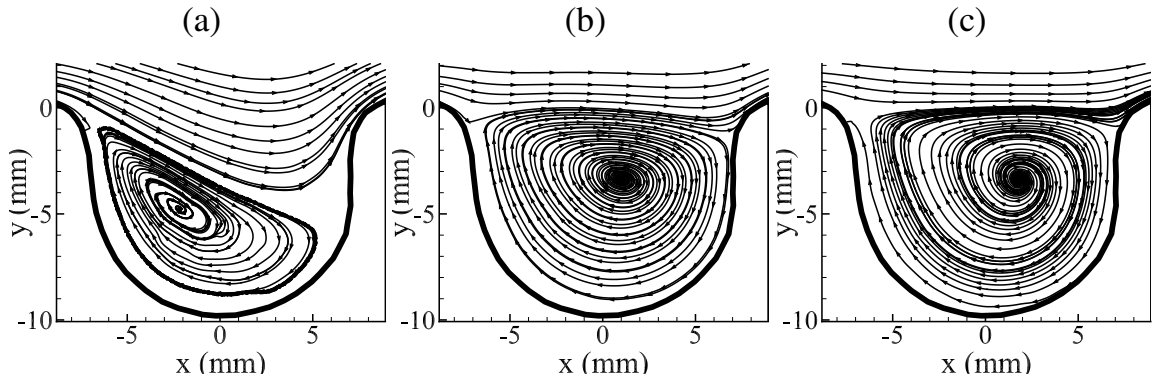

Figure 5.2: Average flow field in aneurysm sac at $\alpha = 5$ for (a) $Re_p = 50$, (b) $Re_p = 150$, and (c) $Re_p = 270$.

5.1.2 Mean flow behavior results for BF=1.6

The time-averaged flow behavior inside the aneurysm for $BF = 1.6$ at different inflow conditions are now shown in Fig. 5.3 and 5.4 for $\alpha = 2$ and $\alpha = 5$, respectively. The mean flow results shown here are from the neck section for this model which captures most of the large-scale flow structures. As seen from the figures, the neck region is dominated by a clockwise vortex structure at different inflow conditions. For $Re_p = 50$ scenarios (i.e., Figs. 5.3(a) and 5.4(a)), the center of the vortical structure is below the neck diameter with the average impinging location near ($x = 4.0mm$,$y = -2.7mm$). High velocity gradients are observed near the neck diameter (i.e., high shear stresses) as the incoming flow gets diverted to the distal side for this Re_p. For $Re_p = 150$ scenarios

(i.e., Figs. 5.3(b) and 5.4(b)), the vortex structure core has moved near the neck diameter (i.e., $x = 0.2mm$,$y = -3.3mm$) with the average impinging locations and high velocity gradients near this the neck area. The vortical shape and characteristics are also observed for $Re_p = 270$ (i.e., Figs. 5.3(c) and 5.4(c)).

The average flow field results show that Re_p highly impacts the vortex structure shape than α. At this BF parameter, similar shapes are still observed at different α and similar Re_p. However, when the two BF models are compared, the mean flow shapes are different between the models. The vortex structure occupies the entire aneurysm sac for $BF = 1.0$, while the vortex is only present near the aneurysm neck diameter for $BF = 1.6$.

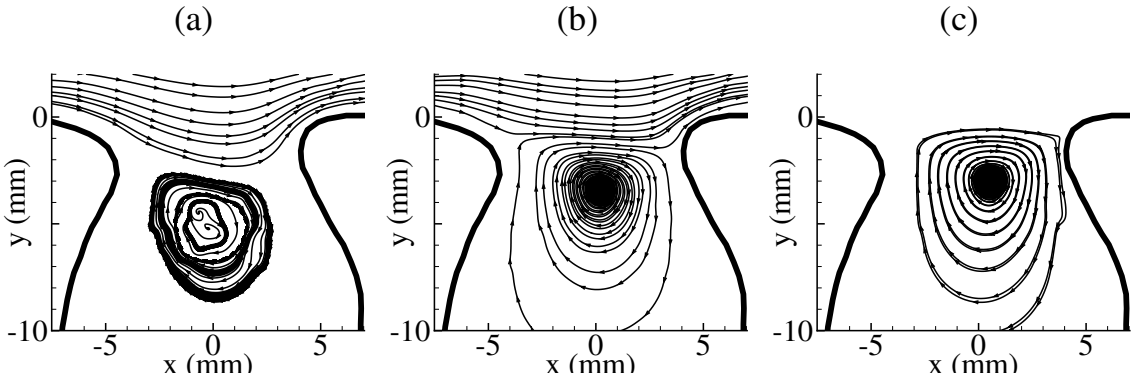

Figure 5.3: Average flow field in aneurysm sac at $\alpha = 2$ for (a) $Re_p = 50$, (b) $Re_p = 150$, and (c) $Re_p = 270$

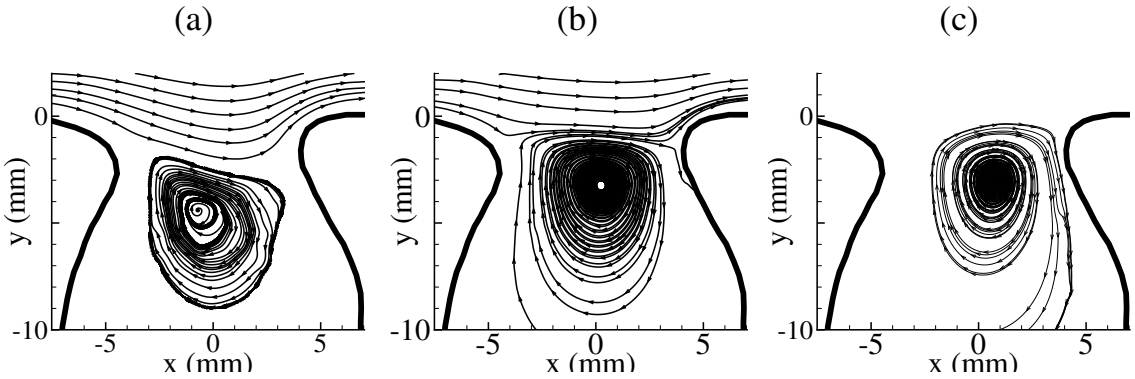

Figure 5.4: Average flow field in aneurysm sac at $\alpha = 5$ for (a) $Re_p = 50$, (b) $Re_p = 150$, and (c) $Re_p = 270$.

5.1.3 Peak vorticity and flow behavior

The observed presence of vortical structures from the previous section motivated us to quantify their characteristic behavior by first looking at their peak vortex strengths. We want to study this parameter as this may lead us in finding an answer on which large-scale flow structures and what inflow conditions increase the likelihood of rupture in aneurysms. As indicated from previous studies, ruptured aneurysms exhibit complex and unstable flow patterns [146, 147]. Cebral et al. [146] found in their CFD simulation of a reconstructed basilar artery aneurysm prior to rupture a complex and unstable flow pattern with several vortices that moved within the aneurysm dome during the cardiac cycle. Also prior to rupture, Sforza et al. [147] found in their CFD simulation of a patient specific model several regions of flow recirculation in the basilar tip aneurysm during the cardiac cycle. These studies have motivated us to investigate the role of the vortical structure to the aneurysm geometry.

Figures 5.5(a)-(d) show the vortex strength values at different inflow conditions and at different geometries. The plots indicate a linear trend of increasing average vortex strengths at increasing Re_p for different α and BF conditions. In terms of the impact of α, it is evident through the peak vorticity values where $\alpha = 5$ (i.e., Fig. 5.5(b)) shows higher vorticity values than $\alpha = 2$ (i.e., Fig. 5.5(a)) for $BF = 1.0$. This is also evident with the inflow conditions for $BF = 1.6$, where $\alpha = 5$ (i.e., Fig. 5.5(d)) conditions still yield higher vorticity values than $\alpha = 2$ (i.e., Fig. 5.5(c)). When the two aneurysm models are compared, the results show that for a fixed α, the vortex strengths at different Re_p values are always higher for $BF = 1.0$ (i.e., Figs. 5.5(a) and 5.5(b)) than $BF = 1.6$ (i.e., Figs. 5.5(c) and 5.5(d)). This can be explained as wider neck opening (i.e., $BF = 1.0$) has more fluid penetrating and thus more fluid mixing in the aneurysm sac than a narrow neck opening (i.e., $BF = 1.6$). This is counter-intuitive with the definition of BF values as higher values are prone to increase risk of rupture [15]. The mean vortex strength

values indicate that $BF = 1.0$ has increased risk of rupture than $BF = 1.6$. The mean value results have therefore motivated us to investigate this behavior further as to why narrow neck openings (i.e., $BF = 1.6$) are considered to have a high risk of rupture. Thus, we now analyze the instantaneous flow evolution for each inflow scenario and quantify possible reasons for this argument.

Note that the linear behavior of the vortical strengths of the vortices allows us to perform a first-order regression analyses for each scenario. These are shown as the curve fit line with the 95% confidence interval for each plot. The equation of the line is also shown for each α and BF scenario which can provide information on the behavior of the average vortical strength of flow structures as Re_p increases. This is an important finding as we now have a model to predict the behavior of the large scale structures for the investigated geometries. Another benefit of this finding is the results can guide future experimental and computational studies on the expected average behavior of the flow.

5.2 Flow evolution results for BF=1.0

We will now look at the instantaneous flow evolution in the aneurysm sac to study how the vortical structure behaves during the cardiac cycle at different inflow scenarios. Understanding the flow field evolution allows us to study the changes in the large-scale structure and their impact to fluid parameters such as impinging location and wall shear stresses along the aneurysm wall which will be discussed later in the text. The flow field evolution is presented for a single pressure cycle using the method discussed in the Approach section.

The flow evolution results for $\alpha = 2$ conditions are shown in Fig. 5.6 for $Re_p = 50$ and Fig. 5.7 for $Re_p = 270$. The velocity fields at each time phases are selected such that distinct flow features as well as the overall picture of the flow evolution are captured. Here the time phases are normalized by the period T of the flow cycle. The first half of the flow evolution are shown in the top half of each figure while the remaining half are

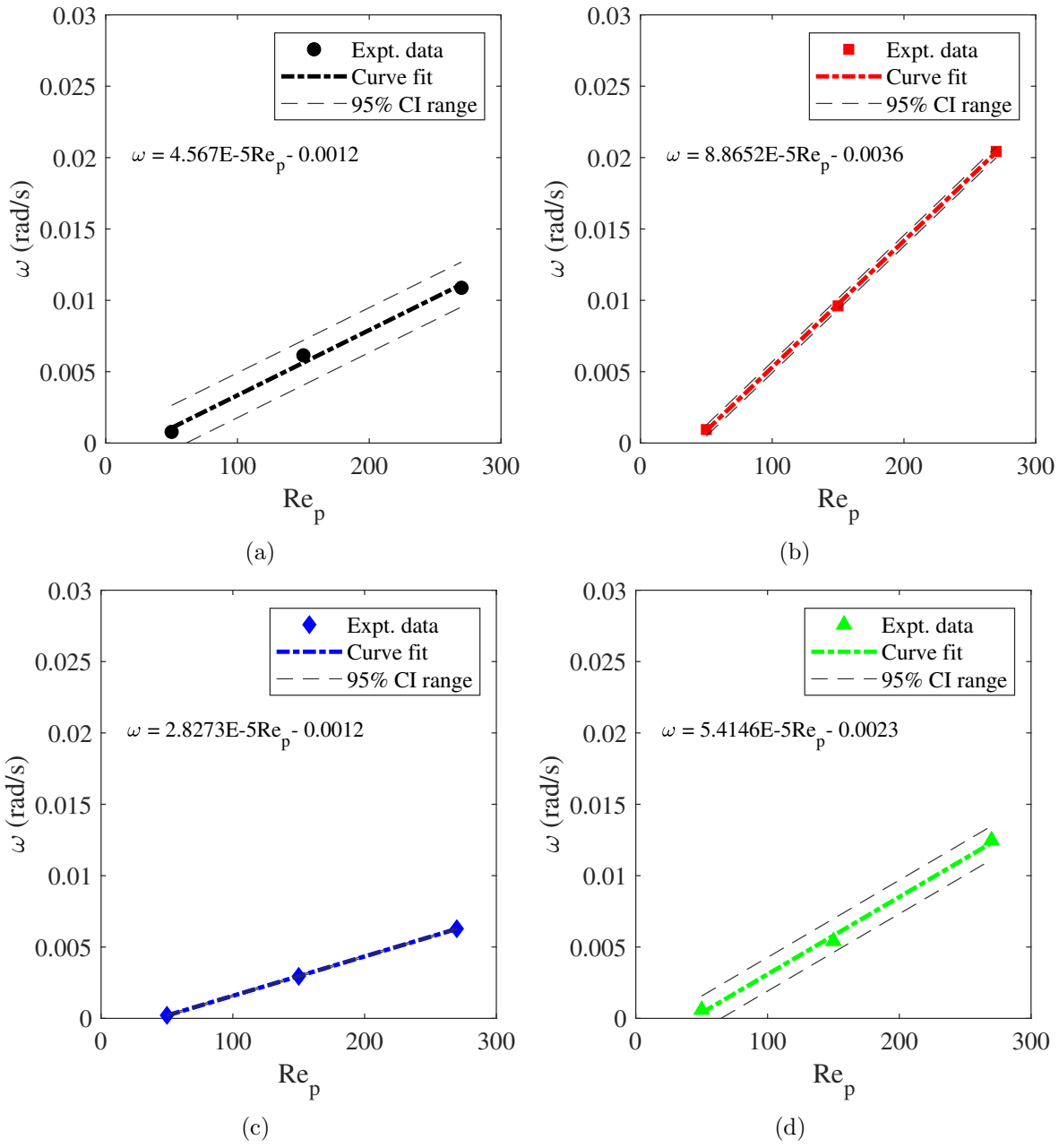

Figure 5.5: Vortex strength as function of Re_p for different inflow conditions. (a) $\alpha = 2$, $BF = 1.0$, (b) $\alpha = 5$, $BF = 1.0$, (c) $\alpha = 5$, $BF = 1.6$, and (d) $\alpha = 5$, $BF = 1.6$.

shown in the second row. At $Re_p = 50$ (i.e., Fig. 5.6), the flow is initially seen with a strong forward flow (i.e., $t/T = 0.00$). As the pipe flow decelerates, a clockwise vortex develops near the proximal side of the aneurysm sac (i.e., $t/T = 0.13$) which grows in size as it moves towards the aneurysm opening and out into the pipe region (i.e., $t/T = 0.21$-$t/T = 0.42$). At the beginning of the acceleration phase (i.e., $t/T = 0.47$), the vortical

structure is seen to get pushed back into the aneurysm dome by the increasing pipe flow velocity. This entire process of vortex formation, growth, and dissipation repeats for the remaining half of the pressure cycle (i.e., $t/T = 0.57$-$t/T = 0.97$). Similar flow structure development is seen for $Re_p = 270$(i.e., Fig. 5.7) where the vortex develops near the proximal side and moves towards the aneurysm opening. The time span of this process for $Re_p = 270$ is more or less similar to $Re_p = 50$ with a few differences. For instance, the vortex forms earlier at a different location for $Re_p = 270$ (i.e., $t/T = 0.03$ at $x = -5mm$,$y = -2.5mm$) than $Re_p = 50$ (i.e., $t/T = 0.13$ at $x = -5mm$,$y = -5mm$). Comparing different flow features for the vortex evolution process shows the impact of Re_p as there are flow structure variation at different phases of the cycle while maintaining the same trend.

The flow behavior for $\alpha = 5$ at different Re_p conditions are now shown in Figs. 5.8-5.9. For this α scenario, the flow structure evolutions for each Re_p are different than the ones observed at $\alpha = 2$. At $Re_p = 50$ and $\alpha = 5$ (i.e., Fig. 5.8), the clockwise vortex initially forms near the proximal side of the aneurysm cavity (i.e., $t/T = 0.11$) which travels towards the distal side and into the dome (i.e., $t/T = 0.21$-$t/T = 0.42$). This process then repeats for the second half of the pressure cycle (i.e., $t/T = 0.53$-$t/T = 0.89$). With $Re_p = 270$ (i.e., Fig. 5.9), on the other hand, a primary vortical structure is observed to be present at different phases of the cycle. This vortical structure moves in a clockwise fashion within the aneurysm sac as a response to the changes in the pressure cycle. Secondary vortical structures (i.e., at $t/T = 0.16$ and $t/T = 0.73$) are also seen to merge with the primary vortex in this Re_p condition which then impacts its overall flow dynamics. Here, it is noted that the process of formation and evolution are different for the two Re_p conditions studied for this α. It is observed that in the current study, the change in Re_p impacts the flow dynamics and presence of secondary vortex structures.

The behavior of the flow structures in this study are also evident in previous investigations. For pressure cycle with near zero flow phases (i.e., $\alpha = 2$ in this dissertation),

Aenis et al. [148] and Yu and Zhao [22] observed that the vortical structure moved into the pipe region. As the acceleration phase began, the vortex structure moved back into the aneurysm with rapidly decreasing strength. This sequence was also observed to repeat itself in their pressure cycle scenario. For pressure cycle with no zero flow phases ($\alpha = 5$ in this paper), previous studies [22, 27, 23, 86, 19] reported the vortex formation near the proximal neck and moves towards the distal neck of the aneurysm sac. The vortex formation and movement process was followed by the dissipation process as the pressure cycle continued. Secondary vortical structures were also observed in these investigations. To further quantify the impact of α and Re_p to the observed changes in the flow structure for each inflow condition, the impinging locations, vortex strengths, and wall shear stress values at different time phases are analyzed and presented in the next few sections.

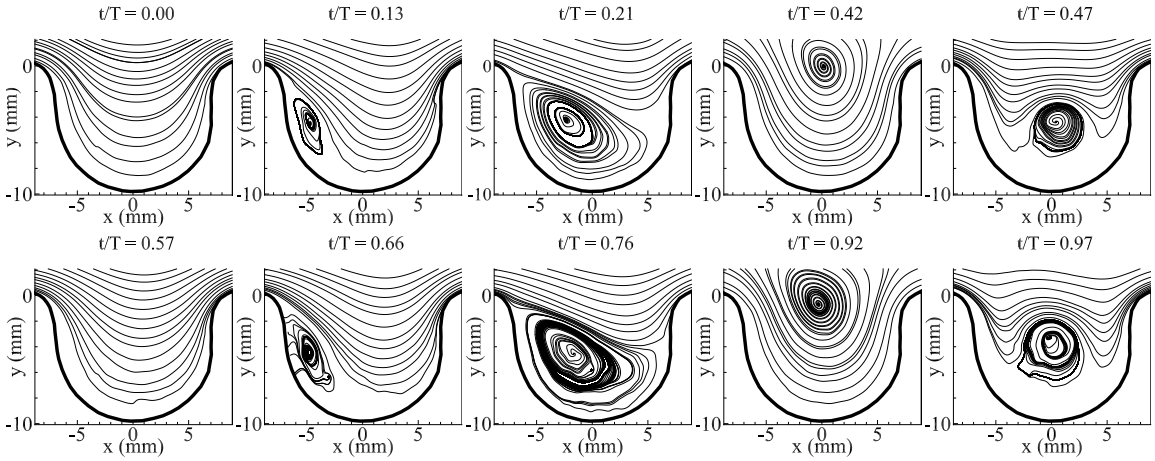

Figure 5.6: Phase-averaged flow evolution for $Re_p = 50$, $\alpha = 2$, and $BF = 1.0$.

5.3 Flow evolution results for BF=1.6

The phase-averaged flow field analysis are performed in the aneurysm model with $BF = 1.6$ at select time phases and different inflow conditions. These are shown for $\alpha = 2$ in Figs. 5.10 and 5.11 for $Re_p = 50$ and $Re_p = 270$, respectively. Meanwhile, the flow field results for $\alpha = 5$ are shown in Figs. 5.12 and 5.13 for $Re_p = 50$ and

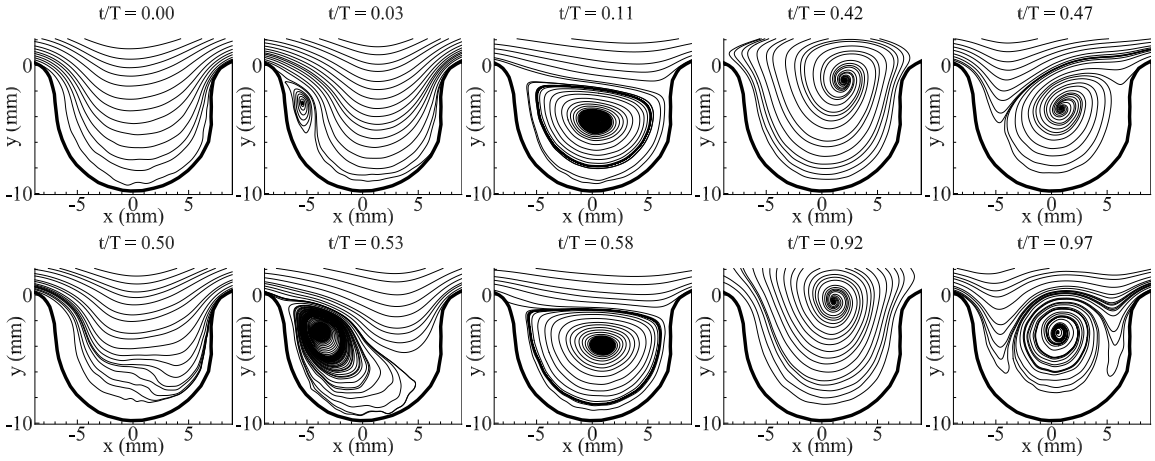

Figure 5.7: Phase-averaged flow evolution for $Re_p = 270$, $\alpha = 2$, and $BF = 1.0$.

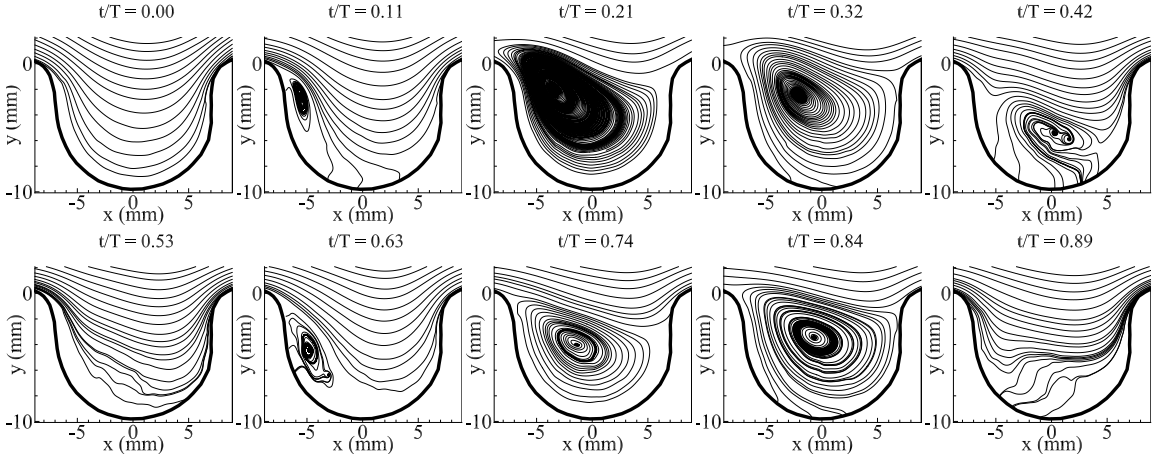

Figure 5.8: Phase-averaged flow evolution for $Re_p = 50$, $\alpha = 5$, and $BF = 1.0$.

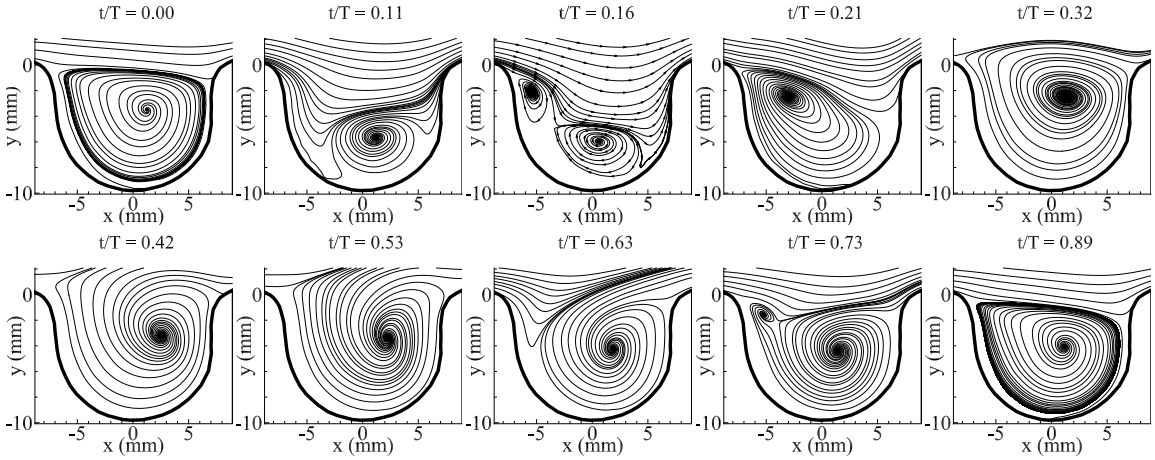

Figure 5.9: Phase-averaged flow evolution for $Re_p = 270$, $\alpha = 5$, and $BF = 1.0$.

$Re_p = 270$, respectively. For $\alpha = 2$ flow conditions, the vortex formation, growth, and movement follow the same trend as the flow behavior observed for $\alpha = 2$ and $BF = 1.0$ (see Figs. 5.6). This indicates that there is vortex formation at the proximal side of the aneurysm sac (i.e., $t/T = 0.00$) which grows and moves towards the aneurysm opening and into pipe region (i.e., $t/T = 0.11$-$t/T = 0.29$). The acceleration of the pipe flow velocity then pushes the vortex back into the aneurysm where it dissipates (i.e., $t/T = 0.34$), and the process repeats for the remaining half of the pressure cycle (i.e., $t/T = 0.55$-$t/T = 0.89$). At $Re_p = 270$, the trend remains similar as with previous cases for $\alpha = 2$. However, the vortex forms earlier and at a different location (i.e., $t/T = 0.03$ at $x = -2.93mm$,$y = -3.83mm$) than $Re_p = 50$ (i.e., $t/T = 0.00$ at $x = -1.32mm$,$y = -5.31mm$). Here it is noted that Re_p impacts the vortical structure duration in the pressure cycle while keeping the formation, translation, and dissipation processes the same. Furthermore, the vortical structures' path does not go past the aneurysm center (i.e., $x = 0.00mm$) for the α scenarios at $BF = 1.6$ when compared to the α scenarios at $BF = 1.0$.

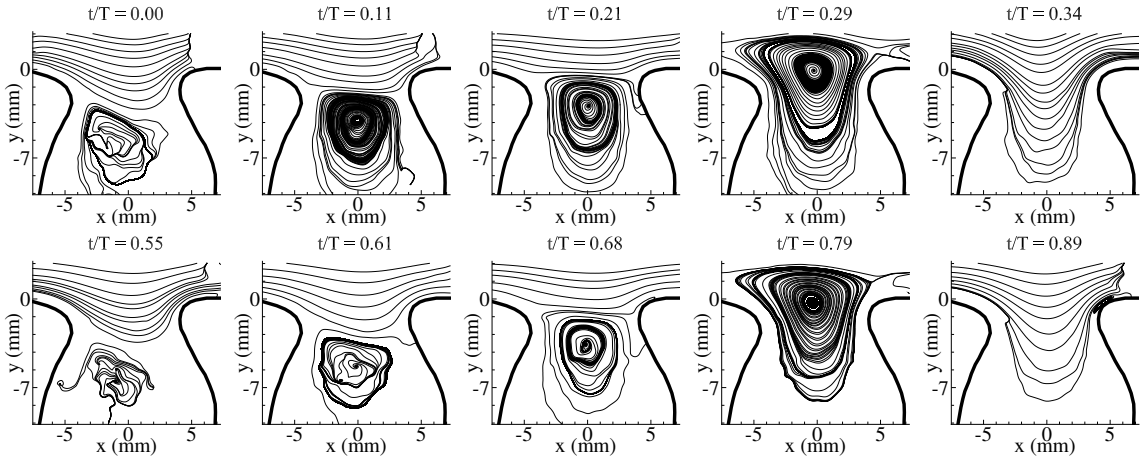

Figure 5.10: Phase-averaged flow evolution for $Re_p = 50$, $\alpha = 2$, and $BF = 1.6$.

The phase-averaged flow field results for $\alpha = 5$ show two different flow phenomena at different Re_p scenarios. For $Re_p = 50$ (i.e., Fig. 5.12), the first half of the cycle shows vortex formation at the neck diameter which grows and moves towards the pipe

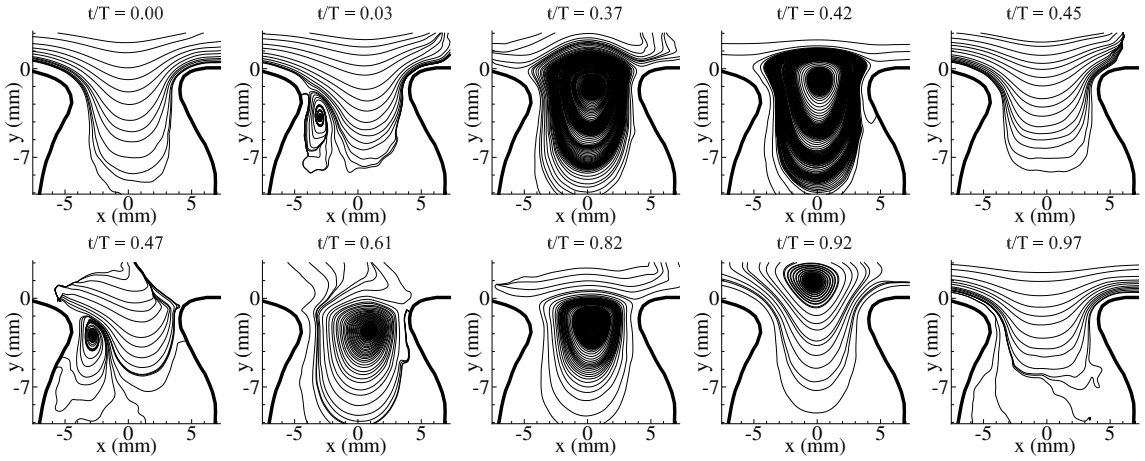

Figure 5.11: Phase-averaged flow evolution for $Re_p = 270$, $\alpha = 2$, and $BF = 1.6$.

region (i.e., $t/T = 0.00$-$t/T = 0.47$). The remaining half of the cycle shows this vortical structure oscillating within the aneurysm neck before dissipating towards the end of the pressure cycle (i.e., $t/T = 0.53$-$t/T = 0.95$). With $Re_p = 270$ scenario (i.e., Fig. 5.13), there is presence of primary vortex structure which oscillates up and down the aneurysm opening throughout the entire pressure cycle. There is also presence of a secondary vortex structure (i.e., $t/T = 0.42$) which recharges the primary vortex, similar to the flow behavior observed for the same α and Re_p for $BF = 1.0$ (i.e., Fig. 5.9).

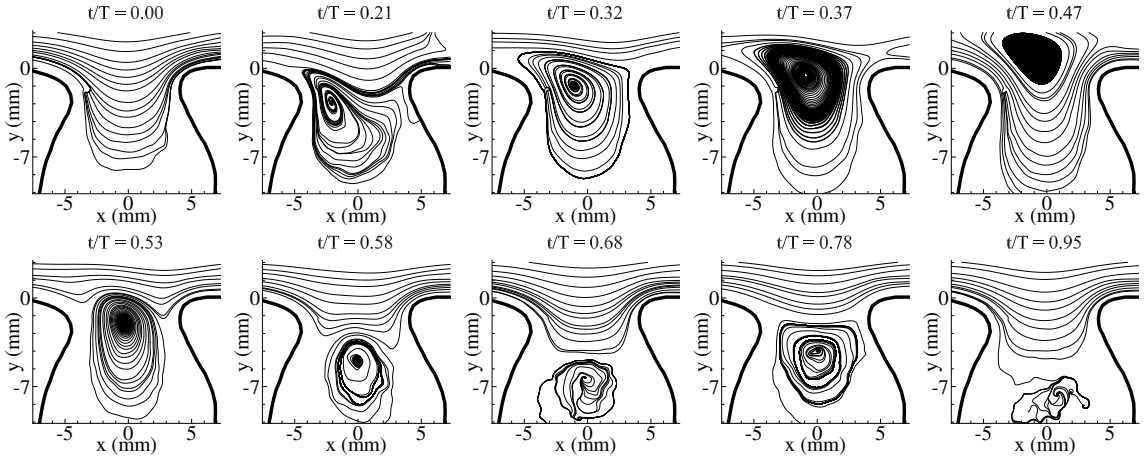

Figure 5.12: Phase-averaged flow evolution for $Re_p = 50$, $\alpha = 5$, and $BF = 1.6$.

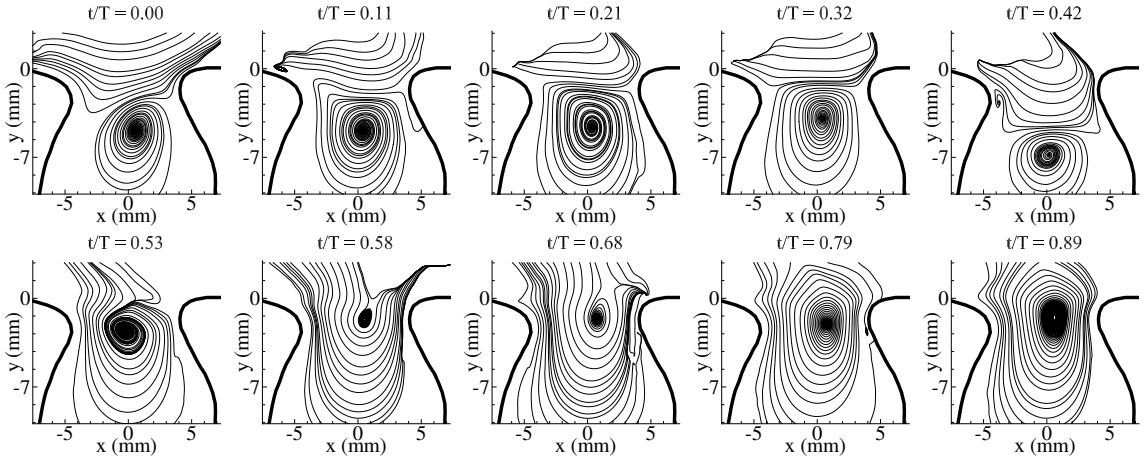

Figure 5.13: Phase-averaged flow evolution for $Re_p = 270$, $\alpha = 5$, and $BF = 1.6$.

5.3.1 Vortex path results for BF=1.0

Now that the flow evolution for different inflow scenarios have been discussed in the previous section, we shall look into the path of these structures in detail. Previous results indicate that for a fixed α scenario, qualitatively similar translation of the vortical structure occurs at different Re_p. For $\alpha = 2$ scenarios, the vortex structure forms from the proximal side and moves towards the aneurysm opening during the cardiac cycle. For $\alpha = 5$ scenarios, vortex formation occurs near the proximal side and moves towards the distal side of the aneurysm. However, the influence of Re_p could not be immediately determined from the flow evolution results. Knowing this information will allow us to know the location of the vortical structure, its properties such as vortex strength and its impact to its surroundings such as wall shear stress and impinging location behavior. Thus, the vortex structures are tracked for each inflow conditions for an entire flow cycle to quantify the vortex structure translation at different inflow scenarios. The x and y locations of the vortex center are recorded at each phase in the flow cycle using vortex center detection method discussed in the Approach section.

Figures 5.14(a), (b), (c) show the vortex path for $\alpha = 2$ for $Re_p = 50, 150$, and 270, respectively. On the other hand, Figs. 5.15(a), (b), (c) show the vortex path for $\alpha = 5$

for $Re_p = 50, 150$, and 270, respectively. It is observed from these cases that the vortices are not always present for every phase in the cycle. For this α, the results show that the vortex forms near D_{max} on the proximal side of the aneurysm sac during the first half of the flow cycle. This vortex moves towards near the center of aneurysm orifice and upwards towards the aneurysm opening. During the acceleration phase of the fluid in the pipe, the rotating flow heads back down to the aneurysm sac and dissipates. A new vortex forms in the second half of the flow cycle and follows the same trajectory as the first vortex. It is also observed that the instantaneous impinging location moved in the same direction as the vortex structure for this α. A similar trend is seen for Re=150 (Fig. 5.14(b)) and $Re_p = 270$ (Fig. 5.14(c)) with the difference being the curvature of the trajectories across the Re. It also is observed that the vortex trajectory goes to the center of the aneurysm orifice and gets past it as Re_p is increased.

The vortex follows a different path for α of 5 when compared to α of 2. Figure 5.15(a), (b), (c) show the vortex paths for $Re_p = 50, 150$, and 270, respectively. For $Re_p = 50$, the vortex forms near the proximal region of the aneurysm sac and moves towards the center of the aneurysm opening and into the aneurysm dome, which is in contrast to the movement observed for α of 2. This vortex dissipates as it reaches the aneurysm dome and followed by a forward flow inside the aneurysm sac. For the second half of the flow cycle, a new vortex forms and follows a similar trend as the first vortex. For Re=150, the vortex forms near the proximal side of the aneurysm and convects near the center of aneurysm sac. For the later half of the flow phase, gradual downward movement of this vortex is observed before dissipating into the aneurysm dome. For Re=250, a vortex structure is present in the entire flow cycle. This vortex structure behaves similarly as vortex observed for Re=150; however, the initiation or formation of this main vortex comes from the secondary vortex that is seen in the flow. Two instances of secondary vortex structures are observed for this Re. The first secondary vortex(i.e. blue square symbol in Fig. 5.15(c)) gets dominated when the main vortex is strong to maintain

overall flow behavior, and a second instance of secondary vortex(i.e. red square symbol in Fig. 5.15(c)) to recharge the main vortex. It is observed that the vortex path goes to the center of aneurysm opening and shifts more to the right as Re is increased.

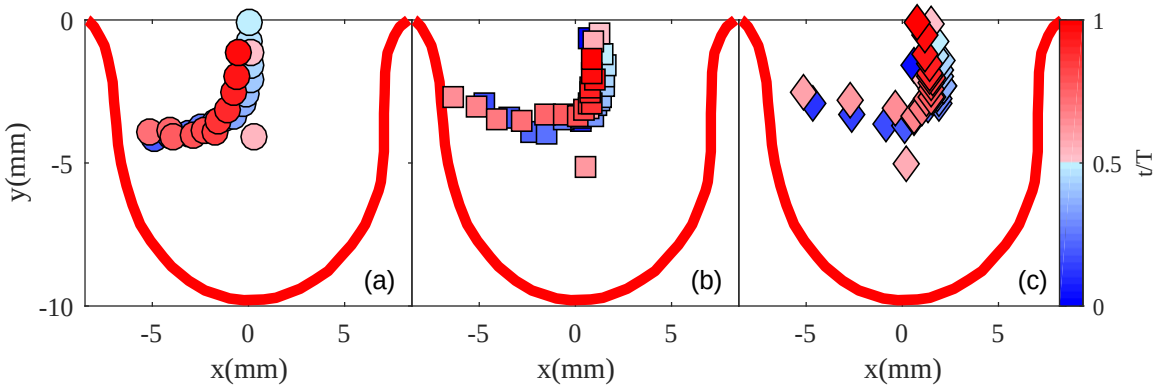

Figure 5.14: Vortex path in the aneurysm sac for α of 2 for (a) $Re_p = 50$, (b) $Re_p = 150$, and (c) $Re_p = 270$.

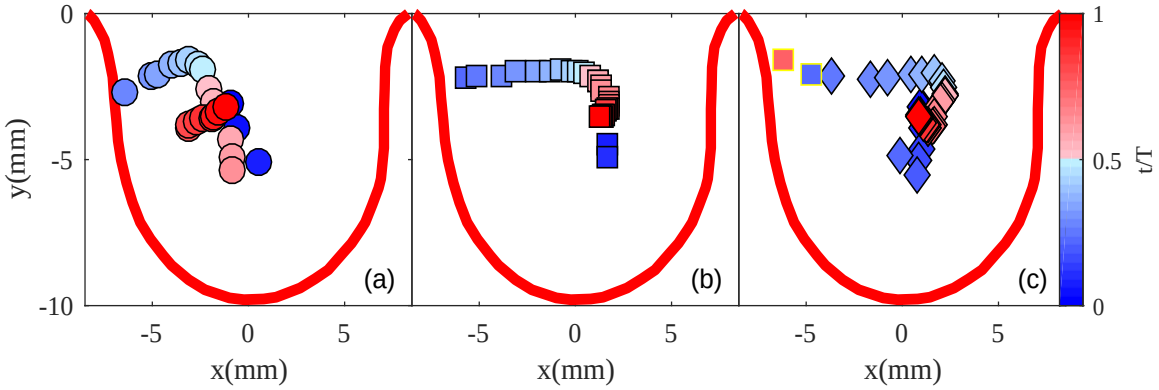

Figure 5.15: Vortex path in the aneurysm sac for α of 5 for (a) $Re_p = 50$, (b) $Re_p = 150$, and (c) $Re_p = 270$

5.3.2 Vortex path results for BF=1.6

The vortex paths are determined for α of 2 at different Reynolds number. Figs. 5.16(a),(b), and (c) show the vortex paths for $Re_p = 50, 150$, and 270, respectively. For this α, the vortex structures moved in similar fashion as the flow behavior observed for $BF = 1.0$. This means that the vortex structure forms from the proximal side of the aneurysm sac and convects upwards towards the pipe region. The acceleration of the fluid in the pipe

region pushes the vortex back to the aneurysm sac and dissipates. Furthermore, two vortices are also observed to form and dissipate in one pressure cycle for all Re numbers investigated. The vortex paths are observed to have curvature similar to the ones observed for BF of 1. However, the vortex paths do not seem to go past the center of the aneurysm orifice for all Re unlike the ones observed for $BF = 1.0$.

Different flow phenomena are observed at different Re for α of 5. Figure 5.17(a),(b), and (c) show the vortex path for $Re_p = 50, 150$, and 250. The vortex path, in general travels upwards towards the aneurysm opening unlike the flow behavior observed for the same α for BF of 1. For $Re_p = 50$, the vortex forms near the proximal neck and convects towards the aneurysm opening, and the acceleration of the fluid in the pipe pushes the vortex back into the aneurysm sac. This vortex is observed to go up and down at the center of the aneurysm sac before dissipating completely at the end of the cycle. For $Re_p = 150$, the vortex structure forms near the proximal neck and travels towards the aneurysm orifice. This vortex stays around the aneurysm opening for a few phases in the cycle, slowly heads to the aneurysm neck, then rapidly decays while moving towards the aneurysm dome. Lastly, there is no clear indicator for the formation of the vortex for $Re_p = 250$. The vortex structure is present throughout the entire pressure cycle where it travels up and down around the center of the aneurysm orifice. This may indicate the presence of the rotating flow structure throughout the entire measurement for this case scenario. It is observed that the vortex structure is pulled near the proximal neck from time to time which may indicate the vortex being recharged similar to the one observed for the same Re and α for $BF = 1.0$.

5.3.3 Vortex strength results for BF=1.0

The vortex strength of the flow structures observed are evaluated to quantify the magnitude of the rotational motion inside the aneurysm sac. Understanding this behavior helps us to understand the flow field behavior as well as quantify the quality of mixing of

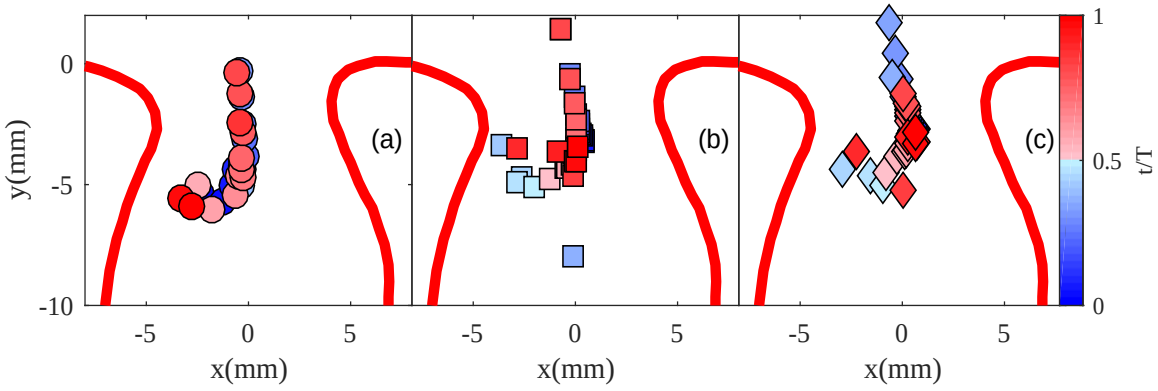

Figure 5.16: Vortex path in the aneurysm sac for α of 2 for (a) $Re_p = 50$, (b) $Re_p = 150$, and (c) $Re_p = 270$.

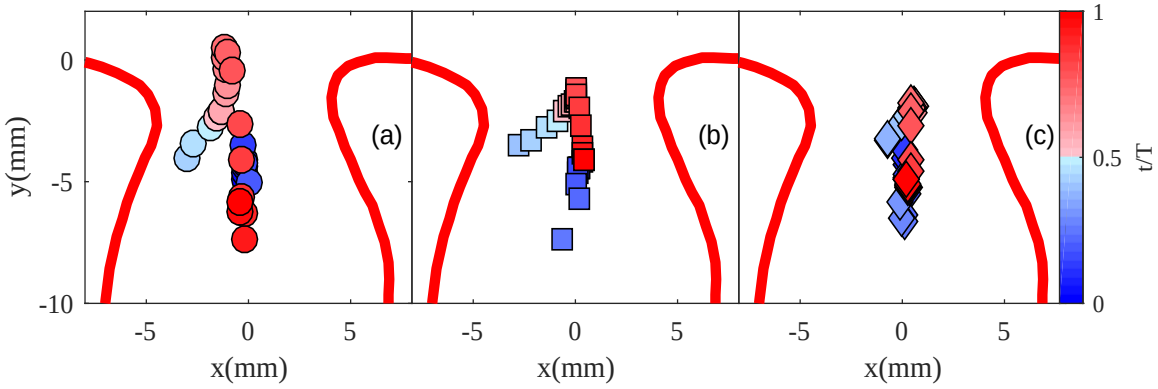

Figure 5.17: Vortex path in the aneurysm sac for α of 5 for (a) $Re_p = 50$, (b) $Re_p = 150$, and (c) $Re_p = 270$

fluid in the aneurysm sac. Furthermore, understanding the vortex strength may provide us insight to the contribution of the vortical structure to increase risk of rupture.

To perform this analysis, the vortex strength is determined by taking the curl of the velocity field at different phases in the pressure cycle for each test cases. Furthermore, the peak vortex strength at the center of the vortical structure for each phase of the cycle is determined using a vortex center identification method by [131]. Figure 5.18(a) shows the vortex strength for $\alpha = 2$ cases while Figure 5.18(b) show the vortex for the $\alpha = 5$ cases. It is observed that the vortex strength varies at different phases in the driving pressure cycle. For $\alpha = 2$ flow conditions (i.e., Fig. 5.18(a)), the vortex strengths of the flow structures vary at different phases as they form and decay throughout pressure

cycle (see Figs. 5.6 and 5.7). It is also observed that each of the vortices rapidly decay in strength as they enter back in the aneurysm cavity during the acceleration phases of the pressure cycle. Furthermore, the vortex formation and dissipation process for one of the vortices is higher than the second vortex, and this corresponds to the higher velocity peaks observed from the pipe centerline velocity results. This increase vortex strength and rapid decay was also observed with experimental studies by [22]. In the current study, the impact of Re_p to the vortex strength behavior of the flow structures in the aneurysm is shown.

Figure 5.18(b) shows the vortex strength values at $\alpha = 5$ for $Re_p = 50$ and $Re_p = 270$ flow conditions. Here, the vortex strength trends at different Re_p for this α is different when compared to $\alpha = 2$ (i.e., Fig. 5.18(a)). For this α, the vortices observed slowly decrease in strength throughout the pressure cycle. Two different vortices are observed for $Re_p = 50$ (i.e., Fig. 5.8) with strengths that respond to incoming pipe flow velocity. For $Re_p = 270$, a complex interaction of vortices is observed. The two secondary vortices of same strength (see green diamond symbols in Fig. 5.9) merge with the primary vortical structure. One of the secondary vortex structure energizes the primary vortical structure which can be seen as a rapid rise in vortex strength of the newly formed vortex structure.

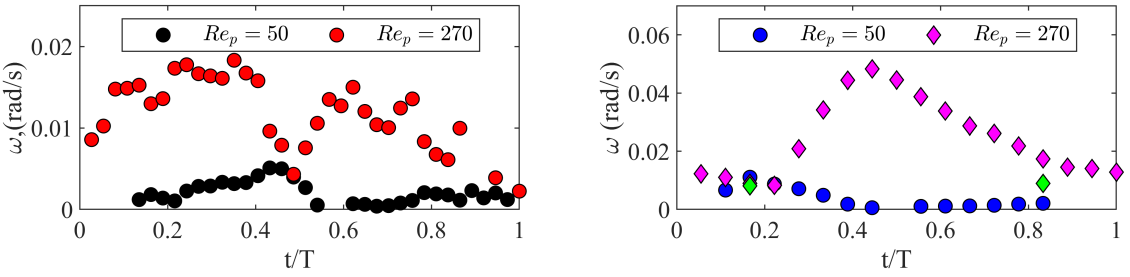

Figure 5.18: Phase-averaged vorticity in aneurysm sac for (a) $\alpha = 2$ (b) $\alpha = 5$.

5.3.4 Impinging location results for BF=1.0

The flow impingement is an important parameter to study as this may be correlated to the increased risk of rupture [88, 132]. Cebral et al. [88] reported that the inflow jet most frequently entered the distal aneurysm neck which impacted the aneurysm wall. In their study, they reported that aneurysms with changing impingement regions all ruptured. Furthermore, their study also showed that the ruptured aneurysms had small impingement zones, while unruptured aneurysms have large impingement zones. Baek et al. [132] used CFD to study the wall shear stress and pressure distribution in internal carotid artery with aneurysm and found that locations of high pressure coincide with rupture locations. These studies have motivated us to investigate the instantaneous impinging location behavior during the pressure cycle and identify how the flow structures are influencing the impinging location distribution.

Impinging locations are tracked throughout the pressure cycle to identify potential locations of high pressure points in the aneurysm sac. In this study, this is done by identifying a possible impinging location along the aneurysm geometry. Figure 5.19(a) shows the schematic of the aneurysm geometry where the stagnation locations are determined along the arc length s, and the impinging location method discussed in the Approach section is implemented for this analysis.

The impinging locations for each phase in the pressure cycle are presented as frequency distribution for each test cases. For these plots, the arc length s is first divided into nine intervals where the impinging location occurrences are counted in each interval. These number of occurrences (n_j) are then divided by the total number of phases (N) in the pressure cycle to give the frequency distribution. The results for $\alpha = 2$ conditions are now shown in Figs. 5.19(b) for $Re_p = 50$ and 5.19(c) for $Re_p = 270$. On the other hand, the results for $\alpha = 5$ conditions are shown in Figs. 5.19(d) for $Re_p = 50$ and 5.19(e) for $Re_p = 270$. The results show that for $\alpha = 2$ conditions, the impinging locations appear

to have high distribution near D_{max} to s. The impinging locations are more spread out for $Re_p = 50$ (i.e., Fig. 5.19(b))(∼10%), while for $Re_p = 270$ (i.e., Fig. 5.19(c)) high probability occurs towards s (∼30%). This suggests that Re_p for the same α condition impacts the impinging locations in the aneurysm sac. Although the flow trend is similar for both Re_p scenarios (see 5.2), the flow structures' variation for each Re_p may cause the high pressure points to be more spread out at $Re_p = 50$ over the distal region of the sac than $Re_p = 270$ where the high pressure points become concentrated towards the distal neck. The trend observed is also similar for $\alpha = 5$ conditions. At $Re_p = 50$ (i.e., Fig. 5.19(d)), the impinging locations are distributed along D_{max} to s (∼15% -20%). The $Re_p = 270$ flow scenario (i.e., Fig. 5.19(e)) now shows most of the distribution near the distal neck (∼75%) than with the same Re_p at $\alpha = 2$(∼30%). The results obtained for the different inflow scenarios then suggest that Re_p appears to have a strong influence over the impinging location than α.

The impingement behavior and location are also observed in previous studies. [88] reported that the inflow jet most frequently entered the distal aneurysm neck which impacted the aneurysm wall. In their study, they reported that aneurysms with changing impingement regions all ruptured. Furthermore, their study also showed that the ruptured aneurysms had small impingement zones (i.e., size of impingement compared to the size of the aneurysm), while unruptured aneurysms have large impingement zones. Here, the current experimental study shows changing impingement regions (i.e., spread out distribution of impinging location in this paper) and small impingement zones (i.e., concentrated distribution of impinging location in this paper) increase the risk of aneurysm rupture.

5.3.5 Impinging location results for BF=1.6

The impinging locations are also determined for $BF = 1.6$ for a single pressure cycle at different inflow conditions. The results are shown in Figs. 5.20(b)-(d), and the schematic

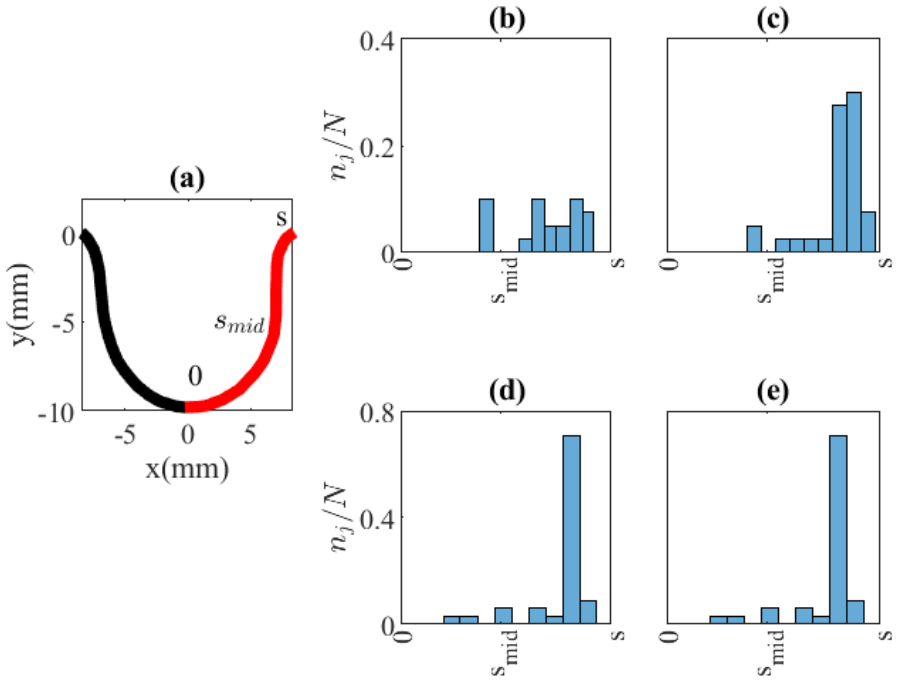

Figure 5.19: Impinging locations and their probability in aneurysm sac for a single pressure cycle. (a) Aneurysm schematic with arc length s, (b) $\alpha = 2$, $Re_p = 50$, (c) $\alpha = 2$, $Re_p = 270$, (d) $\alpha = 5$, $Re_p = 50$, and (e) $\alpha = 5$, $Re_p = 270$.

of the aneurysm geometry is shown in Fig. 5.20(a) where the impinging locations are tracked. The results show qualitatively that for all inflow conditions investigated in this study, the impinging locations are located near the distal aneurysm neck. For $\alpha = 2$ conditions (Fig. 5.20(b)), the impinging points are concentrated near s_{mid} ($\sim 25\%$) for one pressure cycle. This concentrated impinging points shifts upward (i.e.,s_{mid}-s) for $Re_p = 270$ (Fig. 5.20(c)) ($\sim 45\%$) as the vortical structure stays longer for this Re_p condition.

The high pressure points for $\alpha = 5$ flow conditions also show the locations at $s_{mid} - s$ for a single pressure cycle. The impinging locations for $Re_p = 50$ show finer distribution than its $\alpha = 2$ counterpart. Nevertheless, the impinging locations are still concentrated near s_{mid} ($\sim 7.5\%$). Two locations of increased impinging locations ($\sim 22\%$) exposure are seen for $Re_p = 270$ (i.e., Fig. 5.20(e)). The lower impinging location frequency

distribution seen in this scenario is due to the shape of the vortex structure where its center is near D_{neck}. This indicates that the for this Re_p scenario, there is more shearing stresses involved than impinging occurrences.

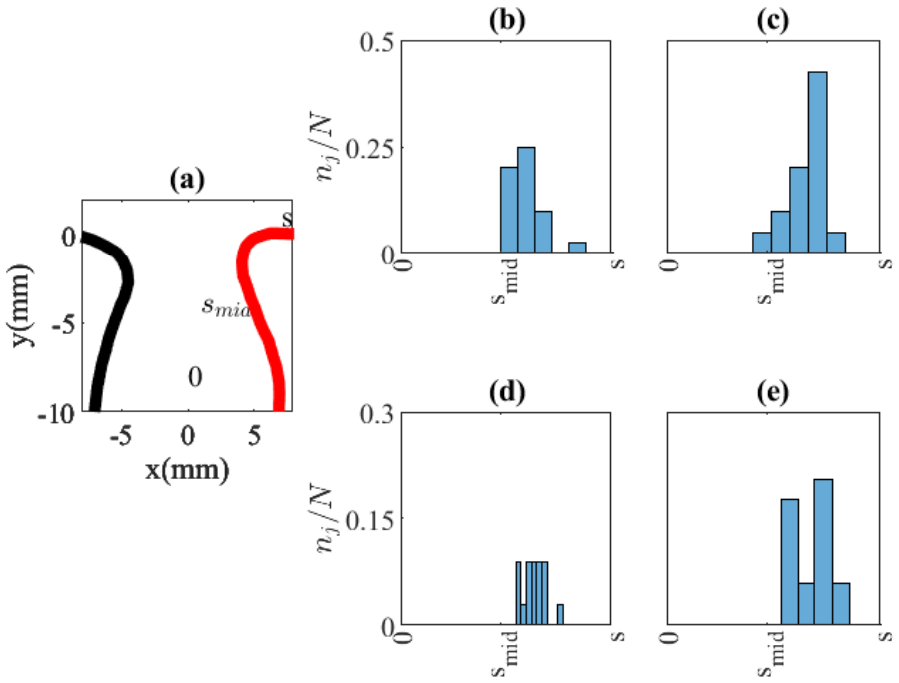

Figure 5.20: Impinging locations and their probability in aneurysm sac for a single pressure cycle. (a) Aneurysm schematic with arc length s, (b) $\alpha = 2$, $Re_p = 50$, (c) $\alpha = 2$, $Re_p = 270$, (d) $\alpha = 5$, $Re_p = 50$, and (e) $\alpha = 5$, $Re_p = 270$.

5.3.6 WSS results for BF=1.0

Wall shear stresses along the aneurysm sac are analyzed throughout the pressure cycle to determine possible locations of increased likelihood of rupture [146, 45]. We want to investigate the wall shear stress distribution along the aneurysm geometry during the pressure cycle, and identify the impact of the flow structure to the wall shear stresses. The wall shear stresses are determined along the arc length s (i.e., Fig. 5.19(a)) for each phase in the pressure cycle at different inflow conditions. With no-slip condition at the aneurysm walls, the velocity components parallel and $0.7mm$ away to every strip ds are

extracted. Details of this wall shear stress calculation are provided in the Approach section.

Figure 5.21(a) and (b) show the τ results for a complete flow cycle at $\alpha = 2$ and $Re_p = 50$ and $Re_p = 270$, respectively. Figure 5.22(a) and (b) show the τ results for $\alpha = 5$ and $Re_p = 50$ and $Re_p = 270$, respectively. The results for $\alpha = 2$ conditions indicate increased τ values near s which occurs during the peaks of the pressure cycle. For $Re_p = 50$ (i.e., Fig 5.21(a)), the high τ values occurs during the vortex formation stages (see Fig. 5.6 at $t/T = 0.00$-$t/T = 0.21$). Initially, the flow is attached along the aneurysm sac profile with accelerating flow near the distal side. At the vortex formation instances, flow separation occurs at the proximal wall, and the incoming flow gets diverted towards the distal wall. For $Re_p = 270$ and $\alpha = 2$ (i.e., Fig 5.21(b)), high τ values near s also occur during the peaks of the pressure cycle (see Fig. 5.7 at $t/T = 0.00$-$t/T = 0.11$) as flow trend of the vortical structures is similar to $Re_p = 50$ (i.e., vortex comes out of the aneurysm sac). Here τ values of nearly four times than τ values at $Re_p = 50$ is observed here since the Re_p increased fivefolds. It is also important to observe here that low τ values occur at $0 - D_{max}$ as fluid moves slow near the dome area at all time phases of the pressure cycle.

High τ values are also shown near s for $\alpha = 5$ flow conditions. The $Re_p = 50$ flow scenario (i.e., Fig 5.22(a)) show high WSS values during the vortex formation phases (see Fig. 5.8 at $t/T = 0.00$-$t/T = 0.21$) which is similar to its $\alpha = 2$ counterpart. Low τ values are also seen from $0 - D_{max}$ at all phases in the flow cycle for this Re_p condition. For $Re_p = 270$ (i.e., Fig 5.22(b)), τ values are distributed at different locations along s. Peak τ appear near s during the vortex merging process of the pressure cycle (see Fig. 5.9 at $t/T = 0.00$-$t/T = 0.53$). During these phases in the flow cycle, the secondary vortical structure is merging with the primary vortex to create a new vortex which travels towards the distal end of the aneurysm sac. This Re_p condition also shows τ values near D_{max} during the vortex convection phases (i.e.,$t/T = 0.42 - 0.53$). Lastly, the τ values

of nearly five times than τ values at $Re_p = 50$ is observed here.

The observed high shear stress locations near s in the aneurysm sac are also evident in previous investigations [22, 149, 150, 27]. In our study, the results now highlight the impact of the inflow parameters to the observed τ locations and links them to the flow structure at particular time phases. The current investigation also shows that the inflow conditions primarily influence the distal region of the aneurysm sac as high τ are observed from $D_{max} - s$ at all inflow scenarios. For a fixed α, impact of Re_p is highlighted further through the increased in shear stress at the distal neck region. Meanwhile, for a fixed Re_p, the impact of α is seen through the higher shear stress values at $\alpha = 5$ than $\alpha = 2$.

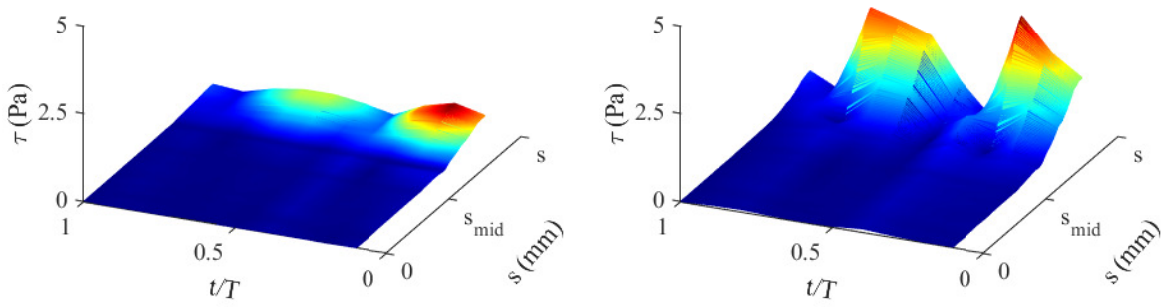

Figure 5.21: Phase-averaged wall shear stress in aneurysm sac for $BF = 1.0$ for $\alpha = 2$. (a) $Re_p = 50$ and (b) $Re_p = 270$.

5.3.7 WSS results for BF=1.6

Wall shear stresses throughout the pressure cycle are also determined for $BF = 1.6$ at different inflow conditions. This is determined along the arc length s_{neck} for each phase in the pressure cycle at different inflow conditions. No-slip conditions are still applied along the aneurysm neck, while the velocity components parallel and $0.5mm$ away from the walls are extracted. Figure 5.23 shows the τ results for $\alpha = 2$ flow scenarios while Fig. 5.24 shows the τ results for $\alpha = 5$.

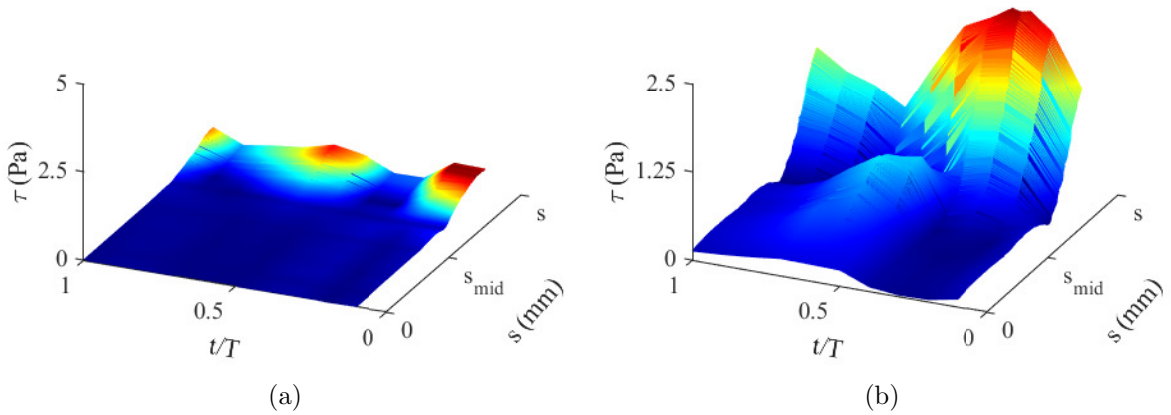

Figure 5.22: Phase-averaged wall shear stress in aneurysm sac for BF = 1.0 for $\alpha = 5$. (a) $Re_p = 50$ and (b) $Re_p = 270$.

Wall shear stress results for $\alpha = 2$ show high τ values from $0 - D_{neck}$ at several phases in the pressure cycle. For $Re_p = 50$ (i.e., Fig. 5.23(a)), these high τ values occur during the vortex formation and growth stages (see Fig. 5.10 at $t/T = 0.00$-$t/T = 0.21$) where the formed vortical structure approaches the center of the aneurysm geometry. This high τ exposure at $0 - D_{neck}$ repeats for the remaining half of the cycle as a separate vortical structure forms and decays (see Fig. 5.10 at $t/T = 0.55$-$t/T = 0.68$). With $Re_p = 270$ (i.e., Fig. 5.23(b)), similar observation can be concluded as the flow evolution is similar to $Re_p = 50$. The shear stresses, however, are more prominent with $Re_p = 270$ than $Re_p = 50$ as there are a sharp increases in values for a short amount of time in the pressure cycle. In addition, the τ values experienced at the distal wall for $Re_p = 270$ are double of the τ values for $Re_p = 50$, and low shear stresses are found from $D_{neck} - s_{neck}$ for both Re_p scenarios.

With $\alpha = 5$ flow conditions, the τ experienced by the distal aneurysm wall are different than the ones observed for $\alpha = 2$. For $\alpha = 5$ and $Re_p = 50$ (i.e., Fig. 5.24), increased τ values are found near $0 - D_{neck}$ during vortex formation (i.e., $t/T = 0.0.00$-$t/T = 0.21$) and vortex oscillation and dissipation phases inside the aneurysm (i.e.,$t/T = 0.58$-$t/T = 0.95$). The τ values are also found to be comparable in magnitude with the $\alpha = 2$ and

$Re_p = 50$ flow condition. The presence of the vortical structure which moves in upward-downward oscillating fashion for $Re_p = 270$ (i.e., Fig. 5.24) results in τ values to rapidly increase and decrease along $0 - D_{neck}$. These high τ values occur when the vortex core is at D_{neck} where high velocity gradients are observed due to the aneurysm curvature.

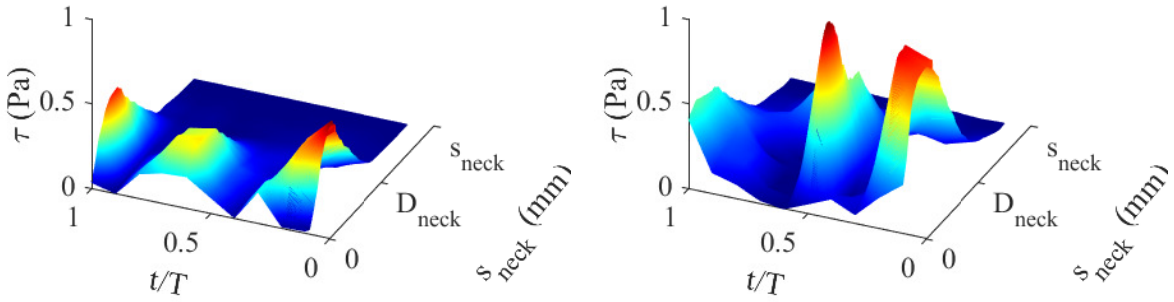

Figure 5.23: Phase-averaged wall shear stress in aneurysm sac for BF = 1.6 for $\alpha = 2$. (a) $Re_p = 50$ and (b) $Re_p = 270$.

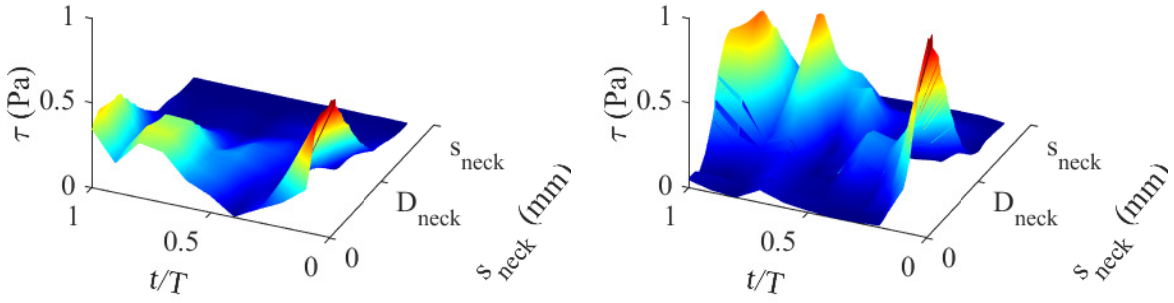

Figure 5.24: Phase-averaged wall shear stress in aneurysm sac for BF = 1.6 for $\alpha = 5$. (a) $Re_p = 50$ and (b) $Re_p = 270$.

5.4 POD results

Based on the PIV flow field data, the large-scale flow structures exhibit a complex evolution in the pressure cycle at different inflow scenarios. The mean flow results illustrated that aneurysms contain a vortical structure that take different shapes and characteristics depending on the inflow profile. By looking at the entire flow evolution in a pressure cycle, the flow evolution results show that this vortical structure begins its formation near the proximal side of the cavity, grows in shape and strength, moves into the aneurysm opening or the distal location, and decays at the end of the pressure cycle. The complex behavior from initial analyses leads us to investigate further on how this phenomena occurs and how we can look at the problem at a different perspective or decompose the flow into smaller key features. The phenomena observed motivated us to look into using data decomposition methods to provide further insight into the flow in greater detail than before.

We now discuss the application of advance data analysis techniques on the velocity flow field to study the large-scale flow structures in detail and understand the mechanisms that contribute to the observed flow behavior. The results from Proper Orthogonal Decomposition are first presented which contain key results obtained from POD modes, energies, time-varying coefficients, and low-order reconstruction. The results are organized such that each section contains the important information provided by the method.

5.4.1 POD modes for BF=1.0

The POD mode results are first presented here as they provide insight to the large-scale flow structures and their underlying behavior. The POD modes are the basis functions or eigenvectors ($\overrightarrow{\Psi}(x,y)$) of the POD kernel ($\mathbf{R}$) given in Eq. 4.11 that are optimally determined to best represent the flow field. The modes shown here provide a mathematical description of the behavior of the flow structures present in the aneurysm

and are orthogonal to each other. The POD modes are shown in order of importance, as each mode is related to the captured kinetic energies in the flow. Furthermore, the modes determined represent the fluctuating energetic flow structures in the flow field which can tell us about the coherent flow features influencing the overall flow behavior (see 5.2 results). As the POD modes will have components $\psi_{uu}(x, y)$ and $\psi_{vv}(x, y)$, the streamwise components (i.e., u-component of velocity) and transverse components (i.e., v-component of velocity) are analyzed at different inflow conditions in this section. Each inflow scenario captured $\sim$ 13000 modes where the first few modes in each cases are discussed in next few paragraphs.

The streamwise components for the first three POD modes ($\psi_{uu}(x, y)$) for $Re_p = 50$ and $\alpha = 2$ are shown in Figs. 5.25(a)-(c) while the transverse components ($\psi_{vv}(x, y)$) are shown in Figs. 5.26(a)-(c). The first three modes are only presented here as their total energy contribution captures more than 95% of the total fluctuating kinetic energy for this inflow scenario. A more detailed discussion of the POD modes' energy and their contribution are presented in the POD energies section of this dissertation (see 5.4.2). The POD mode results shown indicate presence of different fluctuating structures. Looking at the figures, it can be qualitatively seen that the mode shapes are different for each given Re_p condition. High peak components of the first mode shape relating to the u-component of velocity are observed near the proximal and distal side of the aneurysm (Fig.5.25(a)). This shows that the flow conditions are the same from the upstream and downstream locations of the aneurysm. The entrance of the aneurysm shows a gradient of components, which shows penetration of this component of fluid velocity inside the aneurysm. The first mode shape relating to the v-component of velocity(Fig.5.26(a)) also has high components near the proximal and distal sides of the aneurysm. This shows high magnitudes of v-component of velocity enters and exits the aneurysm, and further suggest high shear stress zones. The second mode shape relating to the u-component of velocity shows high components at the aneurysm opening while a magnitude of u-

component of velocity of the same order engulfs the aneurysm sac (Fig.5.25(b)). The second mode shape relating to the v-component of velocity(Fig.5.26(b))has high values which again suggests high shear stress zones. The third mode shape(Figs.5.25(c) and (Figs.5.26(c) has structures that are similar to the ones observed with the first mode but have a low energy content.

The difference is first observed when the first POD modes for the two scenarios are compared as they are opposite of each other. The second mode shape for $Re_p = 50$ looked similar to the third mode shape for $Re_p = 270$, while the third mode shape for $Re_p = 50$ is similar to the mode shape for $Re_p = 270$. While first POD mode remains the same for both Re_p, the order of the structure for the second and third mode will depend on the flow regime. The same approach can be used with the POD modes related to the v-component of velocity, shown in Figs.5.26 and 5.28, respectively. The second mode shape for $Re_p = 50$ is similar to the third mode shape for $Re_p = 270$, while the third mode shape for $Re_p = 50$ is similar to the second mode shape for $Re_p = 270$. This indicates that the change in Re_p while keeping the α the same suggest change in the order of the POD modes. This points to the importance of the order of POD modes which changes the dynamics of the flow.

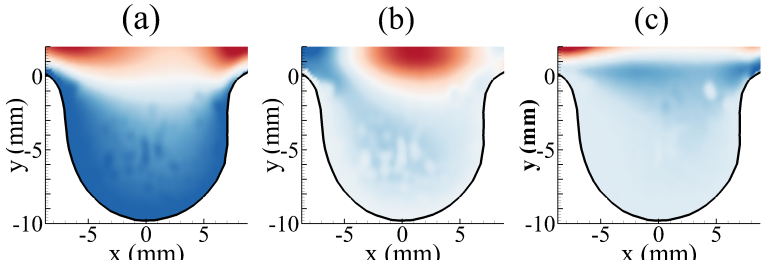

Figure 5.25: Streamwise POD modes for $Re_p = 50$ and $\alpha = 2$. (a) ψ^1_{uu}, (b) ψ^2_{uu}, and (c) ψ^3_{uu}.

Similar analysis are performed for $Re_p = 270$ and $\alpha = 2$ for the first three streamwise ($\psi_{uu}(x, y)$) and transverse ($\psi_{vv}(x, y)$) POD modes which are shown in Figs. 5.27(a)-(c) and Figs. 5.28(a)-(c), respectively. The first three modes have captured 95% of the fluctuating kinetic energy and sufficient to describe the inflow scenario. Here the first

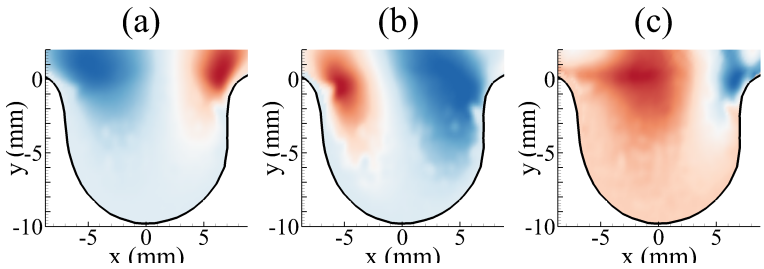

Figure 5.26: Transverse POD modes for $Re_p = 50$ and $\alpha = 2$. (a) ψ^1_{vv}, (b) ψ^2_{vv}, and (c) ψ^3_{vv}.

mode shape relating to the u-component of velocity(Fig.5.27(a)) has high components near the proximal and distal side of the aneurysm. There is also a gradient of components which indicates penetration of this component of velocity into the aneurysm. This flow penetration is not as deep and inclined as Re=50, and thus the peak components are near neck of the aneurysm. The first mode shape relating to the v-component of velocity (Fig.5.28(a)) shows high components near the entrance and exit of the aneurysm, with the flow going into the aneurysm occupying a large area while the fluid exiting uses a small area. The components near the distal side also shows a high gradient which suggest a high shear stress zone. The second mode shape relating to the u-component of velocity (Fig.5.27(b)) shows structures that impinges and goes deep at the distal side of the aneurysm sac, while the v-component shows structures at the entrance and exit of the aneurysm. The third mode relating to the u-component of velocity also shows high values at the entrance and the proximal side of the aneurysm, while very low values at the distal end of the sac. The mode which relates the v-component shows high and low values at the proximal and entrance of the aneurysm, which may indicate a presence of vortex and high shear stress zone on the proximal side of the aneurysm.

Here, we see the impact of Re_p to the flow condition for the same α scenario. For $Re_p = 270$, the POD modes for both streamwise and transverse components of velocity are similar and different than the POD modes for $Re_p = 50$. Similar in a sense that the modes are visually same as $Re_p = 50$ with contour field just shifted to the right. Although a single fluctuating feature (i.e., POD mode) may not be entirely describing a flow field

in this scenario, this is because it requires a combination of the POD modes to represent the flow field for a particular phase in the pressure cycle. The results here indicate that the flow fields seen in the phase-averaged results for $Re_p = 270$ are a combination of the POD modes. The combination of POD modes represents the coherent flow structures in the flow field that will become evident when we analyze the POD energy results and time-varying coefficient results.

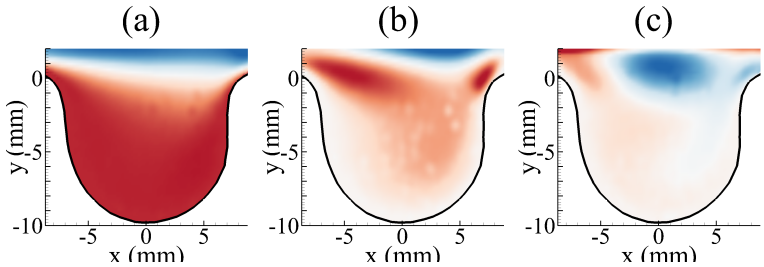

Figure 5.27: Streamwise POD modes for $Re_p = 270$ and $\alpha = 2$. (a) ψ^1_{uu}, (b) ψ^2_{uu}, and (c) ψ^3_{uu}.

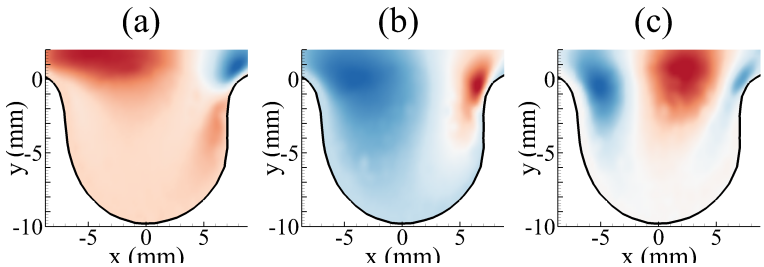

Figure 5.28: Transverse POD modes for $Re_p = 270$ and $\alpha = 2$. ((a) ψ^1_{vv}, (b) ψ^2_{vv},, and (c) ψ^3_{vv}.

We now analyze the POD mode results for $\alpha = 5$ and $Re_p = 50$ flow conditions. The streamwise modes ($\psi_{uu}(x, y)$) are shown in Figs. 5.29(a)-(e) while the transverse POD modes are shown in Figs. 5.30(a)-(e). The first five POD modes are included for this α condition as more number of modes are required to capture almost 95% of the total fluctuating kinetic energy than the $\alpha = 2$ condition. The results also show a different set of spatial structures for this α than $\alpha = 2$ for the same Re_p scenario (see Figs. 5.25 and 5.26). The first mode shape for the u-component of velocity(Fig.5.25(a)) shows a uniform structure inside the aneurysm sac while low components of this component of

velocity are in the proximal and distal sides. The first mode of the v-component of velocity(Fig.5.26(a)) shows a high and low peak values near the neck of the aneurysm sac. This suggests a strong forward flow inside the aneurysm sac. The second mode of the u component of velocity (Fig.5.25(b)) has a uniform structure inside the aneurysm sac while the POD mode for the v-component of velocity(Fig.5.26(b)) shows a symmetrical structure near the aneurysm neck. This suggest a uniform flow inside the aneurysm sac but a coherent structure might be present near the aneurysm opening. A flow structure can also be observed for the third POD mode (Fig.5.25(c) and Fig.5.26(c)) near the proximal neck while uniform flow is present inside the aneurysm sac. As observed in the figures, the first and second POD modes show symmetry at the aneurysm model center ($x = 0mm$) while the third POD mode does not exhibit symmetry. The fourth and fifth POD modes look similar in shape (Figs. 5.25(d)-5.25(e)) but differ in kinetic energy content.

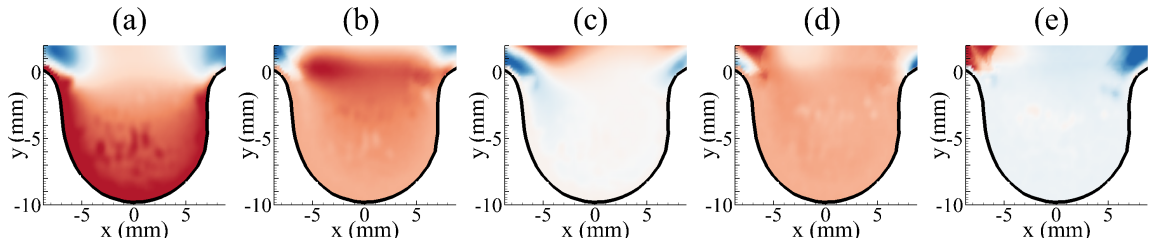

Figure 5.29: Streamwise POD modes for $Re_p = 50$ and $\alpha = 5$. (a) ψ^1_{uu}, (b) ψ^2_{uu}, (c) ψ^3_{uu}, (d) ψ^4_{uu}, and (e) ψ^5_{uu}.

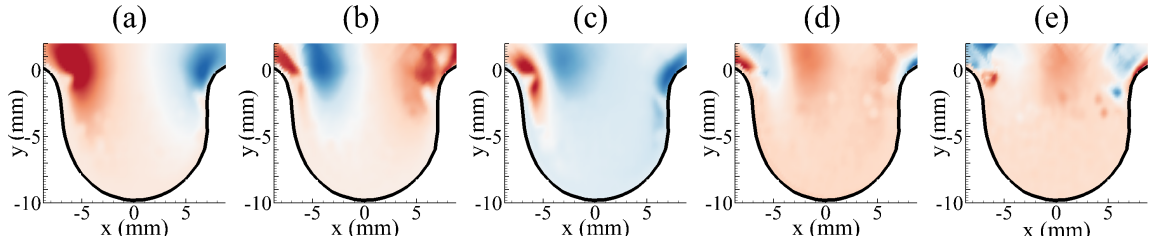

Figure 5.30: Transverse POD modes for $Re_p = 50$ and $\alpha = 5$. (a) ψ^1_{vv}, (b) ψ^2_{vv}, (c) ψ^3_{vv}, (d) ψ^4_{vv}, and (e) ψ^5_{vv}.

The POD modes for $Re_p = 270$ and $\alpha = 5$ are analyzed and presented in Figs. 5.31(a)-(e) for the streamwise component of velocity and Figs. 5.32(a)-(e) for the transverse

component of velocity. The modes in this flow condition also require five POD modes to capture 95% of the fluctuating kinetic energy which is similar to the amount of modes for $Re_p = 50$ and $\alpha = 5$ scenario. Here, we now highlight the different and unique structures captured by POD for this condition. The mode shapes show presence of different and intricate spatial structures in the aneurysm cavity.

The first POD mode (i.e., Figs. 5.31(a) and 5.32(a)) high and low values near the upstream and downstream lips of the aneurysm. This first POD mode shape is similar to previous modes in other flow scenarios (see Figs. 5.25(a) and 5.26(a), Figs. 5.27(a) and 5.28(a), and Figs. 5.29(a) and 5.30(a)). The second POD mode (i.e., Figs. 5.31(b) and 5.32(b)) shows a structure near the aneurysm opening and symmetry features near $x = 0mm$. The third POD mode (i.e., Figs. 5.31(c) and 5.32(c)) resembles the same mode shape as $Re_p = 270$ and $\alpha = 2$ (see Figs. 5.27(c) and 5.28(c)) which contain high and low values of u and v components of velocity near the upstream and downstream lips of the aneurysm. These features are also present with the fourth POD mode (i.e., Figs. 5.31(d) and 5.32(d)) with one near the upstream lip and the other at the distal end of the aneurysm. Lastly, the fifth POD mode (i.e., Figs. 5.31(e) and 5.32(e)) show a spatial feature at the distal end of the aneurysm. These first few POD mode shapes are the most important spatial features that can describe the flow field for this α condition. The POD mode shapes also highlight the complexity of the flow field in the phase-average results as each coherent structure contains the combination of these modes that have different energy content.

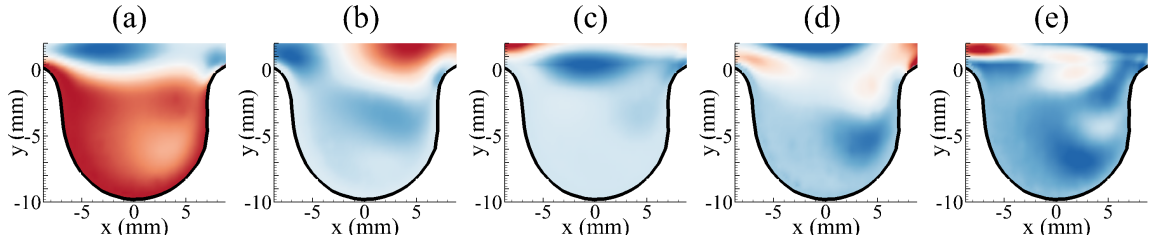

Figure 5.31: Streamwise POD modes for $Re_p = 270$ and $\alpha = 5$. (a) ψ^1_{uu}, (b) ψ^2_{uu}, (c) ψ^3_{uu}, (d) ψ^4_{uu}, and (e) ψ^5_{uu}.

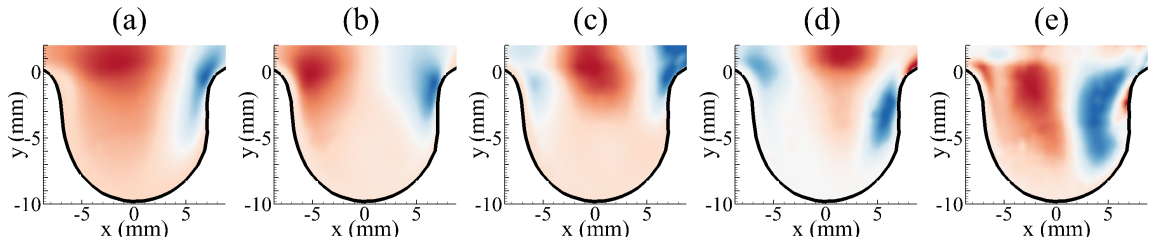

Figure 5.32: Transverse POD modes for $Re_p = 270$ and $\alpha = 5$. (a) ψ^1_{vv}, (b) ψ^2_{vv}, (c) ψ^3_{vv}, (d) ψ^4_{vv}, and (e) ψ^5_{vv}.

The POD mode results presented in this section for $BF = 1.0$ show that the inflow conditions impact the POD modes for each scenario. We note that the change in α shows may change the POD modes that are necessary to capture a percent threshold of turbulent kinetic energy in the flow. In this study, the $\alpha = 5$ flow scenario contain complex features as more POD modes are required to break down and capture its flow dynamics than $\alpha = 2$ scenarios. For a fixed α and different Re_p conditions, the inflow conditions may have similar POD mode shapes but their of importance or contribution will be different. These are important findings as the POD mode shapes tell us what spatial features are captured in the flow field. The mode shapes that describe the flow conditions can also tell us why certain inflow conditions are complex. Lastly, certain POD mode shapes maybe similar at various conditions, but their level of importance or contribution to the flow are different. To further understand the POD modes and their contribution to the flow, we will now look at the POD mode energy results.

5.4.2 POD energies for BF=1.0

The POD energy (λ_i) results are presented here to provide insight on the contribution of each POD mode shapes to the observed flow behavior. The POD energy are the eigenvalues from the discrete POD formulation given in Eq. 4.11. We present the POD energy results as a relative contribution (i.e., the ratio of energy captured by each POD mode and total fluctuating kinetic energy) where the total fluctuating kinetic energy can be estimated by summing all the λ_i for a given flow scenario. The results are shown in

Fig. 5.33 for the first ten modes out of $\sim$ 13000 captured modes for the studied flow conditions. The results indicate that each POD mode has certain percentage of kinetic energy contribution to the total fluctuating component of the flow. As observed from the figure, the contribution of each POD mode decreases with increasing POD mode numbers. For instance, for $Re_p = 50$ and $\alpha = 2$ scenario, the first mode captures $\sim 85\%$ of the total kinetic energy. The second mode adds $\sim 9\%$ to the total kinetic energy for this flow scenario, while the third mode only contains $\sim 2\%$ of the total kinetic energy content. These results allow us to justify the three POD mode shapes presented for this inflow condition in the POD modes section (see Figs. 5.25 and 5.26) as these mode shapes already captured $\sim 95\%$ of the total fluctuating kinetic energy. Thus, the mode shapes from four and beyond have smaller contributions compared to the first three modes. Similar conclusions can be deduced for $Re_p = 270$ and $\alpha = 2$ scenario (i.e., three modes), and $\alpha = 5$ scenarios (i.e., five POD modes).

The POD energy results tell us that for the studied cases, about 95% of the fluctuating energy can be captured either by the first three or five POD modes. For flow scenarios with $\alpha = 2$, the first three mode shapes are likely to have dominating influences on the flow behavior in the aneurysm. This is in contrast with $\alpha = 5$ flow conditions, where five POD modes are needed to meet the 95% threshold. Since the POD method allow us to decompose the data into optimally determined mode shapes to describe the flow, the combination of these mode shapes allow for formation and convection of vortical structures. The POD energy results now add insight to complex interplay of POD modes and is influenced by Re_p and α at different flow scenarios.

5.4.3 POD time-varying coefficients for BF=1.0

We now analyze the impact of the POD mode shapes to the flow field at a given instance t in the pressure cycle. This can be evaluated by determining the time-varying coefficients ($a_i(t)$) of the POD modes. The time-varying coefficients can be determined

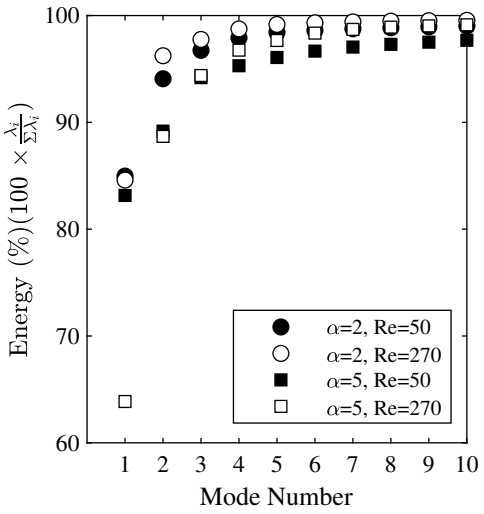

Figure 5.33: Sum of energies for $\alpha = 2$ and $\alpha = 5$ for different Re_p numbers.

by projecting the velocity field at a time t (i.e., $\overrightarrow{U}(x, y, t)$) on each of the POD modes ($\overrightarrow{\Psi^i}(x, y)$) (i.e., Eq. 4.12). These $a_i(t)$ values tell us the importance of the ith POD mode at time t. The $a_i(t)$ are determined for the first three POD modes for $\alpha = 2$ scenarios while the first five $a_i(t)$ are calculated for $\alpha = 5$ scenarios.

Figure 5.34 contains the phase portrait plots for first three time-varying coefficients for $\alpha = 2$, while Fig. 5.35 contains the first five $a_i(t)$s for $\alpha = 5$. The $a_i(t)$ are normalized by the square root of respective energies (i.e., λ_i). For each sub-figure, $a_i(t)$ values are sequenced to a single pressure cycle using the hardware synchronization method (see 4.1) where time information of the coefficients is determined by correlating the PIV trigger and the piston position from the experiments. The plots thus contain the scatter plot for each time-varying coefficient, and a curve fit operation is performed to determine a mathematical relationship for each coefficient. The results provided give us a general idea that there is an intricate interplay between the various POD modes at different points in the pressure cycle. The combination of the POD modes and their respective coefficients at a time t will allow for capturing the large-scale flow structures observed in an aneurysm at that time instance. This will become more evident when we look at the low-order flow reconstruction results. This indicates that the large-scale structure we

observed from the phase-average data at a certain time phase comprises of POD modes appropriately weighted by their time-varying coefficients. To elucidate this further, we look at $Re_p = 50$ and $\alpha = 2$ plot (Fig. 5.34). There are few points in the cycle where particular time-varying coefficients might not be present (i.e., $a_i(t) = 0$) while the other coefficients have particular values. This means that certain POD modes and their time varying coefficients are have high impact to the flow and thus that particular flow behavior might be present during that point in the cycle. For example, the a_2 and a_3 have zero values while $a_1/\sqrt{\lambda_1}$ at t/T = 0.1 has a value of ~ -0.375. Looking at the phase averaged results (Fig. 5.6) shows an attached flow inside the aneurysm sac at this point in the cycle. Furthermore, at t/T = 0.3, the presence of a_2 and hence the vortical structure behavior becomes more dominant at this point in the cycle while the other modes have zero values (i.e. $a_1 = a_3 = 0$).

The time-varying coefficient results also show us the impact of inflow conditions which can be observed through the changes in the time-varying coefficient plots. For a fixed α, changing Re_p condition changes the interaction among the $a_i(t)$ coefficients. There is amplitude variation in the coefficients, particularly for $a_2(t)$ and $a_3(t)$ for $Re_p = 270$ than $Re_p = 50$. This suggest that certain POD modes may be highly impactful to the flow at certain phases of the pressure cycle. At $\alpha = 2$, there are only three POD mode interactions to capture 95% percent of the kinetic energy. With the change in α conditions, there are more POD mode variation to capture the dynamics. The results then suggest the flow complexity observed at $\alpha = 5$ conditions from the phase-average results are due to the complex interaction of the POD modes and their coefficients.

5.4.4 POD low-order reconstruction for BF=1.0

The POD results from previous sections are combined together to create a low-order reconstruction for each flow condition. The low-order reconstruction allows us to gain insight on the dynamics of the flow through the interaction of the POD mode shapes

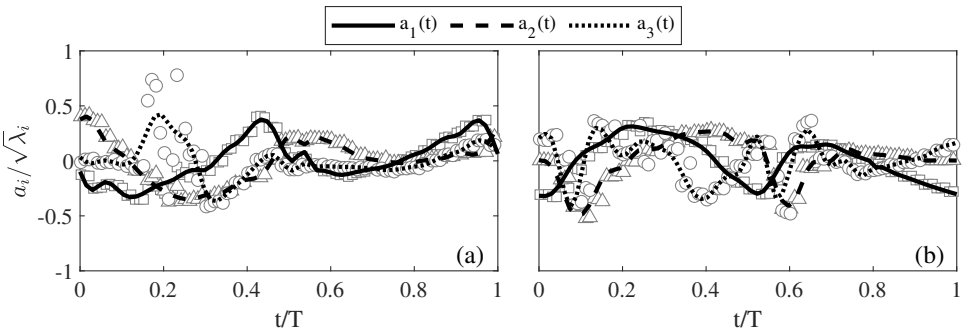

Figure 5.34: Time-varying coefficient for $\alpha = 2$. Square, upward-pointing triangle, and circle markers represent the experimental data for a_1,a_2, and a_3, respectively. The lines represent their curve fit data. (a)$Re_p = 50$. (b)$Re_p = 270$.

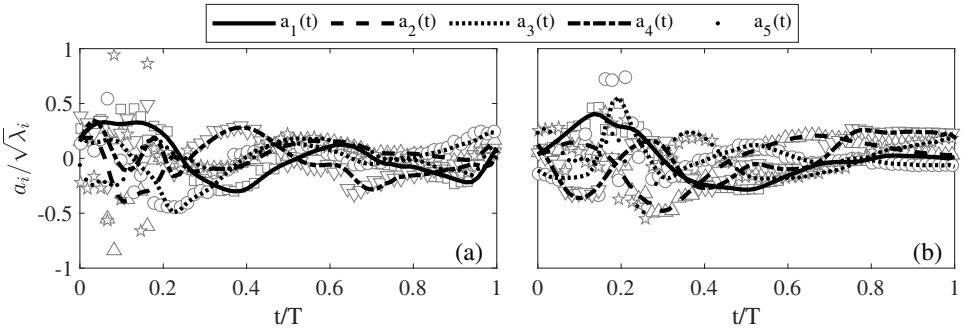

Figure 5.35: Time-varying coefficient for $\alpha = 2$. Square, upward-pointing triangle, circle, downward-pointing triangle, and pentagram markers represent the experimental data for a_1,a_2, a_3, a_4, and a_5, respectively. The lines represent their curve fit data. (a)$Re_p = 50$. (b)$Re_p = 270$.

and appropriately weighted coefficients. The reconstruction results also enable us to use a mathematical model to predict the behavior of the flow field. To create a low-order reconstruction model, Eq. 4.5 is used for selected N POD modes. The number of modes is determined based on the amount of kinetic energy in the flow field to be reconstructed. In this study, 95% of the turbulent kinetic energy is selected which is sufficient to capture enough flow details. This corresponds to the first three POD modes for $\alpha = 2$ scenarios and the first five POD modes for $\alpha = 5$ scenarios (see 5.4.2).

The low-order velocity reconstruction for selected time phases for $\alpha = 2$ are shown in Figs. 5.52-5.53 for $Re_p = 50$ and $Re_p = 270$, respectively. Meanwhile, the velocity field reconstructions for $\alpha = 5$ are shown in Figs. 5.54-5.55 for $Re_p = 50$ and $Re_p = 270$, respectively. A clockwise vortex initiates near the proximal side of the aneurysm (i.e.,

t/T=0.21) as seen in the figure. This vortex convects near the center of the bulge (i.e., t/T=0.37) and then out of the aneurysm opening during the deceleration phase of the flow cycle (i.e., t/T=0.41). The vortex then moves back towards the aneurysm dome and dissipates when the flow from the pipe begins accelerating (i.e., t/T=0.44). A new vortex forms once more and begins behaving similar to the previous vortex for the second half of the cycle. For $Re_p = 270$ and same α (Fig. 5.53), similar trend was also observed. However, the vortical flow structure fills up the entire aneurysm sac (i.e., t/T=0.17) much earlier in the cycle than as compared to $Re_p = 50$ case (i.e., t/T=0.37). An important observation from these figures is that the vortical structure stays in the aneurysm sac for a longer duration (i.e., for t/T=0.17 to 0.50) for $Re_p = 270$ case than the $Re_p = 50$ case (i.e., t/T=0.37 to 0.50). The impact of this temporal behavior is also displayed in the observed flow structure for $Re_p = 50$ and 270 at $\alpha = 2$ (as shown in Figs. 5.1(a) and 5.1(c)). The overall movement of the vortical structure was found to be similar for both studied Re_p cases at $\alpha = 2$ of the variation in the temporal flow structures,.

Low-order reconstruction results for $\alpha = 5$ at different Re_p were also analyzed and foundt that flow structures observed for this α are different than the ones seen at $\alpha = 2$ flow conditions. For $Re_p = 50$ and $\alpha = 5$ flow condition, the vortex initially forms at the proximal side of the cavity (i.e., t/T=0.04), which then moves towards the distal side of the aneurysm, impinging the neck region (i.e., t/T=0.27) and dissipating towards the aneurysm dome (i.e., t/T=0.37). This vortex formation and dissipation process repeats for the remaining half of the cycle (i.e., t/T=0.43 to 0.84). Meanwhile, the $Re_p = 270$ and $\alpha = 5$ flow condition shows presence of vortical structure throughout the cycle that stays near the center of the cavity. This vortex structure moves in a clockwise fashion throughout the flow cycle (i.e., t/T=0.00 to 0.11). These few instances in the flow cycle initiate a secondary vortex structure where the two vortices then merge together to form a new vortex (i.e., t/T=0.14 to 0.17). This process of clockwise vortex movement repeats itself thereafter. The behavior of the vortical structures for the same α condition is found

to impact the overall temporal behavior and presence of secondary structures due to the change in Re_p. Moreover, the difference in temporal behavior with the change in Re_p can be seen in the overall mean structures for $Re_p = 50$ and $Re_p = 270$ at $\alpha = 5$ (as shown in Figs. 5.2(a) and 5.2(c)).

POD was able to capture the flow evolution in the aneurysm sac at different inflow conditions with the low-order flow reconstruction. Results from POD provided information on the uniqueness of each inflow condition, the important mode shapes that were contained in each scenario, and the interaction of POD modes and time-varying coefficients that impact the flow features. The low-order reconstruction with POD results were able to capture the vortex formation, evolution, and convection, which were correlated with the change in α and Re_p.

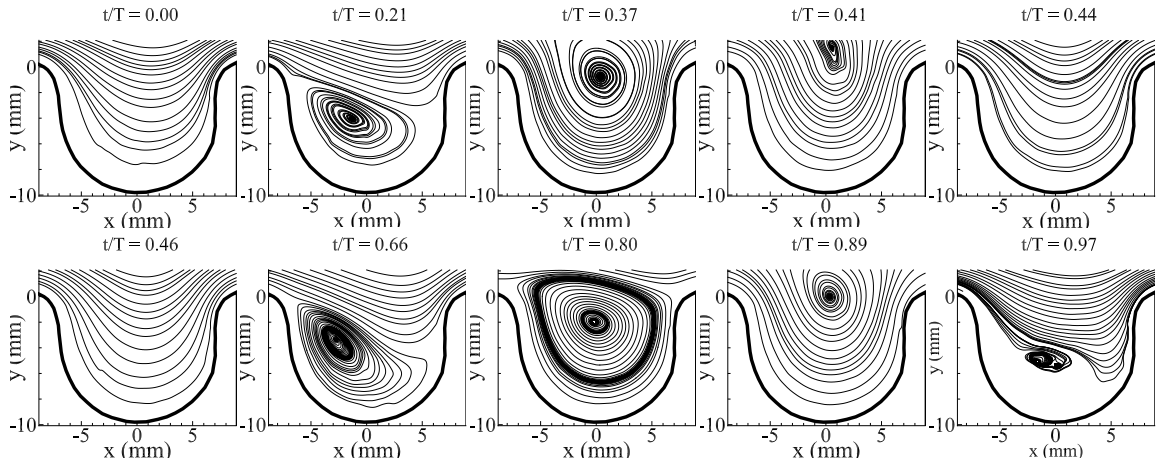

Figure 5.36: POD low-order reconstruction for $Re_p = 50$ and $\alpha = 2$ for selected time phases. The velocity reconstruction uses three POD modes. Average normalized RMS error observed in low-order reconstruction is ϵ_{avg}=2.107%, with minimum normalized RMS error of ϵ_{min}=0.7964% and maximum normalized RMS error of ϵ_{max}=5.043%. The RMS is normalized by the centerline velocity.

5.5 DMD results

The previous sections show the complexities involved in aneurysm flows. We first show the results in the phase-averaged data and illustrate the changes in the flow dynamics in

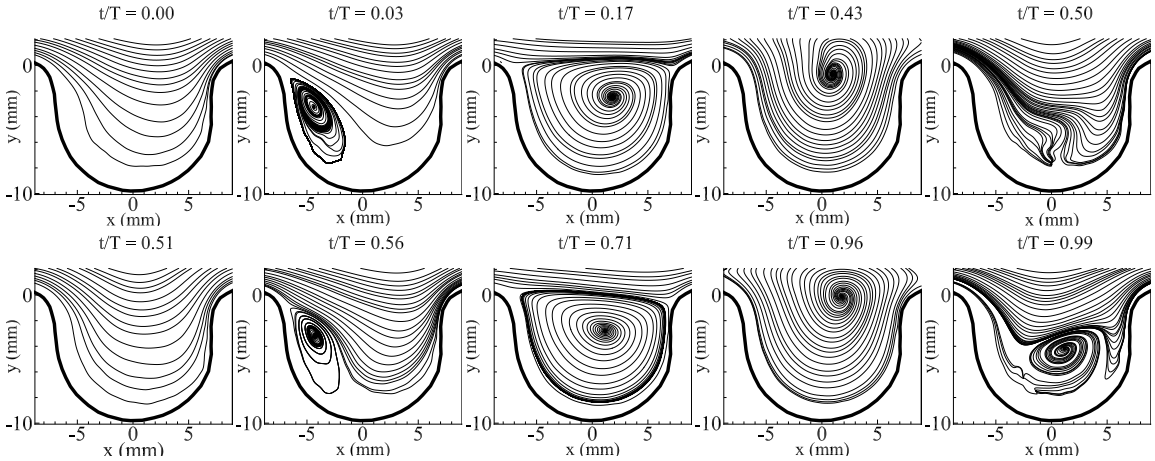

Figure 5.37: POD low-order reconstruction for $Re_p = 270$ and $\alpha = 2$ for selected time phases. The velocity reconstruction uses three POD modes. Average normalized RMS error observed in low-order reconstruction is ϵ_{avg}=0.7344%, with minimum normalized RMS error of ϵ_{min}=0.187% and maximum normalized RMS error of ϵ_{max}=1.469%. The RMS is normalized by the centerline velocity.

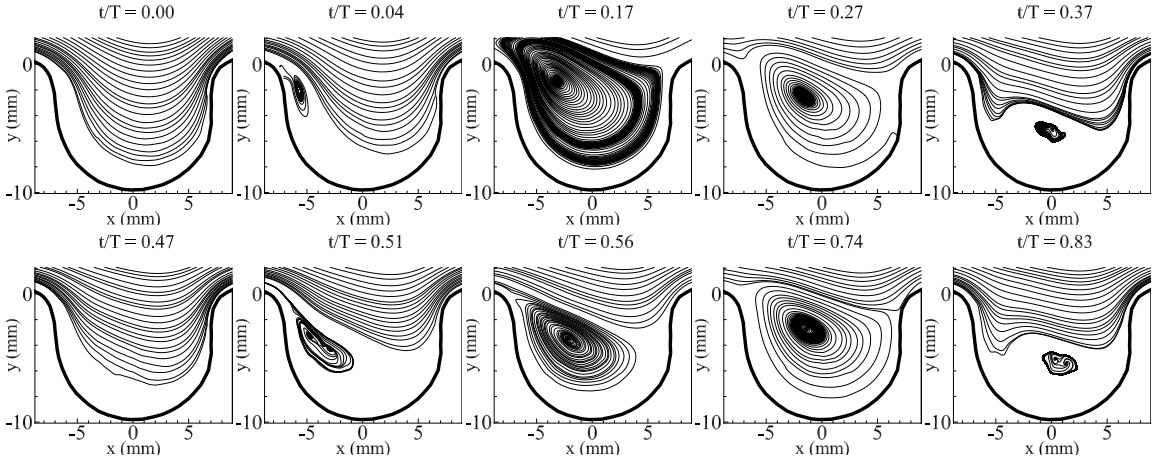

Figure 5.38: POD low-order reconstruction for $Re_p = 50$ and $\alpha = 5$ for selected time phases. The velocity reconstruction uses five POD modes. Average normalized RMS error observed in low-order reconstruction is ϵ_{avg}=0.775%, with minimum normalized RMS error of ϵ_{min}=0.487% and maximum normalized RMS error of ϵ_{max}=1.389%. The RMS is normalized by the centerline velocity.

the aneurysm at different inflow conditions. Next, the complex flow behavior at different scenarios have been studied using POD which led to understanding that the flow field observed from PIV phase-averaged data can be described as a combination of different spatial mode shapes. Furthermore, the dynamics we see in the flow are the interactions

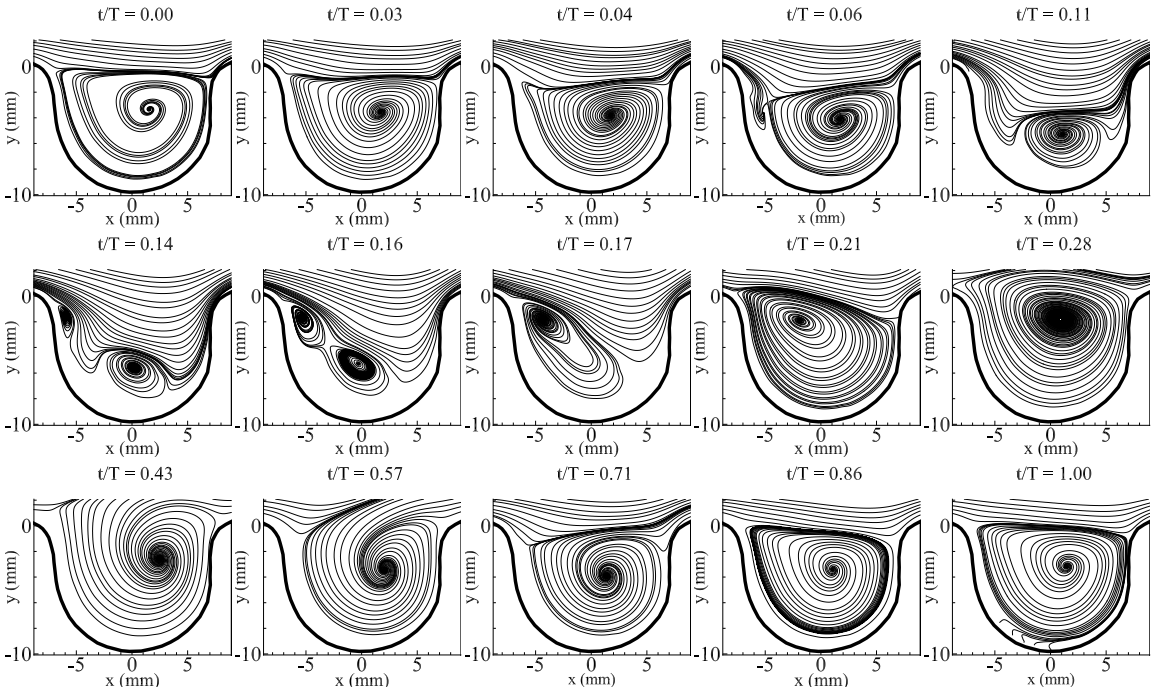

Figure 5.39: POD low-order reconstruction for $Re_p = 270$ and $\alpha = 5$ for selected time phases. The velocity reconstruction uses five POD modes. Average normalized RMS error observed in low-order reconstruction is ϵ_{avg}=1.126%, with minimum normalized RMS error of ϵ_{min}=0.791% and maximum normalized RMS error of ϵ_{max}=1.787%. The RMS is normalized by the centerline velocity.

of these spatial mode shapes ranked by their kinetic energy. However, the dynamical behavior of these structures and their temporal information are not captured by POD. This is important as it can tell us how the physically important modes are behaving in time through growth or decay information. This motivated us to use a different approach to extract the spatiotemporal behavior of the large-scale structures.

We present the results of application of Dynamic Mode Decomposition method on the velocity flow field to study the spatiotemporal behavior of the large-scale structures at different inflow conditions. The results from DMD are divided into two parts. The first part presents the DMD results to justify the use of traditional flow field measurements such as PIV with a low-frame rate setting for use in advance data analysis such as DMD. DMD is a method to extract pertinent flow processes and thus require sampling of data to be taken at a sufficiently high frequency. This minimum sampling criteria is given

by the Nyquist criterion [33]. We show in this part of the dissertation that similar information can be captured when an inflow scenario is acquired at different sampling rates. For this part of the DMD analysis, we analyze an inflow scenario of $Re_p = 50$, $\alpha = 2$ and $BF = 1.0$ sampled at camera frame rate of $5Hz$. The impact of sampling will be discussed, along with DMD sensitivity analysis such as impact of different rank selection, frequency selection, number of cycles, and impact of DMD amplitude.

The second part of this section presents the DMD results on the PIV data acquired at a low-frame rate setting (see Table 3.3). DMD is thus applied to the velocity data where phase-averaging and POD have been applied and analyzed. The DMD frequency, growth or decay rates, and contribution results are first presented in this section. This is followed by the DMD modes and low-order reconstruction results for each inflow condition.

5.5.1 DMD on low-frame rate applications

This subsection provides the results of using DMD for several scenarios and justify its use for traditional flow field measurements such as PIV acquired with a low-frame rate setting. For this study, 2000 PIV measurements for an inflow scenario of $Re_p = 50$ and $\alpha = 2$ was acquired using a camera sampling rate of $f_s = 5Hz$. The $\alpha = 2$ corresponds to a pump frequency of $0.4Hz$. DMD is then performed on this data set at several scenarios to identify impact of data structure to the DMD frequencies, growth rate behavior, amplitudes, and modes.

Impact of sampling

The impact of sampling rates is discussed here. The idea of this study is to investigate influence of different sampling rates to the DMD results and understand the information that can be extracted from these conditions. For this study, DMD was performed on a single pressure cycle for the $f_s = 5Hz$ data set (i.e., original data set). This single pressure cycle was captured using 12 PIV images with $\Delta t = 0.2s$ between the images. DMD was

then performed on other scenarios where the same data set was now sub-sampled at $f_s = 2.5Hz$ and $f_s = 1.0Hz$. A single pressure cycle was captured using 7 PIV images with $\Delta t = 0.4s$ for $f_s = 2.5Hz$, while 10 PIV images and $\Delta t = 1.0s$ for $f_s = 1.0Hz$ Lastly, the hardware synchronization approach was also implemented to the $f_s = 1Hz$ scenario (i.e., see 4.1) prior to using DMD. Using the hardware synchronization method to capture a single pressure cycle yields 39 phase-averaged images with $\Delta t = 0.064s$.

Figure. 5.40(a) shows the DMD frequency results (f_i) while Fig. 5.40(b) shows the DMD amplitude results for the different sampling scenarios investigated. Here, the results show the number frequencies that can be captured by DMD at different sampling rates. It is observed that the frequencies detected decreases with the decrease in sampling rate. This is because it is dependent on the number snapshots used where the number frequencies that can be determined is found by

$$N = m - 1, \tag{5.1}$$

where m is the number snapshots used. For example, it can be seen that with $f_s = 5Hz$ sampling (i.e., 12 PIV images), 11 frequencies were determined while for $f_s = 1Hz$ sampling (i.e., 7 PIV images), 6 frequencies were calculated. It can also be seen from Fig. 5.40(a) the maximum frequency that can be detected is half of the sampling frequency f_s for each scenario. This in turn divides that into frequencies where the frequency spacing Δf is determined using

$$\Delta f = 1/(N\Delta t). \tag{5.2}$$

Thus, the smallest frequency that can be detected depends on the time between the snapshots Δt and the number of images N. Based on the results, the frequencies captured using DMD were more or less similar for $f_s = 5Hz$ (i.e., first row in Fig. 5.40(a)),$f_s = 2.5Hz$ (i.e., second row in Fig. 5.40(a)), and phase-averaged of $f_s = 1Hz$ (i.e., fourth row

in Fig. 5.40(a)). For $f_s = 1Hz$ (i.e., third row in Fig. 5.40(a)), up to $0.5Hz$ frequency can be detected with $\Delta f = 0.1Hz$. With the hardware synchronization and phase-averaging approach implemented on the data set (i.e., fourth row in Fig. 5.40(a)), N becomes the number of binned phases in the pressure cycle which are separated by Δt. The hardware synchronization approach allowed different phases of the pressure cycle to be captured, which effectively made the sampling to $f_s = 15Hz$. This in turn allowed the frequencies to be captured similar to original data (i.e., first row in Fig. 5.40(a)). Furthermore, frequencies up to $7.5Hz$ were captured using the phase-averaged approach, and these are not shown in the figure as the frequencies are not physically relevant to the flow.

Along with the frequency results, the growth/decay rate (g_i) information were also captured with DMD. The results show near stable growth/decay rate for each of the determined frequencies for $f_s = 5Hz$ (i.e., first row in Fig. 5.40(a)), $f_s = 2.5Hz$ (i.e., second row in Fig. 5.40(a)), and phase-averaged of $f_s = 1Hz$ (i.e., fourth row in Fig. 5.40(a)). This indicate that the frequencies and thus the modes (i.e., spatial structures) were neither growing nor decaying in the flow. Note that the trend of the growth rates for $f_s = 5Hz$ and phase-averaged of $f_s = 1Hz$ were more or less similar.

The DMD amplitude results are now shown in Fig. 5.40(b) that are calculated using the optimal vector approach (see 4.5). Here, the amplitudes are normalized to the mean frequency (i.e., $0Hz$) for each sampling scenario. Different contributions for each frequency can be seen.

We will now look at the impact of sampling to the DMD mode shape. Figure 5.41(a)-(d) shows the DMD mode results for $0.8Hz$ at different sampling scenarios. The first row in this figure corresponds to the real component of the DMD mode, the second row corresponds to the imaginary part of the DMD mode, the third row for magnitude, and the fourth row for the DMD mode phase. Here we highlight that the $0.8Hz$ mode shapes are in good agreement for $f_s = 5Hz$ (Fig. 5.41(a)) and $f_s = 2.5Hz$ (Fig. 5.41(b)) as the sampling rates are high enough to detect this mode shape. For $f_s = 1.0Hz$,

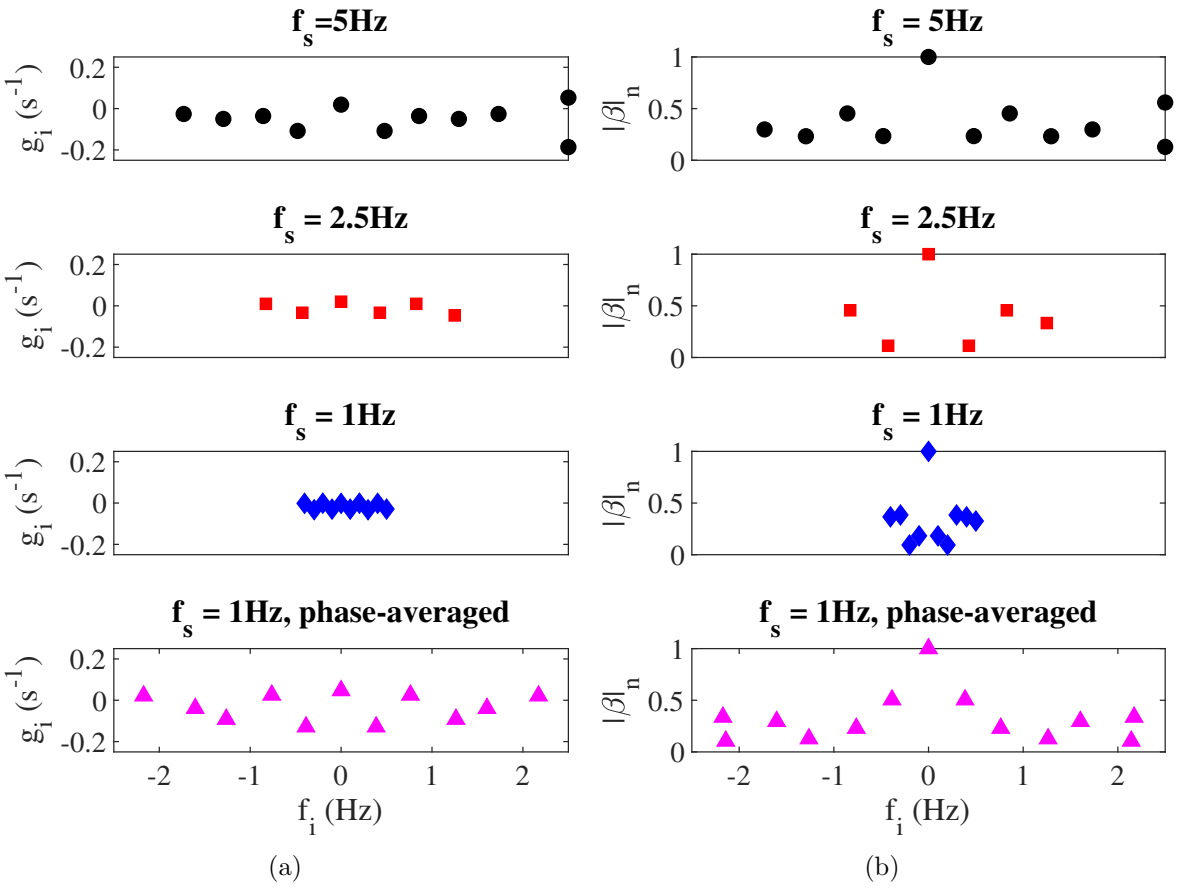

Figure 5.40: DMD results for $Re_p = 50$, $\alpha = 2$ using sampling frequency. (a) DMD growth rate vs. frequency, and (b) amplitude vs. frequency.

however, the $0.8Hz$ mode shape is not captured as the maximum frequency that can be captured is half of the sampling rate $0.5f_s = 0.5Hz$ (see Fig. 5.40). With hardware synchronization method implemented on the $f_s = 1.0Hz$ sampling, DMD can capture the $0.8Hz$ frequency as well as capture the mode shape (Fig. 5.41(d)) in qualitatively good agreement. Differences can be observed as the mode shape for $f_s = 5Hz$ was for a single pressure cycle, while the phase-averaged $f_s = 1.0Hz$ was wrapped back into a single pressure cycle. The results obtained in this study enabled us to justify the use implementing DMD on flow fields acquired with low-frame rate settings. This further enabled us to use DMD to study the flow dynamics in aneurysms for the given flow conditions.

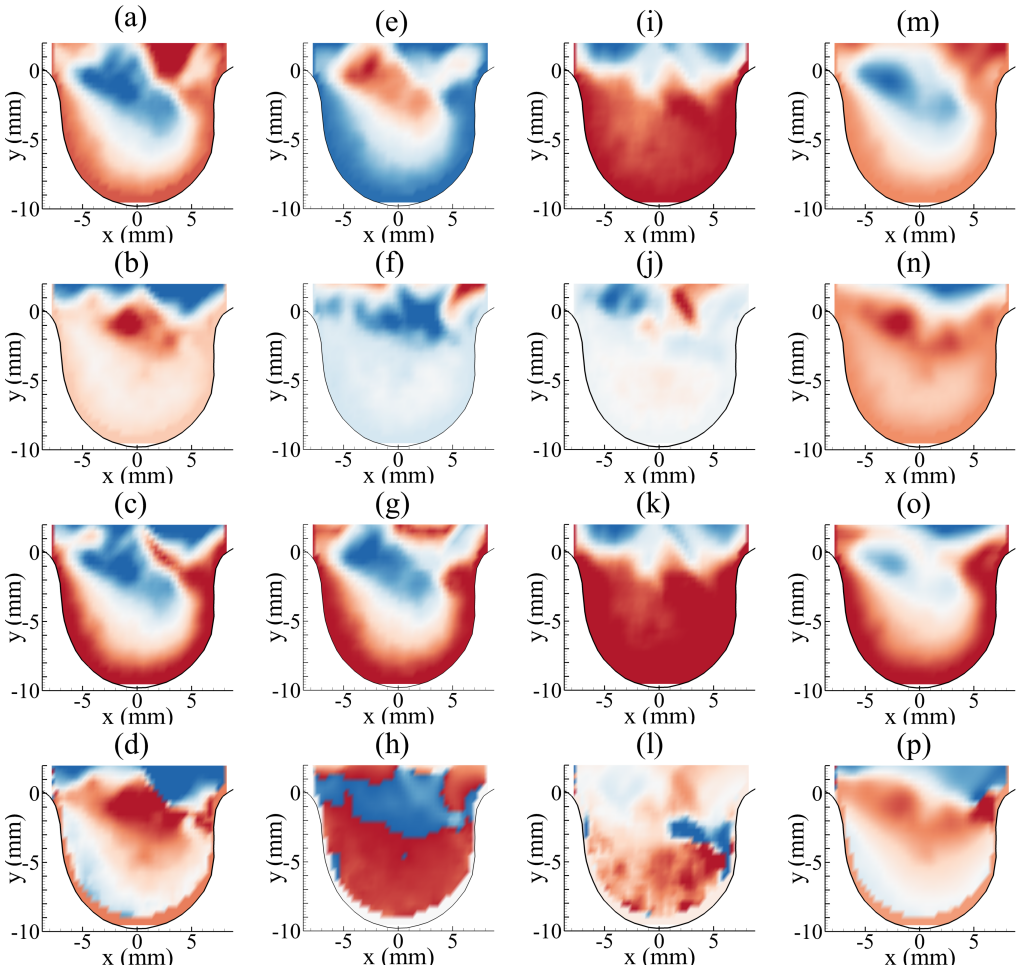

Figure 5.41: DMD modes for $f_s = 5Hz$ using the streamwise component of velocity for different sampling rates. (a)-(d) $0.8Hz$ ($f_s = 5Hz$), (e)-(h) $0.8Hz$ ($f_s = 2.5Hz$), (i)-(l) $0.4Hz$ ($f_s = 1Hz$), and (m)-(p) $0.8Hz$ ($f_s = 1Hz^*$). (a),(e),(i),(m) real components. (b),(f),(j),(n) imaginary components. (c),(g),(k),(o) magnitude. (d),(h),(l),(p) phase.

5.5.2 DMD results for BF=1.0

DMD frequencies, growth rates, and DMD amplitudes

DMD frequency results are presented here to provide the frequency information of the spatial modes in the flow field. The DMD frequencies (λ_i) are the imaginary component of the eigenvalues (Λ) which describe the frequencies of oscillation of the DMD modes (Φ). These frequencies are determined from the eigendecomposition of $\tilde{\mathbf{A}}$. On the other hand, the real components of the eigenvalues (λ_r) represent the exponential growth or

decay rate of the DMD modes. A positive real eigenvalue indicates a growing DMD mode while a negative real eigenvalue indicates a decaying DMD mode. In terms of the actual contribution to the flow field of the DMD modes, it can be quantified by their DMD amplitudes (β). The amplitudes allow us to determine the DMD modes important to the flow field. The total number of frequencies depends on the rank r selected to perform the DMD analysis. Furthermore, the resolved frequencies can be determined from r as $df = 1/(r\Delta t)$. For $\alpha = 2$ conditions, 37 DMD frequencies are resolved (positive and negative) with $df = 0.4Hz$ while 18 DMD frequencies are resolved with $df = 2.4Hz$ for $\alpha = 5$ scenarios.

The DMD frequency spectrum results for $\alpha = 2$ flow scenarios are shown in Fig. C1(a). Here, we only show the positive side of the spectrum as the frequencies extracted are symmetric about the imaginary axis as a consequence of processing real-valued data. The results show that for $\alpha = 2$ flow scenarios (i.e., Fig. C1), the mean flow, an oscillating mode of 0.4 Hz and its harmonics are captured along with their growth/decay rate information. The harmonics are captured as the flow scenarios are cyclical in nature. The growth/decay rate of each frequency is near zero (i.e., $\lambda_r \approx 0$) which suggest stability and presence of these spatial structures throughout the pressure cycle. The corresponding normalized DMD amplitude results obtained for $\alpha = 2$ shown in Fig. C1(b) indicate each frequency's impact to the flow. Here, it should be noted that the $0Hz$ (i.e., mean flow) is removed from the figure to highlight the contribution of the oscillating components. The DMD amplitude results show that the majority of the contribution comes from the first two frequencies (i.e., $0.4Hz$ and $0.8Hz$) and decreasing contributions from higher harmonics (i.e., $\lambda_i > 0.8$ Hz) for both Re_p scenarios. The contributions can be justified as the $0.4Hz$ corresponds to the pump frequency while the $0.8Hz$ corresponds to the impact of the spring-loaded valve system used to create uni-directional flow from sinusoidal driving pressure signal.

DMD frequency spectrum for $\alpha = 5$ flow conditions are analyzed and shown in

Fig. C2(a) and the corresponding normalized DMD amplitudes are shown in Fig. C2(b). The positive frequency spectrum shows the resolved frequencies from $0Hz$ to $7.2Hz$. Higher frequencies (i.e., $> 7.2Hz$) are not shown in the figures as they do not physically represent the flow from the phase-averaged results. For this α condition, the mean flow, the pump driving frequency of $2.4Hz$ and its harmonics are also captured. In terms of their contributions, highest contributions also come from the flow frequency and its first three harmonics. For $Re_p = 50$, the $4.8Hz$ dominates the flow, which corresponds to spatial mode oscillation occurring twice in a cycle (see Fig. 5.8). This is in contrast with $Re_p = 270$ where the dominant mode is the $2.4Hz$ which in line with the pump driving frequency.

The results provided in this section demonstrated the advantage of using DMD to gain insight to the complex flow structures. DMD allows us to extract important spatial features with each feature defined by a single frequency of oscillation and growth/decay rate. The information that DMD provides tells us that certain spatial modes are present in the flow field that oscillate at a particular frequency. These frequencies, along with their contribution, allow us to determine which are the dominant feature that highly impact the overall flow dynamics. Furthermore, DMD also enable us to create mathematical models to predict flow patterns that are governed by these modes which which may not be initially captured with the original velocity field data.

DMD modes

The DMD modes are presented here provide a modal description of the flow structure from the PIV phase-averaged data. In the case of the present investigation, DMD can be used for analyzing spatio-temporal behavior of energetic flow structures in aneurysm. These DMD modes (Φ) are determined using Eq. 4.23 which would yield real and imaginary modes for both streamwise and transverse components of velocity. For brevity, DMD modes are presented here from the frequencies discussed from the previous section.

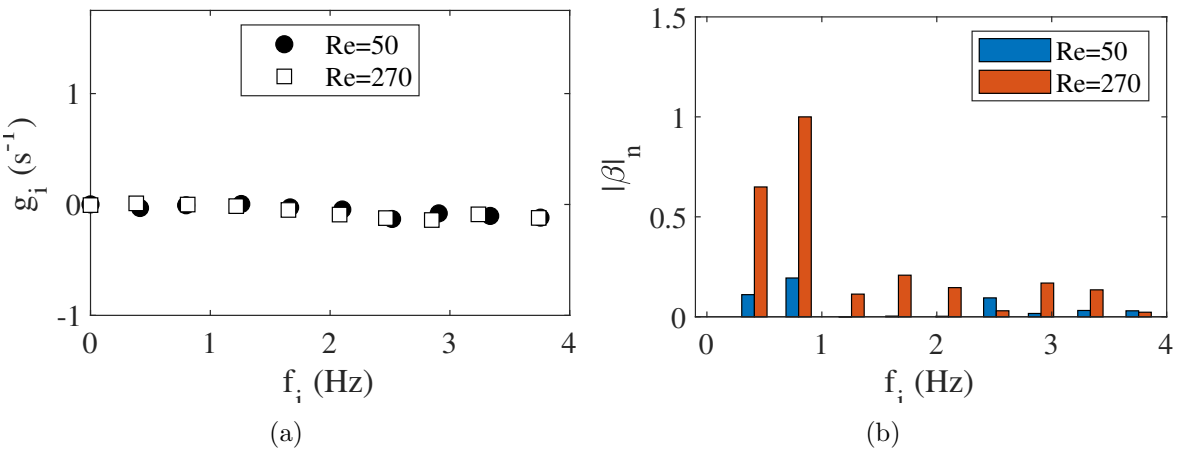

Figure 5.42: DMD frequency, growth rates and amplitudes for $\alpha = 2$ at different Re_p. (a) DMD growth rate vs. frequency, and (b) DMD amplitude vs. frequency.

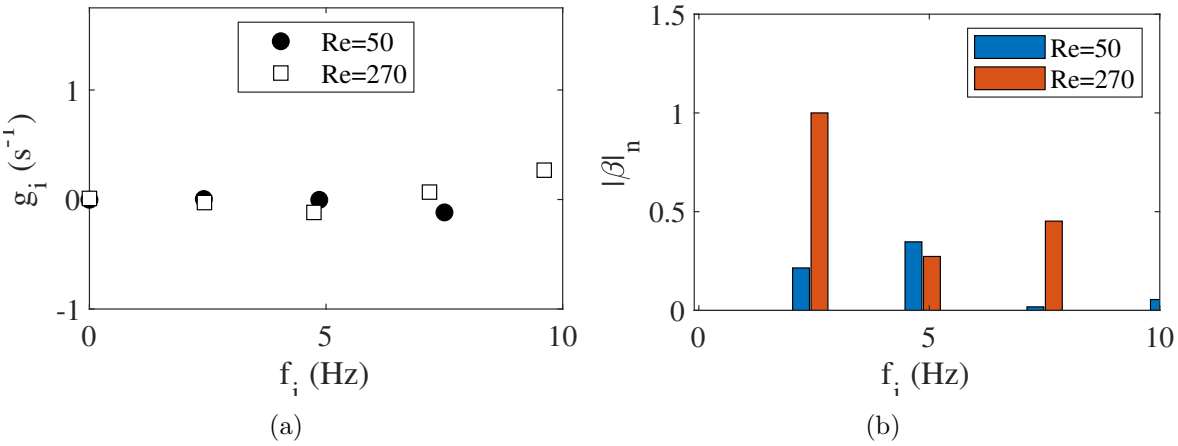

Figure 5.43: DMD frequency, growth rates and amplitudes for $\alpha = 5$ at different Re_p.(a) DMD growth rate vs. frequency, and (b) DMD amplitude vs. frequency.

Streamwise and transverse DMD modes from $0.4Hz - 1.6Hz$ for $\alpha = 2$ and $Re_p = 50$ are shown in Figs. 5.44(a)-(d) and 5.45(a)-(d), respectively. The DMD modes acquired yield real and imaginary modes where the combination of the modes provide a mathematical description of the spatial flow structures and behavior in the aneurysm. In this flow scenario, each mode has a temporal behavior associated with a single frequency, and the flow pattern can be described by combining the real and imaginary u and v components of the modes. The magnitude of the complex DMD mode shows the most active regions of each mode, while the phase shifts show the convective motion of the flow structures

captured by the modes. The results show that the DMD modes are more or less similar in nature as the modes comprises of the fundamental flow frequency and its harmonics. Combining these aspects for a single DMD mode shows the vortical structure movement from the proximal side to the aneurysm opening at a given frequency. Here we now see the capability of using DMD to capture the convective motion and provide a description of its temporal behavior in a single DMD mode. This is in contrast with POD where three or more POD modes are used to capture this motion, but unable to capture the temporal description of the flow field (i.e, associated frequencies with the observed flow structures).

Similar analysis is also performed for $\alpha = 2$ and $Re_p = 270$ flow scenario where the streamwise modes are shown in Fig. 5.46(a)-(d) and the transverse modes are shown in Fig. 5.47(a)-(d). We now highlight the influence of Re_p to the flow structures. Although the DMD modes for both and real and imaginary modes show a vortical structure moving towards the aneurysm opening similar to $Re_p = 50$, the high and low values of the real and imaginary DMD modes are shifted towards the distal side of the aneurysm. This suggests the vortical structure leans more towards the distal side influencing the impinging locations and wall shear stress behavior. Thus, DMD is able to capture the changes in the flow structure and behavior with the change in mode shapes.

We now analyze the DMD modes for $\alpha = 5$ flow conditions. Figures 5.48(a)-(d) show the streamwise DMD modes for Re_p while Figs. 5.49(a)-(d) show the transverse DMD modes at different frequencies. Here the DMD modes show relatively similar shapes as they are from the fundamental frequency (i.e., $2.4Hz$) and its harmonics. For a single DMD mode, a flow structure can be seen to move from the proximal neck to the upstream aneurysm opening oscillating at a particular frequency. A similar description of this motion is captured by POD (see 5.4.1), yet five POD modes are necessary to capture this motion and lacked the temporal information of this behavior. With $Re_p = 270$ (i.e., Figs. 5.50 and 5.51), the DMD modes show shifted mode shapes in comparison with

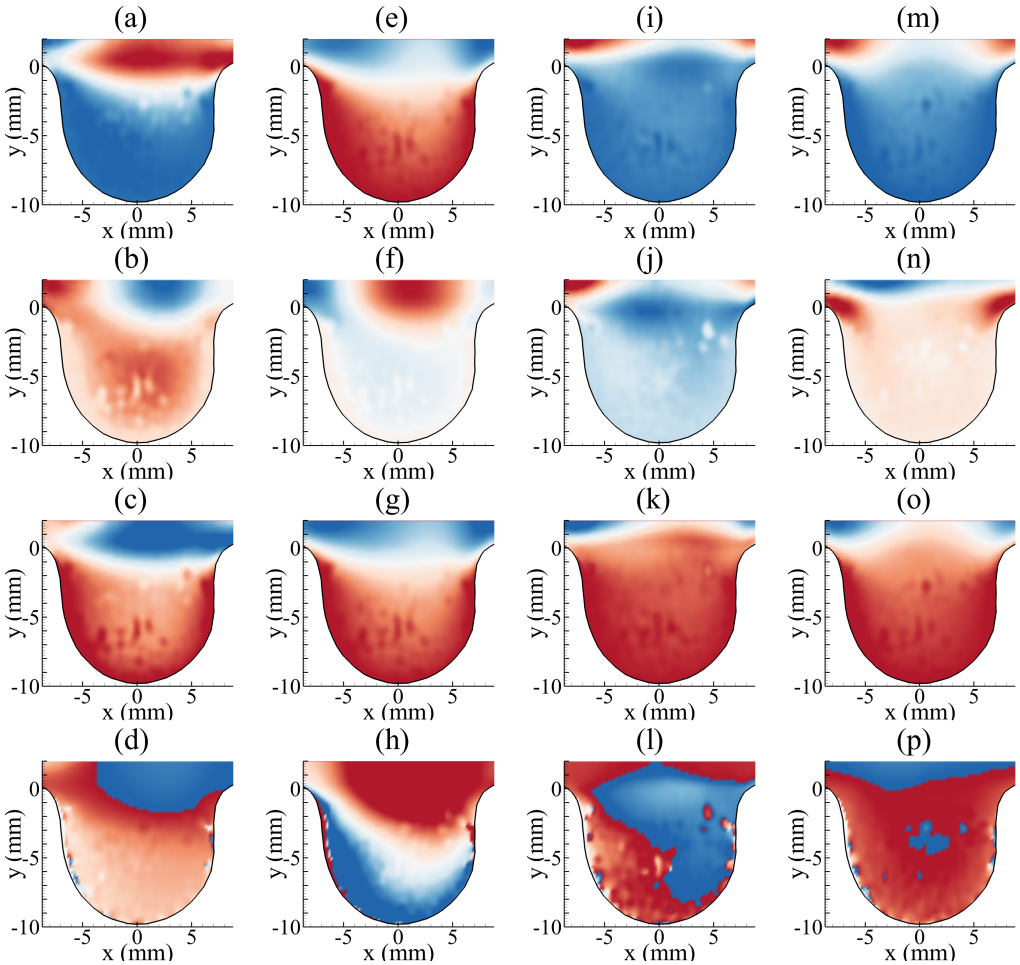

Figure 5.44: DMD modes for $Re_p = 50$, $\alpha = 2$ using the streamwise component of velocity. (a)-(d) $0.4Hz$ (Mode 2), (e)-(h) $0.8Hz$ (Mode 4), (i)-(l) $1.2Hz$ (Mode 6), (m)-(p) $1.6Hz$ (Mode 8). (a),(e),(i),(m) real components. (b),(f),(j),(n) imaginary components. (c),(g),(k),(o) magnitude. (d),(h),(l),(p) phase.

$Re_p = 50$, and the dynamics of the observed vortical structures have changed. The spatial structures are seen near the distal neck region for the fundamental frequency. Similar flow structure movement can be seen for the higher harmonics where the bulk motion of the flow structures impinges the distal neck area. DMD thus highlight the differences in the modes at different inflow conditions through the changes in mode shapes which then influences the flow structure motion.

DMD modes show the capability of the method to gain insight to the mechanisms involved in fluid behavior inside the aneurysm. The results indicate that the change in

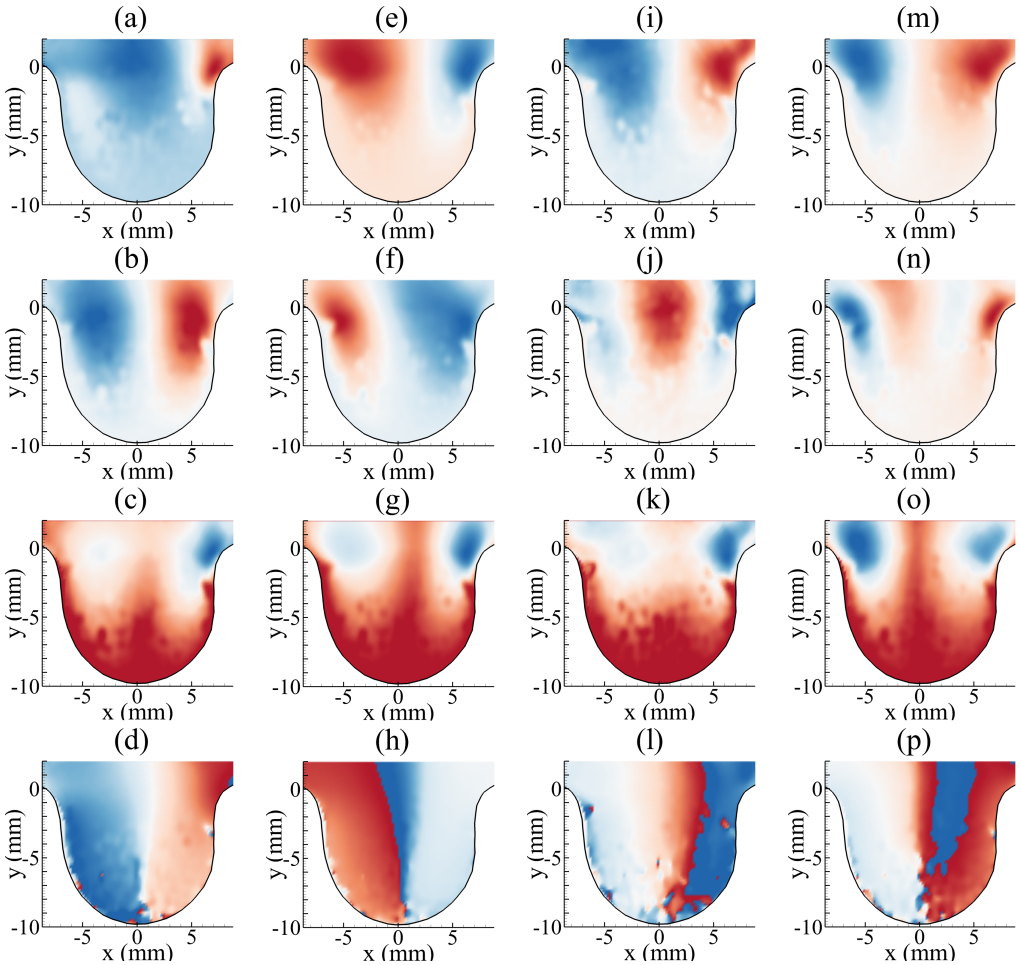

Figure 5.45: DMD modes for $Re_p = 50$, $\alpha = 2$ using the transverse component of velocity. (a)-(d) $0.4Hz$ (Mode 2), (e)-(h) $0.8Hz$ (Mode 4), (i)-(l) $1.2Hz$ (Mode 6), (m)-(p) $1.6Hz$ (Mode 8). (a),(e),(i),(m) real components. (b),(f),(j),(n) imaginary components. (c),(g),(k),(o) magnitude. (d),(h),(l),(p) phase.

inflow conditions, either in Re_p or α, provide different behavioral modes of oscillation. Although similar frequency information are obtained when α is kept the same, different flow oscillations or modes are contained for every Re_p. This suggest the uniqueness of flow behavior for every inflow scenario and the modes responsible for this behavior. Furthermore, the real and complex DMD modes provide information on the movement of the spatial structures at a particular frequency. This information is important as it enables us to determine the flow feature, frequency in a single DMD mode. The DMD mode shapes can be quantified through their contribution by examining the DMD

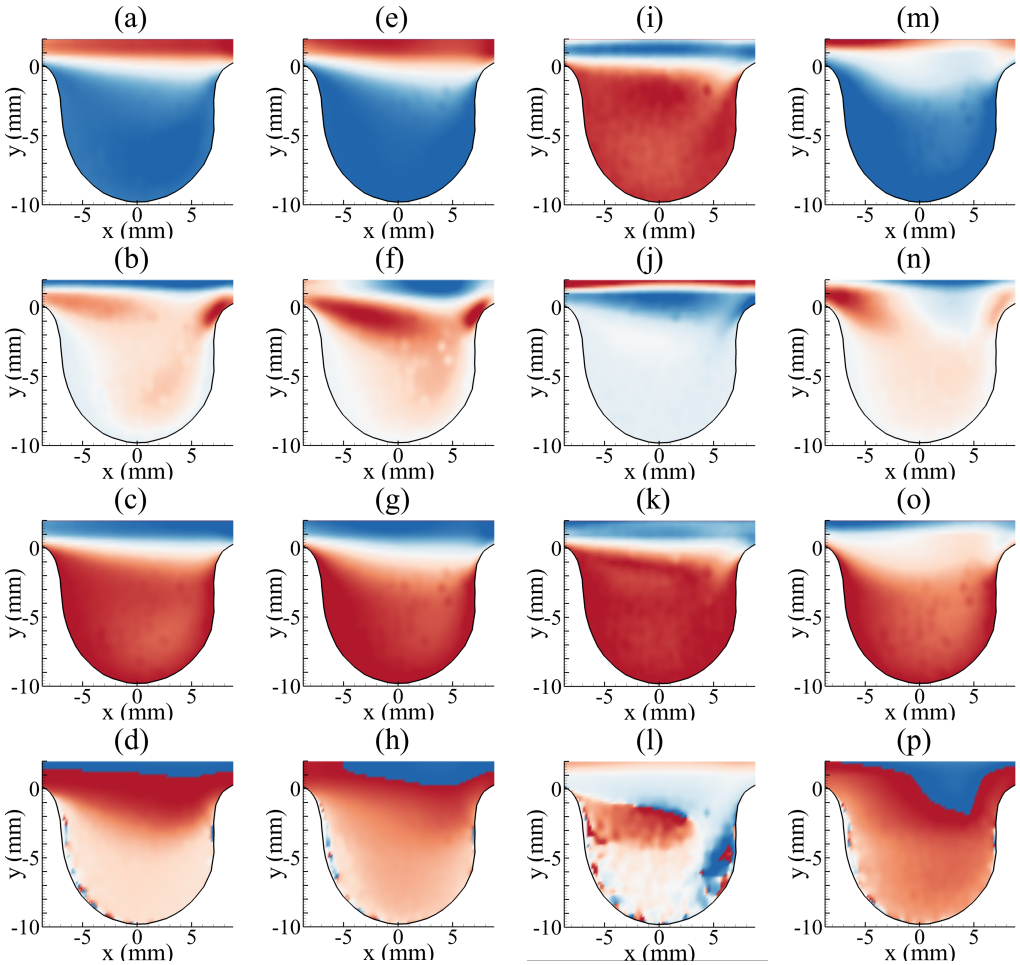

Figure 5.46: DMD modes for $Re_p = 270$, $\alpha = 2$ using the streamwise component of velocity. (a)-(e) $0.4Hz$ (Mode 2), (e)-(h) $0.8Hz$ (Mode 4), (i)-(l) $1.2Hz$ (Mode 6), (m)-(p) $1.6Hz$ (Mode 8). (a),(e),(i),(m) real components. (b),(f),(j),(n) imaginary components. (c),(g),(k),(o) magnitude. (d),(h),(l),(p) phase.

amplitudes (β) and temporal description (Λ) which can be combined together to allow a flow realization of the flow field at a time instance. This realization can be shown by looking at the low-order flow field reconstruction presented in the next section.

DMD low-order reconstruction

A low-order flow field reconstruction using DMD are performed for each inflow scenario to model the large-scale structure behavior at different phases for a single pressure cycle. For this study, the flow realizations are acquired using Eq. 4.24 and selecting key dominant

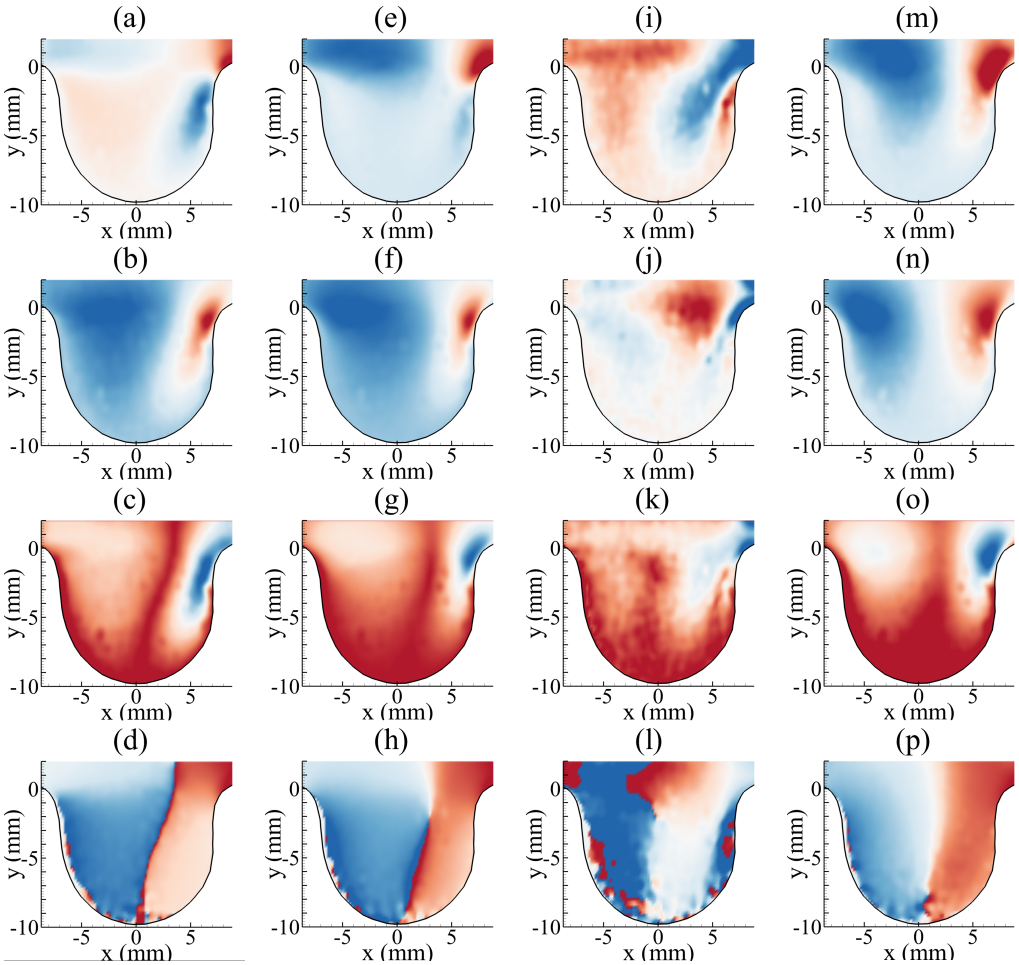

Figure 5.47: DMD modes for $Re_p = 270$, $\alpha = 2$ using the transverse component of velocity. (a)-(e) $0.4Hz$ (Mode 2), (e)-(h) $0.8Hz$ (Mode 4), (i)-(l) $1.2Hz$ (Mode 6), (m)-(p) $1.6Hz$ (Mode 8). (a),(e),(i),(m) real components. (b),(f),(j),(n) imaginary components. (c),(g),(k),(o) magnitude. (d),(h),(l),(p) phase.

DMD modes, and associated frequencies and growth rates. The flow field evolution presented here for selected time phases with $\alpha = 2$ are shown in Figs. 5.52 and 5.53 for $Re_p = 50$ and $Re_p = 270$, respectively. Meanwhile, the flow field reconstruction results with $\alpha = 5$ are shown in Figs. 5.54 and 5.55 for $Re_p = 50$ and $Re_p = 270$, respectively. The velocity field reconstruction for $Re_p = 50$ (i.e., Fig. 5.52) show the flow behavior in the aneurysm at $\alpha = 2$. Here, flow in the pipe is initially seen to enter the aneurysm region with the fluid following the curvature (i.e., t/T=0.00). The fluid exits at the distal side and recovers downstream of the aneurysm. As the flow in the pipe

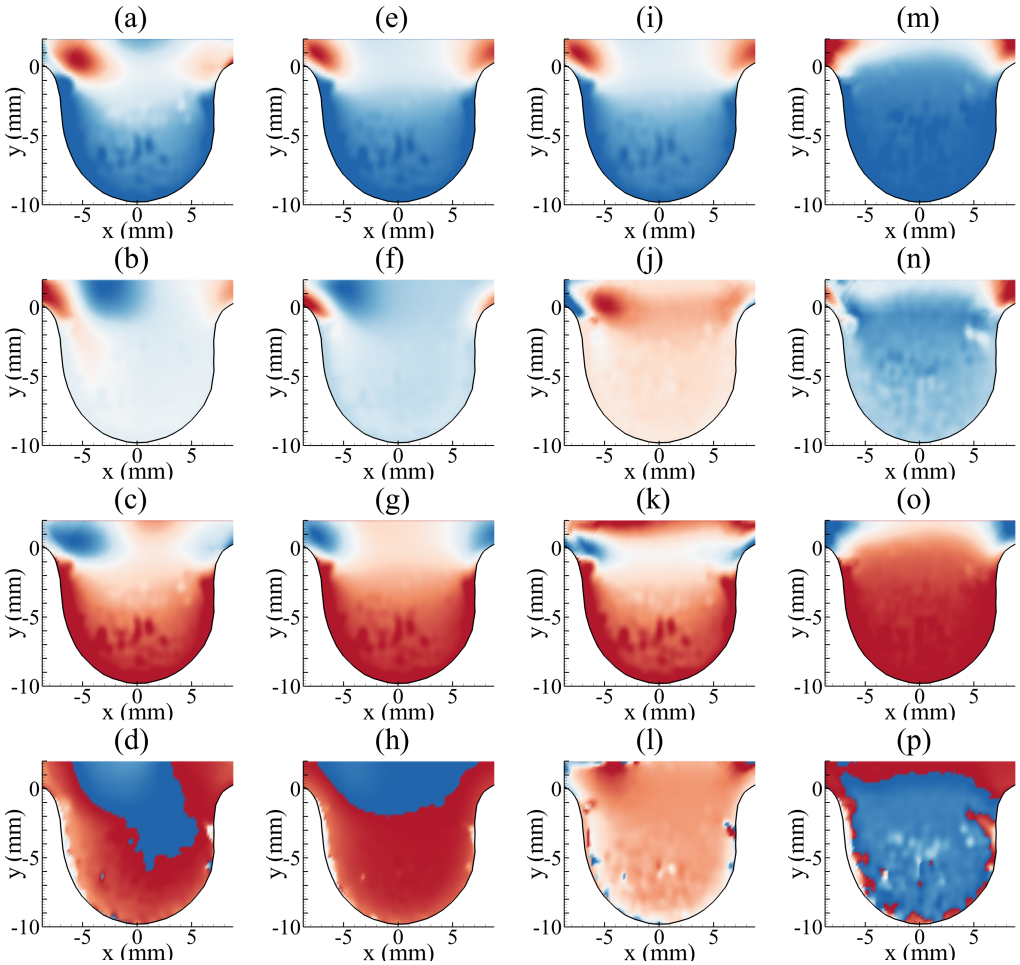

Figure 5.48: DMD modes for $Re_p = 50$, $\alpha = 5$ using the streamwise component of velocity. (a)-(d) $2.4Hz$ (Mode 2), (e)-(h) $4.8Hz$ (Mode 4), (i)-(l) $7.2Hz$ (Mode 6), and (m)-(p) $9.6Hz$ (Mode 8). (a),(e),(i),(m) real components. (b),(f),(j),(n) imaginary components. (c),(g),(k),(o) magnitude. (d),(h),(l),(p) phase.

continuous to slow down, a clockwise vortex appears near the proximal side of the cavity (i.e., t/T=0.04). This vortex gathers in strength as the pipe fluid continuously slows down (i.e., t/T=0.19) while moving towards the aneurysm opening. At the lowest fluid velocity in the pipe region, the aneurysm vortex can be seen to have moved towards the pipe region (i.e., t/T=0.32). As the flow restarts accelerating again, the vortex is observed to move back inside the cavity while rapidly decreases in strength and dissipating (i.e., t/T=0.38). The process repeats itself in the second half of the cycle (i.e., t/T=0.5-1.0), where a newly formed vortex behaves similarly as the previous first vortex structure. Note that the flow

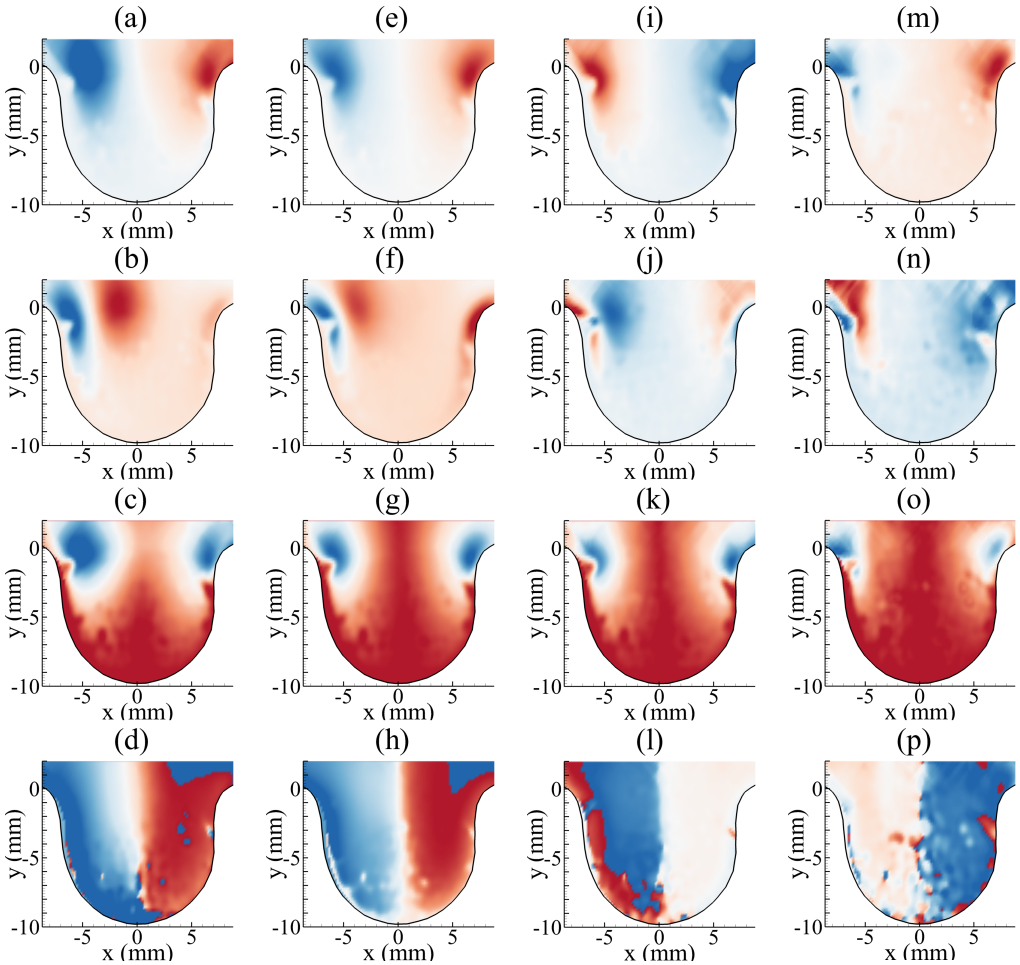

Figure 5.49: DMD modes for $Re_p = 50$, $\alpha = 5$ using the transverse component of velocity. (a)-(d) $2.4Hz$ (Mode 2), (e)-(h) $4.8Hz$ (Mode 4), (i)-(l) $7.2Hz$ (Mode 6), and (m)-(p) $9.6Hz$ (Mode 8). (a),(e),(i),(m) real components. (b),(f),(j),(n) imaginary components. (c),(g),(k),(o) magnitude. (d),(h),(l),(p) phase.

behavior is evident from the DMD modes for this scenario where the real and imaginary components of the modes provide the convective motion of the vortical structure. In addition, the repetition of the flow trend for a single pressure cycle is captured by the dominant DMD amplitude at 0.8 Hz. For $Re_p = 270$ and same $\alpha = 2$ scenario (Fig. 5.53), the flow behavior in the aneurysm region are qualitatively similar to $Re_p = 50$. Using the dominant modes and associated frequencies, vortex initiation starts near the proximal side of the cavity (i.e., t/T=0.04). The vortex still grows in strength but stays in the cavity at a longer duration (i.e., t/T=0.00 to t/T=0.51) than $Re_p = 50$ (i.e., t/T=0.04

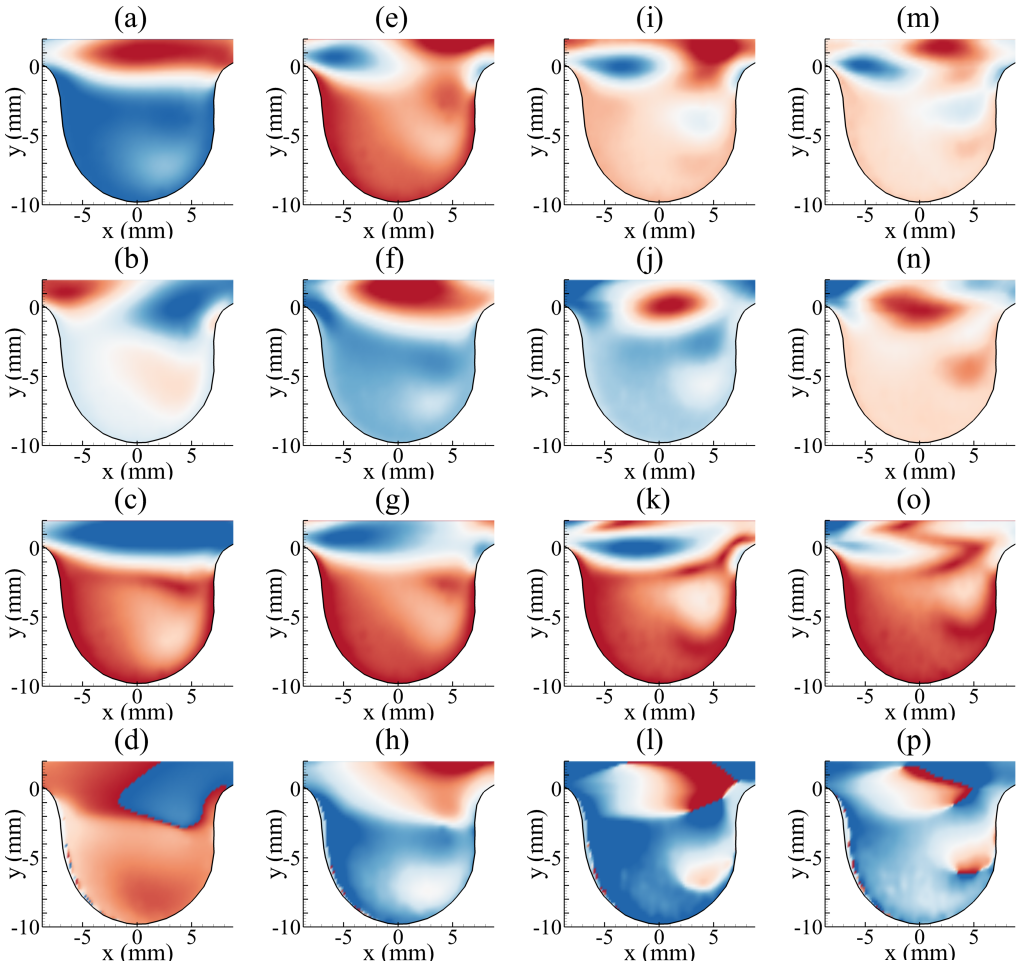

Figure 5.50: DMD modes for $Re_p = 270$, $\alpha = 5$ using the streamwise component of velocity. (a)-(d) $2.4Hz$ (Mode 2), (e)-(h) $4.8Hz$ (Mode 4), (i)-(l) $7.2Hz$ (Mode 6), and (m)-(p) $9.6Hz$ (Mode 8). (a),(e),(i),(m) real components. (b),(f),(j),(n) imaginary components. (c),(g),(k),(o) magnitude. (d),(h),(l),(p) phase.

to t/T=0.38). The vortex structure also does not fully go out of the cavity at this Re_p (i.e., t/T=0.41) when compared to $Re_p = 50$ (i.e., t/T=0.32). The second half of the pressure cycle repeats the process as the first vortex structure (i.e., from t/T=0.54 to t/T=0.98), and the entire cycle is again recognized by DMD as the dominant 0.8 Hz. Qualitatively, the flow trends are similar for $Re_p = 50$ and $Re_p = 270$ at $\alpha = 2$ as seen from the reconstruction figures. DMD differentiates these two scenarios through the change in mode shapes to highlight the impact of change in Re_p conditions.

Flow field reconstruction results for $\alpha = 5$ are now shown in Figs. 5.54 and 5.55 for

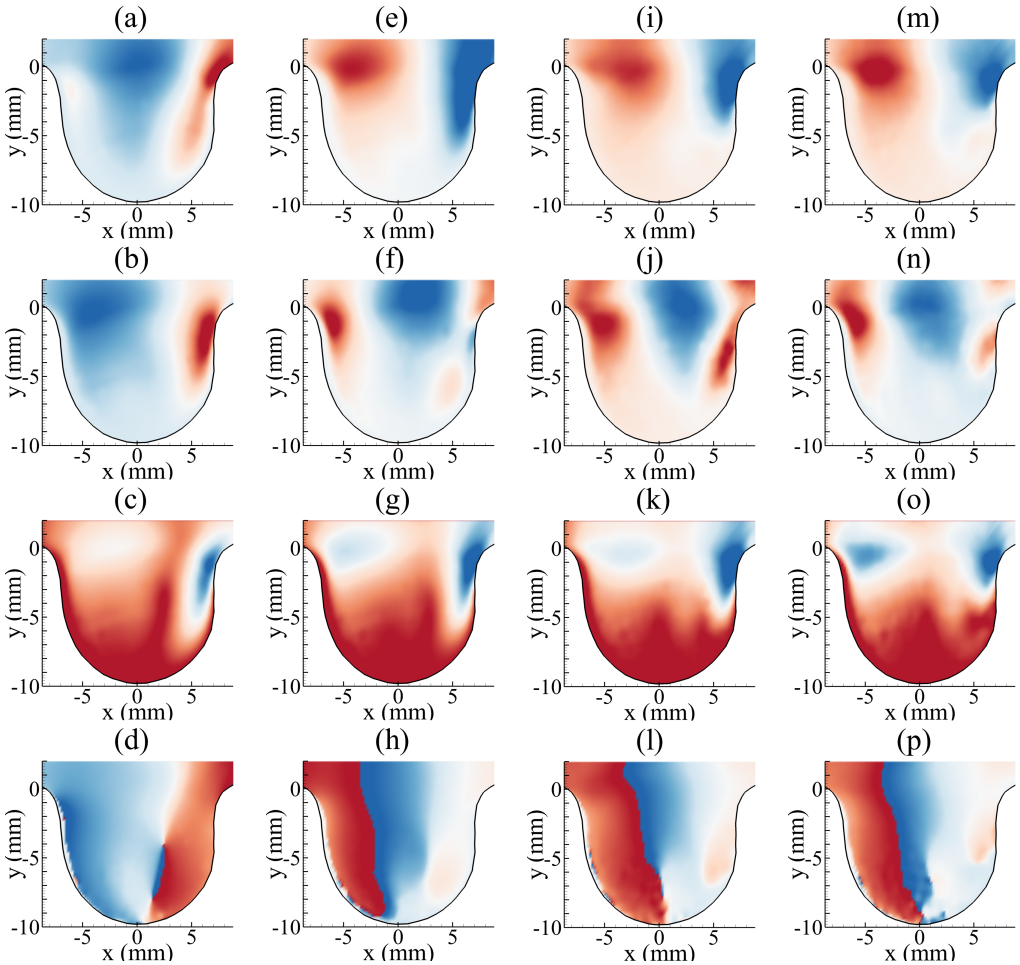

Figure 5.51: DMD modes for $Re_p = 270$, $\alpha = 5$ using the transverse component of velocity. (a)-(d) $2.4Hz$ (Mode 2), (e)-(h) $4.8Hz$ (Mode 4), (i)-(l) $7.2Hz$ (Mode 6), and (m)-(p) $9.6Hz$ (Mode 8). (a),(e),(i),(m) real components. (b),(f),(j),(n) imaginary components. (c),(g),(k),(o) magnitude. (d),(h),(l),(p) phase.

$Re_p = 50$ and $Re_p = 270$, respectively. Here the flow behavior in the aneurysm region for this unsteady scenario is different than the ones discussed for $\alpha = 2$. For $Re_p = 50$ flow scenario, a vortical structure is initially observed to be present near the proximal side of the cavity (i.e., t/T=0.00) which grows and moves towards the distal side before breaking down into the aneurysm dome (i.e., from t/T=0.04) to t/T=0.38). This process is seen to repeat itself for the second half of the cycle (i.e., t/T=0.58 to t/T=1.0), with the DMD amplitude recognizing this behavior as 4.8Hz dominant frequency. The DMD mode shape obtained for this scenarios also tell that the flow trend of the coherent structure will be

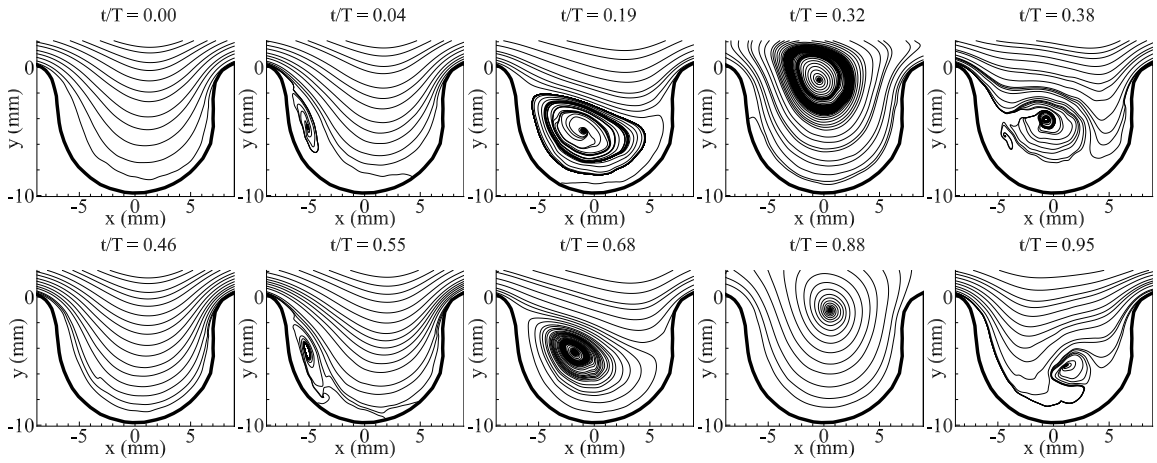

Figure 5.52: DMD low-order reconstruction for $Re_p = 50$, $\alpha = 2$ for selected time phases. Average normalized RMS error observed in low-order reconstruction is ϵ_{avg}=1.767%, with minimum normalized RMS error of ϵ_{min}=0.546% and maximum normalized RMS error of ϵ_{max}=2.947%. The RMS is normalized by the centerline velocity.

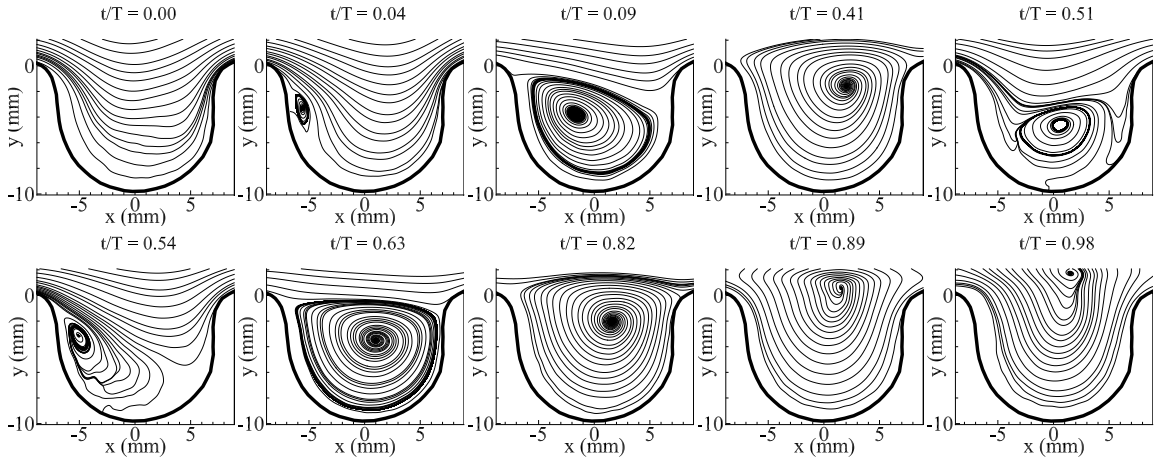

Figure 5.53: DMD low-order reconstruction for $Re_p = 270$, $\alpha = 2$ for selected time phases. Average normalized RMS errors observed in low-order reconstruction is ϵ_{avg}=0.866%, with minimum normalized RMS error of ϵ_{min}=0.520% and maximum normalized RMS error of ϵ_{max}=1.176%. The RMS is normalized by the centerline velocity.

different than $\alpha = 2$ conditions.

For $Re_p = 270$ and $\alpha = 5$ (i.e., Fig. 5.55), the vortex structure is observed throughout the pressure cycle where it experiences different interactions with the incoming pipe flow. Here, vortex structure moves from the proximal to the distal side of the aneurysm cavity before moving towards the dome in a clockwise movement (i.e., t/T=0.0 to t/T=0.23). As the vortex reduces in strength and impinging the neck then dome, a secondary vortex near

the proximal side forms and merges with the first vortex (i.e., t/T=0.31 to t/T=0.37), energizing the flow structure and impinges once more to the distal side of the cavity. This process of vortex movement and secondary vortex appearance to energize the flow in the cavity repeats for every cycle. Note that the DMD amplitude and mode shapes for this Re_p are different than the ones for $Re_p = 50$ at $\alpha = 5$. This illustrates that DMD provides information on the change in the flow behavior through the change in mode shapes and amplitudes, and highlight the impact of different inflow conditions.

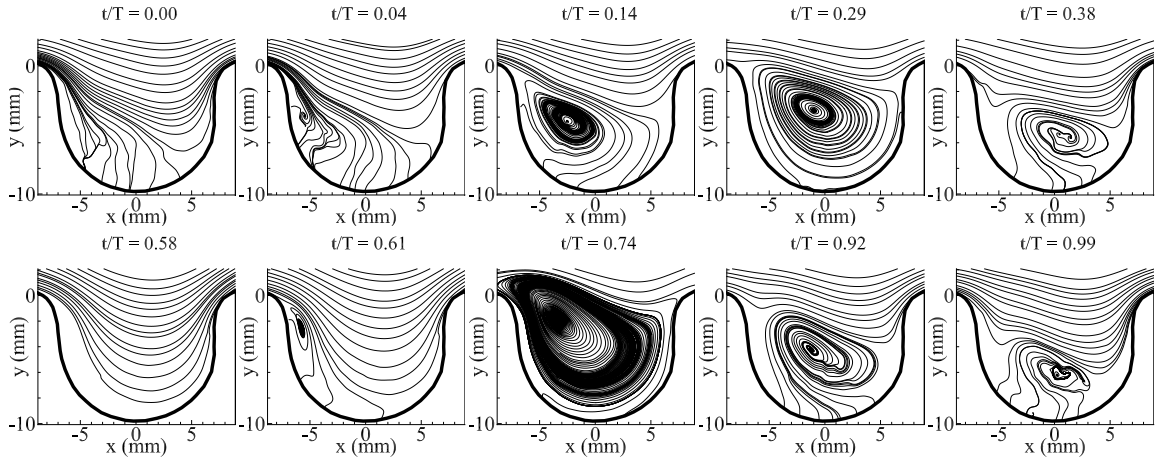

Figure 5.54: DMD low-order reconstruction for $Re_p = 50$, $\alpha = 5$ for selected time phases. Average normalized RMS error observed in low-order reconstruction is ϵ_{avg}=1.272%, with minimum normalized RMS error of ϵ_{min}=0.422% and maximum normalized RMS error of ϵ_{max}=2.783%. The RMS is normalized by the centerline velocity.

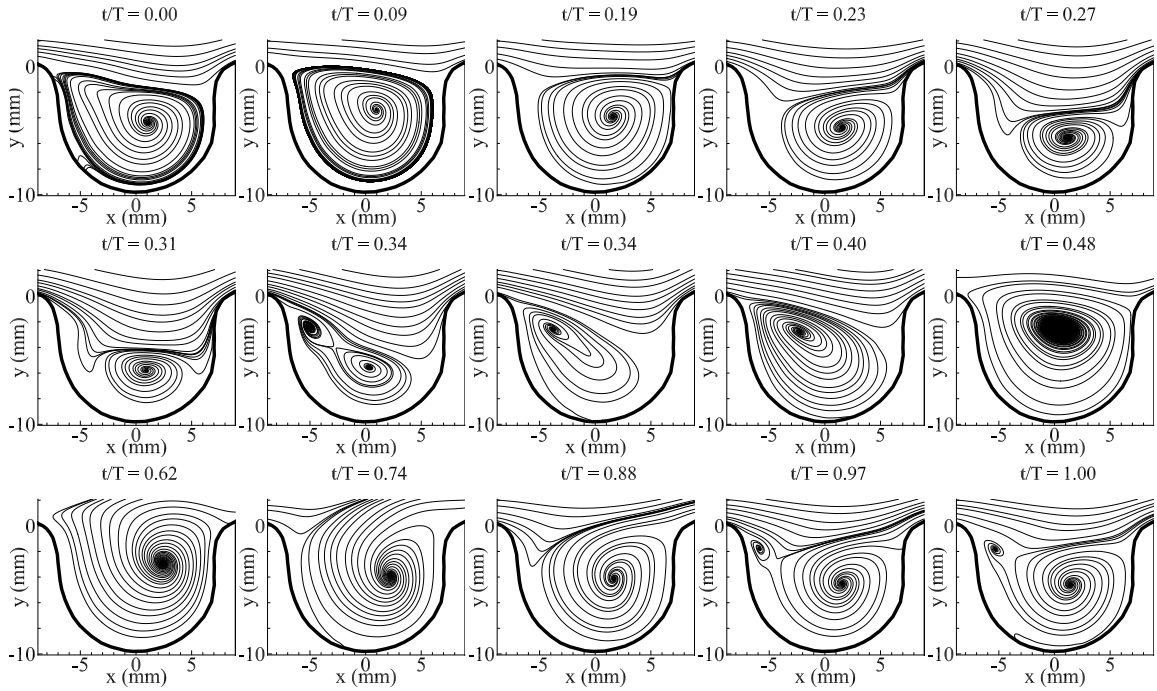

Figure 5.55: DMD low-order reconstruction for $Re_p = 270$, $\alpha = 5$ for selected time phases. Average normalized RMS error observed in low-order reconstruction is ϵ_{avg}=1.151%, with minimum normalized RMS error of ϵ_{min}=0.504% and maximum normalized RMS error of ϵ_{max}=2.857%. The RMS is normalized by the centerline velocity.

CHAPTER 6

Conclusions

2D PIV measurements were performed for two rigid aneurysm models at different inflow conditions to quantify the impact of large-scale structures on the fluid flow parameters in the aneurysm. These structures are studied to identify their influence on fluid dynamics parameters such as impinging location, vortex strength, and wall shear stress. Three different approaches were used to capture the large-scale flow structures in the aneurysm: 1) using hardware synchronization, 2) using Proper Orthogonal Decomposition, and 3) using Dynamic Mode Decomposition. These approaches are used to highlight their advantages and the information they can provide in analyzing complex flow scenarios. To achieve the objectives of the proposed research, 2D PIV measurements were conducted on rigid aneurysm models for a range of inflow parameters of α of 2 and 5, and Re_p of 50 to 270. A SuperPump system was used for accurate inflow control where the driving frequency of the pump was set to 0.4 Hz which corresponds to $\alpha = 2$ and 2.4 Hz which corresponds to $\alpha = 5$. For each inflow condition and models, 500 PIV images were acquired. Key findings in this study are summarized in the next few sections.

The results from the hardware synchronization showed the ability of the method to capture the large-scale flow structures at different inflow scenarios. The approach showed that different inflow scenarios impact the behavior of the flow structures through the changes in vortex evolution in the pressure cycle. It was found that Re_p and α both play a role in the vortex formation process particularly in the growth and decay, path of the structures and vortex strength. These in turn impact the impinging location and wall shear stress distribution along the aneurysm geometry.

Re_p is found to influence the large-scale flow structures in the aneurysm. In this dissertation, Re_p is related to the strength of the vortices, with stronger vortex behavior at increasing Re_p. Furthermore, increasing Re_p shifts the path vortex further towards the distal side of the aneurysm, and presence of secondary vortical structures are also

observed. The impinging location results also showed that increasing Re_p changes the distribution of high pressure points from along the distal wall to a concentrated distribution at the distal neck. Lastly, the wall shear stress values were impacted by the change in Re_p where wall shear stress values increased near the distal neck by increasing Re_p.

α is also found to impact the flow structure behavior in the aneurysm particularly in the vortex formation, growth, and dissipation processes. The vortex strength of the vortical structures were found to be stronger with an increase in α. The results also showed that the vortex path was influenced by the change α where the vortices may exit the aneurysm sac or stay within the sac. α was also found to impact the dissipation process of the vortical structures where rapid dissipation of the vortex structure occurred at low α while gradual dissipation occurred at high α. These in turn influences the impinging location results where α impacts the direction of the impinging location due to the change in the direction of the vortical structure. Lastly, wall shear stress found in the aneurysm cavity are impacted by α where an increasing in α increases the shears stresses.

The impact of the bottleneck also influenced the vortex phenomena inside the aneurysm. The vortices, when they appear, may able to travel towards the distal side of the aneurysm sac for $BF = 1.0$. On the other hand, the vortices were restricted to travel only up to the center of the aneurysm orifice for $BF = 1.6$. The neck constriction also impacts the impinging location. The impinging location was able to spread out inside the aneurysm sac at $BF = 1.0$ due to the wide neck opening. This meant that the incoming fluid was able to penetrate more inside the aneurysm sac. Meanwhile, the impinging locations were limited to the neck area for $BF = 1.6$. This meant that the incoming flow was not able to penetrate inside the aneurysm sac and almost all of the impingement points and increase shear stresses lie on the distal neck area of the aneurysm.

Proper Orthogonal Decomposition was successfully utilized in this dissertation to further understand the behavior of the large-scale structures at different inflow scenarios.

The energetic mode shapes were captured and highlighted the important features that unique for each flow scenario. For a similar α and varying Re_p, similar mode shapes were found yet shifted horizontally due to the impact of Re_p. The similarity in mode shapes for fixed α showed how the flow evolution behavior would be similar. The shift in these mode shapes further tell us where the high and low values have moved, and could be related to the changes observed in the impinging locations and wall shear stress values. With the change in α condition, completely different mode shapes were observed which tells us that the flow behavior has changed. The POD energy results showed how the fluctuating kinetic energy is distributed across different POD modes. More POD modes are required for high α to reach similar energy content than low α. In terms of time-varying results, the results showed the unique and complex interplay of POD modes, and when certain POD modes and their combination are highly impactful to the flow. As similar mode shapes can be found for the same α, unique interaction of the modes are found with different Re_p scenarios and increases in complexity as more modes are considered. Lastly, the low-order reconstruction results were able to provide a clear picture of vortex formation, evolution, and convection inside the aneurysm sac using a combination of the POD modes and their time-varying coefficients for a given α and Re_p condition. These results are in agreement with the flow evolution using hardware synchronization, but we now have information on the dynamics of the spatial structures using POD.

DMD was also successfully utilized to understand the spatiotemporal features of studied inflow conditions. DMD was able to capture the frequencies for each inflow condition. The results obtained showed that Re_p only impacts the DMD mode shapes. With similar α and an increase in Re_p, the DMD mode shapes are relatively similar but shifted which then shifts the convection of the vortical structure. On the other hand, α influences the DMD frequencies as well as mode shapes. The obtained frequencies are different with different α as the flow frequencies has changed. This in turn changes the mode shapes

which shows a different flow trend with different α. Along with the frequency results, the growth rate and amplitude results showed that the first few low frequencies were stable and had high contribution to the flow dynamics. This information allowed us to create a mathematical description of the large-scale structures in the aneurysm through the interplay of the DMD modes, frequencies and growth rates. The mathematical model estimates the flow field behavior using a linear combination of frequencies, mode shapes, and their individual contributions. The combination of these spatial structures that oscillate at different frequencies provides the dynamics of the vortex formation, evolution and convection inside the aneurysm sac. These flow models were in good agreement with the results from hardware synchronization and POD, but now we have insight on the temporal behavior of the oscillating structures present in each inflow scenario with DMD.

The present study provided an overarching work of investigating the spatial and temporal behavior of large-scale flow structures on fluid parameters for a range of inflow conditions. The results obtained using different approaches allowed us to study the aneurysm flow with sufficient detail and meet the objectives presented in the proposed research. With hardware synchronization, the method enabled us to capture the large-scale structures at different points in the pressure cycle. This allowed us to visualize the entire flow evolution, and perform fluid dynamic analysis. For POD, it was used to extract energetic flow features or modes in each flow scenario, and the combination of these modes allowed us to perform a low-order approximation of the flow field. The method also enabled us to study the vortex behavior such as formation and evolution by looking at the interplay of the POD modes and their coefficients and their impact on flow parameters. Similarly, DMD is used to analyze and to differentiate the observed flow behaviors at different inflow conditions based on their frequencies, modes, and amplitudes. Low-order flow reconstruction using DMD was also used to model the flow evolution for each inflow scenario using a combination of the DMD parameters.

The methods used in this dissertation provide alternative methods to study complex flow scenarios through advanced analysis techniques. Both POD and DMD can be used to create mathematical models which can be used to look into the flow evolution at sufficiently great detail and at any time step. With POD, the method provides an approach to look into the flow evolution behavior by analyzing the time-varying coefficients. The phase-portrait of these coefficients can tell us the behavior of the modes (and thus the flow itself) although the PIV images may be randomly distributed over the waveform. On the other hand, an essential step in DMD requires images to be sequenced. This allows the method to extract the flow processes accordingly. In our study, the PIV images and their relation to pressure signal were determined. The synchronization of the PIV trigger and pump waveform enabled us to sequence the PIV images prior to using DMD. Thus, we highlight in this study how we can use POD and DMD to extract pertinent information with the PIV images. These methods can provide an alternative approach to phase-locked measurements which can be time-consuming, expensive, and requires extensive hardware synchronization.

To give some perspective on phase-locked measurements, an experiment can take months to carefully design, one or two months to trouble shoot the experiment and properly synchronize each used equipment, and several months to analyze the data. This then requires a big storage to store the data. The analysis time is greatly amplified as more scenarios are collected and studied. Lastly, the approach and mathematical models of the flow field can be used for validation of numerical and computational data.

Bibliography

[1] Wardlaw, J., and White, P., 2000. "The detection and management of unruptured intracranial aneurysms". *Brain,* **123**(2), pp. 205–221.

[2] Sakalihasan, N., Limet, R., and Defawe, O. D., 2005. "Abdominal aortic aneurysm". *The Lancet,* **365**(9470), pp. 1577–1589.

[3] Munson, B. R., Okiishi, T. H., Huebsch, W. W., and Rothmayer, A. P., 2013. *Fluid mechanics*. Wiley Singapore.

[4] Shankar, P., and Deshpande, M., 2000. "Fluid mechanics in the driven cavity". *Annual review of fluid mechanics,* **32**(1), pp. 93–136.

[5] Ku, D. N., 1997. "Blood flow in arteries". *Annual review of fluid mechanics,* **29**(1), pp. 399–434.

[6] Lasheras, J. C., 2007. "The biomechanics of arterial aneurysms". *Annu. Rev. Fluid Mech.,* **39**, pp. 293–319.

[7] Pressler, V., and McNamara, J. J., 1980. "Thoracic aortic aneurysm natural history and treatment". *The Journal of thoracic and cardiovascular surgery,* **79**(4), pp. 489–498.

[8] Brisman, J. L., Song, J. K., and Newell, D. W., 2006. "Cerebral aneurysms". *New England journal of medicine,* **355**(9), pp. 928–939.

[9] WJ, G., and SP, B., 1954. "Intra-aneurysmal hemodynamics: turbulence.". *Transactions of the American Neurological Association,* **13**(79th Meeting), pp. 163–165.

[10] Jain, K., 1963. "Mechanism of rupture of intracranial saccular aneurysms". *Surgery,* **54**(2), pp. 347–350.

[11] Kallmes, D. F., Altes, T., Vincent, D., Cloft, H., Do, H., and Jensen, M., 1999. "Experimental side-wall aneurysms: a natural history study". *Neuroradiology,* **41**(5), pp. 338–341.

[12] McCormick, W. F., and Acosta-Rua, G. J., 1970. "The size of intracranial saccular aneurysms: an autopsy study". *Journal of neurosurgery,* **33**(4), pp. 422–427.

[13] of Unruptured Intracranial Aneurysms Investigators, I. S., 1998. "Unruptured intracranial aneurysms—risk of rupture and risks of surgical intervention". *New England Journal of Medicine,* **339**(24), pp. 1725–1733.

[14] Ujiie, H., Tachi, H., Hiramatsu, O., Hazel, A. L., Matsumoto, T., Ogasawara, Y., Nakajima, H., Hori, T., Takakura, K., and Kajiya, F., 1999. "Effects of size and shape (aspect ratio) on the hemodynamics of saccular aneurysms: a possible index for surgical treatment of intracranial aneurysms". *Neurosurgery,* **45**(1), pp. 119–130.

[15] Ma, B., Harbaugh, R. E., and Raghavan, M. L., 2004. "Three-dimensional geometrical characterization of cerebral aneurysms". *Annals of biomedical engineering,* **32**(2), pp. 264–273.

[16] Raghavan, M. L., Ma, B., and Harbaugh, R. E., 2005. "Quantified aneurysm shape and rupture risk". *Journal of neurosurgery,* **102**(2), pp. 355–362.

[17] Burleson, A. C., Strother, C. M., and Turitto, V. T., 1995. "Computer modeling of intracranial saccular and lateral aneurysms for the study of their hemodynamics". *Neurosurgery,* **37**(4), pp. 774–784.

[18] Bluestein, D., Niu, L., Schoephoerster, R., and Dewanjee, M., 1996. "Steady flow in an aneurysm model: correlation between fluid dynamics and blood platelet deposition". *Journal of biomechanical engineering,* **118**(3), pp. 280–286.

[19] Asgharzadeh, H., and Borazjani, I., 2016. "Effects of reynolds and womersley numbers on the hemodynamics of intracranial aneurysms". *Computational and mathematical methods in medicine,* **2016**.

[20] Ferguson, G. G., 1972. "Physical factors in the initiation, growth, and rupture of human intracranial saccular aneurysms". *Journal of neurosurgery,* **37**(6), pp. 666–677.

[21] Egelhoff, C., Budwig, R., Elger, D., Khraishi, T., and Johansen, K., 1999. "Model studies of the flow in abdominal aortic aneurysms during resting and exercise conditions". *Journal of biomechanics,* **32**(12), pp. 1319–1329.

[22] Yu, S., and Zhao, J., 2000. "A particle image velocimetry study on the pulsatile flow characteristics in straight tubes with an asymmetric bulge". *Proceedings of the Institution of Mechanical Engineers, Part C: Journal of Mechanical Engineering Science,* **214**(5), pp. 655–671.

[23] Bouillot, P., Brina, O., Ouared, R., Lovblad, K., Pereira, V. M., and Farhat, M., 2014. "Multi-time-lag PIV analysis of steady and pulsatile flows in a sidewall aneurysm". *Experiments in fluids,* **55**(6), p. 1746.

[24] Budwig, R., Elger, D., Hooper, H., and Slippy, J., 1993. "Steady flow in abdominal aortic aneurysm models". *Journal of biomechanical engineering,* **115**(4A), pp. 418–423.

[25] Fukushima, T., Matsuzawa, T., and Homma, T., 1989. "Visualization and finite element analysis of pulsatile flow in models of the abdominal aortic aneurysm". *Biorheology,* **26**(2), pp. 109–130.

[26] Yu, S., and Zhao, J., 1999. "A steady flow analysis on the stented and non-stented sidewall aneurysm models". *Medical Engineering and Physics,* **21**(3), pp. 133–141.

[27] Le, T. B., Borazjani, I., and Sotiropoulos, F., 2010. "Pulsatile flow effects on the hemodynamics of intracranial aneurysms". *Journal of biomechanical engineering,* **132**(11), p. 111009.

[28] Taira, K., Brunton, S. L., Dawson, S. T., Rowley, C. W., Colonius, T., McKeon, B. J., Schmidt, O. T., Gordeyev, S., Theofilis, V., and Ukeiley, L. S., 2017. "Modal analysis of fluid flows: An overview". *Aiaa Journal,* **55**(12), pp. 4013–4041.

[29] Lumley, J. L., 1967. "The structure of inhomogeneous turbulent flows". *Atmospheric turbulence and radio wave propagation.*

[30] Berkooz, G., Holmes, P., and Lumley, J. L., 1993. "The proper orthogonal decomposition in the analysis of turbulent flows". *Annual review of fluid mechanics,* **25**(1), pp. 539–575.

[31] Holmes, P., Lumley, J. L., Berkooz, G., and Rowley, C. W., 2012. *Turbulence, coherent structures, dynamical systems and symmetry.* Cambridge university press.

[32] Rowley, C. W., MEZIC, I., Bagheri, S., Schlatter, P., HENNINGSON, D., et al., 2009. "Spectral analysis of nonlinear flows". *Journal of fluid mechanics,* **641**(1), pp. 115–127.

[33] Schmid, P. J., 2010. "Dynamic mode decomposition of numerical and experimental data". *Journal of fluid mechanics,* **656**, pp. 5–28.

[34] Taira, K., Hemati, M. S., Brunton, S. L., Sun, Y., Duraisamy, K., Bagheri, S., Dawson, S. T., and Yeh, C.-A., 2020. "Modal analysis of fluid flows: Applications and outlook". *AIAA journal,* **58**(3), pp. 998–1022.

[35] Rowley, C. W., and Dawson, S. T., 2017. "Model reduction for flow analysis and control". *Annual Review of Fluid Mechanics,* **49**, pp. 387–417.

[36] Abulkhair, H., 2016. "Experimental investigation of the flow dynamics in a model of an abdominal aortic aneurysm". PhD thesis, Concordia University.

[37] Byrne, G., Mut, F., and Cebral, J., 2014. "Quantifying the large-scale hemodynamics of intracranial aneurysms". *American Journal of Neuroradiology,* **35**(2), pp. 333–338.

[38] Daroczy, L., Abdelsamie, A., Janiga, G., and Thevenin, D., 2017. "State detection and hybrid simulation of biomedical flows". In Tenth International Symposium on Turbulence and Shear Flow Phenomena, Begel House Inc.

[39] Lozowy, R., 2017. "Hemodynamics in abdominal aorta aneurysms".

[40] Janiga, G., 2019. "Quantitative assessment of 4d hemodynamics in cerebral aneurysms using proper orthogonal decomposition". *Journal of biomechanics,* **82**, pp. 80–86.

[41] Vlachopoulos, C., O'Rourke, M., and Nichols, W. W., 2011. *McDonald's blood flow in arteries: theoretical, experimental and clinical principles*. CRC press.

[42] McDonald, D. A., 1974. "Blood flow in arteries".

[43] Wiebers, D. O., Torner, J. C., and Meissner, I., 1992. "Impact of unruptured intracranial aneurysms on public health in the united states.". *Stroke,* **23**(10), pp. 1416–1419.

[44] Vega, C., Kwoon, J. V., Lavine, S. D., et al., 2002. "Intracranial aneurysms: current evidence and clinical practice". *American family physician,* **66**(4), pp. 601–610.

[45] Cebral, J. R., and Raschi, M., 2013. "Suggested connections between risk factors of intracranial aneurysms: a review". *Annals of biomedical engineering,* **41**(7), pp. 1366–1383.

[46] Dolan, J. M., Kolega, J., and Meng, H., 2013. "High wall shear stress and spatial gradients in vascular pathology: a review". *Annals of biomedical engineering,* **41**(7), pp. 1411–1427.

[47] Sadasivan, C., Fiorella, D. J., Woo, H. H., and Lieber, B. B., 2013. "Physical factors effecting cerebral aneurysm pathophysiology". *Annals of biomedical engineering,* **41**(7), pp. 1347–1365.

[48] Mizoi, K., Yoshimoto, T., Nagamine, Y., Kayama, T., and Koshu, K., 1995. "How to treat incidental cerebral aneurysms: a review of 139 consecutive cases". *Surgical neurology,* **44**(2), pp. 114–121.

[49] Beck, J., Rohde, S., El Beltagy, M., Zimmermann, M., Berkefeld, J., Seifert, V., and Raabe, A., 2003. "Difference in configuration of ruptured and unruptured intracranial aneurysms determined by biplanar digital subtraction angiography". *Acta neurochirurgica,* **145**(10), pp. 861–865.

[50] Shum, J., Martufi, G., Di Martino, E., Washington, C. B., Grisafi, J., Muluk, S. C., and Finol, E. A., 2011. "Quantitative assessment of abdominal aortic aneurysm geometry". *Annals of biomedical engineering,* **39**(1), pp. 277–286.

[51] You, S.-H., Kong, D.-S., Kim, J.-S., Jeon, P., Kim, K. H., Roh, H. K., Kim, G.-M., Lee, K.-H., and Hong, S.-C., 2010. "Characteristic features of unruptured intracranial aneurysms: predictive risk factors for aneurysm rupture". *Journal of Neurology, Neurosurgery & Psychiatry,* **81**(5), pp. 479–484.

[52] Valencia, C., Villa-Uriol, M., Pozo, J., and Frangi, A., 2010. "Morphological descriptors as rupture indicators in middle cerebral artery aneurysms". In Engineering in Medicine and Biology Society (EMBC), 2010 Annual International Conference of the IEEE, IEEE, pp. 6046–6049.

[53] Hoh, B. L., Sistrom, C. L., Firment, C. S., Fautheree, G. L., Velat, G. J., Whiting, J. H., Reavey-Cantwell, J. F., and Lewis, S. B., 2007. "Bottleneck factor and height-width ratio: association with ruptured aneurysms in patients with multiple cerebral aneurysms". *Neurosurgery,* **61**(4), pp. 716–723.

[54] Ujiie, H., Tamano, Y., Sasaki, K., and Hori, T., 2001. "Is the aspect ratio a reliable index for predicting the rupture of a saccular aneurysm?". *Neurosurgery,* **48**(3), pp. 495–503.

[55] Prestigiacomo, C. J., He, W., Catrambone, J., Chung, S., Kasper, L., Pasupuleti, L., and Mittal, N., 2009. "Predicting aneurysm rupture probabilities through the application of a computed tomography angiography–derived binary logistic regression model". *Journal of neurosurgery,* **110**(1), pp. 1–6.

[56] Ryu, C.-W., Kwon, O.-K., Koh, J. S., and Kim, E. J., 2011. "Analysis of aneurysm rupture in relation to the geometric indices: aspect ratio, volume, and volume-to-neck ratio". *Neuroradiology,* **53**(11), pp. 883–889.

[57] Tremmel, M., Dhar, S., Levy, E. I., Mocco, J., and Meng, H., 2009. "Influence of intracranial aneurysm-to-parent vessel size ratio on hemodynamics and implication for rupture: results from a virtual experimental study". *Neurosurgery,* **64**(4), pp. 622–631.

[58] Chien, A., Castro, M., Tateshima, S., Sayre, J., Cebral, J., and Vinuela, F., 2009. "Quantitative hemodynamic analysis of brain aneurysms at different locations". *American Journal of Neuroradiology,* **30**(8), pp. 1507–1512.

[59] Hans, F., Krings, T., Reinges, M., and Mull, M., 2004. "Spontaneous regression of two supraophthalmic internal cerebral artery aneurysms following flow pattern alteration". *Neuroradiology,* **46**(6), pp. 469–473.

[60] Meckel, S., Stalder, A. F., Santini, F., Radü, E.-W., Rüfenacht, D. A., Markl, M., and Wetzel, S. G., 2008. "In vivo visualization and analysis of 3-d hemo-

dynamics in cerebral aneurysms with flow-sensitized 4-d mr imaging at 3 t". *Neuroradiology,* **50**(6), pp. 473–484.

[61] Patti, J., Viñuela, F., and Chien, A., 2013. "Distinct trends of pulsatility found at the necks of ruptured and unruptured aneurysms". *Journal of neurointerventional surgery*, pp. neurintsurg–2013.

[62] Ruiz, D. S. M., Yilmaz, H., Dehdashti, A., Alimenti, A., De Tribolet, N., and Rüfenacht, D., 2006. "The perianeurysmal environment: influence on saccular aneurysm shape and rupture". *American Journal of Neuroradiology,* **27**(3), pp. 504–512.

[63] Satoh, T., Omi, M., Ohsako, C., Katsumata, A., Yoshimoto, Y., Tsuchimoto, S., Onoda, K., Tokunaga, K., Sugiu, K., and Date, I., 2005. "Influence of perianeurysmal environment on the deformation and bleb formation of the unruptured cerebral aneurysm: assessment with fusion imaging of 3d mr cisternography and 3d mr angiography". *American Journal of Neuroradiology,* **26**(8), pp. 2010–2018.

[64] Baccin, C., Krings, T., Alvarez, H., Ozanne, A., and Lasjaunias, P., 2006. "Multiple mirror-like intracranial aneurysms. report of a case and review of the literature". *Acta neurochirurgica,* **148**(10), pp. 1091–1095.

[65] Higa, T., Ujiie, H., Kato, K., Kamiyama, H., and Hori, T., 2009. "Basilar artery trunk saccular aneurysms: morphological characteristics and management". *Neurosurgical review,* **32**(2), pp. 181–191.

[66] Songsaeng, D., Geibprasert, S., Willinsky, R., Tymianski, M., TerBrugge, K., and Krings, T., 2010. "Impact of anatomical variations of the circle of willis

on the incidence of aneurysms and their recurrence rate following endovascular treatment". *Clinical radiology,* **65**(11), pp. 895–901.

[67] de Rooij, N. K., Velthuis, B. K., Algra, A., and Rinkel, G. J., 2009. "Configuration of the circle of willis, direction of flow, and shape of the aneurysm as risk factors for rupture of intracranial aneurysms". *Journal of neurology,* **256**(1), p. 45.

[68] Wiebers, D. O., Whisnant, J. P., Sundt Jr, T. M., and O'Fallon, W. M., 1987. "The significance of unruptured intracranial saccular aneurysms". *Journal of neurosurgery,* **66**(1), pp. 23–29.

[69] Scott, R., Ashton, H., Lamparelli, M., Harris, G., and Stevens, J., 1999. "A 14-year experience with 6 cm as a criterion for surgical treatment of abdominal aortic aneurysm". *British Journal of Surgery,* **86**(10), pp. 1317–1321.

[70] Thompson, R. W., 2002. Detection and management of small aortic aneurysms.

[71] Valentine, R. J., DeCaprio, J. D., Castillo, J. M., Modrall, J. G., Jackson, M. R., and Clagett, G. P., 2000. "Watchful waiting in cases of small abdominal aortic aneurysms—appropriate for all patients?". *Journal of vascular surgery,* **32**(3), pp. 441–450.

[72] Budwig, R., Elger, D., Hooper, H., and Slippy, J., 1993. "Steady flow in abdominal aortic aneurysm models". *Journal of biomechanical engineering,* **115**(4A), pp. 418–423.

[73] Drexler, D. J., 1984. "Steady flow through several aneurysm models". PhD thesis, Worcester Polytechnic Institute.

[74] Bluestein, D., Niu, L., Schoephoerster, R., and Dewanjee, M., 1996. "Steady flow in an aneurysm model: correlation between fluid dynamics and blood platelet deposition". *Journal of biomechanical engineering,* **118**(3), pp. 280–286.

[75] Egelhoff, C., 1997. "A model study of pulsatile flow regimes in abdominal aortic aneurysms". In ASME FEDSM97-34-31, ASME Fluids Engineering Division Summer Division Meeting.

[76] Steiger, H. J., Poll, A., Liepsch, D., and Reulen, H.-J., 1987. "Basic flow structure in saccular aneurysms: a flow visualization study". *Heart and vessels,* **3**(2), pp. 55–65.

[77] Steiger, H.-J., 1990. "Pathophysiology of development and rupture of cerebral aneurysms". *Acta Neurochir Suppl.*

[78] Steiger, H., 1991. "Growth of cerebral saccular aneurysms". *Medical & Biological Engineering¡ & Computing,* **29**, p. 19.

[79] Gobin, Y., Counord, J., Flaud, P., and Duffaux, J., 1994. "In vitro study of haemodynamics in a giant saccular aneurysm model: influence of flow dynamics in the parent vessel and effects of coil embolisation". *Neuroradiology,* **36**(7), pp. 530–536.

[80] Taylor, T. W., and Yamaguchi, T., 1994. "Three-dimensional simulation of blood flow in an abdominal aortic aneurysm—steady and unsteady flow cases". *Journal of biomechanical engineering,* **116**(1), pp. 89–97.

[81] Liou, T.-M., Chang, W.-C., and Liao, C.-C., 1997. "Ldv measurements in lateral model aneurysms of various sizes". *Experiments in Fluids,* **23**(4), pp. 317–324.

[82] Stehbens, W., 1974. "Flow disturbances in glass models of aneurysms at low reynolds numbers". *Experimental Physiology,* **59**(2), pp. 167–174.

[83] Niimi, H., Kawano, Y., and Sugiyama, I., 1984. "Structure of blood flow through a curved vessel with an aneurysm". *Biorheology,* **21**(4), pp. 603–615.

[84] Liou, T.-M., and Liao, C.-C., 1997. "Flowfields in lateral aneurysm models arising from parent vessels with different curvatures using ptv". *Experiments in fluids,* **23**(4), pp. 288–298.

[85] Liou, T.-M., Li, Y.-C., and Juan, W.-C., 2007. "Numerical and experimental studies on pulsatile flow in aneurysms arising laterally from a curved parent vessel at various angles". *Journal of biomechanics,* **40**(6), pp. 1268–1275.

[86] Le, T. B., Troolin, D. R., Amatya, D., Longmire, E. K., and Sotiropoulos, F., 2013. "Vortex phenomena in sidewall aneurysm hemodynamics: experiment and numerical simulation". *Annals of biomedical engineering,* **41**(10), pp. 2157–2170.

[87] Baharoglu, M. I., Schirmer, C. M., Hoit, D. A., Gao, B.-L., and Malek, A. M., 2010. "Aneurysm inflow-angle as a discriminant for rupture in sidewall cerebral aneurysms: morphometric and computational fluid dynamic analysis". *Stroke,* **41**(7), pp. 1423–1430.

[88] Cebral, J. R., Castro, M. A., Burgess, J. E., Pergolizzi, R. S., Sheridan, M. J., and Putman, C. M., 2005. "Characterization of cerebral aneurysms for as-

sessing risk of rupture by using patient-specific computational hemodynamics models". *American Journal of Neuroradiology,* **26**(10), pp. 2550–2559.

[89] Hope, T. A., Hope, M. D., Purcell, D. D., von Morze, C., Vigneron, D. B., Alley, M. T., and Dillon, W. P., 2010. "Evaluation of intracranial stenoses and aneurysms with accelerated 4d flow". *Magnetic resonance imaging,* **28**(1), pp. 41–46.

[90] Lu, G., Huang, L., Zhang, X., Wang, S., Hong, Y., Hu, Z., and Geng, D., 2011. "Influence of hemodynamic factors on rupture of intracranial aneurysms: patient-specific 3d mirror aneurysms model computational fluid dynamics simulation". *American Journal of Neuroradiology,* **32**(7), pp. 1255–1261.

[91] Salsac, A.-V., Sparks, S., Chomaz, J.-M., and Lasheras, J., 2006. "Evolution of the wall shear stresses during the progressive enlargement of symmetric abdominal aortic aneurysms". *Journal of Fluid Mechanics,* **560**, pp. 19–51.

[92] Raut, S. S., Chandra, S., Shum, J., and Finol, E. A., 2013. "The role of geometric and biomechanical factors in abdominal aortic aneurysm rupture risk assessment". *Annals of biomedical engineering,* **41**(7), pp. 1459–1477.

[93] Morlacchi, S., and Migliavacca, F., 2013. "Modeling stented coronary arteries: where we are, where to go". *Annals of biomedical engineering,* **41**(7), pp. 1428–1444.

[94] Han, H.-C., Chesnutt, J. K., Garcia, J. R., Liu, Q., and Wen, Q., 2013. "Artery buckling: new phenotypes, models, and applications". *Annals of biomedical engineering,* **41**(7), pp. 1399–1410.

[95] McVeigh, G. E., Hamilton, P. K., and Morgan, D. R., 2002. "Evaluation of mechanical arterial properties: clinical, experimental and therapeutic aspects". *Clinical Science,* **102**(1), pp. 51–67.

[96] Chen, H., Selimovic, A., Thompson, H., Chiarini, A., Penrose, J., Ventikos, Y., and Watton, P. N., 2013. "Investigating the influence of haemodynamic stimuli on intracranial aneurysm inception". *Annals of biomedical engineering,* **41**(7), pp. 1492–1504.

[97] Tateshima, S., Murayama, Y., Villablanca, J. P., Morino, T., Takahashi, H., Yamauchi, T., Tanishita, K., and Viñuela, F., 2001. "Intraaneurysmal flow dynamics study featuring an acrylic aneurysm model manufactured using a computerized tomography angiogram as a mold". *Journal of neurosurgery,* **95**(6), pp. 1020–1027.

[98] Geoghegan, P., Buchmann, N., Spence, C., Moore, S., and Jermy, M., 2012. "Fabrication of rigid and flexible refractive-index-matched flow phantoms for flow visualisation and optical flow measurements". *Experiments in fluids,* **52**(5), pp. 1331–1347.

[99] de Galarreta, S. R., Cazón, A., Antón, R., and Finol, E. A., 2017. "The relationship between surface curvature and abdominal aortic aneurysm wall stress". *Journal of biomechanical engineering,* **139**(8), p. 081006.

[100] Kyriacou, S., and Humphrey, J., 1996. "Influence of size, shape and properties on the mechanics of axisymmetric saccular aneurysms". *Journal of biomechanics,* **29**(8), pp. 1015–1022.

[101] Lu, J., Hu, S., and Raghavan, M. L., 2013. "A shell-based inverse approach of stress analysis in intracranial aneurysms". *Annals of biomedical engineering,* **41**(7), pp. 1505–1515.

[102] Polzer, S., Bursa, J., Gasser, T. C., Staffa, R., and Vlachovsky, R., 2013. "A numerical implementation to predict residual strains from the homogeneous stress hypothesis with application to abdominal aortic aneurysms". *Annals of biomedical engineering,* **41**(7), pp. 1516–1527.

[103] Gasser, T. C., Auer, M., Labruto, F., Swedenborg, J., and Roy, J., 2010. "Biomechanical rupture risk assessment of abdominal aortic aneurysms: model complexity versus predictability of finite element simulations". *European Journal of Vascular and Endovascular Surgery,* **40**(2), pp. 176–185.

[104] Womersley, J. R., 1955. "Method for the calculation of velocity, rate of flow and viscous drag in arteries when the pressure gradient is known". *The Journal of physiology,* **127**(3), pp. 553–563.

[105] Löw, M., Perktold, K., and Raunig, R., 1993. "Hemodynamics in rigid and distensible saccular aneurysms: a numerical study of pulsatile flow characteristics". *Biorheology,* **30**(3-4), pp. 287–298.

[106] Liou, T.-M., and Li, Y.-C., 2008. "Effects of stent porosity on hemodynamics in a sidewall aneurysm model". *Journal of biomechanics,* **41**(6), pp. 1174–1183.

[107] Van de Vosse, F., and Van Dongen, M., 1998. "Cardiovascular fluid mechanics—lecture notes". *Faculty of Applied Physics, Faculty of Mechanical Engineering, Eindhoven University of Technology, Eindhoven, Netherlands.*

[108] Caro, C. G., Pedley, T. J., Schroter, R., and Seed, W., 2012. *The mechanics of the circulation*. Cambridge University Press.

[109] He, X., and Ku, D. N., 1994. "Unsteady entrance flow development in a straight tube".

[110] Budwig, R., 1994. "Refractive index matching methods for liquid flow investigations". *Experiments in fluids,* **17**(5), pp. 350–355.

[111] Miller, P., Danielson, K., Moody, G., Slifka, A., Drexler, E., and Hertzberg, J., 2006. "Matching index of refraction using a diethyl phthalate/ethanol solution for in vitro cardiovascular models". *Experiments in fluids,* **41**(3), pp. 375–381.

[112] Nguyen, T., Biadillah, Y., Mongrain, R., Brunette, J., Tardif, J.-C., and Bertrand, O., 2004. "A method for matching the refractive index and kinematic viscosity of a blood analog for flow visualization in hydraulic cardiovascular models". *Journal of biomechanical engineering,* **126**(4), pp. 529–535.

[113] Wiederseiner, S., Andreini, N., Epely-Chauvin, G., and Ancey, C., 2011. "Refractive-index and density matching in concentrated particle suspensions: a review". *Experiments in fluids,* **50**(5), pp. 1183–1206.

[114] Lowe, M., and Kutt, P., 1992. "Refraction through cylindrical tubes". *Experiments in fluids,* **13**(5), pp. 315–320.

[115] Steiger, H., Poll, A., Liepsch, D., and Reulen, H.-J., 1988. "Haemodynamic stress in terminal aneurysms". *Acta neurochirurgica,* **93**(1-2), pp. 18–23.

[116] Ugron, Á., Farinas, M.-I., Kiss, L., and Paál, G., 2012. "Unsteady velocity measurements in a realistic intracranial aneurysm model". *Experiments in fluids,* **52**(1), pp. 37–52.

[117] Deplano, V., Guivier-Curien, C., and Bertrand, E., 2016. "3d analysis of vortical structures in an abdominal aortic aneurysm by stereoscopic piv". *Experiments in Fluids,* **57**(11), p. 167.

[118] Nowak, M. A., 2011. "Primary and secondary flow structures in a model cerebral aneurysm".

[119] Sheely, M. L., 1932. "Glycerol viscosity tables". *Industrial & Engineering Chemistry,* **24**(9), pp. 1060–1064.

[120] Association, G. P., et al., 1963. *Physical properties of glycerine and its solutions*. Glycerine Producers' Association.

[121] Cheng, N.-S., 2008. "Formula for the viscosity of a glycerol- water mixture". *Industrial & engineering chemistry research,* **47**(9), pp. 3285–3288.

[122] Volk, A., and Kähler, C. J., 2018. "Density model for aqueous glycerol solutions". *Experiments in Fluids,* **59**(5), pp. 1–4.

[123] Fessler, J. R., and Eaton, J. K., 1999. "Turbulence modification by particles in a backward-facing step flow". *Journal of Fluid Mechanics,* **394**, pp. 97–117.

[124] Raffel, M., Willert, C. E., Scarano, F., Kähler, C. J., Wereley, S. T., and Kompenhans, J., 2018. *Particle image velocimetry: a practical guide*. Springer.

[125] Davis, K., Muller, J. H., Meyer, C. J., and Smit, F. E., 2018. "Evaluating the impact of air compliance chamber volumes on valve performance for three different heart valves". In 2018 3rd Biennial South African Biomedical Engineering Conference (SAIBMEC), IEEE, pp. 1–4.

[126] Hessenthaler, A., Gaddum, N., Holub, O., Sinkus, R., Röhrle, O., and Nordsletten, D., 2017. "Experiment for validation of fluid-structure interaction models and algorithms". *International journal for numerical methods in biomedical engineering,* **33**(9), p. e2848.

[127] Liou, T.-M., and Liou, S.-N., 1999. "A review on in vitro studies of hemodynamic characteristics in terminal and lateral aneurysm models.". *Proceedings of the National Science Council, Republic of China. Part B, Life sciences,* **23**(4), p. 133.

[128] Steiger, H. J., Poll, A., Liepsch, D., and Reulen, H.-J., 1987. "Basic flow structure in saccular aneurysms: a flow visualization study". *Heart and vessels,* **3**(2), pp. 55–65.

[129] White, F. M., and Corfield, I., 2006. *Viscous fluid flow*, Vol. 3. McGraw-Hill New York.

[130] Holman, R., Utturkar, Y., Mittal, R., Smith, B. L., and Cattafesta, L., 2005. "Formation criterion for synthetic jets". *AIAA journal,* **43**(10), pp. 2110–2116.

[131] Graftieaux, L., Michard, M., and Grosjean, N., 2001. "Combining piv, pod and vortex identification algorithms for the study of unsteady turbulent swirling flows". *Measurement Science and technology,* **12**(9), p. 1422.

[132] Baek, H., Jayaraman, M. V., and Karniadakis, G. E., 2009. "Wall shear stress and pressure distribution on aneurysms and infundibulae in the posterior communicating artery bifurcation". *Annals of biomedical engineering,* **37**(12), pp. 2469–2487.

[133] Rowley, C., Colonius, T., and Murray, R., 2000. "Pod based models of self-sustained oscillations in the flow past an open cavity". In 6th Aeroacoustics Conference and Exhibit, p. 1969.

[134] Chen, H., Reuss, D. L., Hung, D. L., and Sick, V., 2013. "A practical guide for using proper orthogonal decomposition in engine research". *International Journal of Engine Research,* **14**(4), pp. 307–319.

[135] Sirovich, L., 1987. "Turbulence and the dynamics of coherent structures. i. coherent structures". *Quarterly of applied mathematics,* **45**(3), pp. 561–571.

[136] Grosek, J., and Kutz, J. N., 2014. "Dynamic mode decomposition for real-time background/foreground separation in video". *arXiv preprint arXiv:1404.7592*.

[137] Wu, Z., Laurence, D., Utyuzhnikov, S., and Afgan, I., 2019. "Proper orthogonal decomposition and dynamic mode decomposition of jet in channel crossflow". *Nuclear Engineering and Design,* **344**, pp. 54–68.

[138] Tu, J. H., Rowley, C. W., Luchtenburg, D. M., Brunton, S. L., and Kutz, J. N., 2013. "On dynamic mode decomposition: Theory and applications". *arXiv preprint arXiv:1312.0041*.

[139] Kutz, J. N., Brunton, S. L., Brunton, B. W., and Proctor, J. L., 2016. *Dynamic mode decomposition: data-driven modeling of complex systems*. SIAM.

[140] Chen, K. K., Tu, J. H., and Rowley, C. W., 2012. "Variants of dynamic mode decomposition: boundary condition, koopman, and fourier analyses". *Journal of nonlinear science,* **22**(6), pp. 887–915.

[141] Wynn, A., Pearson, D., Ganapathisubramani, B., and Goulart, P. J., 2013. "Optimal mode decomposition for unsteady flows". *Journal of Fluid Mechanics,* **733**, pp. 473–503.

[142] Jovanović, M. R., Schmid, P. J., and Nichols, J. W., 2014. "Sparsity-promoting dynamic mode decomposition". *Physics of Fluids,* **26**(2), p. 024103.

[143] Proctor, J. L., Brunton, S. L., and Kutz, J. N., 2016. "Dynamic mode decomposition with control". *SIAM Journal on Applied Dynamical Systems,* **15**(1), pp. 142–161.

[144] Boyd, S., Boyd, S. P., and Vandenberghe, L., 2004. *Convex optimization.* Cambridge university press.

[145] O'Brien, V., 1972. "Closed streamlines associated with channel flow over a cavity". *The Physics of Fluids,* **15**(12), pp. 2089–2097.

[146] Cebral, J., Hendrickson, S., and Putman, C., 2009. "Hemodynamics in a lethal basilar artery aneurysm just before its rupture". *American Journal of Neuroradiology,* **30**(1), pp. 95–98.

[147] Sforza, D., Putman, C., Scrivano, E., Lylyk, P., and Cebral, J., 2010. "Blood-flow characteristics in a terminal basilar tip aneurysm prior to its fatal rupture". *American journal of neuroradiology,* **31**(6), pp. 1127–1131.

[148] Aenis, M., Stancampiano, A., Wakhloo, A., and Lieber, B., 1997. "Modeling of flow in a straight stented and nonstented side wall aneurysm model".

[149] Cantón, G., Levy, D. I., Lasheras, J. C., and Nelson, P. K., 2005. "Flow changes caused by the sequential placement of stents across the neck of sidewall cerebral aneurysms". *Journal of neurosurgery,* **103**(5), pp. 891–902.

[150] Baharoglu, M. I., Schirmer, C. M., Hoit, D. A., Gao, B.-L., and Malek, A. M., 2010. "Aneurysm inflow-angle as a discriminant for rupture in sidewall cerebral aneurysms: morphometric and computational fluid dynamic analysis". *Stroke,* **41**(7), pp. 1423–1430.

Appendix A: Impact of different DMD parameters

Impact of DMD amplitudes

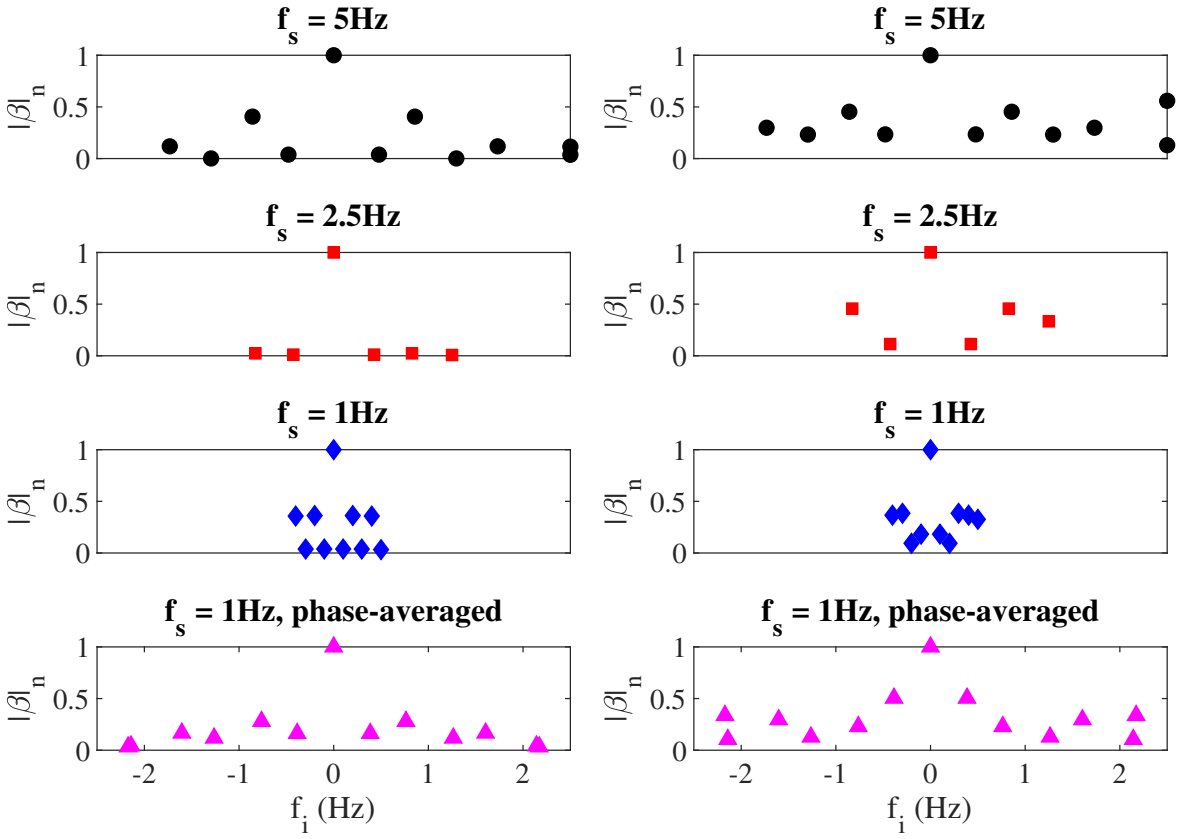

(a) (b)

Figure A1: DMD results for $Re_p = 50$, $\alpha = 2$ using original snapshot and optimal vector approach. (a) original snapshot, and (b) optimal vector amplitude.

Impact of number of cycles

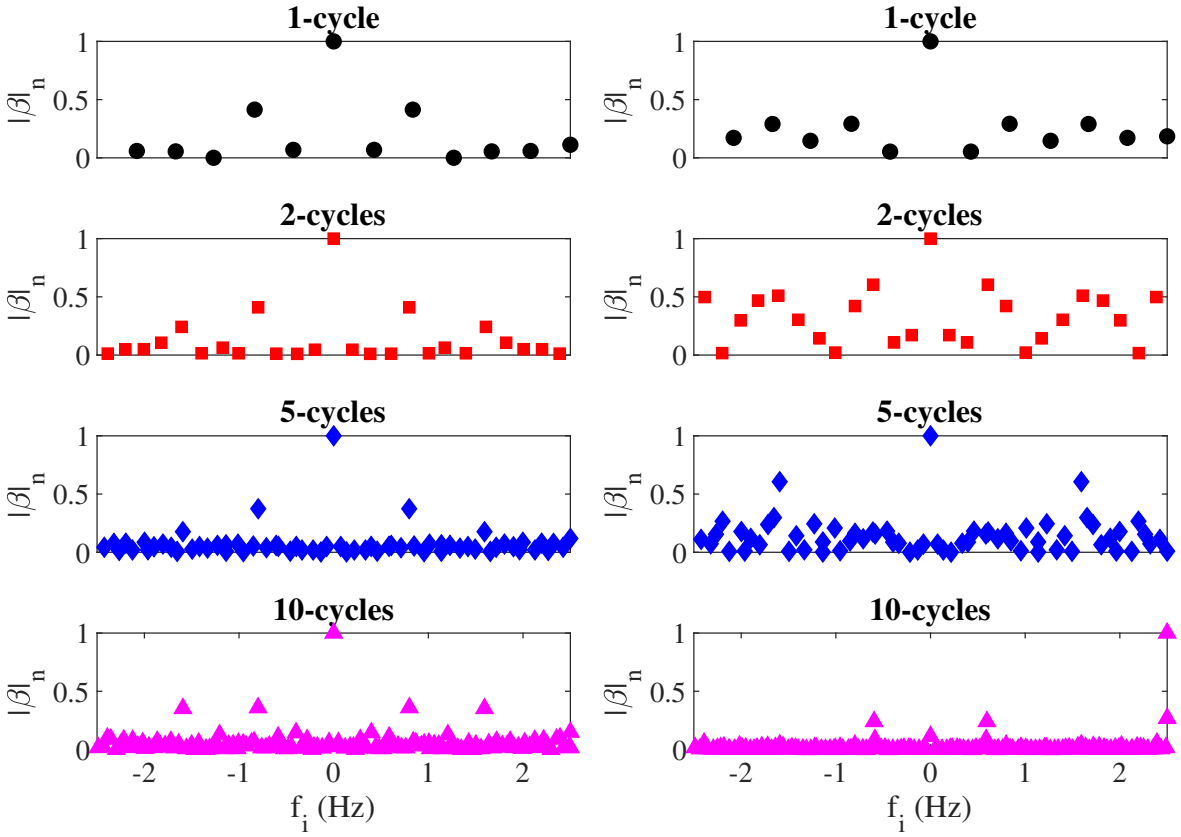

Figure A2: DMD results for $Re_p = 50$, $\alpha = 2$ using original snapshot and optimal vector approach. (a) original snapshot, and (b) optimal vector amplitude.

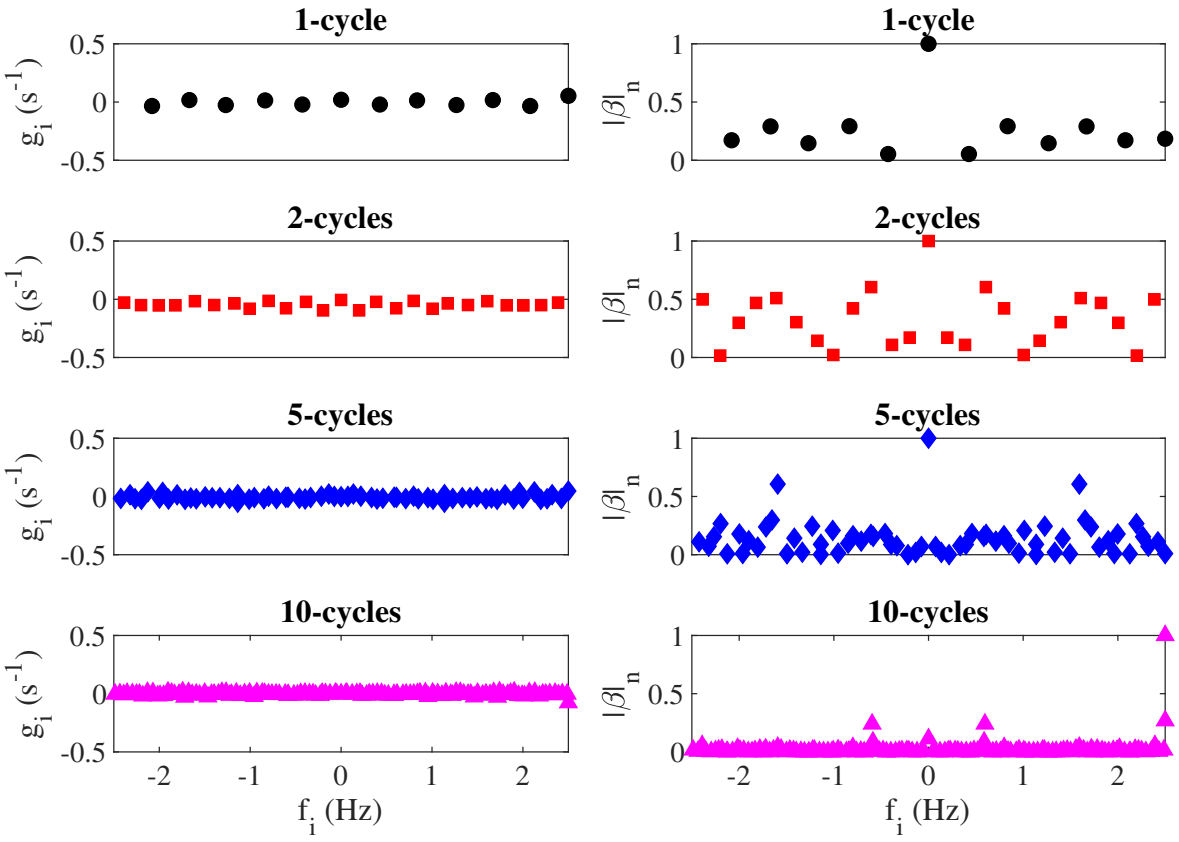

(a) (b)

Figure A3: DMD frequencies and growth/decay rates for $Re_p = 50$, $\alpha = 2$ using different cycles. (a) DMD growth rate vs. frequency, and (b) amplitude vs. frequency.

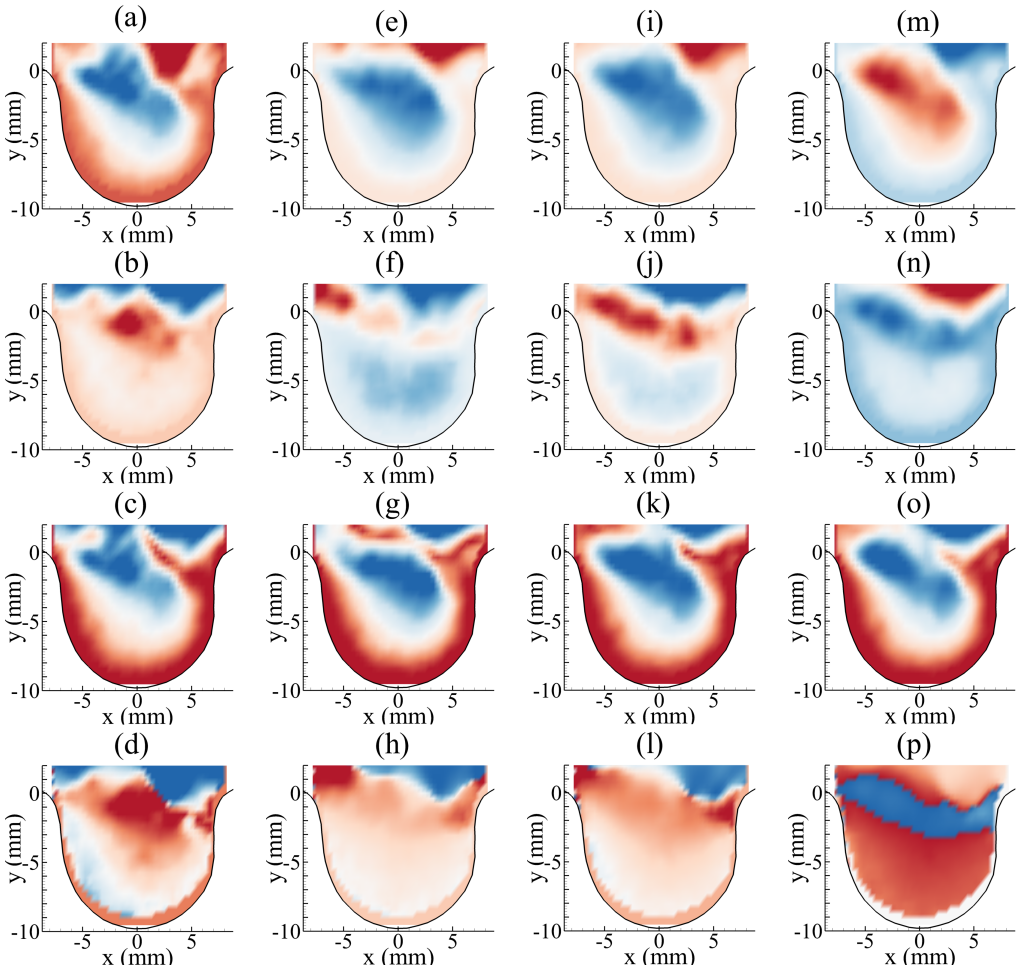

Figure A4: DMD modes for $f_s = 5Hz$ using the streamwise component of velocity for different cycles. (a)-(d) $0.8Hz$ (1-cycle), (e)-(h) $0.8Hz$ (2-cycle), (i)-(l) $0.8Hz$ (5-cycle), and (m)-(p) $0.8Hz$ (10-cycle).(a),(e),(i),(m) real components. (b),(f),(j),(n) imaginary components. (c),(g),(k),(o) magnitude. (d),(h),(l),(p) phase.

Impact of projected and exact DMD

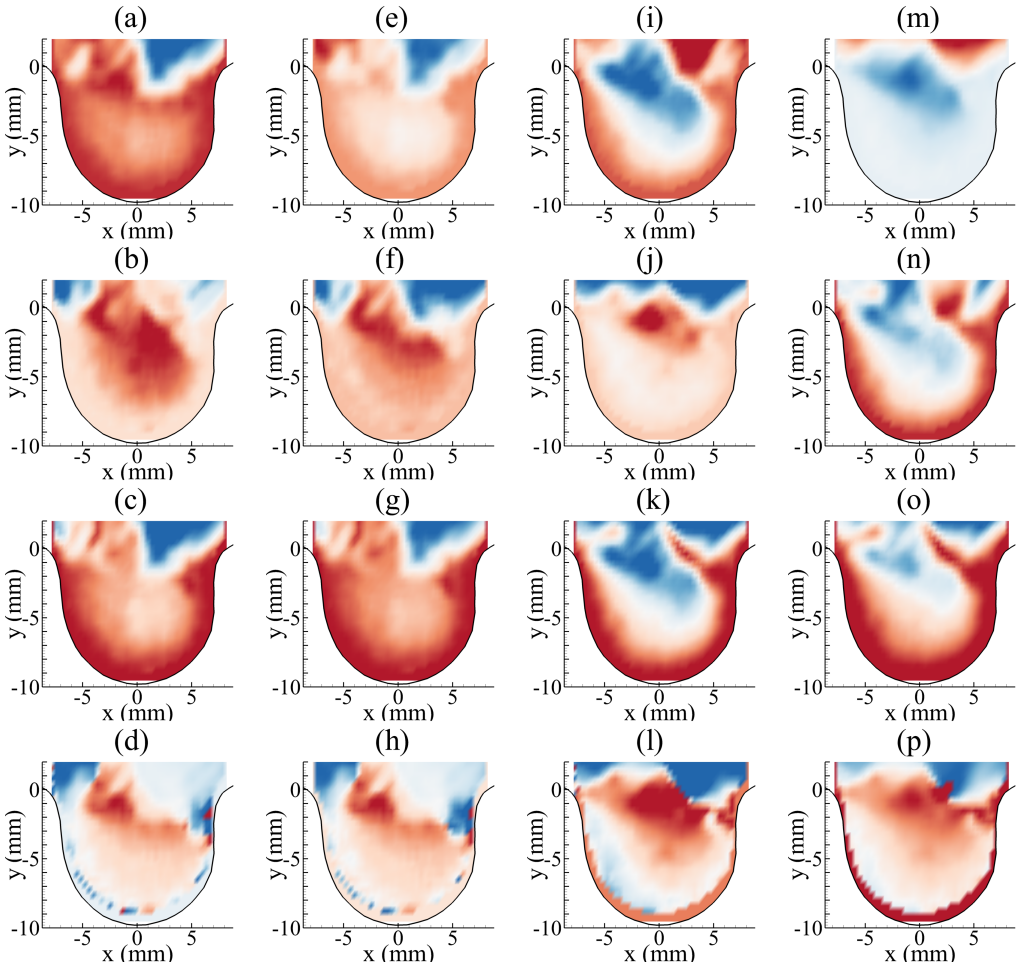

Figure A5: DMD modes for $0.4Hz$ and $0.8Hz$ using the streamwise component of velocity. (a)-(d) $0.4Hz$ (Projected), (e)-(h) $0.4Hz$ (Exact), (i)-(l) $0.8Hz$ (Projected), and (m)-(p) $0.8Hz$ (Exact). (a),(e),(i),(m) real components. (b),(f),(j),(n) imaginary components. (c),(g),(k),(o) magnitude. (d),(h),(l),(p) phase.

DMD mode reconstructions for $BF = 1.0$

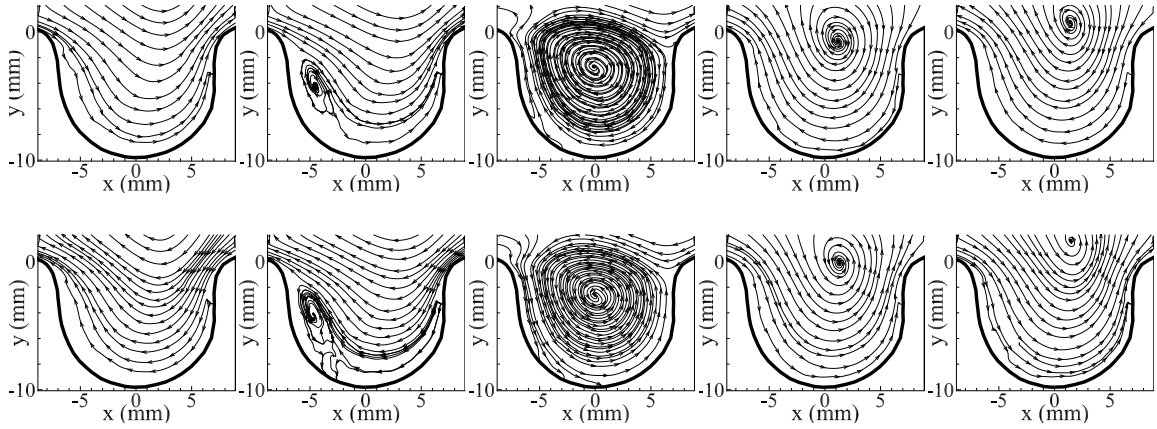

Figure A6: DMD mode for $\alpha = 2$, $Re_p = 50$ constructed for 0.4 Hz for a complete cycle. The other half of the cycle repeats in the same fashion with opposite streamlines.

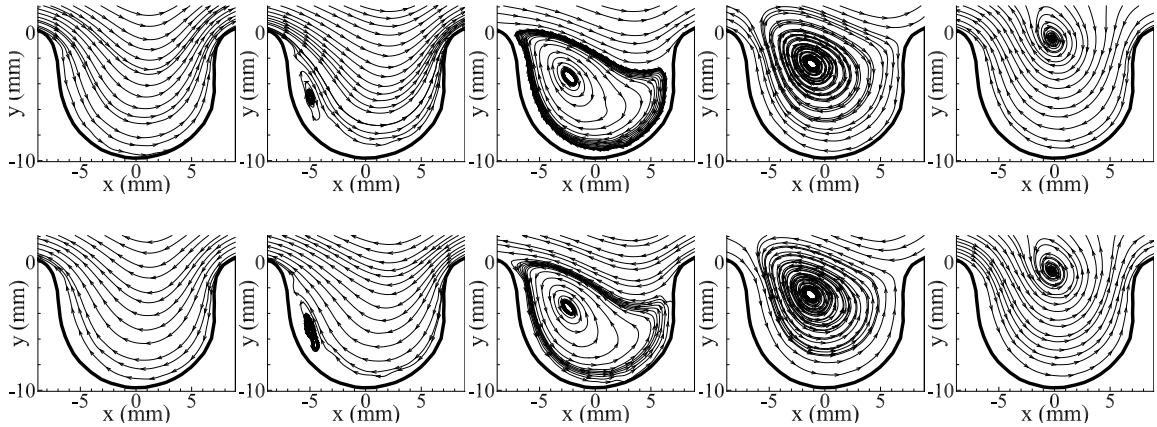

Figure A7: DMD mode for $\alpha = 2$, $Re_p = 50$ constructed for 0.8 Hz for a complete cycle. The other half of the cycle repeats in the same fashion with opposite streamlines.

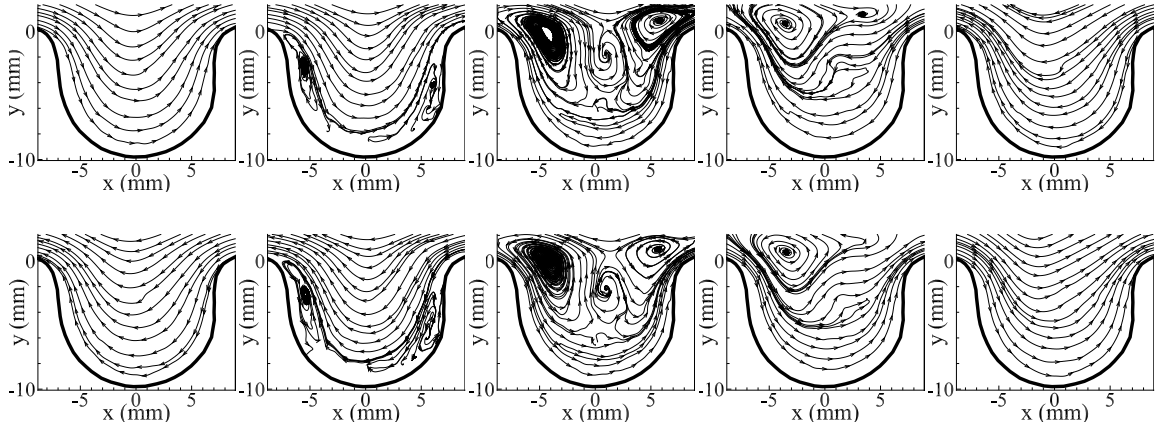

Figure A8: DMD mode for $\alpha = 2$, $Re_p = 50$ constructed for 1.6 Hz for a complete cycle. The other half of the cycle repeats in the same fashion with opposite streamlines.

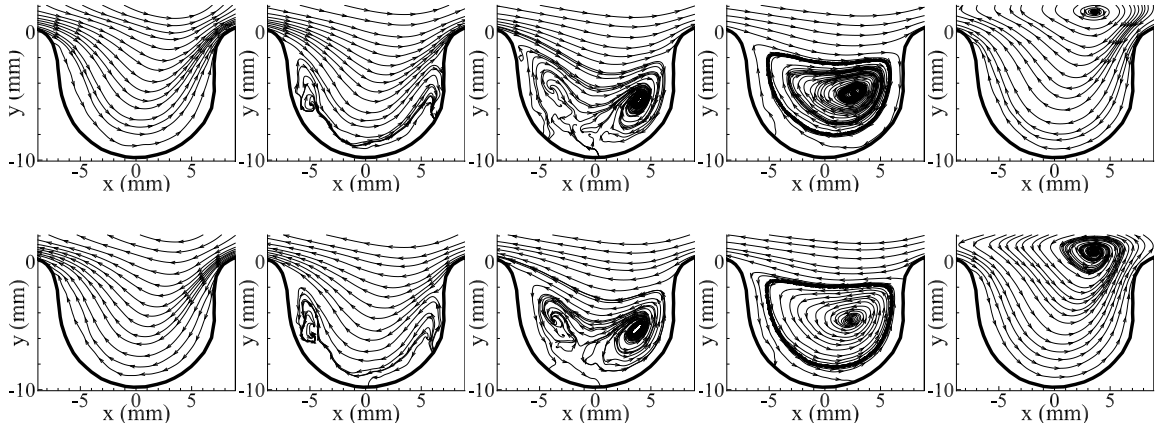

Figure A9: DMD mode for $\alpha = 2$, $Re_p = 270$ constructed for 0.4 Hz for a complete cycle. The other half of the cycle repeats in the same fashion with opposite streamlines.

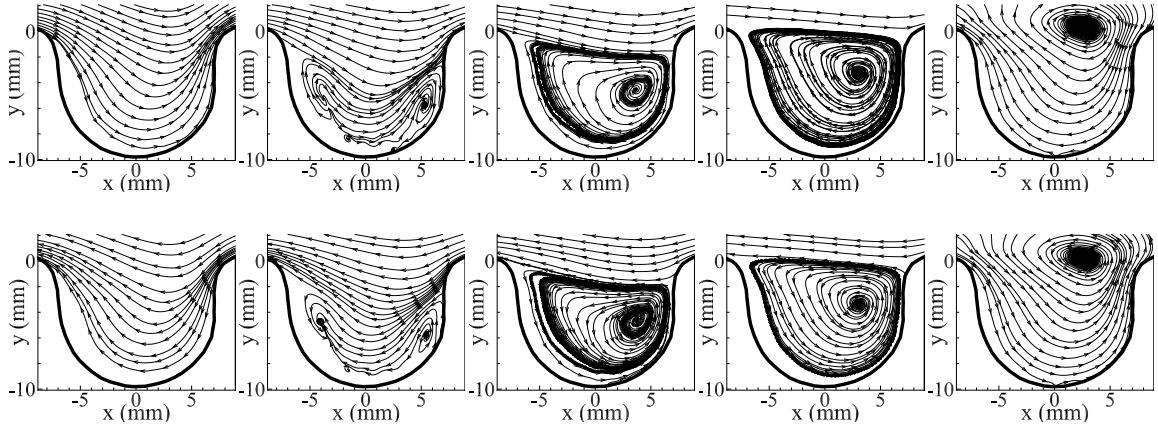

Figure A10: DMD mode for $\alpha = 2$, $Re_p = 270$ constructed for 0.8 Hz for a complete cycle. The other half of the cycle repeats in the same fashion with opposite streamlines.

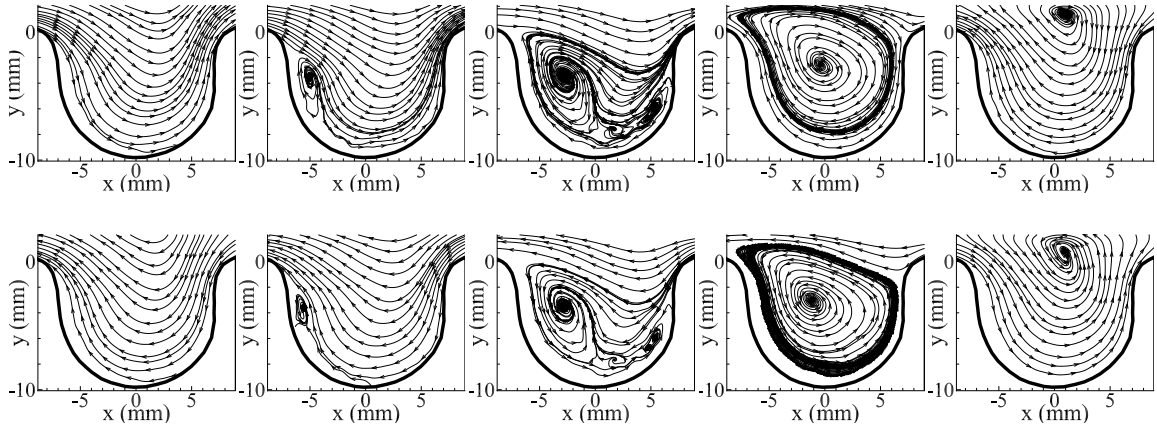

Figure A11: DMD mode for $\alpha = 2$, $Re_p = 270$ constructed for 1.6 Hz for a complete cycle. The other half of the cycle repeats in the same fashion with opposite streamlines.

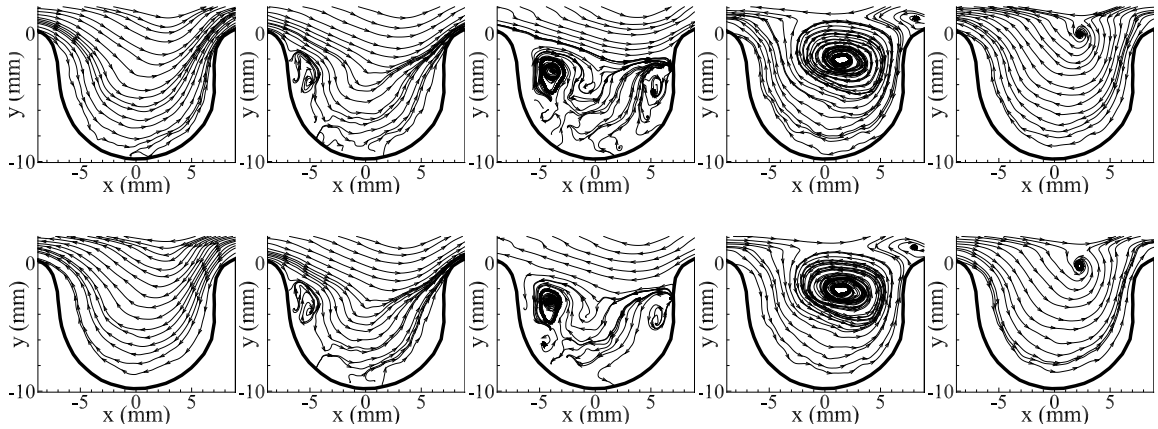

Figure A12: DMD mode for $\alpha = 2$, $Re_p = 270$ constructed for 2.0 Hz for a complete cycle. The other half of the cycle repeats in the same fashion with opposite streamlines.

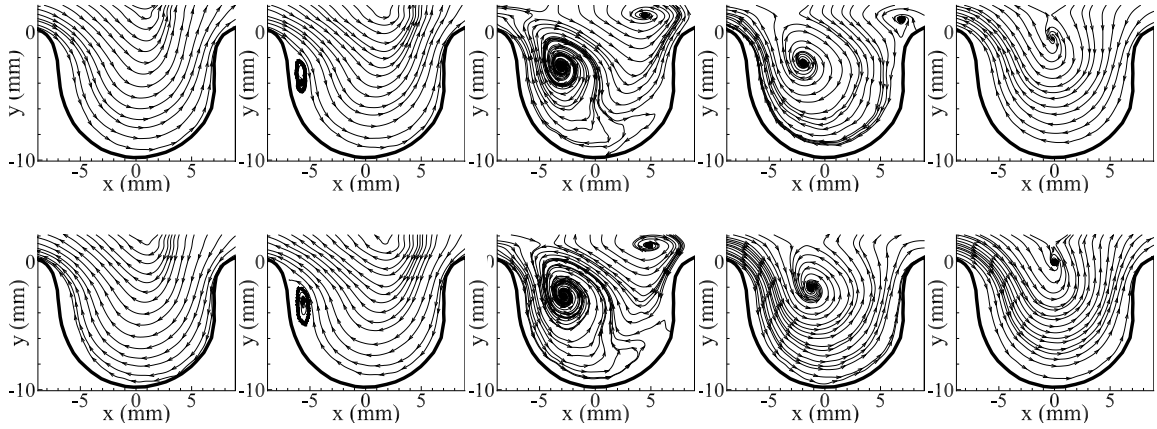

Figure A13: DMD mode for $\alpha = 2$, $Re_p = 270$ constructed for 2.4 Hz for a complete cycle. The other half of the cycle repeats in the same fashion with opposite streamlines.

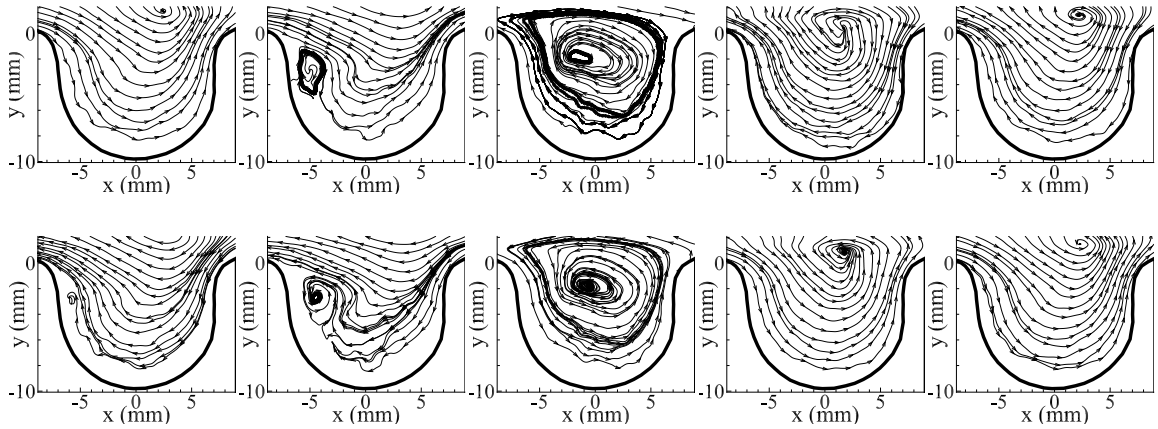

Figure A14: DMD mode for $\alpha = 2$, $Re_p = 270$ constructed for 2.8 Hz for a complete cycle. The other half of the cycle repeats in the same fashion with opposite streamlines.

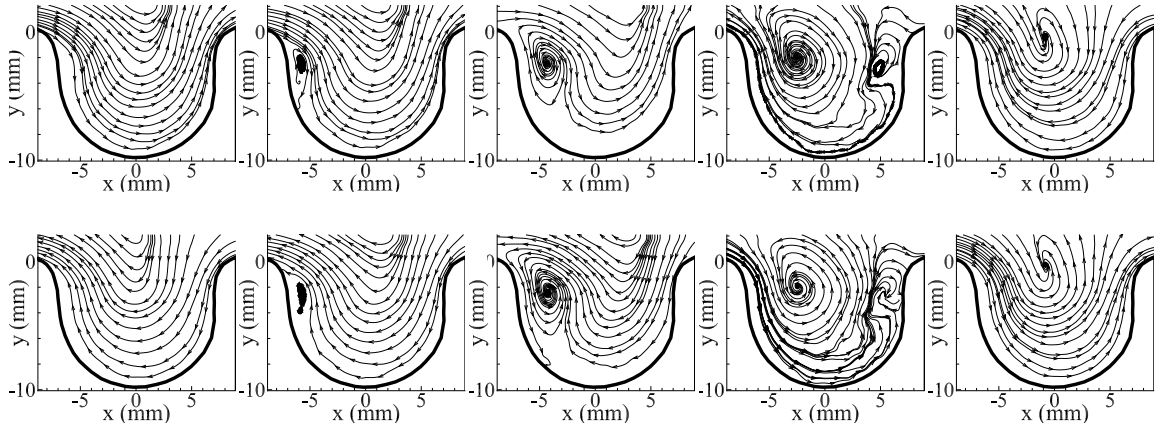

Figure A15: DMD mode for $\alpha = 2$, $Re_p = 270$ constructed for 3.2 Hz for a complete cycle. The other half of the cycle repeats in the same fashion with opposite streamlines.

Appendix B: POD results for $BF = 1.6$

POD modes for $BF = 1.6$

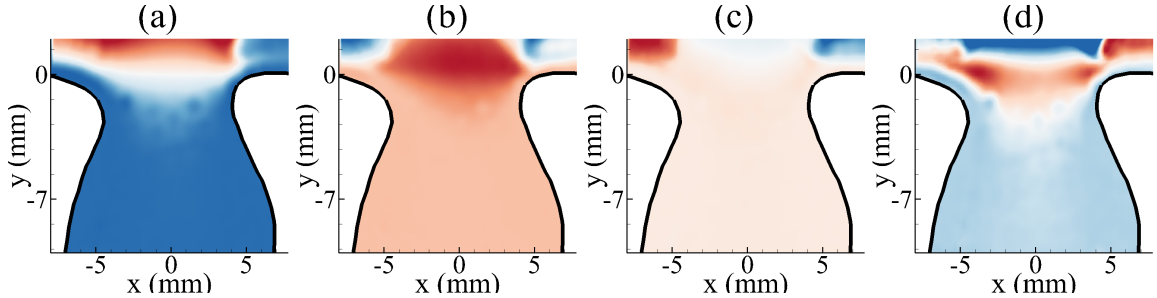

Figure B1: Streamwise POD modes for $Re_p = 50$ and $\alpha = 2$. (a) ψ^1_{uu}, (b) ψ^2_{uu}, (c) ψ^3_{uu}, and (d) ψ^4_{uu}.

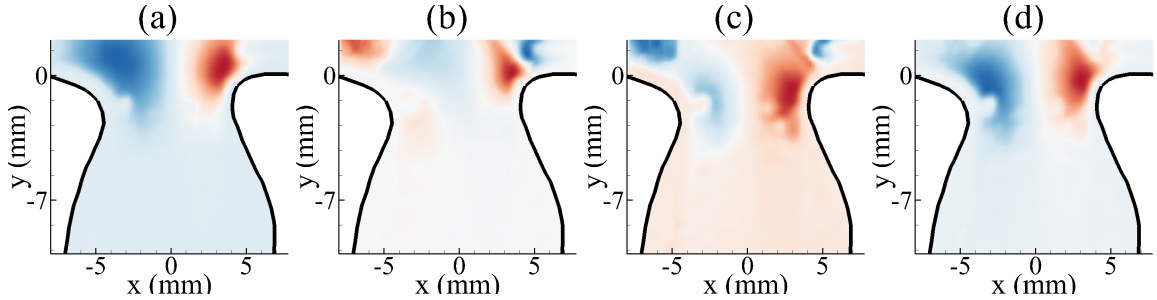

Figure B2: Transverse POD modes for $Re_p = 50$ and $\alpha = 2$. (a) ψ^1_{vv}, (b) ψ^2_{vv}, (c) ψ^3_{vv}, and (d) ψ^4_{vv}.

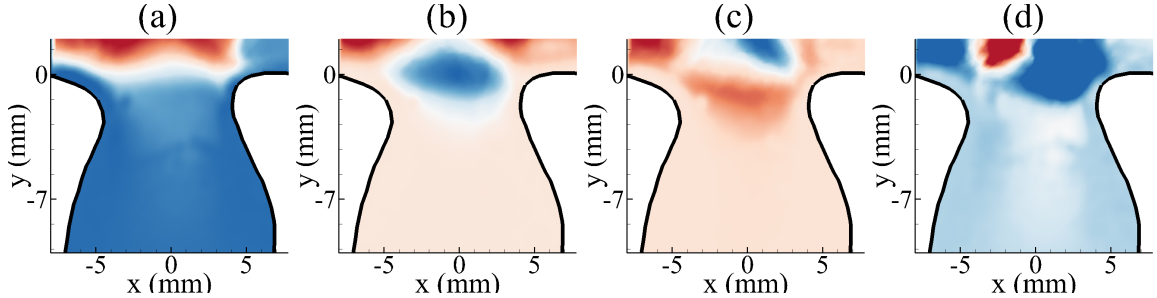

Figure B3: Streamwise POD modes for $Re_p = 270$ and $\alpha = 2$. (a) ψ^1_{uu}, (b) ψ^2_{uu}, (c) ψ^3_{uu}, and (d) ψ^4_{uu}.

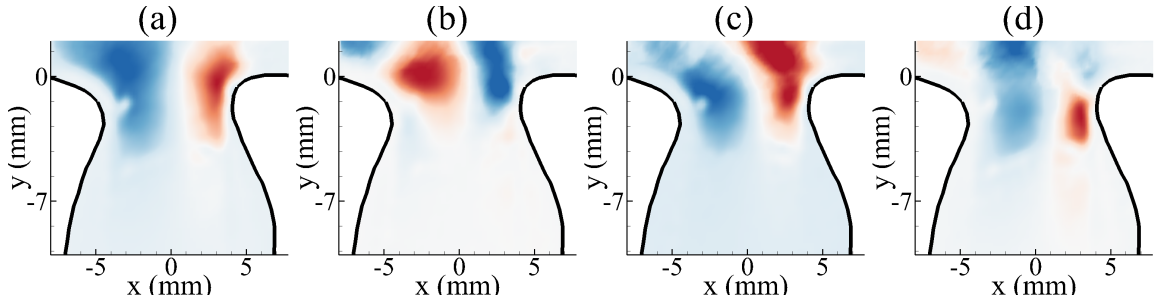

Figure B4: Transverse POD modes for $Re_p = 270$ and $\alpha = 2$. (a) ψ^1_{vv}, (b) ψ^2_{vv}, (c) ψ^3_{vv}, and (d) ψ^4_{vv}.

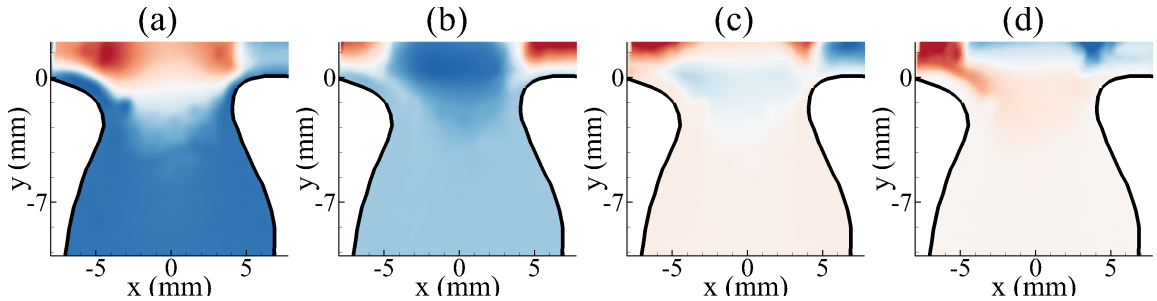

Figure B5: Streamwise POD modes for $Re_p = 50$ and $\alpha = 5$. (a) ψ^1_{uu}, (b) ψ^2_{uu}, (c) ψ^3_{uu}, and (d) ψ^4_{uu}.

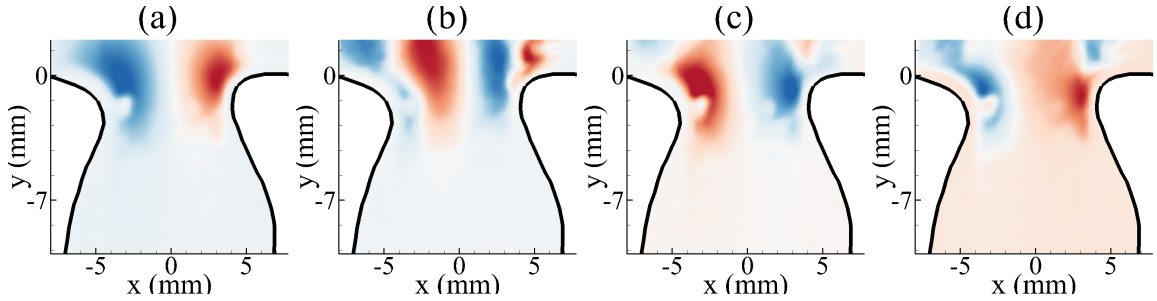

Figure B6: Transverse POD modes for $Re_p = 50$ and $\alpha = 5$. (a) ψ^1_{vv}, (b) ψ^2_{vv}, (c) ψ^3_{vv}, and (d) ψ^4_{vv}.

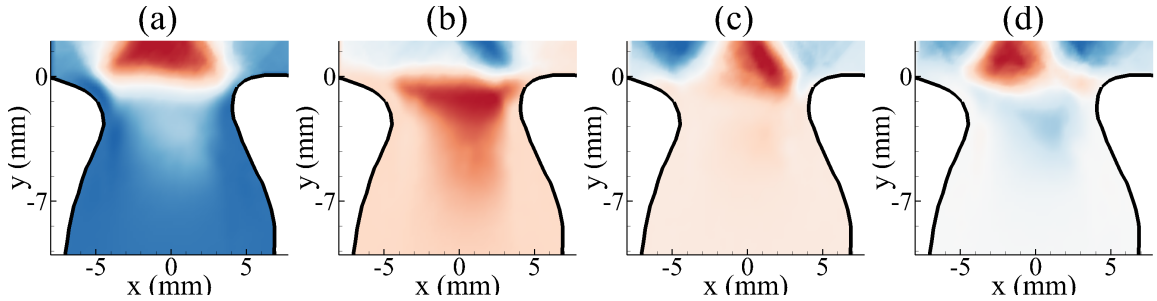

Figure B7: Streamwise POD modes for $Re_p = 270$ and $\alpha = 5$. (a) ψ^1_{uu}, (b) ψ^2_{uu}, (c) ψ^3_{uu}, and (d) ψ^4_{uu}.

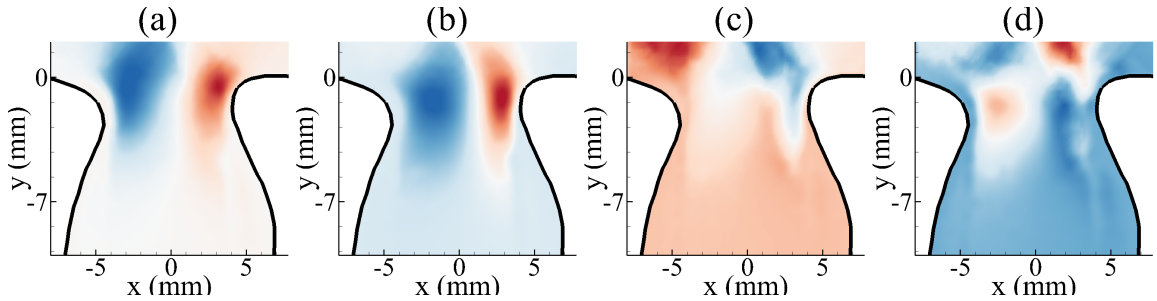

Figure B8: Transverse POD modes for $Re_p = 270$ and $\alpha = 5$. (a) ψ^1_{vv}, (b) ψ^2_{vv}, (c) ψ^3_{vv}, and (d) ψ^4_{vv}

POD low-order reconstruction for $BF = 1.6$

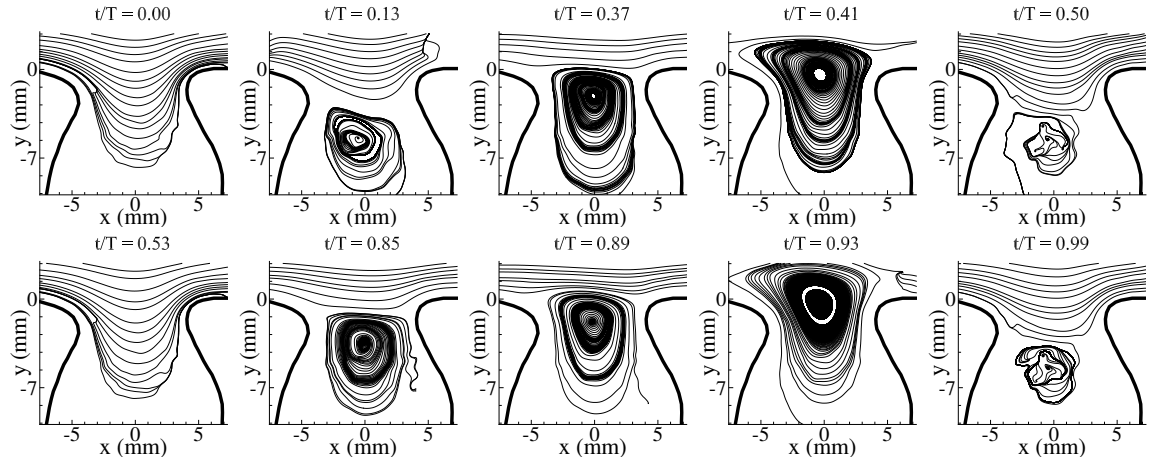

Figure B9: POD low-order reconstruction for $Re_p = 50$, $\alpha = 2$, and $BF = 1.6$.

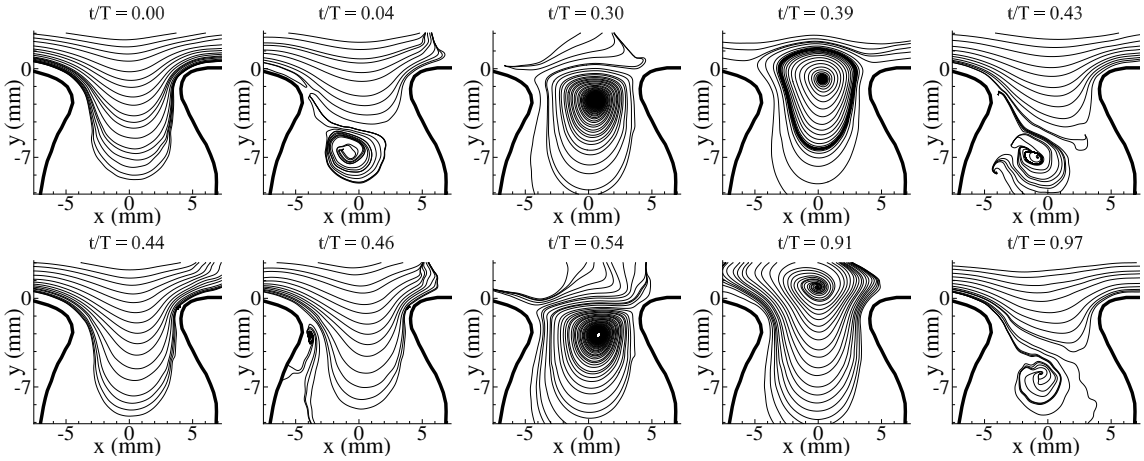

Figure B10: POD low-order reconstruction for $Re_p = 270$, $\alpha = 2$, and $BF = 1.6$.

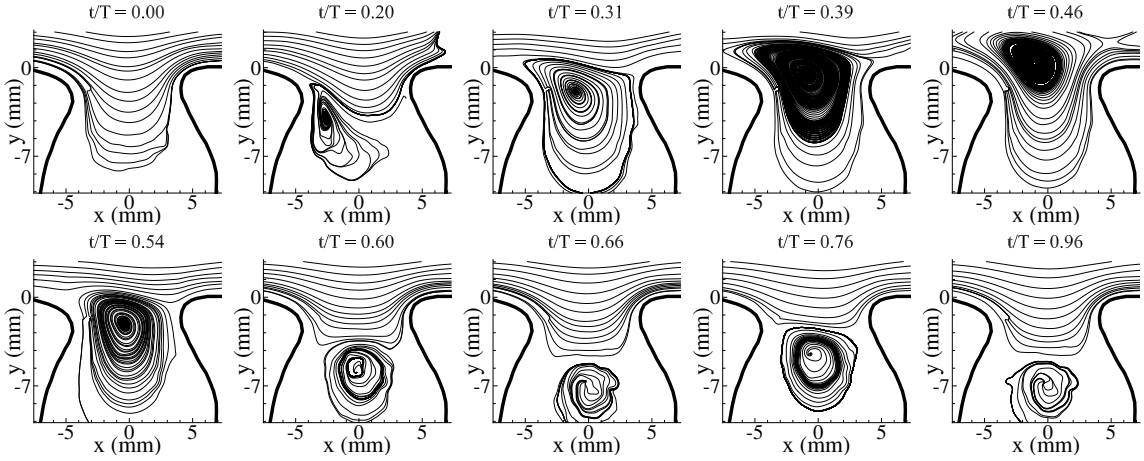

Figure B11: POD low-order reconstruction for $Re_p = 50$, $\alpha = 5$, and $BF = 1.6$.

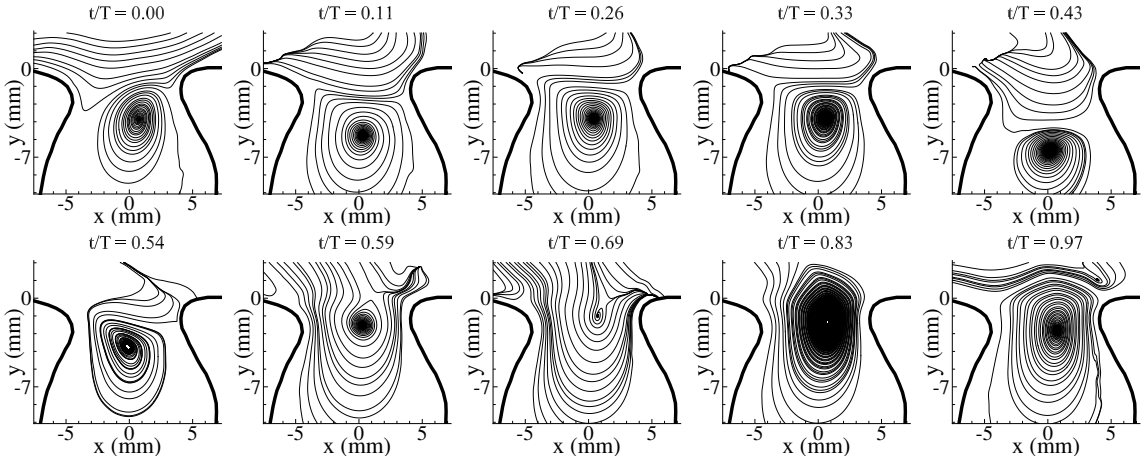

Figure B12: POD low-order reconstruction for $Re_p = 270$, $\alpha = 5$, and $BF = 1.6$.

Appendix C: DMD results for $BF = 1.6$

DMD frequency and amplitude

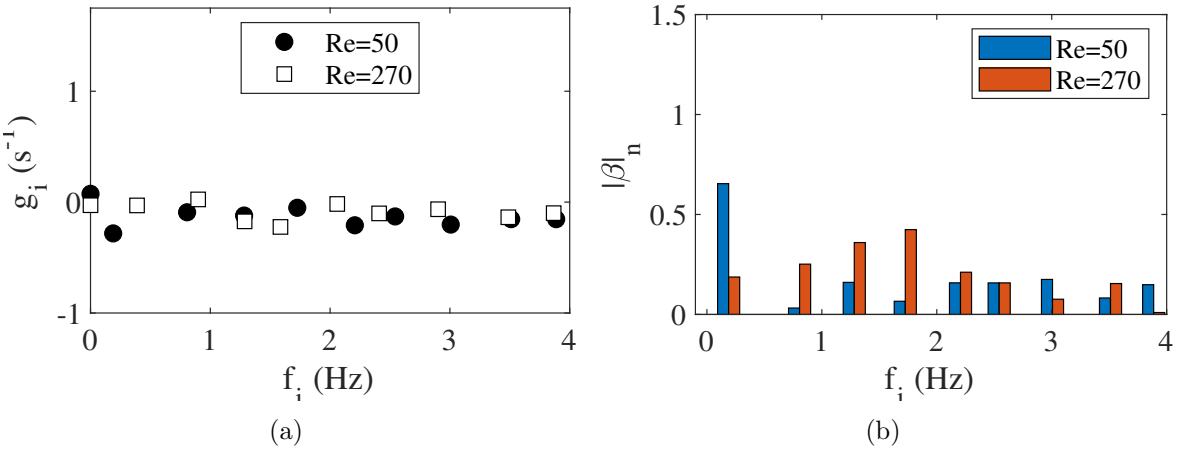

(a) (b)

Figure C1: DMD frequency, growth rates and amplitudes for $\alpha = 2$ at different Re_p. (a) DMD growth rate vs. frequency, and (b) DMD amplitude vs. frequency.

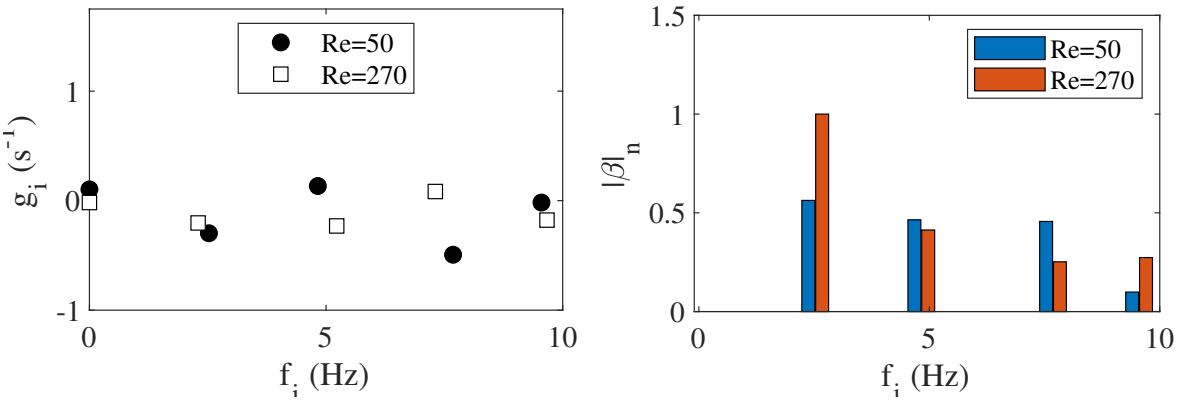

(a) (b)

Figure C2: DMD frequency, growth rates and amplitudes for $\alpha = 5$ at different Re_p.(a) DMD growth rate vs. frequency, and (b) DMD amplitude vs. frequency.

DMD modes

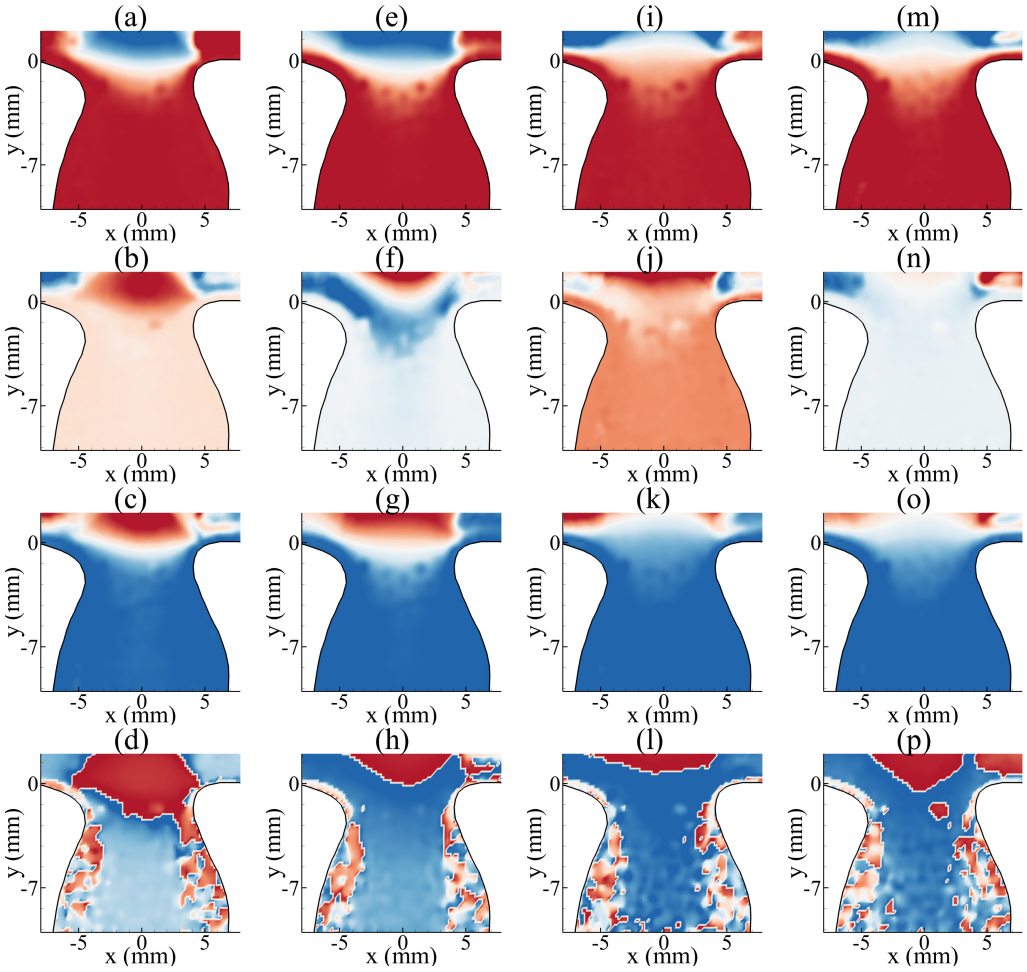

Figure C3: DMD modes for $Re_p = 50$, $\alpha = 2$ using the streamwise component of velocity. (a)-(e) $0.4Hz$ (Mode 2), (e)-(h) $0.8Hz$ (Mode 4), (i)-(l) $1.2Hz$ (Mode 6), (m)-(p) $1.6Hz$ (Mode 8). (a),(e),(i),(m) real components. (b),(f),(j),(n) imaginary components. (c),(g),(k),(o) magnitude. (d),(h),(l),(p) phase.

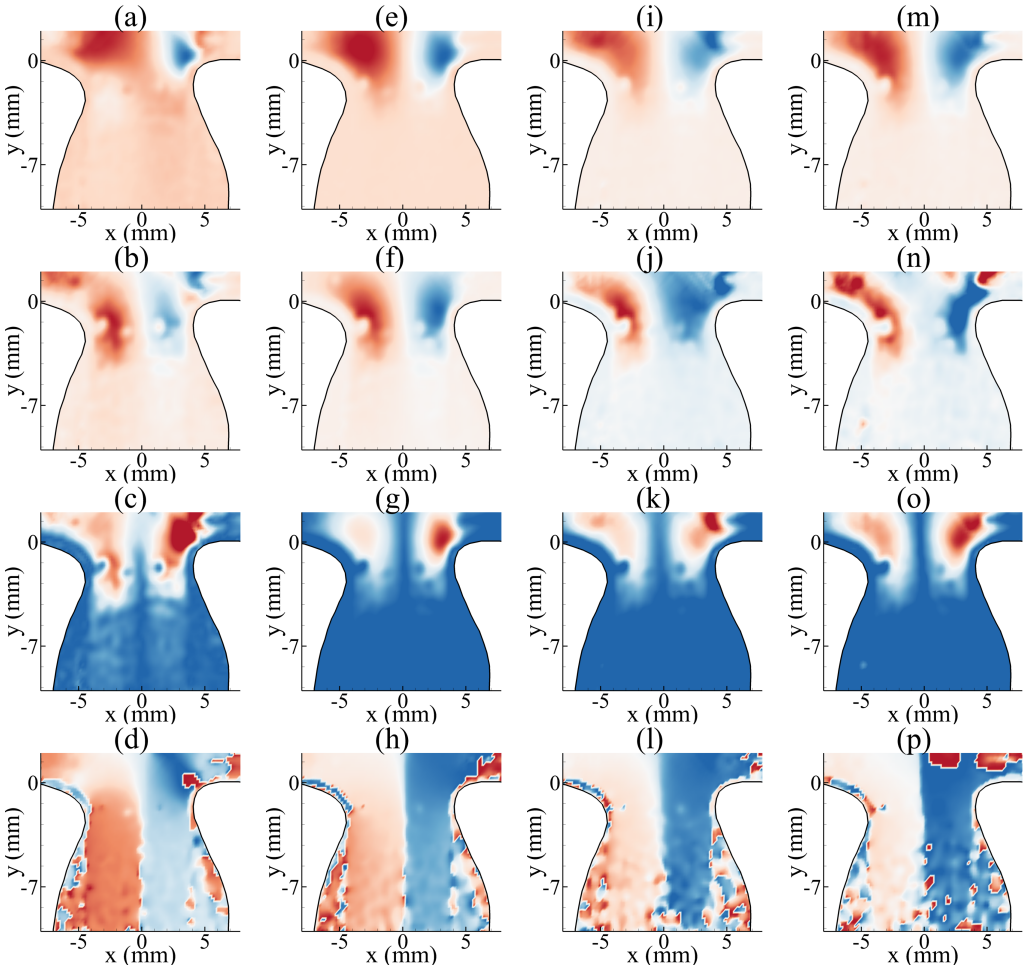

Figure C4: DMD modes for $Re_p = 50$, $\alpha = 2$ using the transverse component of velocity. (a)-(e) $0.4Hz$ (Mode 2), (e)-(h) $0.8Hz$ (Mode 4), (i)-(l) $1.2Hz$ (Mode 6), (m)-(p) $1.6Hz$ (Mode 8). (a),(e),(i),(m) real components. (b),(f),(j),(n) imaginary components. (c),(g),(k),(o) magnitude. (d),(h),(l),(p) phase.

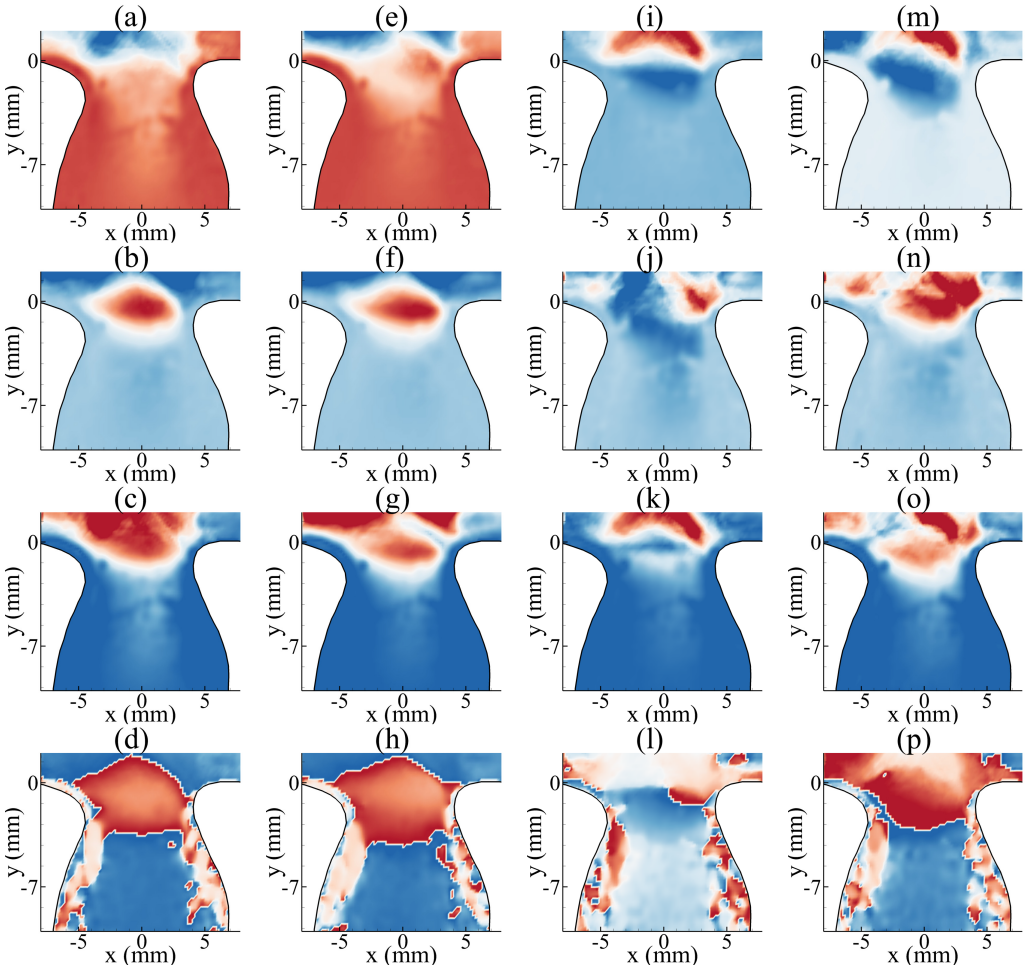

Figure C5: DMD modes for $Re_p = 270$, $\alpha = 2$ using the streamwise component of velocity. (a)-(e) $0.4Hz$ (Mode 2), (e)-(h) $0.8Hz$ (Mode 4), (i)-(l) $1.2Hz$ (Mode 6), (m)-(p) $1.6Hz$ (Mode 8). (a),(e),(i),(m) real components. (b),(f),(j),(n) imaginary components. (c),(g),(k),(o) magnitude. (d),(h),(l),(p) phase.

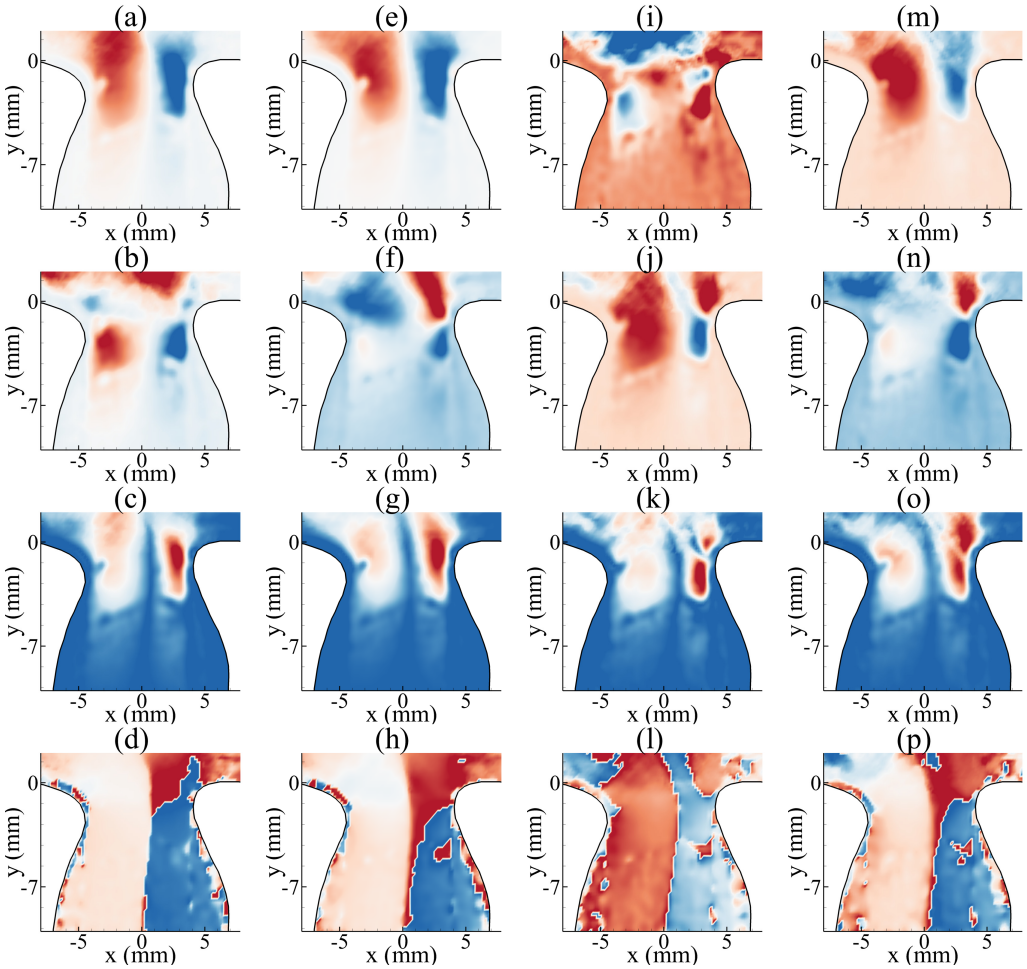

Figure C6: DMD modes for $Re_p = 270$, $\alpha = 2$ using the transverse component of velocity. (a)-(e) $0.4Hz$ (Mode 2), (e)-(h) $0.8Hz$ (Mode 4), (i)-(l) $1.2Hz$ (Mode 6), (m)-(p) $1.6Hz$ (Mode 8). (a),(e),(i),(m) real components. (b),(f),(j),(n) imaginary components. (c),(g),(k),(o) magnitude. (d),(h),(l),(p) phase.

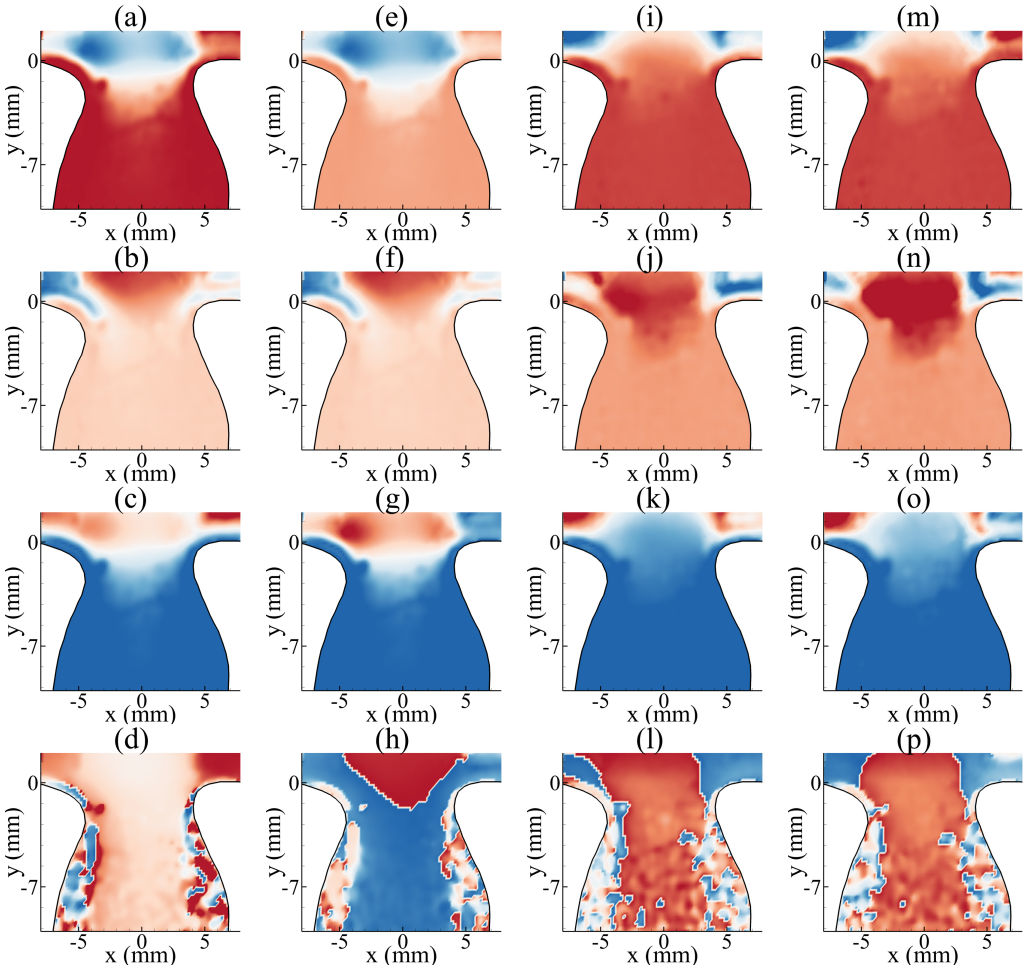

Figure C7: DMD modes for $Re_p = 50$, $\alpha = 5$ using the streamwise component of velocity. (a)-(d) $2.4Hz$ (Mode 2), (e)-(h) $4.8Hz$ (Mode 4), (i)-(l) $7.2Hz$ (Mode 6), and (m)-(p) $9.6Hz$ (Mode 8). (a),(e),(i),(m) real components. (b),(f),(j),(n) imaginary components. (c),(g),(k),(o) magnitude. (d),(h),(l),(p) phase.

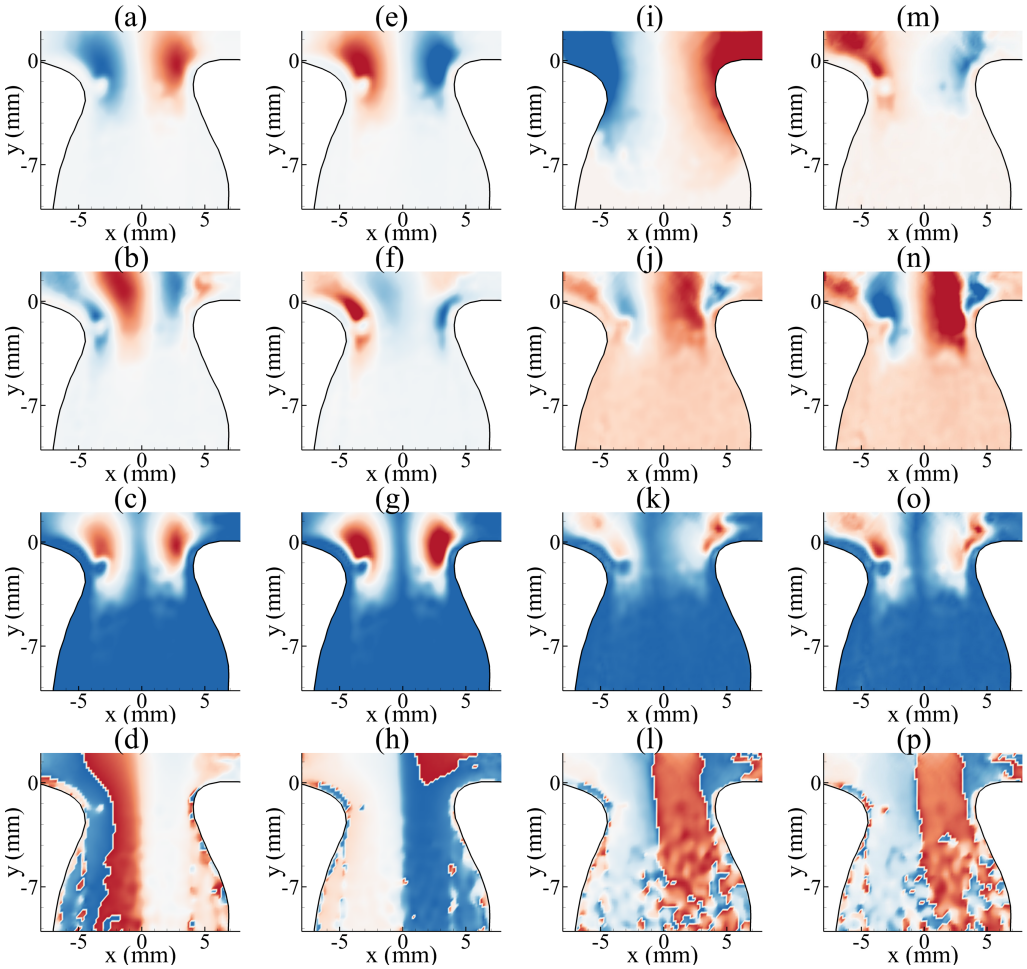

Figure C8: DMD modes for $Re_p = 50$, $\alpha = 5$ using the transverse component of velocity. (a)-(d) $2.4Hz$ (Mode 2), (e)-(h) $4.8Hz$ (Mode 4), (i)-(l) $7.2Hz$ (Mode 6), and (m)-(p) $9.6Hz$ (Mode 8). (a),(e),(i),(m) real components. (b),(f),(j),(n) imaginary components. (c),(g),(k),(o) magnitude. (d),(h),(l),(p) phase.

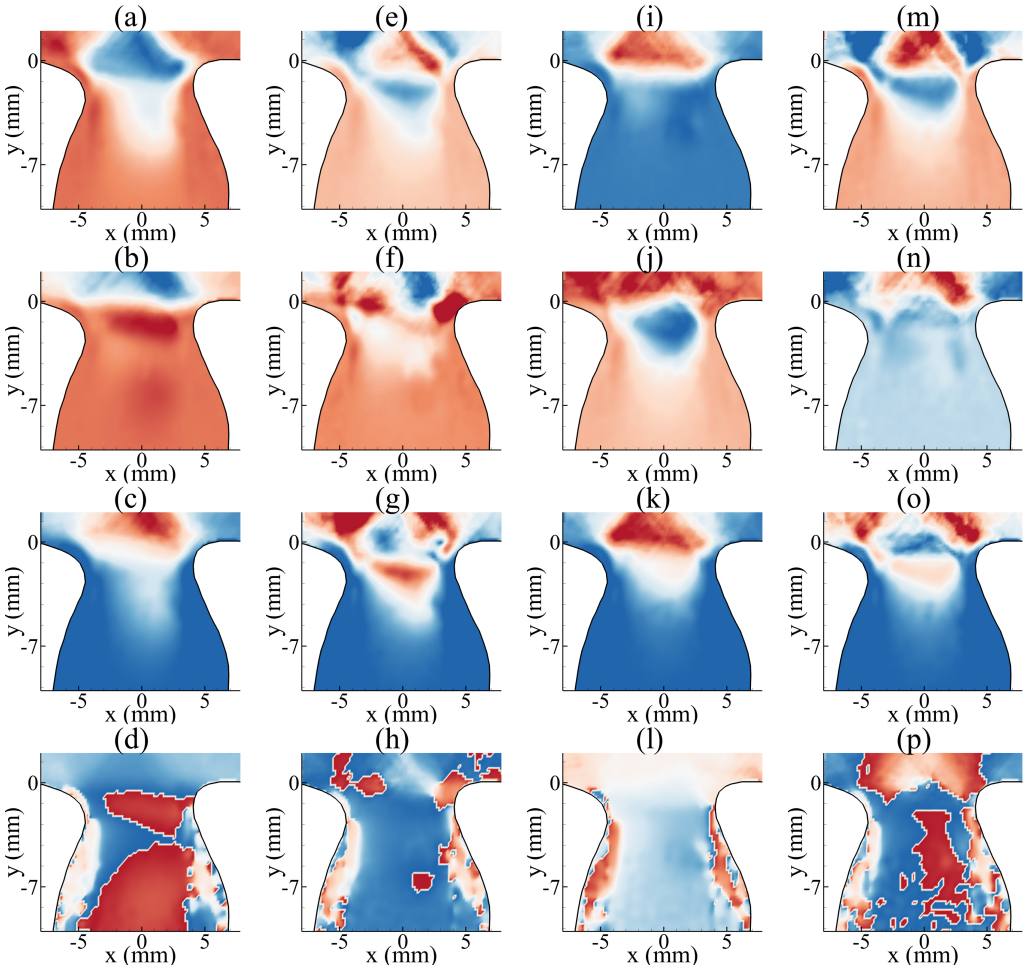

Figure C9: DMD modes for $Re_p = 270$, $\alpha = 5$ using the streamwise component of velocity. (a)-(d) $2.4Hz$ (Mode 2), (e)-(h) $4.8Hz$ (Mode 4), (i)-(l) $7.2Hz$ (Mode 6), and (m)-(p) $9.6Hz$ (Mode 8). (a),(e),(i),(m) real components. (b),(f),(j),(n) imaginary components. (c),(g),(k),(o) magnitude. (d),(h),(l),(p) phase.

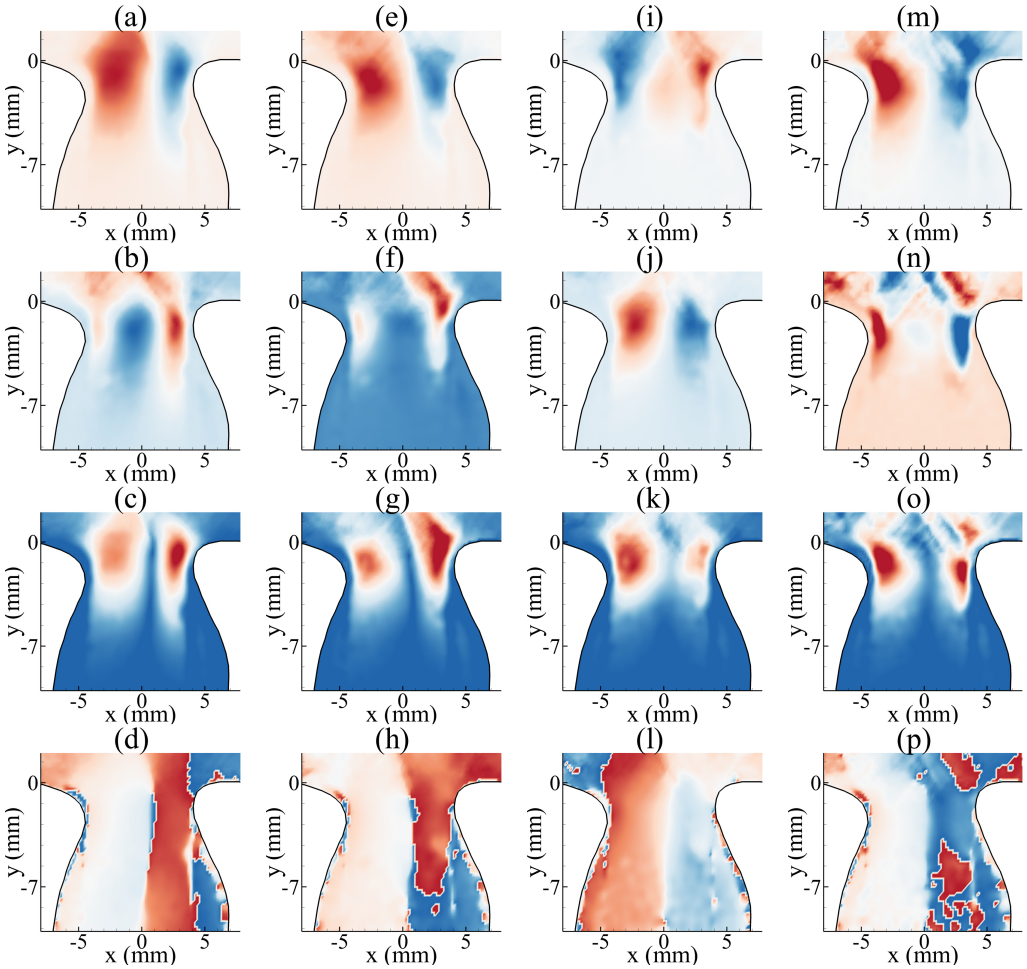

Figure C10: DMD modes for $Re_p = 270$, $\alpha = 5$ using the transverse component of velocity. (a)-(d) $2.4Hz$ (Mode 2), (e)-(h) $4.8Hz$ (Mode 4), (i)-(l) $7.2Hz$ (Mode 6), and (m)-(p) $9.6Hz$ (Mode 8). (a),(e),(i),(m) real components. (b),(f),(j),(n) imaginary components. (c),(g),(k),(o) magnitude. (d),(h),(l),(p) phase.

DMD mode reconstruction for $BF = 1.6$

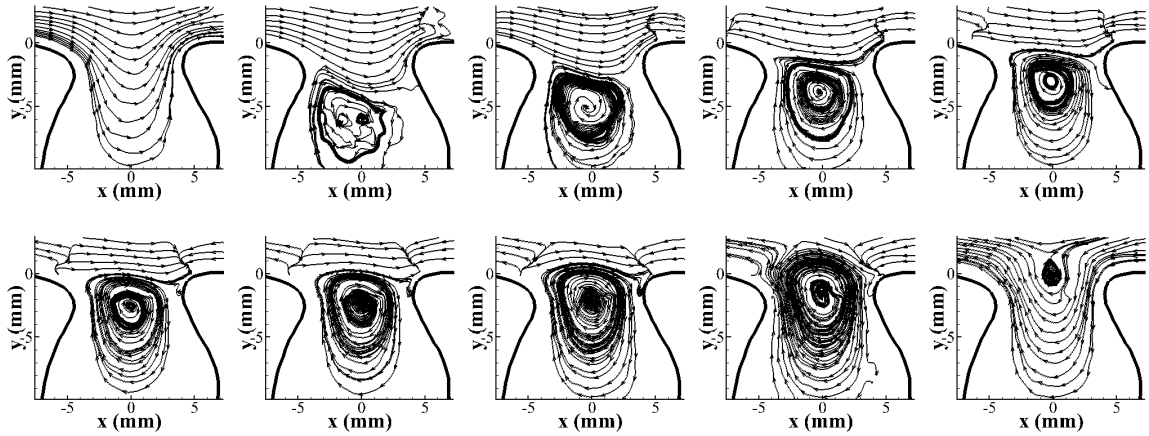

Figure C11: DMD mode for $\alpha = 2$, $Re_p = 50$ constructed for 0.4 Hz. Top row: flow evolution for half-cycle. Bottom row: flow evolution for second half-cycle.

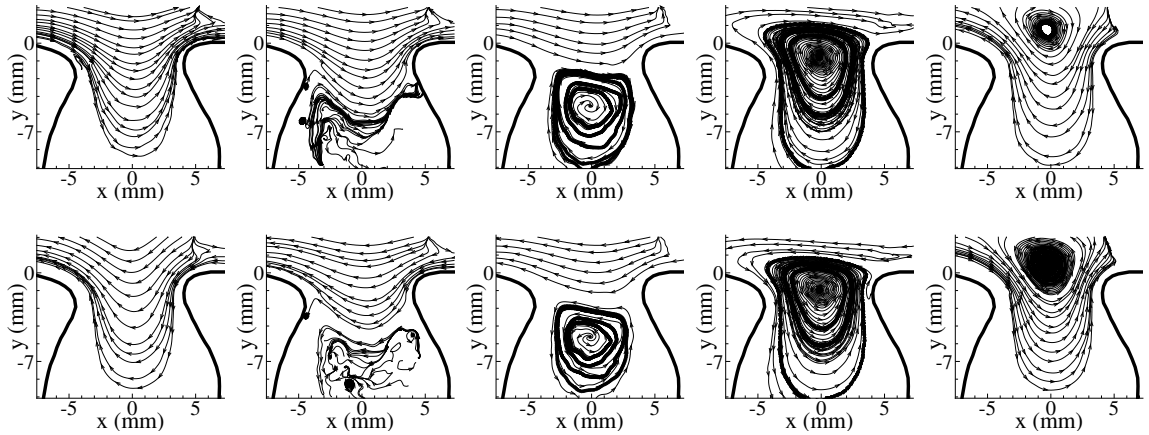

Figure C12: DMD mode for $\alpha = 2$, $Re_p = 50$ constructed for 0.8 Hz. Top row: flow evolution for half-cycle. Bottom row: flow evolution for second half-cycle.

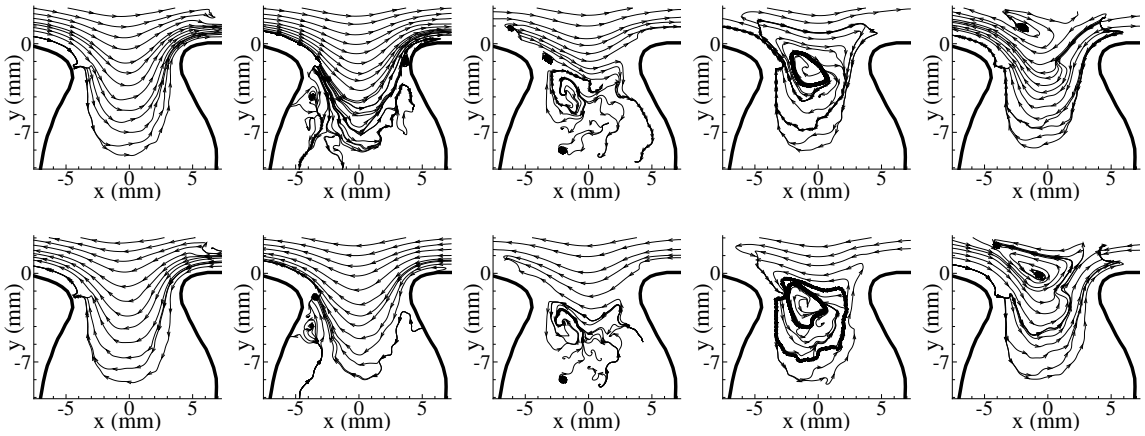

Figure C13: DMD mode for $\alpha = 2$, $Re_p = 50$ constructed for 1.6 Hz. Top row: flow evolution for half-cycle. Bottom row: flow evolution for second half-cycle.

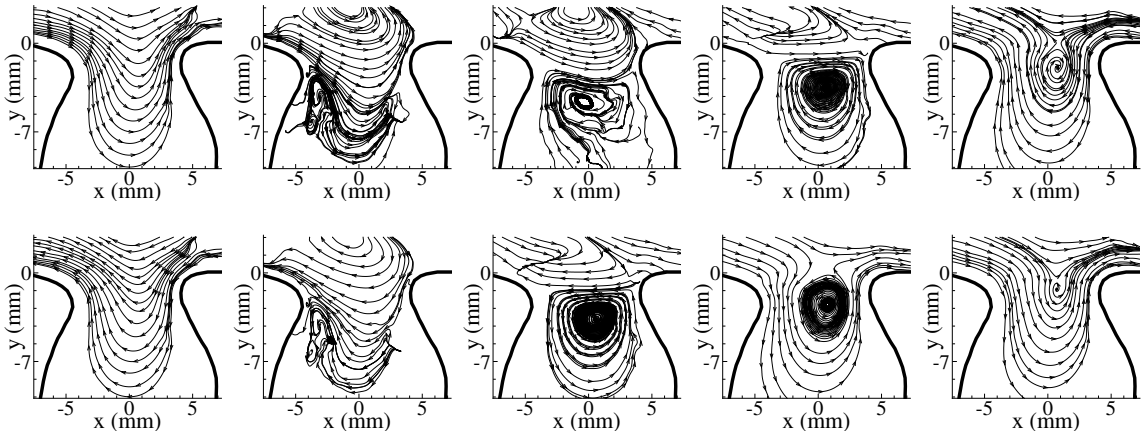

Figure C14: DMD mode for $\alpha = 2$, $Re_p = 270$ constructed for 0.4 Hz. Top row: flow evolution for half-cycle. Bottom row: flow evolution for second half-cycle.

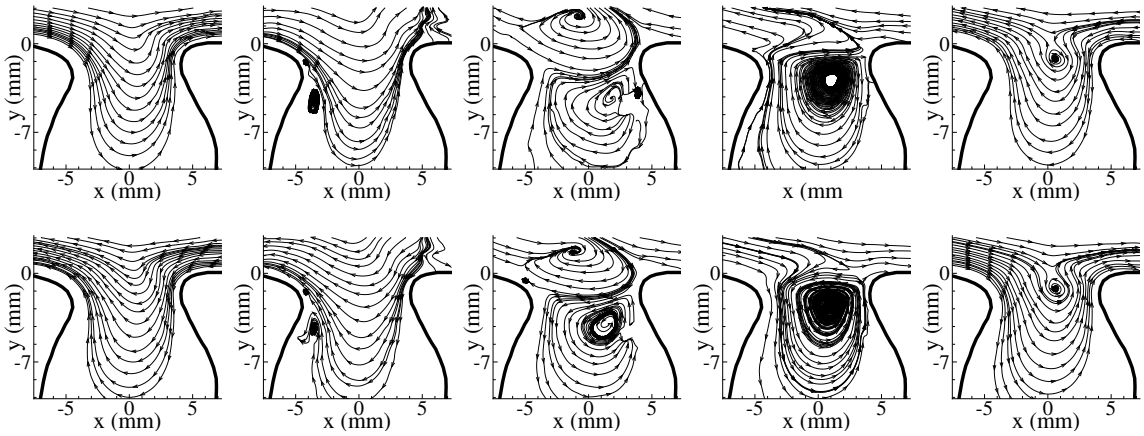

Figure C15: DMD mode for $\alpha = 2$, $Re_p = 270$ constructed for 0.8 Hz. Top row: flow evolution for half-cycle. Bottom row: flow evolution for second half-cycle.

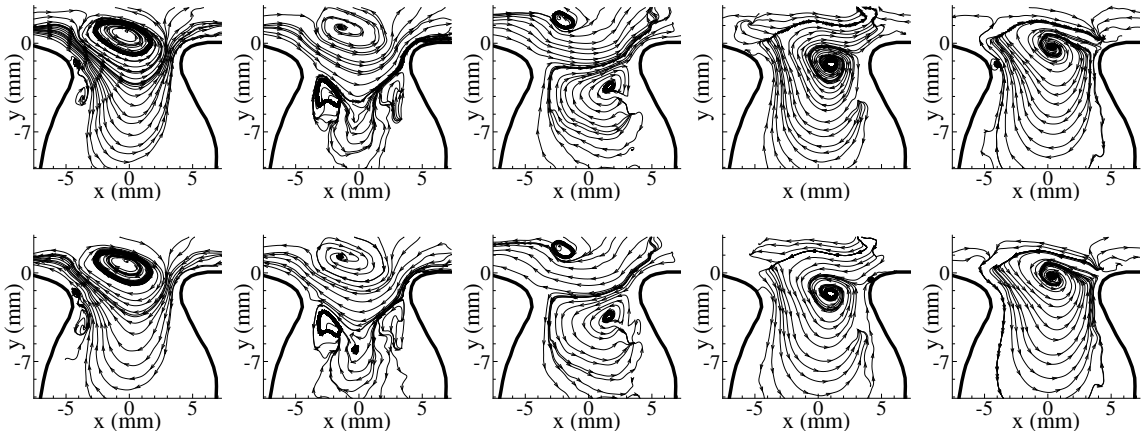

Figure C16: DMD mode for $\alpha = 2$, $Re_p = 270$ constructed for 1.6 Hz. Top row: flow evolution for half-cycle. Bottom row: flow evolution for second half-cycle.

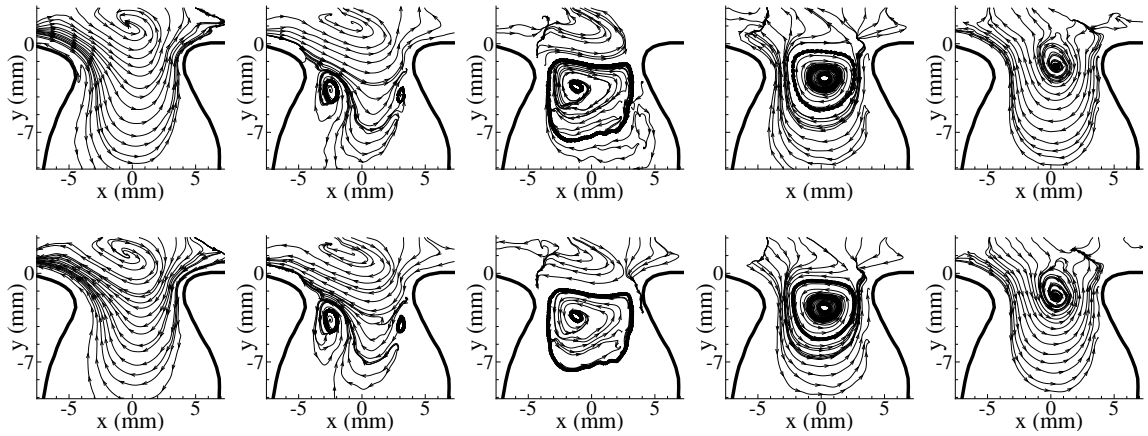

Figure C17: DMD mode for $\alpha = 2$, $Re_p = 270$ constructed for 2.4 Hz. Top row: flow evolution for half-cycle. Bottom row: flow evolution for second half-cycle.

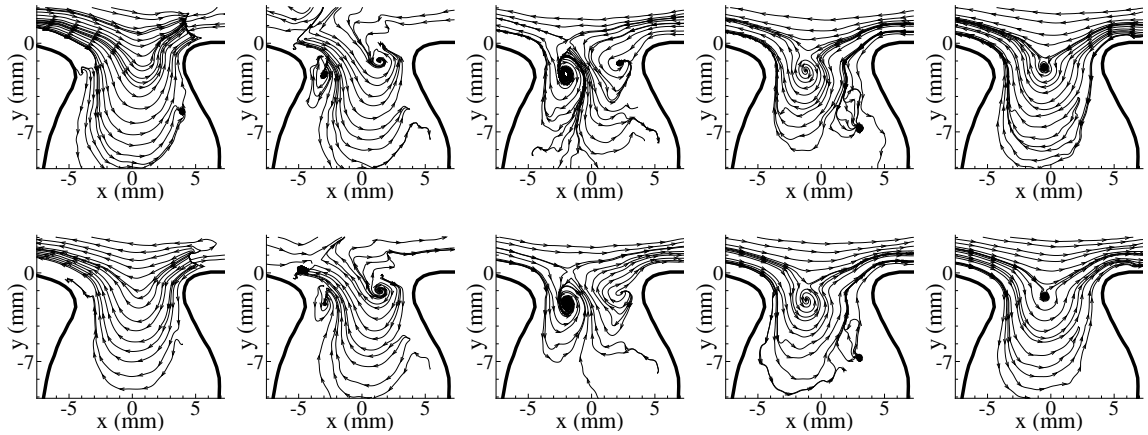

Figure C18: DMD mode for $\alpha = 2$, $Re_p = 270$ constructed for 2.8 Hz. Top row: flow evolution for half-cycle. Bottom row: flow evolution for second half-cycle.

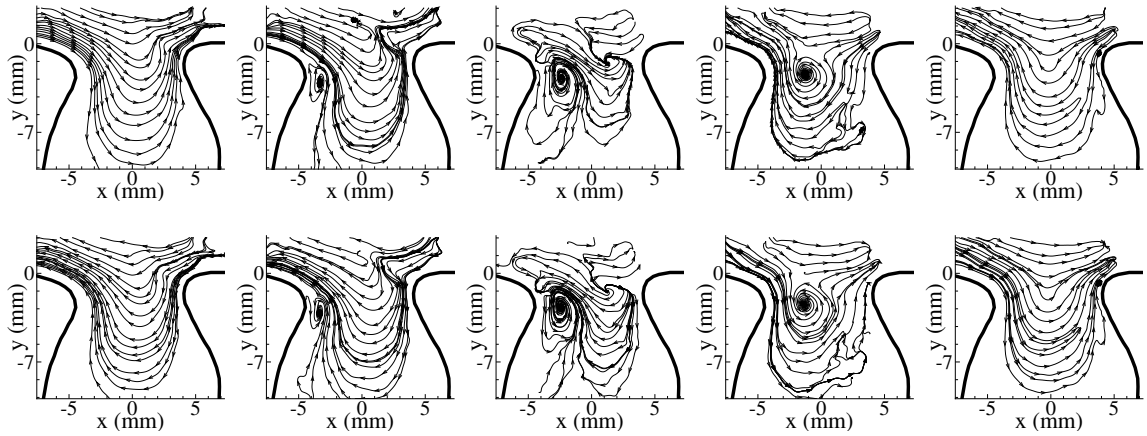

Figure C19: DMD mode for $\alpha = 2$, $Re_p = 270$ constructed for 3.2 Hz. Top row: flow evolution for half-cycle. Bottom row: flow evolution for second half-cycle.

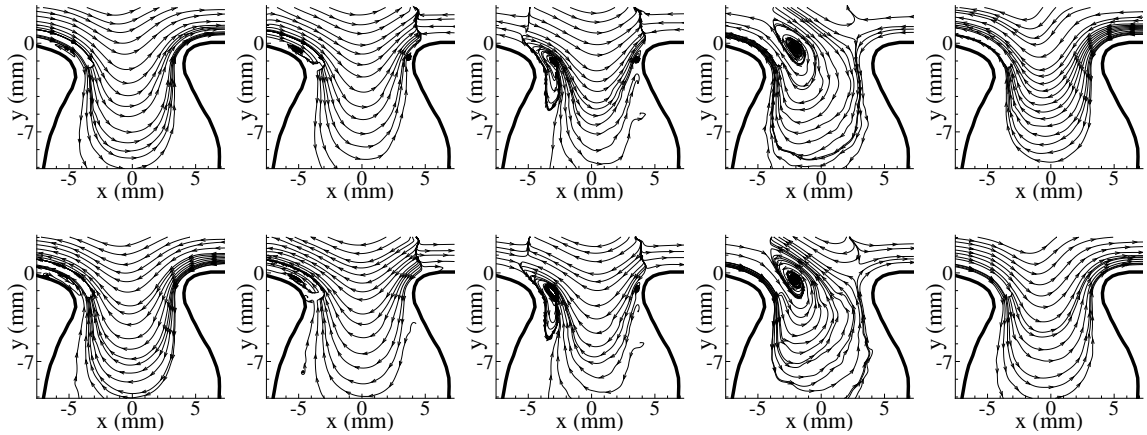

Figure C20: DMD mode for $\alpha = 5$, $Re_p = 50$ constructed for 2.4 Hz. Top row: flow evolution for half-cycle. Bottom row: flow evolution for second half-cycle.

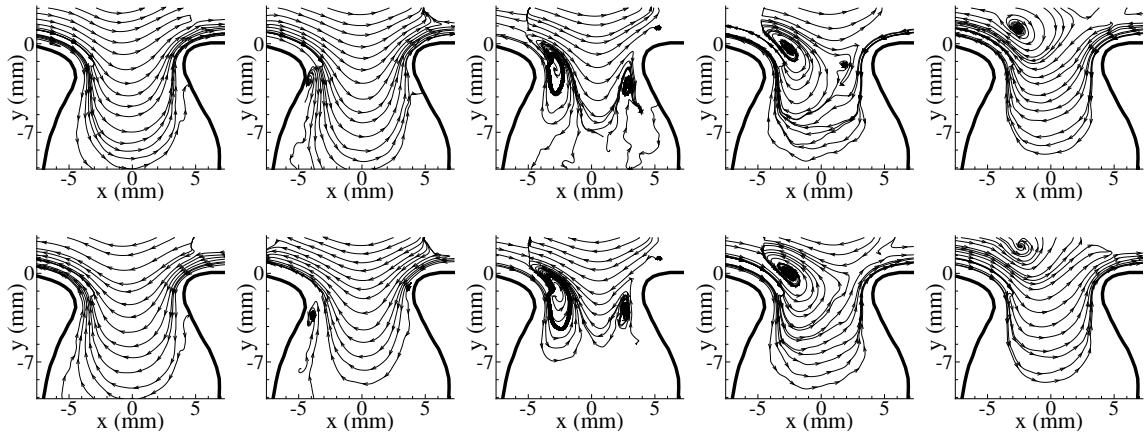

Figure C21: DMD mode for $\alpha = 5$, $Re_p = 50$ constructed for 4.8 Hz. Top row: flow evolution for half-cycle. Bottom row: flow evolution for second half-cycle.

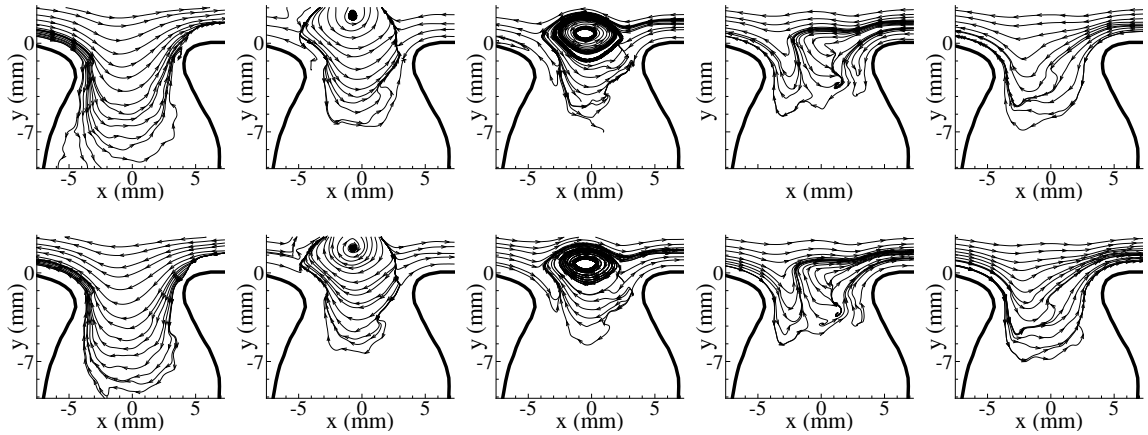

Figure C22: DMD mode for $\alpha = 5$, $Re_p = 50$ constructed for 7.2 Hz. Top row: flow evolution for half-cycle. Bottom row: flow evolution for second half-cycle.

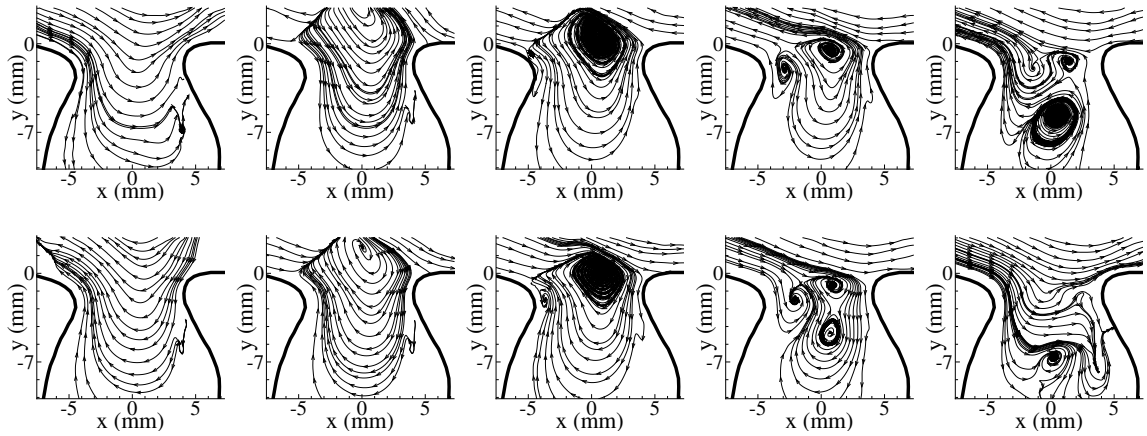

Figure C23: DMD mode for $\alpha = 5$, $Re_p = 270$ constructed for 2.4 Hz. Top row: flow evolution for half-cycle. Bottom row: flow evolution for second half-cycle.

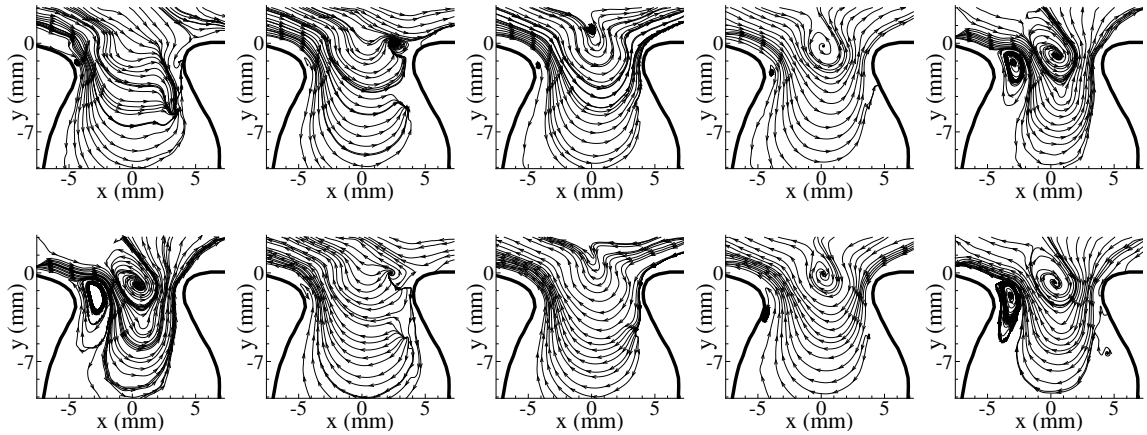

Figure C24: DMD mode for $\alpha = 5$, $Re_p = 270$ constructed for 4.8 Hz. Top row: flow evolution for half-cycle. Bottom row: flow evolution for second half-cycle.

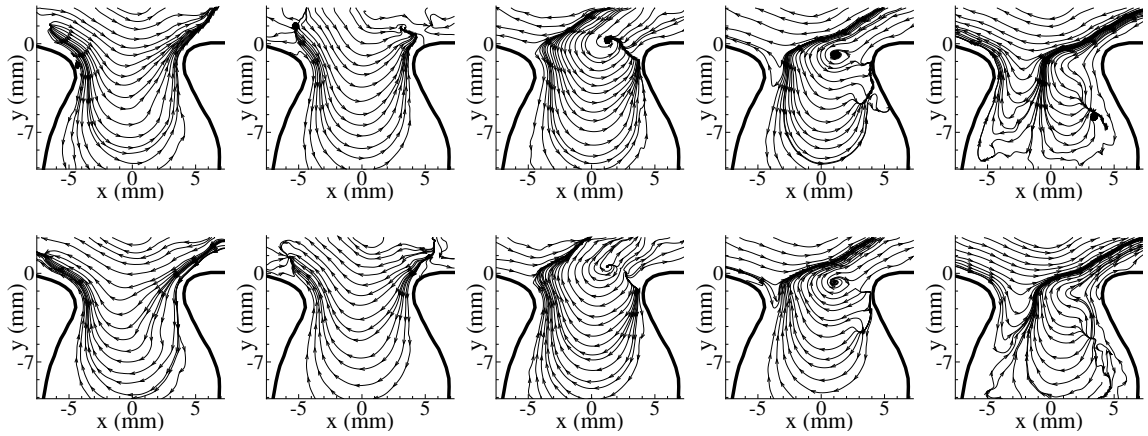

Figure C25: DMD mode for $\alpha = 5$, $Re_p = 270$ constructed for 7.2 Hz. Top row: flow evolution for half-cycle. Bottom row: flow evolution for second half-cycle.

DMD low-order reconstruction for $BF = 1.6$

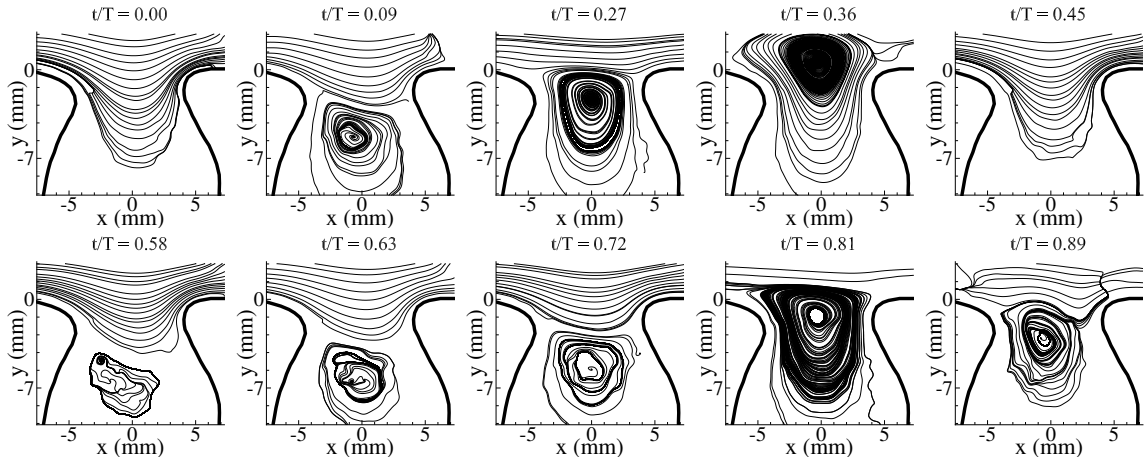

Figure C26: DMD low-order reconstruction for $Re_p = 50$, $\alpha = 2$, and $BF = 1.6$.

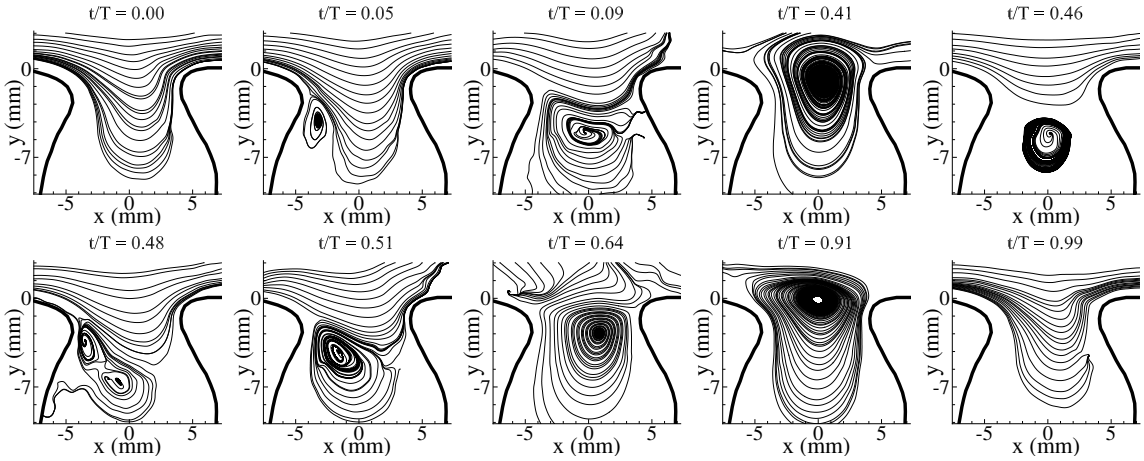

Figure C27: DMD low-order reconstruction for $Re_p = 270$, $\alpha = 2$, and $BF = 1.6$.

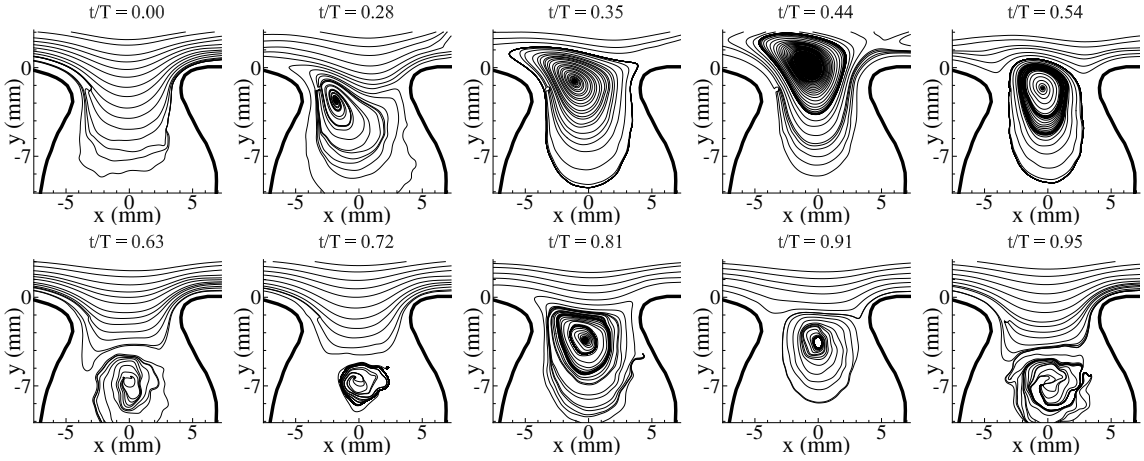

Figure C28: DMD low-order reconstruction for $Re_p = 50$, $\alpha = 5$, and $BF = 1.6$.

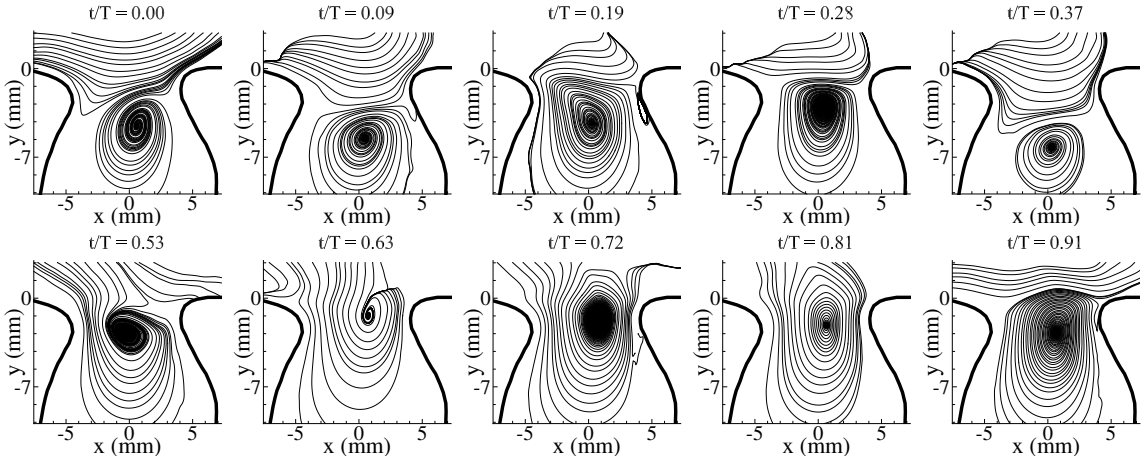

Figure C29: DMD low-order reconstruction for $Re_p = 270$, $\alpha = 5$, and $BF = 1.6$.

Appendix D: Flow conditions

Flow conditions

Table D1: Test conditions used for α of 2 for mid-plane measurement

Region	BF	Window Size (pixel x pixel)	Field of View (mm x mm)	dt(μs)		
				Re=50	Re=150	Re=270
Pipe	1.0	32x32	32x10	2000	1000	500
Neck	1.0	32x32	18x14	3000	3000	1000
Sac	1.0	32x32	18x8	10000	6000	1200
Pipe	1.6	32x32	34x10	2000	1000	400
Neck	1.6	32x32	16x13	8000	4000	5000
Sac	1.6	32x32	17x18	60000	60000	60000

Table D2: Test conditions used for α of 5 for mid-plane measurement

Region	BF	Window Size (pixel x pixel)	Field of View (mm x mm)	dt(μs)		
				Re=50	Re=150	Re=270
Pipe	1.0	32x32	32x10	2000	1500	500
Neck	1.0	32x32	18x14	5000	2000	1000
Sac	1.0	32x32	18x8	10000	6000	1500
Pipe	1.6	32x32	34x10	2000	1500	400
Neck	1.6	32x32	16x13	8000	4000	5000
Sac	1.6	32x32	17x18	60000	60000	60000

Table D3: Test conditions used for α of 2 in the sac region

Plane	BF	Window Size (pixel x pixel)	Field of View (mm x mm)	dt(μs)		
				Re=50	Re=150	Re=270
2mm	1.0	32x32	18x14	5000	3000	1500
4mm	1.0	32x32	18x14	8000	5000	3000

Table D4: Test conditions used for α of 5 in the sac region

Plane	BF	Window Size (pixel x pixel)	Field of View (mm x mm)	dt(μs)		
				Re=50	Re=150	Re=270
2mm	1.0	32x32	18x14	8000	4000	1500
4mm	1.0	32x32	18x14	8000	4000	2000